



Neutron to Hidden Neutron Oscillations in Ultra-Cold Neutron Beams

William Saenz

► To cite this version:

William Saenz. Neutron to Hidden Neutron Oscillations in Ultra-Cold Neutron Beams. Physics [physics]. Normandie Université, 2022. English. NNT : 2022NORMC254 . tel-04023774

HAL Id: tel-04023774

<https://theses.hal.science/tel-04023774>

Submitted on 10 Mar 2023

HAL is a multi-disciplinary open access archive for the deposit and dissemination of scientific research documents, whether they are published or not. The documents may come from teaching and research institutions in France or abroad, or from public or private research centers.

L'archive ouverte pluridisciplinaire **HAL**, est destinée au dépôt et à la diffusion de documents scientifiques de niveau recherche, publiés ou non, émanant des établissements d'enseignement et de recherche français ou étrangers, des laboratoires publics ou privés.



Normandie Université

THÈSE

Pour obtenir le diplôme de doctorat

Spécialité **PHYSIQUE**

Préparée au sein de l'Université de Caen Normandie

Neutron to Hidden Neutron Oscillations in Ultra-Cold Neutron Beams

Présentée et soutenue par
WILLIAM SAENZ

Thèse soutenue le 02/12/2022
devant le jury composé de

M. KLAUS KIRCH	Professeur, Ecole polytechnique fédérale de Zurich	Rapporteur du jury
M. JACOB LAMBLIN	Maître de conférences HDR, Université Grenoble Alpes	Rapporteur du jury
MME LEAH BROUSSARD	Chercheur, Laboratoire national d'Oak Ridge	Membre du jury
MME SACHA DAVIDSON	Directeur de recherche, Université de Montpellier	Membre du jury
M. THOMAS LEFORT	Maître de conférences, Université de Caen Normandie	Membre du jury Co-encadrant
MME STÉPHANIE ROCCIA	Maître de conférences, Université Grenoble Alpes	Membre du jury
M. ETIENNE LIENARD	Professeur des universités, Université de Caen Normandie	Président du jury

Thèse dirigée par **GILLES BAN (Laboratoire de physique corpusculaire (Caen))**



Abstract

Oscillations of the neutron into a hidden sector particle ($n - n'$) are processes predicted in various Standard Model extensions. In case of finding evidence of them, models proposing the existence of hidden sectors, such as those hosting twin copies of all known particles [1, 2], or those introducing a high dimensional bulk of which slices (branes) represent different universes [3], would gain importance in particle physics and cosmology. These theories are of special interest as they could explain big issues in contemporary physics such as baryogenesis and dark matter [4].

It has been proposed that mixing between ordinary and hidden sectors is possible for neutral particles. For example, several studies have looked for photon - hidden photon oscillations with ortho-positronium experiments [5], and for neutrino - hidden neutrino oscillations in shot-baseline neutrino setups [6]. Neutron - hidden neutron oscillations have been searched for low and high mass-splitting (δm) in stored ultra-cold neutrons (UCN) [7–11] and regeneration experiments [12–15], respectively.

Since this extra channel for neutron disappearance has not been tested in large portions of the oscillation parameter space, we present the development of an experiment searching for $n - n'$ oscillations at intermediate δm via the application of magnetic fields in the range $50 - 1100 \mu\text{T}$. The experiment was performed in autumn 2020 at the Institut-Langevin (ILL), using the novel UCN counter GADGET [16] to monitor the UCN beam flux while scanning the magnetic field. This work, which is the first long-term basis test of the GADGET detector, allowed a full characterization of its detection efficiency and the development of the pulse shape analysis technique. Also, as no previous study reports on the UCN flux constancy at the EDM beam port of ILL's PF2 at the scale of seconds, we evaluated the UCN beam stability with a time resolutions of up to μs .

The data revealed non-statistical fluctuations affecting the UCN counting rate, which were explained by the reactor power variations at the scale of seconds. After accounting for such fluctuations and by including the magnetic field inhomogeneities in the analysis, no significant signal of oscillations was found. However, a new limit on the $n - n'$ model parameters was set as

$$\tau_{nn'} > 1 \text{ s for } |\delta m| \in [2 - 69] \times 10^{-12} \text{ eV (95\% C.L.)}.$$

Using the same data set, the bound was also computed within the hidden magnetic field approach [17], which resulted

$$\tau_{nn'} > 1 \text{ s for } B' \in [50 - 1130] \mu\text{T (95\% C.L.)}.$$

Resumen

Las oscilaciones del neutrón en partículas de sectores ocultos ($n - n'$) son procesos descritos en varias extensiones del Modelo Estándar. En caso de encontrar evidencia, modelos como aquellos que proponen la existencia de sectores que albergan copias gemelas de todas las partículas conocidas [1,2], o los que introducen un volumen multi-dimensional cuyas rebanadas representan universos diferentes [3], ganarían importancia en física de partículas y cosmología. Estas teorías son de especial interés, ya que podrían explicar grandes problemas de la física contemporánea como lo son la bariogénesis y la materia oscura [4].

Se ha propuesto que la mezcla entre sectores ordinarios y ocultos es posible para partículas neutras. Por ejemplo, varios estudios han buscado oscilaciones de fotones en fotones ocultos con experimentos de ortopositronios [5], y oscilaciones de neutrinos en neutrinos ocultos con experimentos a corto rango [6]. Del mismo modo, se han buscado las oscilaciones $n - n'$, suponiendo altas y bajas diferencias de masa (δm) en experimentos con neutrones ultra-fríos (UCN) almacenados [7–11] y en experimentos de regeneración [12–15], respectivamente.

Dado que este canal de desaparición de neutrones no se ha probado en grandes porciones del espacio de parámetros, este trabajo presenta el desarrollo de un nuevo experimento buscando las oscilaciones $n - n'$ con δm intermedias mediante la aplicación de campos magnéticos en el rango $50 - 1100 \mu\text{T}$. El experimento, que se llevó a cabo en otoño de 2020 en el Institut-Laue-Langevin (ILL), utilizó el novedoso contador UCN GADGET [16] para monitorear el flujo del haz de UCN mientras se escaneaba el campo magnético. Este trabajo, que representó la primera prueba a largo plazo del detector GADGET, permitió una caracterización completa de su eficiencia de detección y el desarrollo de la técnica de análisis de forma de pulso. Además, dado que ningún estudio anterior ha reportado sobre la constancia del flujo de UCN en el ILL a la escala de segundos, se evaluó aquí su estabilidad con resoluciones de tiempo de hasta algunos μs .

Los datos revelaron fluctuaciones no estadísticas en la tasa de conteo de UCN debidas a variaciones de la potencia del reactor en la escala de segundos. Después de tener en cuenta tales fluctuaciones y de incluir las inhomogeneidades del campo magnético en el análisis, no se encontró ninguna señal significativa de oscilaciones. Sin embargo, se estableció un nuevo límite en los parámetros del modelo $n - n'$, simplificado en

$$\tau_{nn'} > 1 \text{ s para } |\delta m| \in [2 - 69] \times 10^{-12} \text{ eV (95\% C.L.)}. \quad (1)$$

Usando el mismo conjunto de datos, el límite también se calculó dentro del enfoque de campo magnético oculto [17], lo que resultó

$$\tau_{nn'} > 1 \text{ s para } B' \in [50 - 1130] \mu\text{T (95\% C.L.)}. \quad (2)$$

Resumé

Les oscillations des neutrons vers des secteurs cachés ($n - n'$) sont des processus décrits dans diverses extensions du Modèle Standard. Les modèles tels que ceux proposant l'existence de secteurs abritant des copies jumelles de toutes les particules connues [1, 2], et ceux introduisant un volume multidimensionnel dont les tranches représentent différents univers [3], gagneraient en importance en physique des particules et en cosmologie en cas de découverte de preuves d'oscillations $n - n'$. Ces théories présentent un intérêt particulier car elles pourraient expliquer des problèmes majeurs de la physique contemporaine tels que la baryogénèse et la matière noire [4].

Il a été proposé que le mélange entre les secteurs ordinaires et cachés est possible pour les particules neutres. Par exemple, plusieurs études ont recherché des oscillations de photons vers des photons cachés avec des expériences d'orthopositons [5], et des oscillations de neutrinos vers des neutrinos cachés par le biais des expériences à courte distance [6]. De même, des oscillations $n - n'$ ont été recherchées en supposant des différences de masse (δm) élevées avec des neutrons ultra-froids (UCN) stockés [7–11] et δm faibles dans des expériences de régénération [12–15].

Ce travail présente le développement d'une nouvelle expérience recherchant les oscillations $n - n'$ avec une δm intermédiaire en appliquant des champs magnétiques dans la gamme 50 – 1100 μT . Ceci, puisque ce canal de disparition des neutrons n'a pas été testé dans une grande portion de l'espace des paramètres $n - n'$.

Cette expérience réalisée à l'automne 2020 à l'Institut-Laue-Langevin (ILL), a utilisé le nouveau compteur UCN GADGET [16] pour surveiller le flux du faisceau UCN tout en balayant le champ magnétique. Ce travail représente le premier test à long terme du détecteur GADGET. Ce dernier a permis une caractérisation complète de son efficacité de détection et le développement de la technique *Pulse Shape Analysis*. De plus, ce travail fait état de la constance du flux UCN de l'ILL jusqu'à une échelle de quelques μs . Ceci n'avait jamais été réalisé auparavant.

Les données ont révélé des fluctuations non statistiques du taux de comptage UCN dues aux variations de la puissance du réacteur à l'échelle des secondes. Après avoir pris en compte ces fluctuations et inclus les inhomogénéités du champ magnétique dans l'analyse, aucune oscillation significative n'a été trouvée. Cependant, une nouvelle limite a été fixée sur les paramètres du modèle $n - n'$, simplifiée à

$$\tau_{nn'} > 1 \text{ s for } |\delta m| \in [2 - 69] \times 10^{-12} \text{ eV (95\% C.L.)}. \quad (3)$$

En utilisant le même ensemble de données, la limite a également été calculée dans l'approche du champ magnétique caché [17], ce qui a entraîné

$$\tau_{nn'} > 1 \text{ s for } B' \in [50 - 1130] \mu\text{T (95\% C.L.)}. \quad (4)$$

Contents

Abstract	iii
I La thèse en français	1
1 Introduction	3
2 GADGET : Un nouveau compteur UCN	7
3 $n - n'$ oscillations : Description expérimentale	13
4 $n - n'$ oscillations : analyse des données	17
II The part in English	21
Introduction	23
1 UCN and hidden sector searches	25
1.1 Hidden matter	25
1.2 Mixing mechanisms	26
1.3 Neutron - hidden neutron oscillations	28
1.3.1 Oscillation probability: general description	28
1.3.2 Oscillations without environmental hidden potentials ($\Delta E' = 0$) . . .	30
1.3.3 Oscillation in presence of hidden magnetic fields (\vec{B}')	32
1.4 State of the art: Past $n - n'$ oscillation tests	33
1.4.1 Neutron disappearance	33
1.4.2 Neutron regeneration	36
1.5 UCN physics	39
1.5.1 UCN interactions	39
1.5.2 UCN sources	41
1.6 Chapter conclusions	43
2 GADGET: A novel UCN counter	45
2.1 State of the art	45
2.1.1 Overview of UCN detectors	46
2.2 Description and detection principle of GADGET	48

2.2.1	Data acquisition: FASTER	49
2.2.2	Detector entrance window	52
2.2.3	Influence of the ^3He and CF_4 pressures	53
2.3	Pulse Shape Analysis (PSA)	54
2.3.1	PS parameter	55
2.3.2	Dalitz-plots	55
2.3.3	UCN beam in empty gas chamber at ILL	57
2.3.4	γ and β (^{137}Cs source) on CF_4	58
2.3.5	UCN beam on pure CF_4	61
2.3.6	UCN beam on CF_4 (500 mbar) + ^3He (15 mbar) admixture	63
2.4	Optimization of the ^3He and CF_4 gas pressures	65
2.4.1	Measured signal as a function of $P_{^3\text{He}}$ and P_{CF_4}	66
2.4.2	Detection efficiency as a function of $P_{^3\text{He}}$ and P_{CF_4}	67
2.5	Chapter conclusions	69
3	$n - n'$ oscillations: experimental description, data taking procedure and expected sensitivity	71
3.1	Experimental description of the setup	71
3.1.1	Magnetic field and UCN guide arrangement	72
3.2	Data collection technique	74
3.2.1	Resonance width & scanning step	74
3.2.2	UCN flux constancy	75
3.2.3	The ABBC measuring sequence	75
3.2.4	Synchronization and recording algorithm	77
3.3	Expected sensitivity (ideal case)	78
3.4	Preliminary analysis	82
3.4.1	Monte Carlo simulation of UCN tracks	82
3.4.2	GADGET performance in magnetic fields	85
3.4.3	Magnetic field inhomogeneities	87
3.5	Chapter conclusions	90
4	$n - n'$ oscillations: Data analysis	93
4.1	UCN category selection	93
4.2	Acquired data summary	95
4.3	Systematics: UCN flux fluctuations	96
4.3.1	Flux stability within hours (scan level)	97
4.3.2	Flux stability within minutes (cycles level)	97
4.3.3	Flux stability within seconds (within cycles)	100
4.3.4	Flux stability within milliseconds	103
4.3.5	Flux stability within microseconds	105
4.3.6	Data correction from reactor power fluctuations	106
4.4	Probing oscillations as a function of δm ($B' = 0$)	110
4.4.1	Oscillation probability: Numerical and analytical solutions	112
4.4.2	Looking for resonances	118
4.4.3	Parameter exclusion	120
4.4.4	Robustness of the results	123

4.5	Oscillations in presence of hidden magnetic fields ($\delta m = 0$)	126
4.5.1	Numerical solution	126
4.5.2	Parameter exclusion	129
4.6	Chapter conclusions	131
5	Overview and perspectives	133
5.1	Overview	133
5.2	Perspectives	137
	Appendices	139
A	From mirror to hidden neutrons	141
B	Absorption probability	145
C	ABBC and linear drifts	147
D	From rate to R_{ABC} non-statistical fluctuations	149
E	Numerical solution of $\mathcal{H}_{nn'}$	151
E.1	Mass-splitting scenario	151
E.1.1	Biondi's method	151
E.1.2	Liouville-Neumann equation	152
E.2	Hidden magnetic field scenario	153
F	PMT inside magnetic fields	155
G	The n2EDM spin-sensitive counter	157
G.1	Working principle	157
G.2	Past USSA and new version requirements	159
G.3	Modeling the n2EDM USSA	160
G.3.1	Shaping the RF-field	162
G.3.2	Efficiency estimation from spin tracking algorithms	162
G.3.3	Summary	165
	Acknowledgements	179

Part I

La thèse en français

Chapter 1

Introduction

Bien que le rôle des neutrons dans la vie quotidienne ne soit pas évident, car leur neutralité de charge les exempte des interactions électromagnétiques, nous avons appris qu'ils jouent un rôle important dans la liaison des noyaux atomiques. Etant donné que la teneur en neutrons de tous les noyaux stables, à part l'hydrogène, est égale ou supérieure à la teneur en protons, on peut affirmer qu'environ la moitié de la matière de la vie quotidienne est composée de neutrons, c'est-à-dire qu'ils sont responsables de la moitié de la masse de la matière visible. Leur contribution est importante en tant que pièce de la matière, et l'étude des propriétés des neutrons demande des efforts technologiques considérables. Contrairement aux électrons, qui peuvent être facilement retirés des atomes avec des énergies de l'ordre de l'eV, la forte liaison entre les neutrons et les noyaux, due à la force nucléaire, nécessite des énergies aussi importantes que quelques MeV pour expulser un neutron de son noyau d'accueil. De plus, une fois éjecté d'un noyau, un neutron libre n'a pas beaucoup de temps pour marquer les esprits. En moyenne, il survit environ 15 minutes avant de se désintégrer en d'autres types de particules. Par conséquent, lorsque vous regardez votre chat de 2 kg, vous regardez 1 kg de neutrons piégés dans les noyaux du chat. Tous ces neutrons, formés il y a 13,6 milliards d'années, ne survivraient pas plus de deux heures s'ils n'étaient pas liés aux protons du chat.

Même à l'heure actuelle, non seulement les propriétaires de chats, mais de nombreux physiciens nucléaires et des particules sont surpris lorsqu'ils entendent, pour la première fois, parler des techniques expérimentales permettant la manipulation de neutrons libres pendant des périodes aussi longues que la durée de vie des neutrons. Bien que l'idée de stocker les neutrons dans des récipients fermés ait été proposée en 1959 par Zeldovich [18], elle n'a été réalisée expérimentalement que 9 ans plus tard, simultanément par Shapiro *et al.* et Steyerl *et al.* [19]. Essentiellement, lorsque l'énergie des neutrons libres est réduite en dessous du potentiel optique neutronique d'un matériau (par exemple 335 neV pour ^{58}Ni), ils subissent une réflexion totale. Ces propriétés de réflexion, utilisées pour classer les neutrons en tant que neutrons ultra-froids (UCN), peuvent être décrites par la mécanique quantique classique et miment les propriétés de réflexion de la lumière. On parle alors d'optique neutronique.

Depuis la construction des premières bouteilles de stockage UCN, et sur plus de 50 ans, de multiples recherches sur la physique de haute précision ont été menées avec les expériences UCN. Par exemple, dans la mesure du moment dipolaire électrique des neutrons (EDM), la durée de vie des neutrons et ses niveaux d'énergie bornés dans le potentiel gravitationnel de la Terre. Dans ce travail, nous présentons une nouvelle approche pour l'étude des oscillations neutrons

- neutrons cachés provenant de la disparition des neutrons dans les faisceaux UCN. Les états cachés de la matière, qui pourraient correspondre à des secteurs parallèles hébergeant des copies miroir de toutes les particules connues, ou à différentes branes d'un volume multidimensionnel, sont conçus dans un modèle mathématique simple avec une phénoménologie assez riche en physique des particules à basse énergie et en cosmologie.

En adoptant le modèle à deux secteurs, l'hamiltonien décrivant le mélange entre neutrons libres et neutrons libres cachés est

$$\hat{\mathcal{H}}_{nn'} = \begin{pmatrix} E_n & \epsilon_{nn'} \\ \epsilon_{nn'} & E_{n'} \end{pmatrix}, \quad (1.1)$$

avec E_n ($E_{n'}$) l'énergie du neutron (neutron caché) et $\epsilon_{nn'} = \tau_{nn'}^{-1}$ le paramètre de mélange de masse (avec $\hbar = c = 1$). Les éléments de matrice dans l'équation (1.1) sont en fait des matrices 2×2 d'états de spin, qui peuvent être supposées diagonales en raison de la conservation du spin. Néanmoins, si les termes d'énergie E_n et $E_{n'}$ incluent des interactions dépendantes du spin pour lesquelles les axes de quantification privilégiés des secteurs ordinaires et cachés ne coïncident pas, par ex. scénarios avec des champs magnétiques cachés (miroir), un traitement sensible au spin doit être envisagé [17].

Le phénomène de mélange $n - n'$ a été formulé en supposant une symétrie \mathbb{Z}_2 parfaite, à partir de laquelle les masses des neutrons et des neutrons cachés sont identiques $m_n = m_{n'}$. Cependant, il peut arriver que \mathbb{Z}_2 soit spontanément cassé par des corrections quantiques d'ordre supérieur, donnant lieu à un petit dédoublement de masse $\delta m = m_{n'} - m_n$ [20]. Supposons un secteur caché dont la densité de matière sur Terre est suffisamment faible pour que les potentiels cachés de l'environnement, en particulier les champs magnétiques cachés, puissent être négligés. Par conséquent, l'hamiltonien dans l'équation. (1.1) est exprimé comme

$$\begin{aligned} \hat{\mathcal{H}}_{nn'} &= \begin{pmatrix} m_n + \Delta E & \epsilon_{nn'} \\ \epsilon_{nn'} & m_{n'} \end{pmatrix} \\ &= \begin{pmatrix} \Delta E & \epsilon_{nn'} \\ \epsilon_{nn'} & \delta m \end{pmatrix} + m_n \begin{pmatrix} \mathbb{I}_{2 \times 2} & 0 \\ 0 & \mathbb{I}_{2 \times 2} \end{pmatrix} \\ &= \begin{pmatrix} \Delta E & \epsilon_{nn'} \\ \epsilon_{nn'} & \delta m \end{pmatrix}, \end{aligned} \quad (1.2)$$

où nous avons supprimé le terme $m_n \mathbb{I}_{4 \times 4}$ car il ne modifie pas la dynamique d'oscillation $n - n'$. Étant donné que tous les éléments de cette dernière expression sont des matrices diagonales 2×2 , sa solution sur l'équation de Schrödinger est équivalente au très connu système quantique à deux niveaux. Les états de masse et leurs énergies (vecteurs propres et valeurs propres) sont donc donnés par

$$\tilde{E}_{\pm} = \frac{1}{2} \left[(\Delta E - \delta m) \pm \sqrt{(\Delta E - \delta m)^2 + 4 \epsilon_{nn'}^2} \right],$$

et

$$\begin{aligned} |\psi_+\rangle &= \cos \theta |n\rangle + \sin \theta |n'\rangle \\ |\psi_-\rangle &= -\sin \theta |n\rangle + \cos \theta |n'\rangle, \end{aligned}$$

respectivement, où l'amplitude de mélange θ est définie comme

$$\sin^2 2\theta = \frac{4\epsilon_{nn'}^2}{4\epsilon_{nn'}^2 + (\Delta E - \delta m)^2}.$$

Suivant cette notation, un neutron libre à $t = 0$ serait décrit par l'état $|\psi(0)\rangle = |n\rangle = \cos \theta |\psi_+\rangle - \sin \theta |\psi_-\rangle$, dont la propagation dans le temps est

$$|\psi(t)\rangle = \cos \theta e^{-i\tilde{E}_+ t} |\psi_+\rangle - \sin \theta e^{-i\tilde{E}_- t} |\psi_-\rangle. \quad (1.3)$$

Ensuite, la probabilité d'oscillation $n - n'$ après un temps de vol libre t_f est calculée à partir de l'amplitude $|\langle n' | \psi(t_f) \rangle|$, ce qui donne :

$$P_{nn'}(t_f) = \frac{4\epsilon_{nn'}^2}{4\epsilon_{nn'}^2 + (\Delta E - \delta m)^2} \sin^2 \left(\frac{\sqrt{(\Delta E - \delta m)^2 + 4\epsilon_{nn'}^2} t_f}{2} \right). \quad (1.4)$$

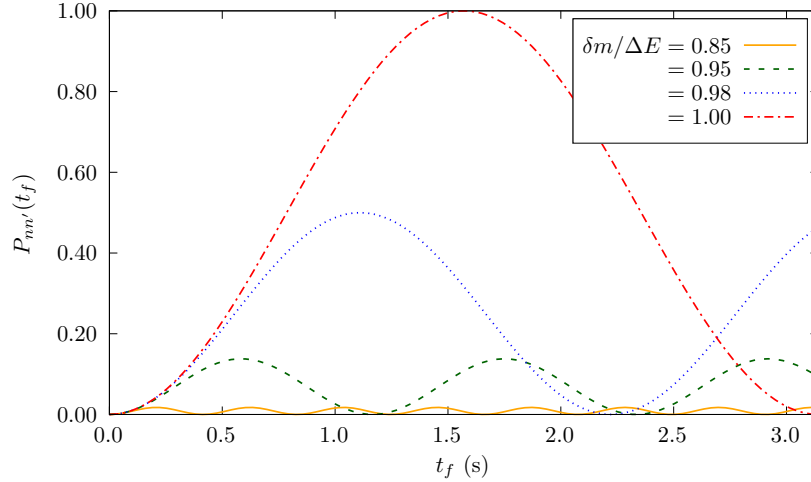


Figure 1.1: $n - n'$ probabilité d'oscillation en fonction du temps de vol libre en supposant $\tau_{nn'} = 1$ s et $\delta m = 10^{-14}$ eV. Le comportement, illustré pour différents rapports $\delta m / \Delta E$, démontre que l'amplitude de mélange $\sin^2 2\theta$ et la fréquence d'oscillation $\frac{1}{2} \sqrt{\Delta_{nn'}^2 + 4\epsilon_{nn'}^2}$ sont respectivement le maximum et le minimum à la résonance $\delta m / \Delta E \rightarrow 1$ ($\Delta_{nn'} = 0$).

Cette dernière expression montre que le mélange maximal est atteint à la condition de résonance où la dégénérescence d'énergie $n - n'$ est complètement supprimée, c'est-à-dire $\sin^2 2\theta = 1$ avec

$$\Delta_{nn'} = \Delta E - \delta m = 0. \quad (1.5)$$

Dans ce cas, la probabilité d'oscillation devient 1 toutes les $(2n + 1)\pi\tau_{nn'}/2$ secondes, avec $n = 0, 1, 2, \dots$. Pour les valeurs hors résonance, non seulement l'amplitude diminue comme $\sim 1/\Delta_{nn'}^2$ mais aussi la fréquence d'oscillation augmente proportionnellement à $\Delta_{nn'}$. Cette double caractéristique des oscillations $n - n'$ est représentée sur la figure 1.1 pour quatre valeurs de ΔE en supposant $\tau_{nn'} = 1$ s et $\delta m = 10^{-14}$ eV. À noter que contrairement aux oscillations

des neutrinos, où l'amplitude de mélange $\sin^2 2\theta$ est fixée par les paramètres du modèle. Le mélange $n - n'$ peut être maximal $P_{nn'} \sim 1$ si nous garantissons $\Delta E = \delta m$ ($\Delta_{nn'} = 0$) et permettons de longues périodes de temps de vol libre ($t_f \sim \epsilon_{nn'}^{-1}$). Par conséquent, pour sonder efficacement les oscillations $n - n'$, on pourrait s'intéresser par exemple à la disparition des neutrons en ajustant expérimentalement $\Delta E = \delta m$ tout en minimisant la fréquence de diffusion des neutrons avec son environnement. Ces deux idées sont à la base de montages expérimentaux sondant les oscillations $n - n'$ avec des neutrons ultra-froids.

Chapter 2

GADGET : Un nouveau compteur UCN

L'un des principaux objectifs de ce travail était la caractérisation et l'optimisation de l'un des détecteurs UCN les plus rapides jamais construits : le détecteur gazeux à scintillation GADGET. Ce nouveau compteur de neutrons a été conçu à l'origine dans le cadre du projet n2EDM, qui vise à mesurer le moment dipolaire électrique du neutron (d_n). Normalement, une mesure hautement sensible de d_n demande des efforts particuliers dans deux directions principales : réduire les effets systématiques et augmenter les statistiques de comptage. Ce dernier nécessite la mise en œuvre de détecteurs UCN à haute efficacité capables de discriminer le bruit de fond et d'effectuer des performances constantes dans des expériences de longue durée. GADGET apparaît comme un détecteur surclassant dans ces deux exigences simultanément [21]. De plus, les impulsions de tension rapides produites par la scintillation dans GADGET en font une option appropriée pour les expériences UCN à flux élevé.

Description et principe de détection

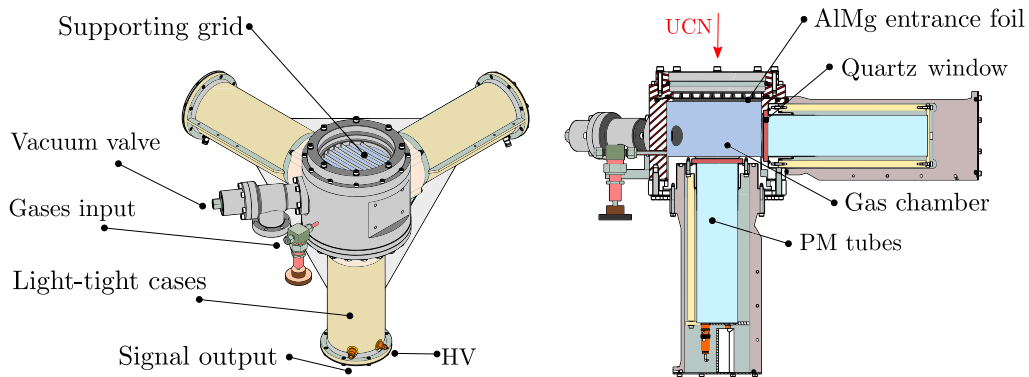
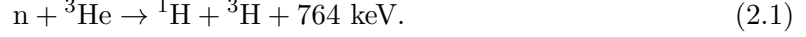


Figure 2.1: Schéma technique du détecteur GADGET indiquant ses composants principaux. Le côté gauche montre une vue 3D du détecteur déjà monté. A droite, une vue en coupe permet de voir l'intérieur des étuis et de la chambre. La flèche rouge indique la direction de l'UCN entrant dans la chambre.

GADGET est un détecteur UCN utilisant deux gaz pour compléter la détection indirecte.

En traversant la feuille d'entrée du détecteur, les neutrons sont absorbés par les noyaux ^3He . Émis après l'absorption, les produits de réaction proton et tritium partagent 764 keV selon



Un deuxième gaz est ensuite utilisé pour transformer une partie de cette énergie libérée en lumière. CF_4 est choisi en raison de son rendement photonique élevé, de sa transparence à sa propre lumière émise, de son inflammabilité, de son accessibilité et de son prix. Le passage du proton et du tritium à l'intérieur de ce gaz produit une ionisation et une scintillation directe à partir des états excités CF_4 [22]. Les durées de vie de ces émissions sont proches de 6 ns [23], ce qui rend la génération d'impulsions de signal très rapide par rapport aux détecteurs gazeux précédents [24]. La dernière étape du processus de détection, la collecte de la lumière, est complétée par un ensemble de trois tubes photomultiplicateurs (PMT) montés sur les fenêtres transparentes en quartz de la chambre à gaz. De la graisse optique est utilisée pour améliorer le contact optique en augmentant la transmission des photons de la fenêtre en quartz au PMT qui sont recouverts de boîtiers en plastique noir afin d'éviter la contamination par la lumière extérieure. La figure 2.1 montre une description générale des principaux constituants du détecteur.

Les formes d'onde d'impulsion produites par les PMT dépendent du processus d'interaction de la particule détectée. Le nombre de photons émis à l'intérieur de la chambre à gaz et la position d'absorption des neutrons sont deux des nombreux paramètres définissant les caractéristiques de ces impulsions. Les différences entre les formes d'onde sont donc exploitées pour déterminer le type de particule détectée. FASTER fournit un module spécialisé pour l'enregistrement d'impulsions qui extrait les principaux paramètres de forme de signal sans stocker l'intégralité du même. Ce module, nommé Qt2t, est basé sur un composant de traitement en ligne qui calcule la charge seuil à seuil, l'amplitude maximale, la durée seuil à seuil, la position du maximum et la charge avant seuil des impulsions [25].

Les principaux paramètres d'impulsion utilisés dans GADGET sont la charge seuil à seuil (Q_{t2t}) et l'amplitude maximale (A_{t2t}). Alors que le premier est proportionnel à la quantité de lumière détectée et donc à l'énergie de l'événement, le second peut être utilisé pour établir la rapidité de la collecte de lumière. Les deux paramètres sont déterminés à partir de l'échantillonnage de tension du signal $V(t)$ tous les 2 ns. Q_{t2t} correspond à l'intégrale temporelle de $V(t)$ entre les franchissements de seuil de pente positive (t_\uparrow) et négative (t_\downarrow), exprimé comme

$$Q_{t2t} = \frac{1}{R} \sum_{t=t_\uparrow}^{t=t_\downarrow} V(t) \Delta t = \frac{2 \times 10^{-9} \text{ s}}{50 \Omega} \sum_{t=t_\uparrow}^{t=t_\downarrow} V(t), \quad (2.2)$$

et l'amplitude maximale représente la plus grande tension entre t_\uparrow et t_\downarrow ($A_{t2t} = V_{\text{max}}$).

La technique de la triple coïncidence dans GADGET a un double objectif : la filtration en arrière-plan et la classification des événements. Normalement, un événement d'émission de lumière produit à l'intérieur de la chambre à gaz serait enregistré si les trois PMT sont déclenchés simultanément dans une fenêtre de temps donnée. Ces événements sont étiquetés avec un drapeau 'groupe' et sont dits *in coincidence*. Au contraire, les événements détectés par un seul PMT sont attribués à des phénomènes provenant de l'extérieur de la chambre à gaz et ne reçoivent aucune étiquette. Dans les événements de coïncidence déclenchés par

la détection de neutrons, chaque forme d'onde des PMT présente une charge particulière et une amplitude maximale pour plusieurs raisons. D'un côté, la propagation de la lumière à l'intérieur de la chambre à gaz après une capture de neutrons dépend des trajectoires d'ionisation suivies par les produits de réaction. De plus, les sommets de ces trajectoires sont complètement déterminés par la position de l'absorption des neutrons. De tels facteurs géométriques font que plus de photons atteignent le PMT se trouvant plus près des chemins d'ionisation. D'autre part, bien que les trois PMT soient du même type, leurs propriétés intrinsèques telles que l'efficacité de conversion des photoélectrons et le gain d'amplification sont différentes. Le résultat global est que les valeurs de Q_{t2t-i} et $A_{Q_{t2t-i}}$ transportent une partie des informations sur l'événement. Pour cette raison, il est naturel de définir la charge intégrée groupée et l'amplitude maximale comme la somme des trois contributions des PMT.

$$Q_{\text{gr}} = \sum_{i=1}^3 Q_{t2t-i}, \quad A_{\text{gr}} = \sum_{i=1}^3 A_{t2t-i}, \quad (2.3)$$

Influence des pressions ^3He et CF_4

La quantité de ^3He et CF_4 à l'intérieur de la chambre à gaz définit dans une large mesure les performances de détection UCN avec GADGET. Ces quantités sont facilement contrôlées par l'appareil de l'usine de gaz, qui alimente les deux gaz avec des pressions réglables dans le détecteur. Selon l'expérience, le détecteur GADGET peut fonctionner avec différentes pressions afin d'optimiser son efficacité de détection. D'un côté, on souhaiterait une pression ^3He élevée ($P_{^3\text{He}}$) pour s'assurer que tous les neutrons traversant le détecteur sont absorbés dans le volume de la chambre. De même, une pression CF_4 élevée (P_{CF_4}) est envisagée pour obtenir un arrêt complet des produits de réaction proton et tritium, convertissant ainsi la majeure partie de leur énergie cinétique en lumière. Bien qu'il existe des effets secondaires défavorables à l'augmentation des pressions des deux gaz, une première estimation des valeurs minimales peut être calculée à partir de la section efficace d'absorption ^3He et du pouvoir d'arrêt du proton et du tritium dans le CF_4 .

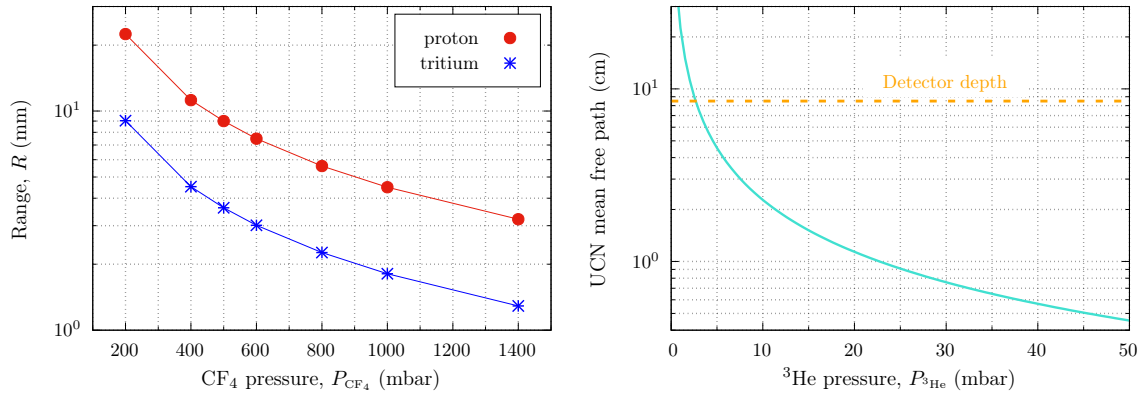


Figure 2.2: (gauche) Parcours du proton et du tritium dans le CF_4 calculés avec SRIM à différentes pressions de gaz. (à droite) Libre parcours moyen des UCN dans ^3He .

À partir du libre parcours moyen des UCN dans ^3He en fonction de la pression du gaz, affiché sur la figure 2.2 (à droite), et en tenant compte du fait que la chambre à gaz GADGET a une profondeur de 8,5 cm, on peut conclure que $P_{^3\text{He}}$ doit être supérieur à 10 mbar pour garantir que les UCN sont absorbés avant d’atteindre le côté opposé de la chambre. Cependant, cette approximation est valable pour des neutrons suivant des trajectoires plus ou moins parallèles à l’axe de la chambre. Sinon, les UCN avec des trajectoires angulaires pourraient arriver sur les parois latérales du détecteur avec des trajets inférieurs à quelques centimètres et ainsi être diffusés ou absorbés par les noyaux des parois sans être détectés. En général, ce n’est pas un problème puisque les UCN passent par des guides verticaux favorisant les trajectoires parallèles à l’axe. Néanmoins, dans les configurations qui ne sont pas agencées avec l’UCN vertical descendant, il convient d’envisager de porter $P_{^3\text{He}}$ jusqu’à 15 ou 25 mbar.

La pression CF_4 joue un rôle important dans la génération des impulsions. Il détermine le parcours du proton et du tritium dans le mélange gazeux. Si P_{CF_4} est trop faible, les produits de réaction pourraient s’échapper de la chambre sans produire le dépôt d’énergie partielle qui conduit à la quantité minimale de lumière détectable par les PMT. L’estimation de la pression CF_4 requise pour assurer un arrêt complet du proton et du tritium est effectuée par des simulations SRIM [26]. La figure 2.2 (à gauche) montre le parcours calculé pour les deux particules à différentes pressions CF_4 avec des énergies spécifiées par la réaction $\text{UCN} + ^3\text{He}$. De toute évidence, ces parcours doivent être mesurés par rapport à la position d’absorption des neutrons, qui se produit principalement à côté de la feuille d’entrée. Étant donné que le proton et le tritium se déplacent dans des directions opposées, le minimum P_{CF_4} peut être défini lorsque le parcours des produits de la réaction est égale au libre parcours moyen du UCN ($\sim 1,5$ cm à $P_{^3\text{He}} = 15$ mbar), soit $P_{\text{CF}_4} \gtrsim 400$ mbar.

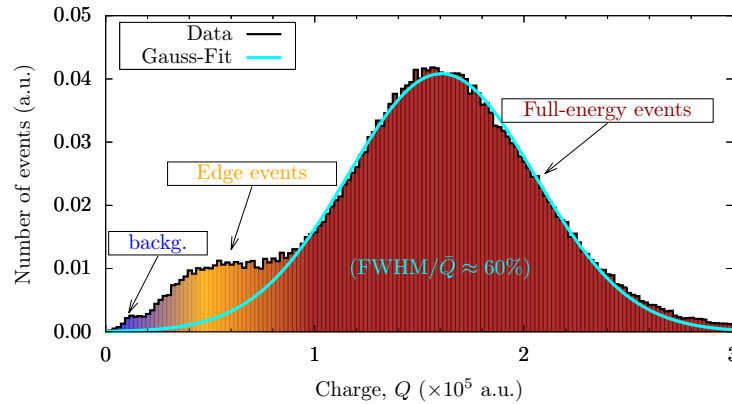


Figure 2.3: Spectre de charge UCN mesuré par le détecteur GADGET. La chambre à gaz était remplie de ^3He et CF_4 à des pressions $P_{^3\text{He}} = 15$ mbar et $P_{\text{CF}_4} = 400$ mbar. Les événements de bord sont présents à ces pressions, mais ne dominent pas les événements de dépôt à pleine énergie.

Comme la plupart des captures UCN se produisent près de la fenêtre d’entrée, la probabilité qu’un des produits de réaction émis par la capture atteigne la fenêtre n’est pas nulle. Dans ces cas, le produit se déplaçant vers la fenêtre dépose une partie de son énergie dans le gaz, tandis que le reste est absorbé par les atomes de la fenêtre. Étant donné que seul le premier processus induit une émission de lumière à l’intérieur de la chambre à gaz, le rendement

moyen en photons collectés par les PMT est réduit par rapport aux événements de dépôt à pleine énergie. Ces événements de dépôt partiel, connus sous le nom d'événements de bord, génèrent des impulsions de tension avec des charges et des amplitudes plus courtes, mais sont toujours enregistrés par les trois PMT. Leur charge mesurée associée se situe alors à des valeurs basses proches des événements de fond. La figure 2.3 montre un spectre de charge UCN ordinaire mesuré avec GADGET rempli de $P_{\text{He}} = 15$ mbar et $P_{\text{CF}_4} = 400$ mbar. Des petites aux grandes charges, trois composants du spectre de charge sont grossièrement identifiés : les événements de fond, de bord et de pleine énergie. Même si les événements de bord s'ajoutent au comptage des neutrons, il est normalement préférable d'utiliser GADGET dans des conditions où ils deviennent minimales.

Chapter 3

$n - n'$ oscillations : Description expérimentale

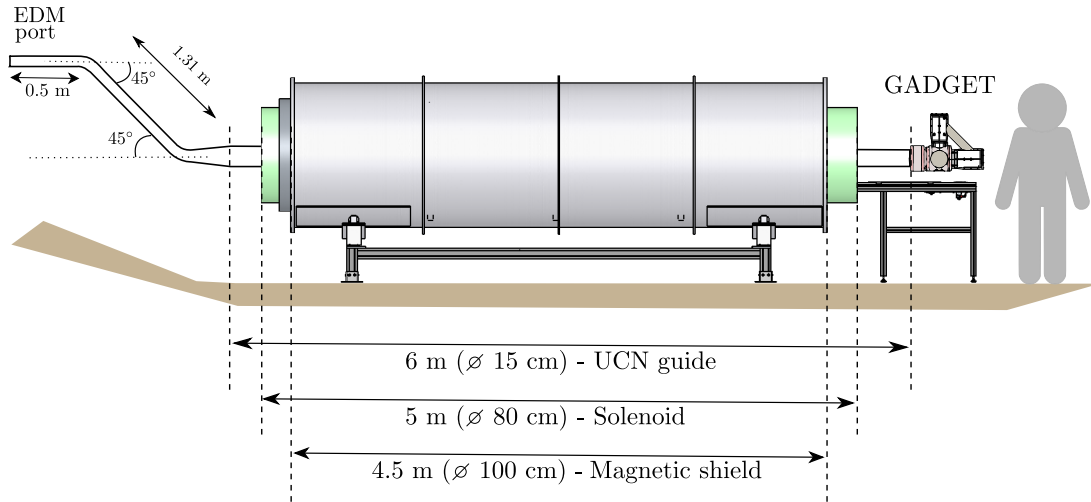


Figure 3.1: Vue de côté de la configuration expérimentale. Le faisceau UCN est conduit à travers trois guides droits et leurs coudes tournants respectifs. Un adaptateur de guide conique est utilisé entre les guides principaux de \varnothing 15 cm et de \varnothing 8,5 cm.

Le champ magnétique appliqué aux UCNs pour supprimer la dégénérescence de l'énergie des neutrons cachés $\Delta_{nn'} = \mu_n B - \delta m$, a été relevé par un système d'aimantation récupéré d'un travail antérieur portant sur la recherche de nouvelles forces à l'aide de noyaux ^3He polarisés [27]. Avec ce système, nous avons balayé la plage d'énergie de séparation de masse $\delta m \in [3 - 66] \times 10^{-12}$ eV, correspondant aux champs magnétiques $B \in [50 - 1100]$ μT . Le système se compose d'un solénoïde principal, d'un blindage magnétique cylindrique et de deux bobines de compensation placées sur les bords du solénoïde pour augmenter l'uniformité du champ magnétique. Le solénoïde principal de 4,8 mètres de long et 80 cm de diamètre est composé de 2270 boucles de 2×1 mm² de fil de cuivre de section rectangulaire autour d'un tube en aluminium de 5 mm d'épaisseur. Les bobines de compensation de 25 cm de long, avec 112 boucles de ~ 80 cm de diamètre chacune, sont connectées en série avec le solénoïde.

La pièce de blindage magnétique correspond à l'un des 17 segments du blindage cylindrique de l'expérience neutron anti-neutron qui s'est déroulée à l'ILL en 1994 [28]. Ce blindage, en mu-métal, entoure le solénoïde comme le montre la figure 3.1 pour augmenter l'uniformité du champ magnétique au niveau du guide UCN et expulser les lignes de champ magnétique des sources externes, en particulier le champ magnétique terrestre. Ses dimensions sont de 4,5 m de longueur, 94,5 cm de diamètre et 1 mm d'épaisseur.

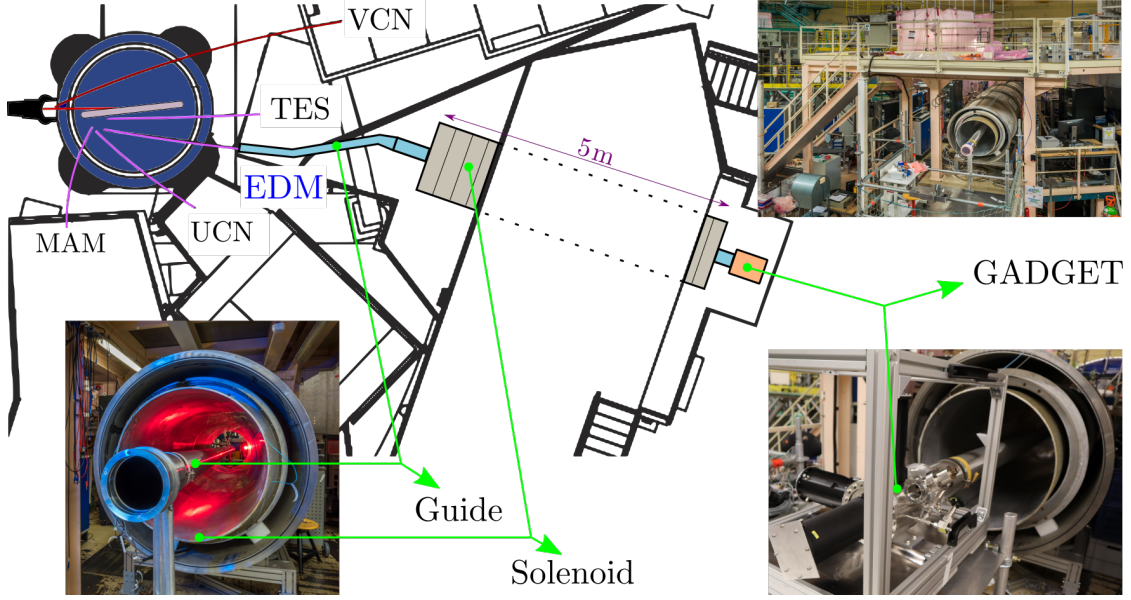


Figure 3.2: Vue de dessus de la configuration expérimentale. Le guide principal UCN et le système de magnétisation ont été placés sous la plate-forme EDM. Photos de Laurent Thion.

Compte tenu de la disponibilité de l'espace et des protocoles de sécurité au PF2, le système de magnétisation était situé à une altitude inférieure par rapport au port du faisceau EDM. Pour cette raison, la disposition des guides utilisés pour transporter l'UCN du port au détecteur en traversant l'axe du solénoïde comprenait trois segments principaux : un guide horizontal d'un demi-mètre au port EDM, un guide incliné de 1,31 m et un guide horizontal de 6 m. Deux coudes pliés ont été placés sur les côtés inclinés du guide et un guide conique a été utilisé pour relier l'un des coudes au guide principal de 6 m ($\varnothing 8,5 \text{ cm} \rightarrow \varnothing 15 \text{ cm}$). Le détecteur GADGET, dont l'acquisition des données a été réalisée par le système FASTER, était situé à l'extrémité du guide de 6 m (à 75 cm du solénoïde). La figure 3.2 montre une vue de dessus du positionnement relatif des éléments de configuration par rapport à la turbine PF2 et aux orifices de faisceau adjacents.

La séquence de mesure ABBC

Au moment de la prise de données $n - n'$ (automne 2020), le faisceau UCN de la turbine PF2 a été partagé avec des cycles de 200 s. Pour synchroniser la détection de flux UCN avec les cycles de livraison de PF2, un signal a été envoyé au système d'acquisition FASTER une fois le positionnement de la turbine terminé. Ces signaux ont été utilisés pour démarrer et arrêter

le comptage UCN (aucune donnée n'a été collectée dans la configuration $n - n'$ pendant les périodes de partage de faisceau).

Afin de compléter le processus de balayage du champ magnétique, on pourrait suggérer de sonder un seul champ magnétique à chaque cycle de livraison. Cependant, le comptage UCN dans ce cas serait sensible aux variations à long terme après plusieurs cycles tels que la puissance de dérive du réacteur, l'échauffement de la source de neutrons froids, le ralentissement de la turbine ou encore les changements dans l'efficacité de comptage de GADGET. Ces comportements de dérive, lorsqu'ils sont corrélés à la source UCN, sont normalement corrigés dans les expériences de stockage UCN au moyen d'un détecteur de moniteur placé à la sortie du port du faisceau. Le présent travail n'adopte pas une telle méthode étant donné que le faible taux de détection habituel dans les moniteurs ajoute de grandes incertitudes statistiques si l'on utilise leur comptage comme facteurs de normalisation. Au lieu de cela, une séquence de mesure auto-normalisée est introduite, qui est indépendante des variations à long terme (d'un cycle à l'autre) et également des dérives linéaires dans les cycles UCN de 200 s. La séquence divise la durée du cycle (t_{cycle}) en quatre fenêtres équivalentes où trois valeurs de champ magnétique sont balayées comme

$$\{A, B, B, C\} = \{B - 20 \mu\text{T}, B, B, B + 20 \mu\text{T}\} \rightarrow \{44 \text{ s}, 44 \text{ s}, 44 \text{ s}, 44 \text{ s}\}. \quad (3.1)$$

Le pas de champ magnétique en cycle de $20 \mu\text{T}$ est choisi plus grand que la résonance FWHM ($1 \mu\text{T}$) de sorte que les oscillations $n - n'$ ne peuvent se produire qu'à l'une des valeurs de champ. De cette façon, le rapport entre UCN comptant au champ B ($N_B + N_B$) aux champs A (N_A) et C (N_C) est

$$R_{ABC} = \frac{N_B + N_B}{N_A + N_C} \begin{cases} = 1, & \text{si aucune oscillation} \\ < 1, & \text{si oscillations au champ } B \\ > 1, & \text{si oscillations au champ } A \text{ ou } C. \end{cases} \quad (3.2)$$

Étant donné que trois champs magnétiques sont testés à chaque cycle, la taille du pas de balayage est définie de telle sorte que le même champ ne soit pas évalué deux fois, mais que l'espacement de $1 \mu\text{T}$ requis par la résonance FWHM soit conservé. En rendant la taille du pas égale à $3 \mu\text{T}$, dont $20 \mu\text{T}$ n'est pas un multiple, on garantit que toutes les valeurs intermédiaires de $B \in [70 - 1080] \mu\text{T}$ sont couvertes par le processus de balayage avec un espacement de $1 \mu\text{T}$.

Chapter 4

$n - n'$ oscillations : analyse des données

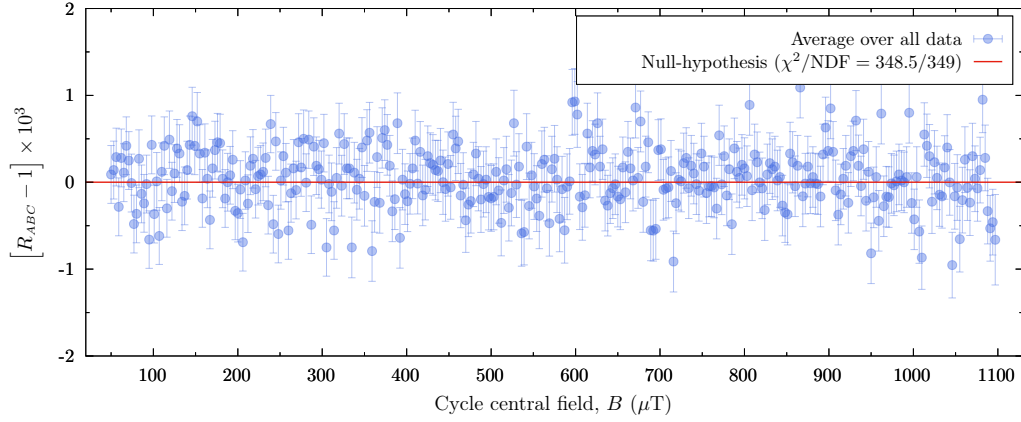


Figure 4.1: Moyenne R_{ABC} sur tous les scans mesurés en fonction du champ central de la séquence ABBC.

Les analyses de cette section sont construites dans le scénario d'une division de masse de neutrons cachés par des neutrons non nuls ($\delta m \neq 0$) et de champs magnétiques cachés extrêmement petits $B' = 0$. Dans ce modèle, le spin est conservé pendant les oscillations et la condition de résonance $\Delta_{nn'} = \mu_n B - \delta m = 0$ n'est remplie que pour un des états de spin. Cela peut être facilement vu à partir de l'hamiltonien écrit comme

$$\hat{\mathcal{H}}_{nn'} = \left(\begin{array}{cc|cc} \mu_n B & 0 & \epsilon_{nn'} & 0 \\ 0 & -\mu_n B & 0 & \epsilon_{nn'} \\ \hline \epsilon_{nn'} & 0 & \delta m & 0 \\ 0 & \epsilon_{nn'} & 0 & \delta m \end{array} \right), \quad (4.1)$$

conduisant aux résonances spin-up et spin-down

$$\begin{aligned} \mu_n B = \delta m & : n_{\uparrow} \rightarrow n'_{\uparrow} \\ -\mu_n B = \delta m & : n_{\downarrow} \rightarrow n'_{\downarrow}. \end{aligned}$$

Par conséquent, à condition que $\delta m > 0$, n_\uparrow oscille en n'_\uparrow pour les champs résonnants $+B$ et n_\downarrow oscille en n'_\downarrow pour les champs résonnants $-B$. Cependant, cela n'est pas pertinent pour l'analyse, puisque le faisceau UCN utilisé dans cette expérience est composé de 50% n_\uparrow et 50% n_\downarrow (non polarisé). Nous pouvons ainsi faire la moyenne des mesures R_{ABC} disponibles à partir de tous les scans quelle que soit l'orientation du champ B appliqué (+ ou -). Le nombre de neutrons qui disparaissent du faisceau en raison des oscillations $n - n'$ est le même pour les deux directions du champ magnétique.

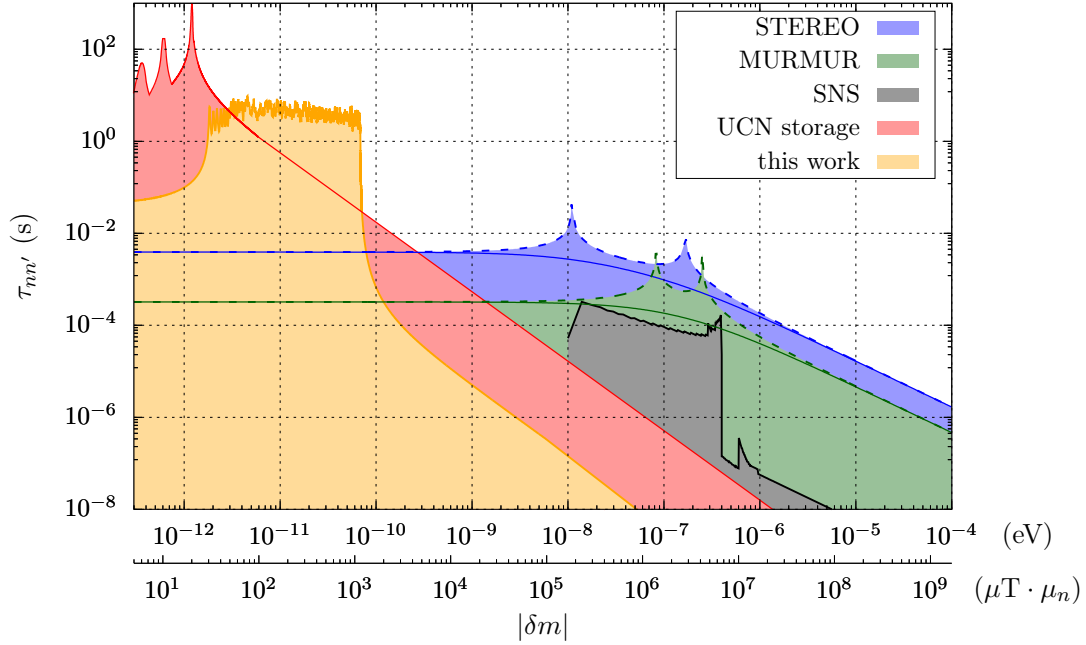


Figure 4.2: Exclusion de l'espace de paramètres $n - n'$ incluant tous les résultats expérimentaux jusqu'en août 2022.

Bien que les données acquises ne contiennent pas de signal significatif, nous pouvons fixer une nouvelle limite aux paramètres du modèle $n - n'$. Ces valeurs limites sont construites par le calcul de la ligne de contour $\chi^2(\delta m, \infty) + 2^2$ qui définit le 95% C.L. région d'exclusion. La limite d'exclusion est utilisée pour contraster la contribution de ce travail à la vue générale des oscillations $n - n'$ avec les mesures passées. En utilisant une sélection de couleurs compatible avec la dernière comparaison publiée [14], l'espace des paramètres mis à jour est présenté dans la figure 4.2. La région d'exclusion issue de ce travail devient ainsi la première mesure sondant les oscillations $n - n'$ avec des valeurs de dédoublement de masse situées entre le stockage UCN et les expériences de traversée de paroi. Même si notre sensibilité est d'environ un ordre de grandeur plus courte que celle des mesures de stockage UCN, la technique expérimentale introduite avec ce travail permet de balayer efficacement une large gamme de valeurs δm . Alors que l'expérience de stockage UCN la plus sensible [11] a consacré 40 jours à tester des oscillations $n - n'$ à deux amplitudes de champ magnétique, nous avons réussi à scanner plus d'un millier de champs avec une campagne expérimentale de 25 jours. La sensibilité de ce nouveau résultat n'est pas négligeable si l'on tient compte du fait que la mesure la plus sensible dans les expériences de traversée de paroi se situe en dessous de $\tau_{nn'} = 10$ ms. Un

fait à garder à l'esprit si vous visualisez une future expérience de faisceau UCN pour balayer des δm plus grands est que la largeur de résonance ($\sim 1 \mu\text{T} \cdot \mu_n$) et l'étape de balayage ne devraient pas changer radicalement. Par conséquent, afin de produire une région d'exclusion importante à $\delta m > 10^3 \mu\text{T} \cdot \mu_n$, l'expérience doit améliorer les statistiques de comptage pour maintenir le même $\tau_{nn'} \sim 1$ s sensibilité.

Part II

The part in English

Introduction

Although the role of neutrons in everyday life is not evident, as their charge neutrality exempts them from electromagnetic interactions, we have learned that they play an important role in the binding of atomic nuclei. In fact, since the neutron content of all stable nuclei, besides hydrogen, is equal or larger than the proton content, one can state that about half of the everyday-life-matter is composed of neutrons, i.e. they are responsible for half the mass of visible matter. Despite their large contribution as building blocks of matter, studying neutron properties demands considerable technological efforts. Unlike electrons, which can be easily removed from atoms with energies of the order of eV, the strong bounding between neutrons and nuclei, due to the nuclear force, requires energies as large as a couple MeV to kick a neutron out of its hosting nucleus. In addition, once ejected from a nucleus, a free neutron does not have much time to make an impression. On average, it survives about 15 minutes before decaying into other types of particles. Therefore, when looking at your 2 kg cat, you are looking at 1 kg of neutrons trapped within the cat's nuclei. All of those neutrons, formed 13.6 billion of years ago, would not survive more than a couple of hours if they were not bounded to the cat's protons.

Even at present, not only cat owners, but many nuclear and particle physicists are surprised when hearing for the first time about the experimental techniques allowing the manipulation of free neutrons during time periods as long as the neutron life-time. Although the idea of storing neutrons in closed vessels was firstly proposed in 1959 by Zeldovich [18], it was only experimentally achieved 9 years later simultaneously by Shapiro *et al.* and Steyerl *et al.* [19]. In essence, when the energy of free neutrons is reduced below the neutron-optical potential of a given material (for example 335 neV for ^{58}Ni), they undergo total reflection on the surface independently of the angle of incidence. These reflection properties, used to classify neutrons as ultra-cold neutron (UCN), can be described by classical quantum mechanics and mimic the properties of light reflection. One then talks about neutron optics.

Since the construction of the first UCN storage bottles, and over more than 50 years, multiple searches on high-precision physics have been carried out with UCN experiments. For example, in the measurement of the neutron electric dipole moment (EDM), the neutron life-time and even its bounded energy levels in Earth's gravitational potential. In this work, we present a new approach to the study of neutron - hidden neutron oscillations from neutron disappearance in UCN beams. Hidden states of matter, which could correspond to parallel sectors hosting mirror copies of all known particles, or to different branes of a high-dimensional bulk, are conceived within a simple mathematical model with a rather rich phenomenology in low-energy particle physics and cosmology.

In the first chapter, the motivation and mathematical formalism behind hidden sectors models, as well as a brief introduction to UCN physics, will be presented. At the end of

the chapter, the state of the art of past $n - n'$ experimental tests will be discussed. Moving to a technical study, the second chapter is dedicated to the description of the novel UCN gaseous detector, GADGET. Special emphasis will be given to its detection efficiency as a function of the gasses pressure and to the pulse shape analysis. In the third chapter, the new experimental technique to probe $n - n'$ oscillations in UCN beams with magnetic fields is introduced. A detailed explanation of the data collection technique, determination of a $n - n'$ signal, expected sensitivity, a preliminary analysis on UCN trajectories and a magnetic field characterization will be exposed. The fourth chapter is separated into two parts. First is a summary of the data collected during the 2020 experimental campaign at the Institut Laue Langevin (ILL), which will be followed by the systematics analysis. In particular, the search and characterization of non-statistical fluctuations is developed by analyzing the UCN beam counting rate at different time scales. Evaluation of a possible data correction by means of the ILL reactor power will be considered. The second part of the fourth chapter focuses on the data analysis of $n - n'$ oscillations in the beam experiment. The search for a signal and exclusion of the model parameters are studied for two different scenarios: a non-negligible mass splitting δm between neutron and hidden neutron, and the possible influence of hidden magnetic fields (B'). In the last chapter, an overview of the whole work and some perspectives regarding future $n - n'$ UCN beam experiments are presented.

Chapter 1

UCN and hidden sector searches

This chapter exposes the theoretical considerations and experimental implications around the hidden universe hypotheses. In the first part, we present a chronological description on how hidden matter models became important in theoretical approaches exploring physics beyond the standard model. Then, the most likely mechanisms for particle mixing between our universe and hidden versions are mentioned. In particular, the phenomenology accounting for the mixing of neutron with hidden sectors is examined, while listing the constraints imposed on such new interactions. In the third part, the discussion focuses on recalling past experimental results with UCN and other neutron setups to define the still admissible hidden sector model parameters. In the last part, in order to explain the fundamentals of the experimental techniques employed in this work, a brief introduction to UCN physics is given.

1.1 Hidden matter

The introduction of a new sector of hidden particles has been proposed from different contexts to work around some of the standard model limitations. Initially, hidden particles were presented as ‘mirror particles’ when Lee & Yang intended to explain the parity symmetry breaking in the weak sector [29]. In order to provide a mechanism for which parity was still conserved, they argued the possibility of parity degeneracy. Whereas particles in the ordinary sector would favor one parity state, mirror particles would prefer the opposite one. In this way, even if parity is violated locally within both sectors, in the general picture it remains conserved. Such conception of global parity would also allow explaining why one only observes left-handed neutrinos: they transform into their twins mirror right-handed neutrinos after mirror parity inversion.

The recognition of mirror matter as a potential source of new physics was strongly debated among physicists influenced by symmetric principles (for a thoughtful chronological summary, see [30]). More than 20 years after the first experiments evidencing P and CP breaking [31,32], the idea of hidden or mirror matter was recovered by the physicist R. Foot. He developed the formalism behind the notion of hidden matter as a candidate for dark matter [33]. R. Foot proposed, assuming the \mathbb{Z}_2 symmetry which assigns a degenerate hidden particle to each known particle, the coexistence of two sectors locally governed by the same interactions, $\mathcal{L}_{\text{SM}}(e, u, d, \gamma, W, Z, \dots)$ and $\mathcal{L}_{\text{SM}'}(e', u', d', \gamma', W', Z', \dots)$ in the ordinary and hidden sectors, respectively, which might potentially mix between each other through extra terms (besides

gravity) not contained within standard model interactions \mathcal{L}_{mix} . The global Lagrangian of the joint sectors would then be expressed as

$$\mathcal{L} = \mathcal{L}_{\text{SM}}(e, u, d, \gamma, W, Z, \dots) + \mathcal{L}_{\text{SM}'}(e', u', d', \gamma', W', Z', \dots) + \mathcal{L}_{\text{mix}}. \quad (1.1)$$

Note that, given that the \mathbb{Z}_2 mirror symmetry that copies all masses and decay times from ordinary to hidden particles, new parameters in this theoretical model appear only in the mixing term \mathcal{L}_{mix} . Therefore, since interactions between SM' particles would be exactly the same as the ones in SM, hidden matter might describe properties similar to ordinary matter. Although, as stated above, accounting for such properties cannot be done through the known interactions besides gravity, the last term in the right-hand side of Eq. (1.1) opens a portal for testing the nature of hidden matter at the quantum level. In other words, if hidden matter happens to be the same as dark matter, the yet unexplained cosmological phenomena governed by gravity effects could be further analyzed by particle physics experiments probing SM-SM' mixing at Earth.

In recent years, the double-degenerated mirror theory of hidden particles has been formulated as the particular case of more extensive models. For example, Dvali & Redi [1] explain that, in order to solve the hierarchy problem between weak and gravitational scales, the number of allowed SM copies can go up to 10^{32} , i.e. instead of \mathbb{Z}_2 one could face multiple sectors with overall symmetries represented by $\mathbb{Z}_{10^{32}}$ [34]. Similarly, from a rather geometrical point of view, hidden particles can instead be thought of as ordinary particles transitioning into different layers (branes) of a high dimensional bulk [35]. The universe as we observe it would correspond to a three-dimension sheet embedded in a hyperspace, where multiple versions of SM particles are constrained to live in. Within this picture, dark matter is conceived as hidden particles located in other layers, thus requiring gravity to propagate along the bulk. Nevertheless, independently of the physical content of the theoretical approach followed to describe the matter - hidden matter mixing, the mathematical treatment in all the aforementioned models yields to the same phenomenology [3].

1.2 Mixing mechanisms

The first attempts to define the mixing terms in Eq. (1.1) were driven by symmetry (\mathbb{Z}_2 , gauge, Lorenz) laws and renormalization restrictions [2]. Application of these minimal requirements leads to mixing processes of neutral bosons, such as photon - hidden photon ($\gamma - \gamma'$), Z - hidden Z and Higgs - hidden Higgs. While the two first arise from kinetic (quadratic) mixing, the latter is entirely due to quartic interactions:

$$\mathcal{L}_{\text{mix}} = \frac{\epsilon}{2} F^{\mu\nu} F'_{\mu\nu} + \lambda \phi^\dagger \phi \phi'^\dagger \phi', \quad (1.2)$$

where $F_{\mu\nu}$ ($F'_{\mu\nu}$) is the ordinary (hidden) $U(1)$ gauge boson field strength tensor and ϕ (ϕ') is the ordinary Higgs (hidden) field. Note that, in virtue of the \mathbb{Z}_2 symmetry, the only input parameters of the hidden model are ϵ and λ .

Out of the two mixings $\gamma - \gamma'$ and $Z - Z'$ included in the first term on the right-hand side of Eq. (1.2), only the former has a sensitivity large enough to be studied experimentally [33]. After proper diagonalization of this mixing term, one finds out that hidden charged particles

are given a small electric charge ϵe , which allows them to couple to ordinary photons* [36]. A direct consequence of this small charge is that hidden particles could be detected in dark matter experiments such as DAMA/LIBRA [37] and CoGeNT [38]. In fact, the 1-year modulated signals detected in previous phases of DAMA/LIBRA experiments could correspond to static hidden matter interacting with the detector as Earth moves back and forth in the galaxy. Similarly, the $-\epsilon e$ charge of hidden electrons permits the creation of hidden electron hidden positron pairs through the process $e^+e^- \rightarrow e'^+e'^-$ (see Figure 1.1), which would occur with an amplitude 2ϵ times the amplitude of the Bhabha annihilation $e^+e^- \rightarrow e^+e^-$ [39]. This result is relevant in positronium physics given that it represents an invisible channel for the ortho-positronium decay, thus affecting its life-time. Although past experiments have not observed a significant deviation from QED calculations, ortho-positronium life-time measurements have set the bound $\epsilon < 1.55 \times 10^{-7}$ [5]. Interestingly, reducing this limit will be useful to test the value of ϵ required to explain the DAMA/LIBRA modulated signal $\epsilon \sim 10^{-9}$. Regarding the Higgs - hidden Higgs mixing derived from the second term on the right-hand side of Eq. (1.2), recent analyses have shown that ATLAS and CMS give Higgs suppression factors compatible with predictions in case of mass differences between Higgs mass eigenstates greater than their decay widths [40]. For a more complete discussion, see [41–43].

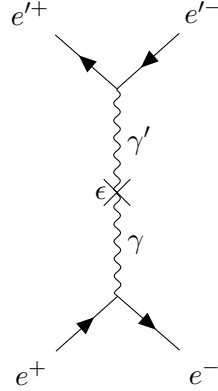


Figure 1.1: Feynman diagram of $e^+e^- \rightarrow e'^+e'^-$. The cross represents the mixing.

Extra terms could be added to \mathcal{L}_{mix} if considering for example that neutrino oscillations require including interactions in the SM Lagrangian providing neutrinos with masses. It is then possible that hidden neutrinos exist with alike sub eV masses and, as long as neutrino masses are due to the type-I[†] seesaw mechanism, mass mixing between neutrinos and hidden neutrinos occur [17, 33]. Whereas long-baseline neutrino experiments can be completely explained by the three-flavor oscillation model, the reactor antineutrino anomaly [44] could represent a hint for neutrino - hidden neutrino oscillations. Although the hidden (sterile) neutrino hypothesis has been extensively revised during the last decade with many short-baseline neutrino setups (see a status review in [6]), most of the results could not positively conclude on the existence of neutrino - hidden neutrino oscillations. Nowadays, only the SM-3 reactor [45] measurement is still compatible with the hidden neutrino mixing scenario [46]. If future experiments manage to stringently exclude the neutrino - hidden neutrino oscillations hypothesis, one

*The opposite does not hold though: hidden photons do not couple to ordinary matter.

[†]Compatible with gauge and \mathbb{Z}_2 symmetries.

could then think of two possibilities, either these oscillations are extremely tiny or they are zero (as it happens for type-II and type-II seesaw models [33]). This being said, a different explanation to the reactor antineutrino anomaly was presented by Serebrov [47]. Instead of observing an antineutrino counting defect, reactor measurements might overestimate the number of actual β -decays at the source. This could happen if a fraction of the fission neutrons rather than decaying through the known channels undergo oscillations into hidden neutrons ($n - n'$ oscillations). Such baryonic matter oscillations have been widely studied in the neutron life-time puzzle context [48] and are currently being tested in short-baseline neutrinos experiments [14]. They are the main focus of this work.

1.3 Neutron - hidden neutron oscillations

Mixing of the neutron n with its hidden counterpart n' can be safely included in \mathcal{L}_{mix} as it respects \mathbb{Z}_2 , gauge and Lorentz symmetries [33]. The effective operator in this case corresponds to a 9-dimension coupling between three ordinary and three hidden quarks

$$\mathcal{L}_{nn'} \sim \frac{1}{\mathcal{M}^5} (udd)(u'd'd') + h.c., \quad (1.3)$$

where \mathcal{M} represents the large cutoff scale involving new physics. Using the QCD energy scale $\Lambda \approx 200$ MeV, one can estimate the $n - n'$ oscillation time parameter as

$$\tau_{nn'} = \epsilon_{nn'}^{-1} \sim \left(\frac{\mathcal{M}}{10 \text{ TeV}} \right)^5 \times 1 \text{ s}. \quad (1.4)$$

Following the reasoning in [49], a first bounding on $\tau_{nn'}$ can be extracted from neutron - antineutron oscillation limits, which give $\tau_{nn'} > 1$ s, i.e. $\mathcal{M} \sim 10$ TeV. This is convenient since $n - n'$ oscillations could be even faster than the neutron life-time ($\tau_n \approx 880$ s), thus allowing the probe of $\tau_{nn'}$ with free-neutron experiments. Note that, because of the \mathbb{Z}_2 symmetry, $n - n'$ oscillations cannot occur in bound-neutron of stable nuclei as hidden neutron masses are smaller ($m_n = m_{n'}$, or at least $m_n \approx m_{n'}$ as later discussed) than the mass difference between isotopes (A, Z) and $(A - 1, Z)$.

$n - n'$ oscillations with characteristic times in the scale of seconds would have a strong influence on quantities such as the neutron life-time [48], and at the same time they would play a key role in the description of cosmological phenomena. For example, breaking of \mathcal{B} symmetry by $n - n'$ mixing ($\Delta\mathcal{B} = 1$), which is not excluded in beyond the standard models, could shed some light through the Sakharov conditions on the baryogenesis problem [4]. Note that although both the baryon and hidden baryon numbers (\mathcal{B} and \mathcal{B}' , respectively) are simultaneously violated by $\mathcal{L}_{nn'}$, the total quantum number $\bar{\mathcal{B}} = \mathcal{B} + \mathcal{B}'$ is conserved. Imposing such a general symmetric constrain $n - \bar{n}$ and $n' - \bar{n}'$ oscillations are forbidden processes [49].

1.3.1 Oscillation probability: general description

As previously indicated, whether $n - n'$ oscillations are caused by mixing between two or 10^{32} sectors, or even if they correspond to neutron swapping into a high dimensional bulk, their phenomenology is always the same. For this reason, without loss of generality, we adopt

the two sector model where the Hamiltonian associated to Eq. (1.3) describing the mixing between free-neutrons and free-hidden-neutrons is

$$\hat{\mathcal{H}}_{nn'} = \begin{pmatrix} E_n & \epsilon_{nn'} \\ \epsilon_{nn'} & E_{n'} \end{pmatrix}, \quad (1.5)$$

with E_n ($E_{n'}$) the neutron (hidden neutron) energy and $\epsilon_{nn'} = \tau_{nn'}^{-1}$ the mass mixing parameter (with $\hbar = c = 1$). Matrix elements in Eq. (1.5) are in fact 2×2 matrices of spin states, which can be assumed diagonal due to spin conservation. Nevertheless, if energy terms E_n and $E_{n'}$ include spin-dependent interactions for which the privileged quantization axes of ordinary and hidden sectors do not coincide, e.g. scenarios with hidden (mirror) magnetic fields, a spin-sensitive treatment should be considered [17].

Value of E_n and $E_{n'}$

Throughout this work, we will discuss on results from free-neutrons experiments where E_n is defined by the neutron interactions with its environment. They are generally determined by magnetic fields in UCN setups (see section 1.4.1), or by Fermi potentials at nuclear reactors in passing-through-wall experiments (see section 1.4.2). Following the arguments that presented hidden matter as dark matter, one could estimate the nature of $E_{n'}$ by revising the main interactions that a hidden neutron on Earth would have with hypothetical surrounding hidden/dark matter. Given the low density of dark matter captured by the solar system, predicted to go up to $\rho_{DM} = 4 \times 10^{-25} \text{ g/cm}^3$ [50], one would attribute hidden neutron ambient interactions to hidden electromagnetism and gravity (long interaction range forces) and safely neglect hidden nuclear forces.

On the one hand, hidden electromagnetic fields, which reduce to hidden magnetic fields due to the charge neutrality of interstellar medium [51], are predicted between 0.01 and 3 μT assuming the presence of high density hidden H_2 clouds [35]. Although magnetic fields fall to $\sim 1 \text{ nT}$ in cloud portions with regular densities, it was stated in [17] that, “by chance”, the solar system might be currently crossing a huge mirror matter cloud for which hidden magnetic fields can go up to 10 μT . On the other hand, according to the multiple-brane picture [35], contributions from gravitational interactions are relevant provided that the difference between the gravitational fields experienced by a neutron in our brane (V_+) and in another brane (V_-) is different from zero: $|V_+ - V_-| \equiv \hbar|\eta| \neq 0$. In other words, the gravitational potential of a given mass depends on the brane where it is located. Even if gravity permeates over the high-dimensional bulk, its strength might be modulated by the branes separation (d) according to

$$M' \sim M e^{-kd}, \quad (1.6)$$

with M' the apparent mass of an object with ordinary mass M , and k a constant depending on the brane properties. Although determination of $|\eta|$ is unachievable in practice, a rough estimation can be made from ordinary gravitational fields V_+ due to Earth, Moon, Sun and Milky Way: $\hbar\eta \sim 1 \text{ meV} - 1 \text{ keV}$.

Mass splitting δm

Up to now, the $n - n'$ mixing phenomenon was formulated assuming perfect \mathbb{Z}_2 symmetry, out of which neutron and hidden neutron masses are identical $m_n = m_{n'}$. However, it might

happen that \mathbb{Z}_2 is spontaneously broken by higher order quantum corrections, giving place to a small mass splitting $\delta m = m_{n'} - m_n$ [20]. Such interactions could be written as the coupling of a scalar field $\tilde{\eta}$ and the ordinary and hidden Higgses (see Eq. (1.2))

$$\lambda \tilde{\eta} (\phi^\dagger \phi - \phi'^\dagger \phi'), \quad (1.7)$$

with λ a dimensional coupling constant. Berezhiani [52] explains that, depending on the mass ordering between neutron and proton in both sectors, hidden matter would depict different properties. If $m_{p'} > m_n > m_{n'} > m_p$ with $m_{p'} > m_{n'} + m_{e'}$, hidden protons would be unstable while hidden neutrons stable. This would imply a hydrogen-free self-scattering hidden matter scenario. On the contrary, if $|m_{p'} - m_{n'}| < m_{e'}$, i.e. stable hidden proton and hidden neutron, hidden matter corresponds to a mixture of self-scattering and dissipative matter. Although determining the value of $m_{n'}$ is not possible, the largest allowed magnitude of δm is extracted from Be^9 stability: $\delta m_{\text{max}} \approx 1.573$ MeV [52]. Note that δm adds as an extra model parameter, which allows rewriting the hidden neutron energy as

$$E_{n'} = m_n + \delta m + \Delta E',$$

where $\Delta E'$ includes all the aforementioned hidden matter interactions. The reader might suspect that, from a practical point of view, one has to assume either $\delta m = 0$ or $\Delta E' = 0$ so that the degeneracy-lifting energy difference, written as

$$\begin{aligned} \Delta_{nn'} &\equiv E_n - E_{n'} \\ &= (m_n + \Delta E) - (m_{n'} + \Delta E') \\ &= (\Delta E) - (\delta m + \Delta E') \end{aligned}$$

with E_n the environmental neutron energy, only deals with one hidden parameter, namely δm or $\Delta E'$. If that is not the case, the theoretical model gains one degree of freedom, thus complicating the parameter exclusion analysis.

1.3.2 Oscillations without environmental hidden potentials ($\Delta E' = 0$)

Let us first assume a hidden sector whose matter density at Earth is low enough so that environmental hidden potentials, especially hidden magnetic fields, can be neglected. Hence, the Hamiltonian in Eq. (1.5) is expressed as

$$\begin{aligned} \hat{\mathcal{H}}_{nn'} &= \begin{pmatrix} m_n + \Delta E & \epsilon_{nn'} \\ \epsilon_{nn'} & m_{n'} \end{pmatrix} \\ &= \begin{pmatrix} \Delta E & \epsilon_{nn'} \\ \epsilon_{nn'} & \delta m \end{pmatrix} + m_n \begin{pmatrix} \mathbb{I}_{2 \times 2} & 0 \\ 0 & \mathbb{I}_{2 \times 2} \end{pmatrix} \\ &= \begin{pmatrix} \Delta E & \epsilon_{nn'} \\ \epsilon_{nn'} & \delta m \end{pmatrix}, \end{aligned} \quad (1.8)$$

where we have dropped the term $m_n \mathbb{I}_{4 \times 4}$ as it does not change the $n - n'$ oscillation dynamics. Given that all elements in this last expression are 2×2 diagonal matrices, its solution on the

Schrödinger equation is equivalent to the very well known two-level quantum system. The mass states and their energies (eigenvectors and eigenvalues) are thus given by

$$\tilde{E}_{\pm} = \frac{1}{2} \left[(\Delta E - \delta m) \pm \sqrt{(\Delta E - \delta m)^2 + 4\epsilon_{nn'}^2} \right],$$

and

$$\begin{aligned} |\psi_+\rangle &= \cos \theta |n\rangle + \sin \theta |n'\rangle \\ |\psi_-\rangle &= -\sin \theta |n\rangle + \cos \theta |n'\rangle, \end{aligned}$$

respectively, where the mixing amplitude θ is defined as

$$\sin^2 2\theta = \frac{4\epsilon_{nn'}^2}{4\epsilon_{nn'}^2 + (\Delta E - \delta m)^2}.$$

Following this notation, a free-neutron released at $t = 0$ would be described by the state $|\psi(0)\rangle = |n\rangle = \cos \theta |\psi_+\rangle - \sin \theta |\psi_-\rangle$, whose propagation in time is

$$|\psi(t)\rangle = \cos \theta e^{-i\tilde{E}_+ t} |\psi_+\rangle - \sin \theta e^{-i\tilde{E}_- t} |\psi_-\rangle. \quad (1.9)$$

Then, the $n - n'$ oscillation probability after a free-flight time t_f is computed from the amplitude $|\langle n' | \psi(t_f) \rangle|$, which results:

$$P_{nn'}(t_f) = \sin^2(2\theta) \sin^2 \left(\frac{\sqrt{(\Delta E - \delta m)^2 + 4\epsilon_{nn'}^2} t_f}{2} \right). \quad (1.10)$$

This last expression shows that the maximum mixing is achieved at the resonance condition where the $n - n'$ energy degeneracy is completely lifted, i.e. $\sin^2 2\theta = 1$ with

$$\Delta_{nn'} = \Delta E - \delta m = 0. \quad (1.11)$$

In such case, the oscillation probability becomes 1 every $(2n + 1)\pi\tau_{nn'}/2$ seconds, with $n = 0, 1, 2, \dots$. For off-resonance values, not only the amplitude decreases as $\sim 1/\Delta_{nn'}^2$, but also the oscillation frequency increases proportional to $\Delta_{nn'}$. This double feature of $n - n'$ oscillations is depicted in Figure 1.2 for four values of ΔE assuming $\tau_{nn'} = 1$ s and $\delta m = 10^{-14}$ eV. Note that opposite to neutrino oscillations, where the mixing amplitude $\sin^2 2\theta$ is fixed by the model parameters, the $n - n'$ mixing can profit of maximal mixing $P_{nn'} \sim 1$ if correctly matching $\Delta E = \delta m$ ($\Delta_{nn'} = 0$) and allowing long free-flight-time periods ($t_f \sim \epsilon_{nn'}^{-1}$). Therefore, to efficiently probe for $n - n'$ oscillations, one could look for example at the neutron disappearance by experimentally tuning $\Delta E = \delta m$ while minimizing the frequency of neutron scattering with its environment. These two ideas are the basis of experimental setups probing $n - n'$ oscillations with ultra-cold neutrons.

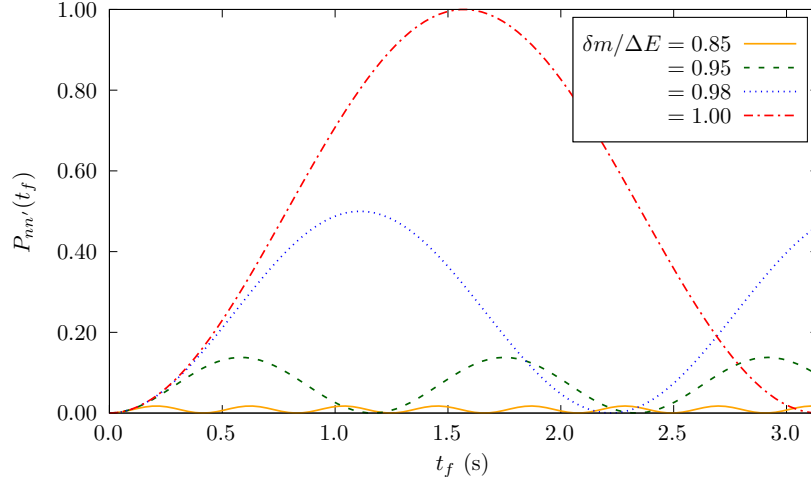


Figure 1.2: $n - n'$ oscillation probability as a function of the free-flight time assuming $\tau_{nn'} = 1$ s and $\delta m = 10^{-14}$ eV. The behavior, illustrated for different ratios $\delta m/\Delta E$, demonstrates that the mixing amplitude $\sin^2 2\theta$ and oscillation frequency $\frac{1}{2}\sqrt{\Delta_{nn'}^2 + 4\epsilon_{nn'}^2}$ are maximum and minimum, respectively, at the resonance $\delta m/\Delta E \rightarrow 1$ ($\Delta_{nn'} = 0$).

Effective mass splitting

The oscillation phenomenology described above was constructed assuming the more simplistic scenario where all interactions between the hidden neutron and its environment were neglected. The hidden neutron energy was then reduced to its rest mass, which could happen to be different from the neutron mass. However, as it is not possible to distinguish between a pure mass splitting δm and other spin-independent hidden neutron environmental interactions (Eq. (1.10) does not change if replacing $\delta m \rightarrow \Delta E'$), one could have included them within an effective mass splitting defined as

$$\delta m_{\text{eff}} = \delta m + V'_{\text{Fermi}} + V_- \hbar + \dots \quad (1.12)$$

where V'_{Fermi} corresponds to the Fermi potential experienced by n' in a hidden medium. Since the $n - n'$ oscillation probability is invariant under such redefinition, in the present work, δm refers to the effective mass splitting in Eq. (1.12).

1.3.3 Oscillation in presence of hidden magnetic fields (\vec{B}')

Physics underlying $n - n'$ oscillations when the hidden neutron energy is governed by a hidden magnetic field has been presented in detail in [17]. The main difference with respect to the approach followed so far is that no explicit mass-splitting is considered ($\delta m = 0$) and $\Delta E'$ is purely defined by the hidden neutron spin states:

$$\Delta E' = \vec{\mu}_n \cdot \vec{B}' = \mu_n \vec{B}' \cdot \vec{\sigma}, \quad (1.13)$$

with μ_n the neutron magnetic[‡] moment and $\vec{\sigma} = (\sigma_x, \sigma_y, \sigma_z)$ the Pauli matrices. In that case, if the energy degeneracy $\Delta_{nn'}$ is experimentally lifted by means of an ordinary magnetic field

[‡]Although it might happen $\mu_n \neq \mu'_n$ [53], such scenario is not taken into account in this work.

acting on the ordinary neutron, the $n - n'$ interaction Hamiltonian reads

$$\hat{\mathcal{H}}_{nn'} = \begin{pmatrix} \mu_n \vec{B} \cdot \vec{\sigma} & \epsilon_{nn'} \\ \epsilon_{nn'} & \mu_n \vec{B}' \cdot \vec{\sigma} \end{pmatrix}. \quad (1.14)$$

The solution to the Schrödinger equation under these conditions deals with the fact that \vec{B} and \vec{B}' are not strictly parallel. Given the ignorance on the magnitude and direction of \vec{B}' , one needs to introduce an extra model parameter, namely the angle between hidden and ordinary magnetic fields

$$\beta = \cos^{-1} \left(\frac{\vec{B} \cdot \vec{B}'}{|\vec{B}| |\vec{B}'|} \right). \quad (1.15)$$

In configurations with $\beta \neq 0$, the preferred quantization axes defined by the hidden and ordinary magnetic fields are not the same. For this reason, $n - n'$ oscillations with spin inversions $n_{\uparrow} \rightarrow n'_{\downarrow}$ and $n_{\downarrow} \rightarrow n'_{\uparrow}$ are allowed by the Hamiltonian in Eq. (1.14). The oscillation probability, which accounts for the spin inversion through the parameter β , is then written as [54]

$$P_{nn'}(t) = \frac{\sin^2[(\omega - \omega')t]}{2\tau_{nn'}^2(\omega - \omega')^2} (1 + \cos \beta) + \frac{\sin^2[(\omega + \omega')t]}{2\tau_{nn'}^2(\omega + \omega')^2} (1 - \cos \beta), \quad (1.16)$$

with $2\omega = |\mu_n B|$ and $2\omega' = |\mu_n B'|$ [§]. Note that in practice, one normally has $\tau_{nn'}(\omega + \omega') \gg 1$, hence the second term on the right-hand side of Eq. (1.16) can be neglected most of the time (this term becomes significant when $\beta = \pi$). Therefore, $n - n'$ oscillations in the presence of hidden magnetic fields describe a time evolution similar to the one expressed through the mass splitting approach (Eq. (1.10)). The main difference here is the factor $1 + \cos \beta$, which hinders the $n - n'$ oscillations.

1.4 State of the art: Past $n - n'$ oscillation tests

Although the first bound on $\tau_{nn'}$ was established in 2006 by Berezhiani [49] using data from neutron-antineutron oscillations experiments [28], just one year later, Ban *et al.* [7] achieved the first test of $n - n'$ oscillations through a specially dedicated setup. At the time of this experiment, it was already established that $n - n'$ could actually be detected through two different experimental approaches [55], referred to as *neutron disappearance* and *neutron regeneration* [56]. In this section, the detection principle of both approaches and their individual results are presented. In the end, exclusion regions on the $n - n'$ model parameter space constructed from all experiments performed so far are compared.

1.4.1 Neutron disappearance

Up to now, six experiments have been devoted to the search of $n - n'$ oscillations through the neutron disappearance method [7–11, 57]. In all of them, the same idea was applied: look for signals of neutron disappearance in UCN storage bottles (see section 1.5.1). By

[§]These characteristic frequencies are proportional to the Larmor precession frequencies in both sectors: $\omega = \omega_{\text{Larmor}}/4$ and $\omega' = \omega'_{\text{Larmor}}/4$

carefully accounting for the known channels of UCN losses during storage periods (β -decay, up-scattering, absorption, etc.), this approach assigns any neutron counting defect to the process $n \rightarrow n'$. From a theoretical viewpoint, this technique can be said of order one since neutrons undergoing “half a $n - n'$ oscillation”, with a probability $P(n \rightarrow n') \sim (t_f/\tau_{nn'})^2$, would become hidden neutrons thus crossing and escaping the storage bottle walls[¶].

Historically, first experiments by Ban *et al.* [7] (2007) and Serebrov *et al.* [8] (2008) considered negligible hidden magnetic fields and focused on lifting the energy degeneracy due to the neutron interaction with Earth’s magnetic field. In other words, they aimed to screen environmental ordinary magnetic fields to fulfill $\Delta_{nn'} = \mu_n B \sim 0$. In particular, tests in [7] (2007) profited from the magnetic shielding system constructed for the nEDM collaboration [58], which allowed reaching vanishing magnetic fields $B \ll 10$ nT associated to $\Delta_{nn'} \ll 10^{-21}$ eV (similar small magnetic fields were achieved in [8] (2008)). Limits reported by both groups were $\tau_{nn'} > 103$ s (95 % C.L.) [7] (2007) and $\tau_{nn'} > 414$ s (95 % C.L.) [8] (2008).

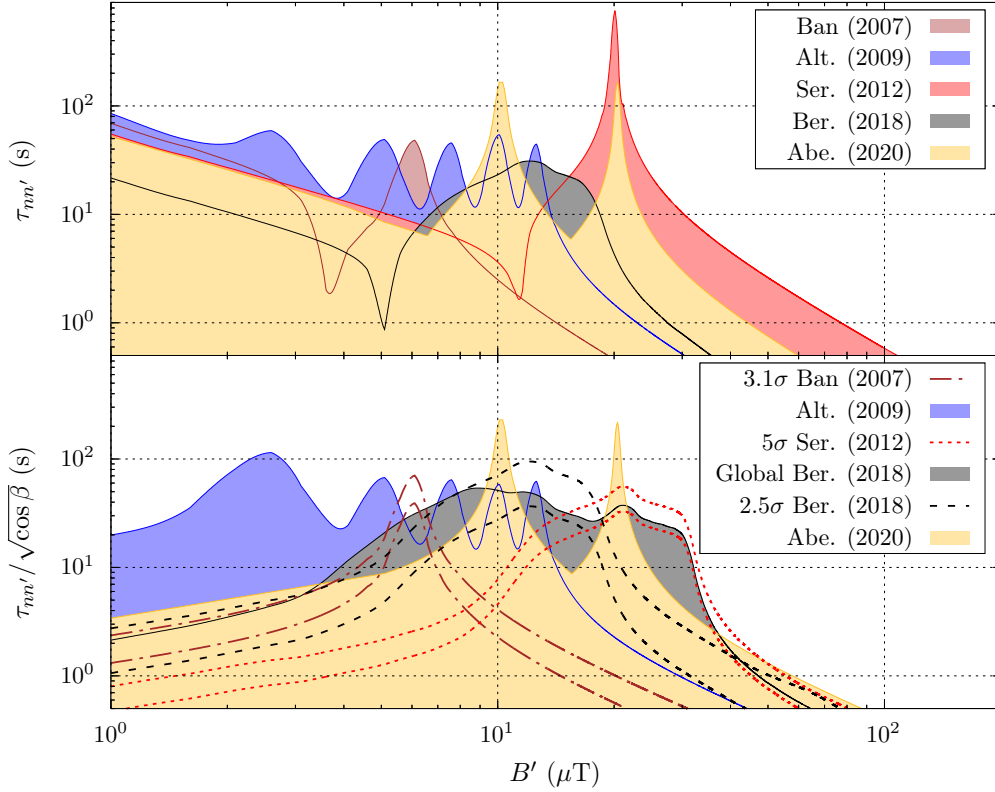


Figure 1.3: 95% C.L. boundaries of $\tau_{nn'}$ from previous UCN storage measurements through the ratio (top) and asymmetry (bottom) channels. The signals in the asymmetry channel reported by Berezhiani *et al.* [10, 54] (2018) from data in [7] (3.1σ Ban (2007)), [8] (5σ Ser. (2012)) and [10] (2.5σ Ber. (2018)) are displayed with dashed lines. The black solid line represents the global boundary as reported in [10]. *Courtesy: Abel et al.* [11]

[¶]Regeneration processes are of order two, with $P(n \rightarrow n' \rightarrow n) \approx P(n \rightarrow n')^2$. See next subsection.

Even if B' -fields were neglected in the first tests, their results could be extrapolated to cases where $B' \neq 0$. This was possible thanks to the *ratio* and *asymmetry* channels introduced by Berezhiani [17] (2009). Using Eq. (1.16), he demonstrated that by joining the measurements of neutron counting at null magnetic field (N_0) and at both directions of a given B -field (N_B and N_{-B}), one can express $\tau_{nn'}$ as a function of

$$A_{\uparrow\downarrow} \equiv \frac{N_B - N_{-B}}{N_B + N_{-B}}, \quad (1.17)$$

$$E_0 \equiv \frac{2N_0}{N_B + N_{-B}}, \quad (1.18)$$

a few experimental parameters and the hypothetical hidden B' -field. These signal channels are written as

$$\text{Asymmetry channel: } \frac{\tau_{nn'}^2}{\cos \beta} = \frac{t_s}{\langle t_f \rangle A_{\uparrow\downarrow}} f_A(B, B'), \quad (1.19)$$

$$\text{Ratio channel: } \tau_{nn'}^2 = \frac{t_s}{\langle t_f \rangle E_0} f_E(B, B'), \quad (1.20)$$

where t_s is the storage time, $\langle t_f \rangle$ the average UCN free-flight-time within the bottle and $f_A(B, B')$ and $f_E(B, B')$ are basic functions on the applied and hidden magnetic fields. In this way, if no signal is observed, i.e. $|A_{\uparrow\downarrow}| < \zeta \Delta A_{\uparrow\downarrow}$ and $|E_0 - 1| < \zeta \Delta E_0$ with ζ a constant depending on the confidence level and $\Delta A_{\uparrow\downarrow}$ (ΔE_0) the uncertainty of $A_{\uparrow\downarrow}$ (E_0), rather than constructing a single limit for $\tau_{nn'}$, the asymmetry and ratio channels allow excluding portions of the parameter spaces $(B', \tau_{nn'}/\sqrt{\cos \beta})$ and $(B', \tau_{nn'})$, respectively. Note that opposite to the asymmetry channel, which is sensitive to the angle β , the ratio channel leads to a more general evaluation of $n - n'$ oscillations as it can be included within the generic two-parameter model $(\tau_{nn'}, \delta m)$ of Eq. (1.10). This is convenient for the later comparison against neutron regeneration results.

Reanalysis of data in [7] (2007) and [8] (2008) by allowing the influence of an undetermined B' -field through the asymmetry channel revealed 3.1σ and 5σ signals, respectively [54] (2012). The overall fit, including also the non-signal exclusion results by Altarev *et al.* [9] (2009), pointed towards a potential signal around $B' = 11 \mu\text{T}$, $\tau_{nn'} = 14 \text{ s}$ and $\tau_{nn'}/\sqrt{\cos \beta} = 20 \text{ s}$ (region (a) and (b) in [54] (2012)), but it also favored a wide region of large hidden B' -fields: $[20 - 200] \mu\text{T}$ with $\tau_{nn'} \sim 0.1 \text{ s}$ (region (c) in [54] (2012)). These potential signals motivated extra searches through measurements of $A_{\uparrow\downarrow}$ and E_0 in UCN storage experiments at short magnetic fields ($B \sim 10 \mu\text{T}$) to probe regions (a) and (b) (for a detailed overview, see [59]), and through the UCN flux monitoring at high magnetic fields to probe region (c) (present work).

Experiments by Berezhiani *et al.* [10] (2018) reported a new 2.5σ deviation from the asymmetry channel about $B' = 12 \mu\text{T}$, but also excluded portions of the parameter space in the asymmetry and ratio channels. In addition, this work performed a second reanalysis of data in [8] (2008) since it was stated that significant B -field spatial gradient had to be included in the fit. Such a revaluation transformed the favored regions (a), (b) and (c) in [54] (2012) into the magenta region in [10] (2018). In particular, the (c) region was removed from the potential favored parameters. More recently, measurements at PSI by Abel *et al.* [11] (2021) probed oscillations at $B = 10, 20 \mu\text{T}$ but did not confirm any of the previous significant signals.

A summary of all the results up to 2021 are displayed in the exclusion plots of Figure 1.3. The 95% C.L. exclusion regions peaking at the tested magnetic fields are displayed with filled curves in the ratio channel (top) and asymmetry (bottom) channels. On top of them, parameters favored by signals reported in the asymmetry channel are contained within the dashed-line bands, which correspond to the 95% C.L. interval of each signal. Special interest is given to the 5σ and 2.5σ bands overlapping around $B' \sim 16 - 19 \mu\text{T}$.

Besides the experiment introduced in this work, further tests of $n - n'$ oscillations are foreseen. For example, new experimental data was recently collected from UCN storage at PSI [57] and a new proposal has been passed at the European Spallation Source (ESS) [60] to look for neutron regeneration processes.

1.4.2 Neutron regeneration

Instead of estimating the number of neutron disappearing in a given setup, neutron regeneration experiments aim at counting neutrons completing an “entire $n - n'$ oscillation”, i.e. following the sequence $n \rightarrow n' \rightarrow n$. In order to guarantee detected that the events correspond to neutrons undergoing a round trip between the ordinary and hidden sectors, a high density stopper of ordinary neutrons is placed between the source and the counter. While no ordinary neutron is expected to cross the stopping wall, the low interacting hidden neutrons would easily traverse it. Once on the other side of the wall, hidden neutrons might oscillate back into ordinary neutrons and then be detected. This is the reason why neutron regeneration experiments are also called *passing-through-wall* experiments. The reader might suspect that, given the already low probability of neutron disappearance in UCN storage experiments, estimated in $P(n \rightarrow n') < 7 \times 10^{-6}$ [61], the probability of detecting a neutron completing the process

$$n \xrightarrow{P} n' \xrightarrow{P} n \quad (1.21)$$

might be even tinier than $P(n \rightarrow n' \rightarrow n) \sim P(n \rightarrow n')^2 = 10^{-12}$. Hence, regeneration experiments, rather than dealing with deviations from large neutron counting, focus on separating few neutron detection from background events. That being said, a positive signal in neutron disappearance experiments can only be attributed to actual $n - n'$ oscillations if a regeneration experiment confirms the fitted parameters. If that is not the case, neutron losses in storage bottles would just indicate a new exotic decay channel.

Experimental efforts in regeneration experiments have raised two different techniques, initially with cold neutron beams [62, 63] and more recently with fission neutrons from reactor facilities [12–14]. Whereas $n - n'$ oscillations in the former are induced by tuning magnetic fields $B \approx B'$, the latter can use the Fermi potential of neutrons inside the reactor core, regeneration blocks^{||} and the detector itself to lift the energy degeneracy $\Delta_{nn'} = V_{\text{Fermi}} - \delta m$. Compared to UCN storage experiments, the $n - n'$ sensitivity in cold neutron beams and fission neutron setups profit from larger neutron fluxes, e.g. $\Phi_{\text{cold}} \sim 2 \times 10^{10}$ n/s in the cold neutron beam at the Spallation Neutron Source (SNS) at Oak Ridge National Laboratory (ORNL) [63], and $\Phi_{\text{thermal}} \sim 10^{14} - 10^{15}$ n/cm²/s within the heavy water moderator at the ILL [14].

^{||}These blocks, made of materials with large neutron scattering cross-sections, are placed after the neutron wall stopper to increase the probability of regeneration $n' \rightarrow n$.

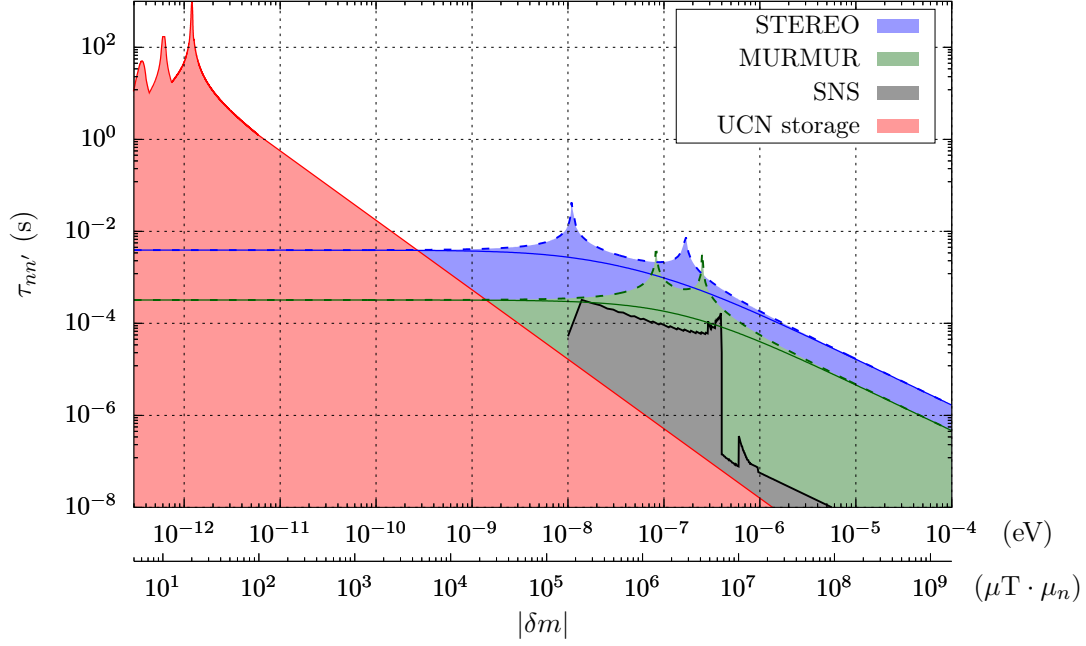


Figure 1.4: Exclusion regions in the parameter space by neutron disappearance (UCN storage, see Figure 1.4) and neutron regeneration (CN beams [15] and reactor thermal neutrons [13, 14]) experiments. The dashed (solid) lines of STEREO and MURMUR limits correspond to $\delta m > 0$ ($\delta m < 0$).

Although both approaches for neutron regeneration measurements are of order two in the oscillation probability $P(n \rightarrow n')^2$, the time evolution of a neutron state $|n\rangle = \cos\theta |\psi_+\rangle - \sin\theta |\psi_-\rangle$ is different for CN beams and thermal neutrons. Given that CN beam vessels are vacuumed, cold neutrons are weakly interacting with matter and therefore the oscillation probability $P(n \rightarrow n' \rightarrow n)$ is computed in the regime of quasi-degenerate states ($|\Delta_{nn'}| < \epsilon_{nn'}$), i.e. the time evolution of $|\psi(t)\rangle = (\psi_+(t), \psi_-(t))$ follows slow oscillations and requires exact estimation of the free-flight-times. On the other hand, fission neutrons inside reactor moderators experience large environmental potentials, which forces $n - n'$ oscillations to have small amplitudes and fast oscillation frequencies (non-degenerate regime: $|\Delta_{nn'}| \gg \epsilon_{nn'}$). In such case, the oscillation probability for thermal neutrons within reactor moderators (Eq. (1.10)) is averaged to [12]

$$P_{nn'} = \frac{2\epsilon_{nn'}^2}{(\Delta E - \delta m)^2}. \quad (1.22)$$

By means of this last expression, Stasser *et al.* [13] probed in 2021 $n - n'$ oscillations with the specially dedicated MURMUR experiment at the BR2 research reactor (SCK-CEN, Mol, Belgium). The setup consisted of the neutron converter at the reactor core, mostly composed of Be, C and D₂O, the biological shielding which acts as a neutron wall, a regenerator block made of lead, ³He and other neutron scattering materials, and a ³He-based neutron detector. Analyses of the counting rates yielded to the limit $P_{\text{MURMUR}} < 4.0 \times 10^{-10}$ at 95% C.L.. Somewhat similar was done by Almazán *et al.* [14] in 2022 using the STEREO detector located at 10 m from the center of the high flux ILL reactor. Although STEREO was originally

conceived to test for $\nu - \nu'$ oscillations [64] by looking at the flux of reactor antineutrinos, its detection principle exploits the inverse beta decay, $\bar{\nu} + p \rightarrow n + e^+$, hence converting it into a very sensitive neutron detector (neutron detection in STEREO is due to capture in Gd and Li scintillators). Comparison of neutron counting rates in reactor ‘power ON’ and ‘power OFF’ configurations lead to the limit $P_{\text{STEREO}} < 3.1 \times 10^{-11}$ at 95% C.L.

Table 1.1: Summary of the Fermi potentials in the converter and regenerator of MURMUR and STEREO experiments.

	V_{Fermi} (neV)		Γ_{coll} (s^{-1})	
	Converter	Regenerator	Converter	Regenerator
MURMUR	252 (Be)	83 (Pb)	2.078×10^5	3.3×10^{-5}
STEREO	167 (D ₂ O)	11 (Scint.)	1.0731×10^5	5.2×10^{-3}

In order to construct the exclusion boundaries in the $(\delta m, \tau_{nn'})$ space from the regeneration experimental results above, one has to take into account the neutron collision rate at the reactor core converter $\Gamma_{\text{coll}}^{\text{conv.}}$. Added to the low oscillation probability in the non-degenerate regime, the swapping of neutrons into hidden neutrons is suppressed by the neutron collision rate [5, 12], which transforms Eq. (1.22) into [14]

$$P_{nn'} = \frac{2\epsilon_{nn'}^2}{(\Delta E - \delta m)^2 + (\hbar\Gamma_{\text{coll}}/2)^2}, \quad (1.23)$$

where one normally adds the neutron Fermi potential to account for the neutron-medium interaction: $\Delta E = V_{\text{Fermi}}$. Following the same reasoning, the hidden neutron - neutron swapping would depend on the hidden neutron collision rate within the regenerator ($\Gamma_{\text{coll}}^{\text{rege.}}$) volume and the detector for the MURMUR setup, and within the scintillators for the STEREO setup. The total $n \rightarrow n' \rightarrow n$ probability is then written as

$$\begin{aligned} P_{n \rightarrow n' \rightarrow n} &\approx P_{nn'} \times P_{n'n} \\ &= \frac{2\epsilon_{nn'}^2}{(V_{\text{Fermi}}^{\text{conv.}} - \delta m)^2 + (\hbar\Gamma_{\text{coll}}^{\text{conv.}}/2)^2} \times \frac{2\epsilon_{nn'}^2}{(V_{\text{Fermi}}^{\text{rege.}} - \delta m)^2 + (\hbar\Gamma_{\text{coll}}^{\text{rege.}}/2)^2}. \end{aligned} \quad (1.24)$$

where the values of Γ_{coll} , computationally estimated in [13] and [14], and the Fermi potentials for both experiments are reported in Table 1.1.

Using Eq. (1.24) and the limiting oscillation probabilities, one can construct the 95% C.L. exclusion plots in the $(\delta m, \tau_{nn'})$ parameter space by solving $\epsilon_{nn'}$ as a function of δm . However, depending on whether δm is positive or negative, MURMUR and STEREO results determine two exclusion boundaries each. If $\delta m > 0$, the oscillation probability can be resonantly increased, thus featuring maximum exclusions at the converter and regenerator Fermi potentials $\delta m = V_{\text{Fermi}}^{\text{conv.}}$ and $\delta m = V_{\text{Fermi}}^{\text{rege.}}$, respectively. On the other hand, if $\delta m < 0$, the exclusion boundary is mostly flat. Both cases are displayed for the MURMUR and STEREO limits next to the overall exclusion from UCN storage limits** and the recent measurement with CN at the SNS [15] in Figure 1.4. This representation permits evidencing that the sensitivity in regeneration experiments is almost 4 orders of magnitude smaller than the one

**See in Appendix A how these limits are converted from the mirror to the hidden context.

in UCN storage. However, limits from the former extend over a wide range of small and large δm values. The versatile hidden matter evaluation of the STEREO setup introduces a new path to test for $n - n'$ oscillations. In fact, recent analyses have proposed the use of experiments such as IsoDAR, SNO and Borexino to probe extra portions of the $n - n'$ parameter space [65].

1.5 UCN physics

Ultra-cold neutrons are interesting quantum systems since their dynamics are sensitive to the four fundamental forces. As it happens with neutron energies in all ranges, UCNs are not constrained to a fixed energy interval, but instead they are categorized in virtue of their macroscopic properties. In this section, we briefly introduce the UCN interactions and describe their production in two different facilities.

1.5.1 UCN interactions

Opposite to higher energy neutrons, UCN temperatures are not linked to the moderator temperature [66]. The term ultra-cold is rather assigned to neutrons capable of total reflection regardless the incidence angle in material surfaces. This phenomenon is possible for neutrons with very low energies ~ 300 neV (2 mK), although it is highly dependent on the material features. If properly chosen, such materials can be used to construct confinement bottles to store UCN and then perform precise measurements of neutron properties. A few examples would be the neutron EDM, the neutron life-time, the energy levels of the neutron in Earth's gravitational field and of course $n - n'$ oscillations. During these experiments, UCN physicists mainly concern on the following UCN interactions.

Weak interaction

The main limitation on the time duration of UCN storage experiments derives from the weak interaction. With a mass excess of $1.293\,332\,36\,(46)$ MeV [67] with respect to the proton mass, the neutron is an unstable system which decays through β -emission. The conversion of one of its down-quarks into a top-quark leads to the emission of a W^- boson, which in turns decays into an electron and an electron antineutrino. The overall process is resumed as

$$n \rightarrow p^+ + e^- + \bar{\nu}_e. \quad (1.25)$$

The neutron life-time, as reported by the Particle Data Group, is $\tau_n = 879.4 \pm 0.6$ s [68]. Although this value corresponds to the weighted average over several UCN storage measurements, a second estimation from neutron beam experiments yields $\tau_n = 888.0 \pm 2.1$ s [69]. The 3.9σ difference between both results is known as the neutron life-time puzzle [70].

Magnetic interaction

Couplings to magnetic fields are a consequence of the non-zero neutron magnetic moment $\mu_n = 1.91304273(45)\mu_N \approx -60.3$ neV/T. Besides the well-known Larmor precession induced

by the torque $\vec{\tau} = \vec{\mu}_n \times \vec{B}$, the dynamics of a neutron can be affected if the magnetic field exhibits a gradient. The force acting on a neutron immerse in such a field is written as

$$\vec{F} = -\mu_n \nabla(\vec{\sigma} \cdot \vec{B}), \quad (1.26)$$

with σ the neutron spin direction. In the adiabatic limit, i.e. the magnetic field rate of change much smaller than the Larmor frequency, this last expression can be rewritten as

$$\vec{F} = \pm |\vec{\mu}_n| |\nabla| \vec{B}|, \quad (1.27)$$

where the sign ‘+’ corresponds to antiparallel spin orientation $\vec{S} \uparrow \downarrow \vec{B}$, thus giving a neutron accelerating into high magnetic fields, referred to as *high-field seeker*, and the sign ‘-’ corresponds to parallel spin orientation $\vec{S} \uparrow \uparrow \vec{B}$ leading to a neutron being repulsed from positive field gradients, referred to as *low-field seeker* [71]. Therefore, with a magnetic field of 1 T, one can raise a potential barrier of about 60.3 neV. This effect is normally used to construct UCN magnetic bottles and spin-sensitive filters.

Gravitational interaction

Probably the most unusual effect in particle physics, Earth’s gravitational potential plays an important role in UCN dynamics. Using the classical description of Newton’s gravitational law, the gravitational potential of a neutron at a height h with respect to Earth’s surface is given by

$$V_{\text{grav}} = m_n g h \approx 102 \text{ neV/m} \cdot h, \quad (1.28)$$

with $m_n = 939.565 \text{ MeV}/c^2$ the neutron mass and $g = 9.8 \text{ m/s}^2$. Given that such potential is of the same order as UCN kinetic energies, one can think of UCN traps whose bottom and side walls are made of magnetic surfaces and which upper confinement results from gravity. An example of such a device is used at the Los Alamos National Laboratory to measure the neutron life-time [72]. Gravitational effects are also exploited in experimental setups to shift in a controlled way UCN energy spectra. For instance, one can let UCNs fall into a vertical guide so that they gain the energy necessary to cross detectors entrance windows without being reflected (see section 2.2.2).

Strong interaction

The strong interaction is the responsible for keeping protons and neutrons bound within nuclei, making possible the existence of stable atoms and all the more complex matter structures. When a slow free-neutron impinges a nucleus, it is normally repulsed because its wave function features multiple oscillations within nuclear potential wells, which hardly satisfies the stringent boundary conditions for effective attraction. Indeed, the large difference between UCN energies ($K_{\text{UCN}} \sim 300 \text{ neV}$) and nuclear well potentials ($U_{\text{nuc}} \sim 40 \text{ MeV}$) produces a drastic change on the wave functions of UCN in the vicinity of nuclei, impeding the use of perturbation theory to describe the scattering process [73]. However, given that the UCN De Broglie wavelength is of the same order as the atomic distance in solids, rather than interacting with a single nucleus UCN experience the short-range nuclear potential of multiple nuclei. In this way, each

nucleus behaves as a dispersive center of spherical waves allowing to express the UCN matter interaction through the effective potential known as “Fermi potential”

$$V_{\text{Fermi}} = \frac{2\pi\hbar^2}{m_n}Nb, \quad (1.29)$$

with N the number density of dispersive centers and b the nuclear scattering length associated to that material. Then, UCNs with energies sufficiently small perceive a material as a potential step and can be totally reflected from it if their kinetic energies fulfill

$$K_{\text{UCN}} \sin^2 \theta_{\text{inc}} \leq V_{\text{Fermi}}, \quad (1.30)$$

with θ_{inc} the incidence angle. This last expression implies that UCN with kinetic energies $K_{\text{UCN}} \leq V_{\text{Fermi}}$ are always reflected under all incidence angles.

Among the most frequent experimental uses of Eq. (1.29), with materials such as ^{58}Ni whose $V_{\text{Fermi}} = 335$ neV, there are the UCN guides and the storage material bottles. Whereas the former allow transporting UCN from the source to the experimental setups, the latter is commonly employed in long-lasting measurement such as the neutron EDM and the neutron life-time. Unlike magnetic bottles, material ones suffer from UCN losses due to the neutron wave function penetration into the reflecting surface. The overlapping of this evanescent wave with nuclei in the material can result in UCN absorption or energy transfer. During this last process, referred to as “up-scattering”, UCN receive energy from the thermal vibrations of nuclei, making that their kinetic energies exceed the Fermi potential and therefore are no longer reflected. In either case, the UCN loss probability upon reflection is normally low for most of the materials used in UCN guide and bottles coverings ($10^{-4} - 10^{-5}$).

1.5.2 UCN sources

The short life-time of neutrons makes the finding of free-neutrons in nature very unlikely events. Therefore, neutron sources focus on extracting these baryons from bound nuclei. Currently, free-neutron production is efficiently carried out through two different processes: from fission reactions in nuclear reactors and from spallation reactions in particle accelerators. In the following, experimental techniques to obtain UCN from these two types of facilities are presented. In fact, the given examples correspond to the UCN sources employed for the detector testing in section 2.4 and the analysis of $n - n'$ oscillations (chapters 3 and 4).

UCN from spallation at the Paul Scherrer Institute

Neutrons produced by this source come from the proton spallation of lead. The Paul Scherrer Institute (PSI) cyclotron accelerates protons at 590 MeV, with a beam current slightly higher than 2 mA. The proton beam operates in pulsed mode with kicks that last 8 s, every 300 s. Product of the proton-to-lead collisions, fast neutrons (~ 2 MeV) are generated at rates of about 10^{17} s^{-1} [74]. Once liberated, the first stage of neutron moderation is completed by 3.6 m³ of heavy water surrounding the target at room temperature. At this point, neutrons reach thermal energies (~ 25 meV). Next, a solid deuterium crystal (sD₂) located in the middle of the heavy water tank with a temperature of about 6 K, continues the moderation process until leaving the neutrons with energies close to 10 meV. At this energy range, neutrons start interacting with the crystal as a whole rather than with the individual deuterium nuclei.

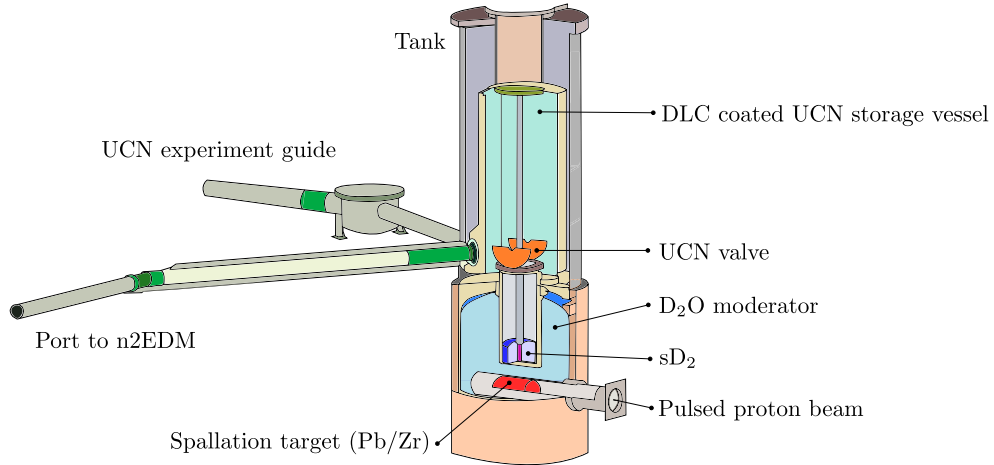


Figure 1.5: UCN source at PSI in Villigen, Switzerland. The 7 m height tank houses the spallation Pb/Zr target, $\sim 3.6 \text{ m}^3$ of heavy water (D_2O), $\sim 30 \text{ dm}^3$ of sD_2 and the $\sim 2 \text{ m}^3$ storage vessel ($\sim 2.5 \text{ m}$ height).

They transfer their energy to the lattice via phonon excitation. After several scattering processes of this kind, neutrons emerge from the crystal with energies $< 300 \text{ neV}$. Using diamond-like-carbon (DLC) coatings ($V_{\text{Fermi}} = 304 \text{ neV}$ [75]), UCN are transferred from the sD_2 crystal volume through the storage vessel till the delivery ports as shown in Figure 1.5.

UCN from the ILL reactor

Since 1972 the high flux reactor at the ILL has been the center for many projects in a quite vast variety of research disciplines, going from biology, chemistry and material science to nuclear and particle physics. Among other neutron facilities, the ILL reactor stands out due to its large constant neutron flux: $\sim 5 \times 10^{18} \text{ n/s}$ with a nuclear power of 57 MW. Hot, thermal and cold sources distribute these neutron fluxes from the reactor core towards the experimental halls through 16 beam-tubes crossing the reactor biological shielding. Depending on the spectrum energy of each beam line, different setups exploit the neutron-matter interaction to study the structure of atoms, molecules and even nuclei. In particular, low energy particle physics experiments are normally carried out at the PF2 apparatus, located at the highest hall (level D) within the reactor containment building. These experiments use neutrons extracted from the reactor core through the vertical cold source (VCS), which delivers PF2 with cold and ultra-cold neutron beams.

Comparative studies have placed the UCN source at ILL as one with the largest densities [76]. UCN in this facility have origin in the fission of 93% high-enriched ^{235}U . Following the induced fission of ^{235}U nuclei at the reactor core, the surrounding heavy water (D_2O) pool generates the first moderation of the fast fission neutrons ($E_n \sim 2 \text{ MeV}$, $v_n \sim 2 \times 10^4 \text{ km/s}$). After a few collisions with D nuclei, neutrons reach the thermal regime: $E_n \sim 0.025 \text{ eV}$ ($v_n \sim 2.2 \text{ km/s}$). The second cooling process takes place inside the liquid deuterium cold source at $\sim 20 \text{ K}$ [77], placed within the pool in the uranium fuel vicinity (see Figure 1.6). Extra thermalization in this cold volume leaves neutrons with energies of a few μeV ($v_n \sim 50 \text{ m/s}$). At that point, they become cold and are extracted through a bent vertical

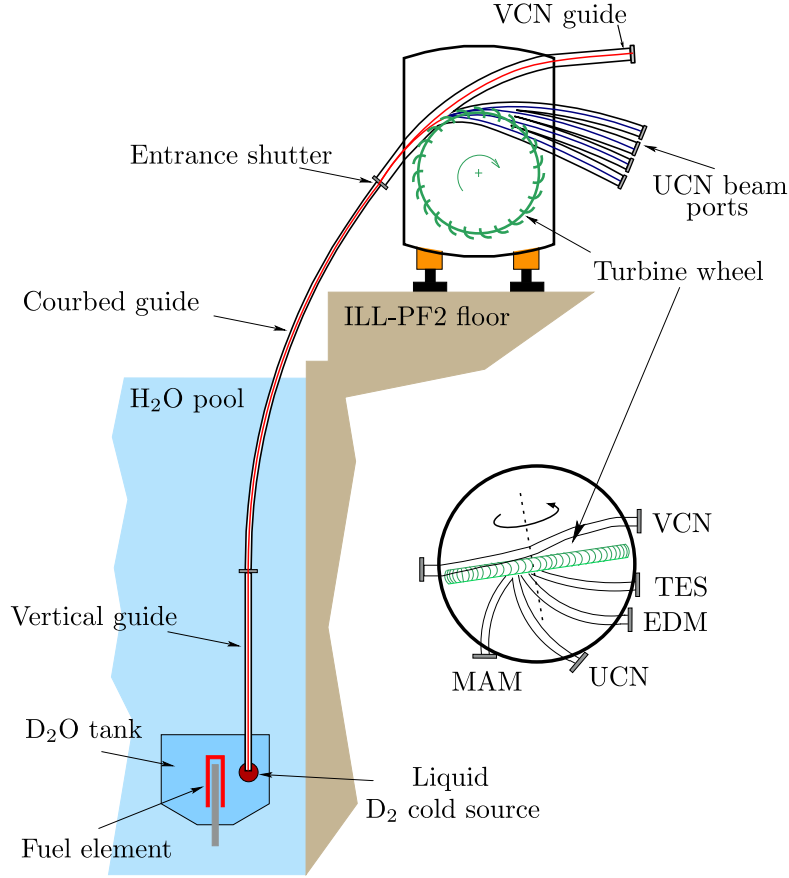


Figure 1.6: UCN source at the Institut Laue-Langevin. The cooling process starts at the reactor moderating pool and finishes at the PF2 turbine.

guide. Only low energy neutrons capable to afford the guide curvature are transmitted to the PF2-instrument, which lies 15 m above the reactor core. In fact, the ascending movement in the gravitational potential makes that neutrons further lose a fraction of their kinetic energies. The already cold neutron beam at the top of the vertical bent guide is then divided in two sections: one half is transferred to a very-cold-neutron (VCN) exit port and the other enters the ILL UCN turbine [78]. Inside this turbine, neutrons are reflected by one of the 690 nickel-covered blades that rotate with a radial velocity $v_{\text{rot}} = v_n/2 = 25$ m/s. After undergoing such Doppler-shift reflection, neutrons finally become ultra-cold: $E_n \sim 214$ neV ($v_n \sim 6.4$ m/s) and can be directed towards dedicated high flux UCN beam lines (‘EDM’, ‘UCN’, ‘MAM’). A fourth port (TES) is also always available, but it counts with a low UCN flux ($\sim 15 \times 10^3$ s⁻¹) and is mainly dedicated to test simple setups.

1.6 Chapter conclusions

Hidden sectors propose an elegant solution to several SM issues, including the explanation of dark matter and baryogenesis. The construction of these BSM models is rather simplistic from a mathematical point of view, but at the same time they offer a phenomenology reachable

from cosmological observation and testable through low and high energy particle physics experiments. Regardless the theoretical approach used to explain the possible mixing/swapping of neutral particles into hidden sectors, equations describing the time evolution of such exotic processes reveal resonant behaviors similar to the Rabi oscillations. Therefore, in order to prompt the transition of particles into the hidden versions, experimental efforts have focused on lifting the energy degeneracy raised from the particle interactions in both (or multiple) sectors.

Evaluation of $n - n'$ oscillations has been tested in several setups. Historically, they were firstly searched by looking at the neutron disappearance in UCN storage bottles and more recently by measuring the neutron regeneration from thermal neutrons at the core of nuclear reactors. Although results in the last experimental campaign with UCN storage at PSI by Abel *et al.* [11] did not confirm the most updated reported signals by Berezhiani *et al.* [10], the parameter space still hosts favored regions which have motivated the proposal of new experiments [57, 60]. In addition, since the parameter exclusion has been mostly bounded at low mass-splitting ($\tau_{nn'} \gtrsim 10$ s for $\delta m < 10^{-12}$ eV) in UCN storage experiments, and less efficiently ($\tau_{nn'} \gtrsim 10^{-1}$ s) at large mass-splitting (up to $\delta m \approx 10^{-8}$ eV) from regeneration measurements, one could wonder whether $n - n'$ oscillations would indeed happen at the scale of seconds in the yet unexplored region at large mass-splitting.

Chapter 2

GADGET: A novel UCN counter

One of the main objectives in this work was the characterization and optimization of one of the fastest UCN detectors ever built: the scintillation gaseous detector GADGET. This novel neutron counter was originally designed within the n2EDM project, which aims at the measurement of the neutron electric dipole moment (d_n). Normally, a high sensitive measurement of d_n demands special efforts in two main directions: reducing the systematic effects and increasing the counting statistics. The latter requires implementing high efficiency UCN detectors capable of background discrimination and constant performing in long-lasting experiments. GADGET appears as a detector outclassing in both of these requirements simultaneously [21]. In addition, the fast voltage pulses product of the scintillation in GADGET make it a suitable option for high-flux UCN experiments.

This chapter focuses on the description of UCN detection with GADGET. In the first part, an overview on past UCN detectors and their operation is presented. Then, we introduce the detection principle and a detailed explanation of the main components of the GADGET detector. The third part is dedicated to the Pulse Shape Analysis technique, specially developed for this detector with UCN experiments performed at the PSI and ILL sources. In the end, a study on the influence of the gas admixture pressure in the UCN detection efficiency is exposed.

2.1 State of the art

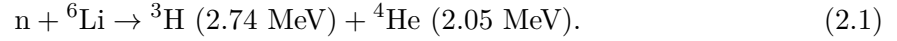
Since the discovery of the neutron in 1932 by Chadwick, neutron detectors have been characterized by their indirect working principle. The zero net charge of neutrons excludes them from processes such as atomic excitation and ionization, that are the most exploited phenomena in particle detection. Thus, in order to be detected, neutrons have to be either absorbed or scattered through an initial nuclear reaction out of which reaction products lead to the desired ionization or light emission. Most of the time, absorption reactions are preferred over scattering ones because of their larger share of energy release. Following the general rule stating that the larger the energy released, the higher the detection resolution and signal-to-noise ratio, neutron detectors are designed while looking for high Q -value reactions and a mechanism to collect most of the emitted energy. Since the neutron energy is frequently much shorter than the reaction energy, information of the first is most of the time lost.

2.1.1 Overview of UCN detectors

There are some features of UCN detectors that differentiate them from higher energy neutron detectors. Often, the sensitive volume size is smaller for the former, since the absorption cross-section becomes quite larger at such energies. Another difference is the existence of a critical velocity v_c for UCN [24]. This parameter is defined by the material composing the entrance window of the detector. In order to avoid UCN reflection, this first layer has to have a Fermi potential low enough so to allow the UCN transmission. In the following, a brief discussion of some UCN detectors tested and utilized in previous experiments will be given.

⁶Li-doped glass scintillator

⁶Li glass scintillator, known in the literature as GS*x*, contains Ce₂O₃, SiO₂, MgO, Al₂O₃ and Li₂O oxides. It takes advantage of the ⁶Li isotopes to capture neutrons ($\sigma_a = 344667$ barn*) via the reaction

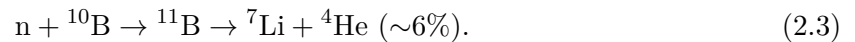
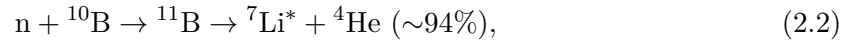


The emitted products, whose energies amount to 4.79 MeV[†], trigger the scintillating process after ionizing the Ce atoms (Ce³⁺). The scintillated light is characterized with a maximum wavelength at 395 nm for all the GS*x* types. Given the fast decay time (60-75 ns) of the light-emitting states [79], this detector is a good choice in high flux UCN experiments.

The particularity of this detector is found in its double-layer configuration. As shown in Figure 2.1, the glass front face is ⁶Li-depleted (GS3 or GS30) while the remaining portion is ⁶Li-doped (GS10 or GS20). Such partitioning reduces the probability of escape events that give place to partial energy deposition counts ($E_{\text{det}} < 4.79$ MeV). Since the first layer is almost transparent to UCN, neutron capture is more likely in the second layer. Therefore, the energy deposition tracks of tritium and helium start near the crystal center. Compared to gaseous detectors, this detector has a larger sensitivity to gamma background (the cross-section for gamma-ray interaction is larger in crystal materials).

Cascade detector

This kind of detector is based on the ¹⁰B neutron capture. The large UCN absorption cross-section of boron ($\sigma_a = 1.4 \times 10^6$ barn) is used to stop neutrons in a 100- μ m-thick layer via the reactions



The ⁷Li and ⁴He are emitted with kinetic energies near 1.47 MeV and 0.84 MeV, respectively, which subsequently are deposited in an argon-CO₂ gas mixture through ionization processes. The reaction product's tracks, whose lengths are in the order of a few mm at atmospheric pressure [80], give place to a cascade effect when the primary electrons are drifted towards the

*Value scaled from thermal energies with the $1/v$ law: $\sigma_{\text{UCN}} = \sigma_{\text{th}} \times v_{\text{th}}/v_{\text{UCN}}$.

[†]This available energy benefits the discrimination of neutrons against the background, mainly composed of gamma-radiation.

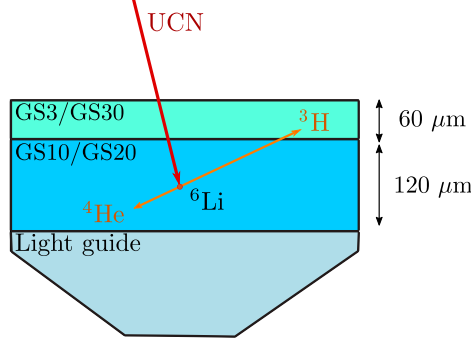


Figure 2.1: Graphical representation of UCN interaction in the ${}^6\text{Li}$ -doped glass scintillator. The first ${}^6\text{Li}$ -depleted layer (GS3 or GS30), transparent to UCN, avoids the escape of the reaction products. Following, a ${}^6\text{Li}$ -doped layer (GS10 or GS20), in charge of the UCN absorption. The scintillated photons are collected at the end of the light guide (bottom part).

holes in a gas electron multiplier (GEM) foil[‡]. Here, the number of electrons is amplified by means of a potential difference supplied at both sides of the foil. The electron cloud steaming from the holes is detected with a readout 2D structure, composed of 256 pixels in a total area of 200 mm². Figure 2.2 sketches the main elements in the detection chain. Because the UCN conversion and the ionization occur in different regions, this detector is characterized with a dead layer. Around 10-15% of the reaction products are totally absorbed within the finite thickness boron layer and lost from the counting electronics.

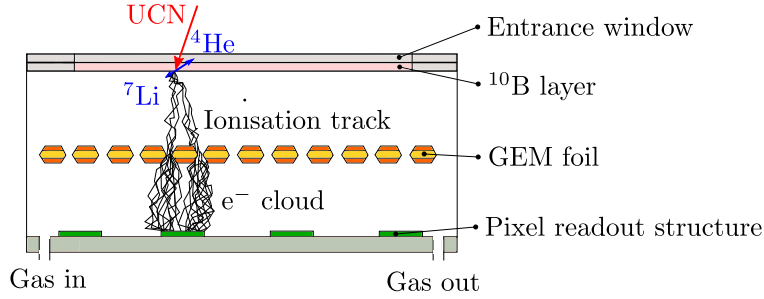


Figure 2.2: Basic representation of the working principle in a cascade detector. The number of primary electrons is increased after passing through the GEM foil. The Ar-CO-2 gas mixture circulates in continuous mode to minimize aging effects.

${}^3\text{He}$ gaseous detector (Strelkov)

${}^3\text{He}$ based detectors have been widely used in neutron experiments [81–83]. In fact, the UCN absorption cross-section by ${}^3\text{He}$ is even larger than that of ${}^{10}\text{B}$ ($\sigma_{\text{ab}, {}^{10}\text{B}} \approx 0.8\sigma_{\text{ab}, {}^3\text{He}}$). The detection principle in these detectors exploits the charged particle emission from the absorption reaction,



[‡]Normally, a GEM is a 50 μm thick kapton foil, copper clad on each side.

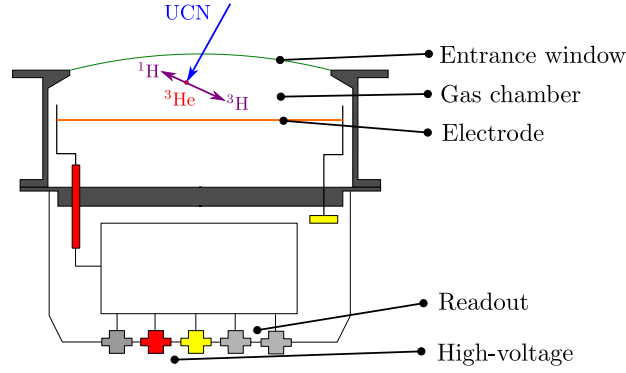


Figure 2.3: Diagram of a Strelkov ^3He detector. Figure adapted from [24].

where 573 keV go for the proton (^1H) and 191 keV for the tritium (^3H). A second gas fed into the same gas chamber next to ^3He works as stopper for the reaction products. The energy deposition in this gas releases electrons, which are collected by a high-voltage wire electrode located at the bottom of the gas chamber (see Figure 2.3). Although Strelkov detectors can be operated with several ionizable gas mixtures, e.g. Ar-CO_2 , Ar-CH_4 and CF_4 , the pulse signal duration is determined by the charge collection process, amounting to up to a couple μs . This long period represents the main limitations of Strelkov detectors when attempting high counting rates experiments [24].

2.2 Description and detection principle of GADGET

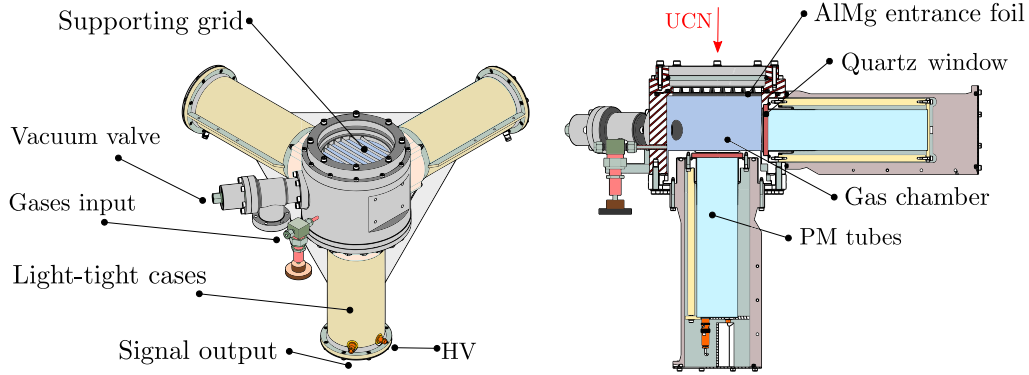


Figure 2.4: Technical drawing of the GADGET detector indicating its mains components. The left side shows a 3D-view of the already mounted detector. On the right, a sectional view allows seeing inside the cases and chamber. The red arrow indicates the direction of UCN entering the chamber.

GADGET is a UCN detector employing two gases to complete the indirect detection. When crossing the detector entrance foil, neutrons are absorbed by ^3He nuclei. Emitted after the absorption, the reaction products proton and tritium share 764 keV according to Eq. (2.4). A second gas is then used to transform part of this released energy into light. CF_4 is chosen due to its high photon yield, transparency to its own emitted light, non-flammability,

accessibility and price. The passage of proton and tritium inside this gas produces ionization and direct scintillation from the CF_4 excited states [22]. The lifetimes of such emissions, close to 6 ns [23], make the signal pulse generation a very fast process when compared to previous gaseous detectors whose signals raise from electron collection [24]. The light collection in GADGET is completed by a set of three photo-multiplier tubes (PMT) mounted on the transparent quartz windows of the gas chamber. Optical grease is used to improve the optical contact by increasing the photon transmission from the quartz window to the PMT that are covered by black plastic cases so to avoid exterior light contamination. Figure 2.4 shows a general description of the main constituents of this detector.

2.2.1 Data acquisition: FASTER

The voltage signals generated by the PMs are processed with the Fast Acquisition SysTem for nucleEar Research (FASTER) developed at *Laboratoire de Physique Corpusculaire* (LPC-Caen) [84]. This digital data acquisition system is based on Field Programmable Gate Arrays (FPGA) whose hardware components are designed in a modular fashion. The FASTER unit module consists of a motherboard (SYROCO_AMC_C5) hosting two daughter boards (CARAS) each equipped with two analog-to-digital converters, both characterized with a sampling capacity of 500 MHz with 12-bits. This acquisition system has been successfully tested in setups where the events counting rate goes up to 10^6 cts/s [85].

The signal treatment, carried out in the FPGA, includes baseline restoration (BLR), low and high pass filters, 2-dimensional threshold triggering, charge integration, among others. The parameters defining these tools are easily manipulated from the visual interface offered by the software *faster_gui*, also developed by the FASTER LPC team. Essential for the GADGET detector is the single clock system, which is synchronized for all the channels (all the PMs). It allows storing the absolute time of each event with a 2 ns resolution.

Qt2t module

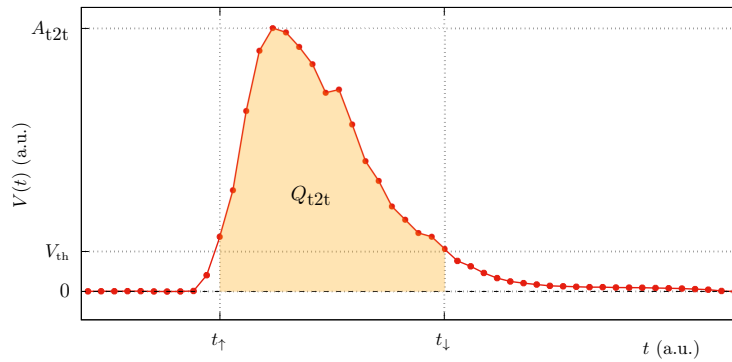


Figure 2.5: a UCN sample pulse detected by a GADGET PMT. The charge integration computed within FASTER runs from the time of positive to negative slope threshold crossings (Eq. (2.5)).

Pulse waveforms produced by GADGET PMTs depend on the interaction process of the detected particle. The number of photons emitted inside the gas chamber and the neutron

absorption position are two of the several parameters defining the pulse features. These differences between waveforms are exploited by a pulse shape technique (see section 2.3). FASTER provides a specialized module for pulse recording that extracts the main waveform parameters without storing the entire signal. This module, named Qt2t, is based on an online processing component that computes the threshold-to-threshold charge, maximum amplitude, threshold-to-threshold duration, position of the maximum and the before-threshold charge of pulses [25].

The main pulse parameters used in GADGET are the threshold-to-threshold charge (Q_{t2t}) and maximum amplitude (A_{t2t}). While the former is proportional to the amount of detected light and therefore to the event energy, the latter can be used to establish the quickness of the light collection. Both quantities are determined from the 2 ns voltage sampling $V(t)$ of the signal. Q_{t2t} corresponds to the time integral of $V(t)$ from the positive (t_{\uparrow}) to the negative (t_{\downarrow}) slope threshold crossings, expressed as

$$Q_{t2t} = \frac{1}{R} \sum_{t=t_{\uparrow}}^{t=t_{\downarrow}} V(t) \Delta t = \frac{2 \times 10^{-9} s}{50 \Omega} \sum_{t=t_{\uparrow}}^{t=t_{\downarrow}} V(t), \quad (2.5)$$

and the maximum amplitude represents the largest voltage between t_{\uparrow} and t_{\downarrow} ($A_{t2t} = V_{\max}$). A sample UCN event detection as seen by a PMT is displayed in Figure 2.5.

Triple coincidence

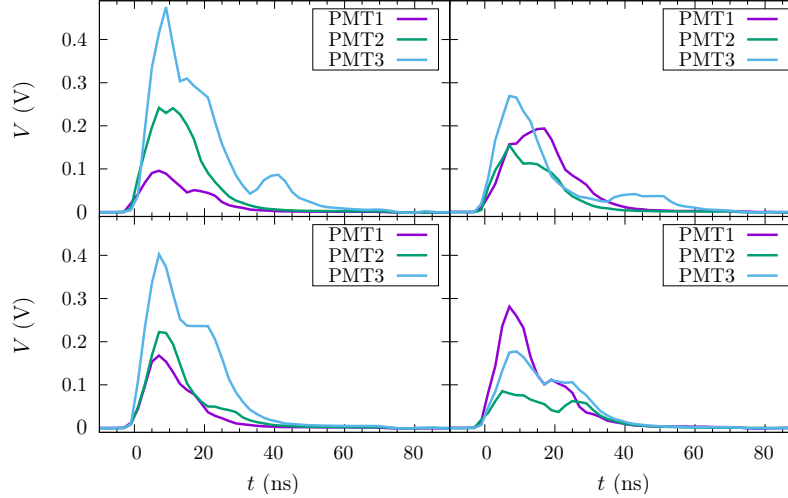


Figure 2.6: Four sample coincidence events measured on a UCN beam using a 50 ns coincidence window.

The triple coincidence technique in GADGET has a double-purpose: background filtration and event classification. Normally, a light emitting event produced inside the gas chamber would be recorded if the three PMTs are triggered simultaneously within a given time window. Those events are labeled with a ‘group’ flag and are said to be *in coincidence*. On the contrary, events detected by a single PMT are attributed to phenomena originated outside the gas chamber and do not receive any label.

In coincidence events raised by neutron detection, each PMT waveform presents a particular charge and maximum amplitude for multiple reasons (see four sample pulses in Figure 2.6). From one side, light propagation inside the gas chamber after a neutron capture depends on the ionization trajectories followed by the reaction products. In addition, the vertexes of these trajectories are completely determined by the position of the neutron absorption. Such geometrical factors make that more photons reach the PMT lying closer to the ionization paths. On the other side, although the three PMTs are of the same type, their intrinsic properties such as photo-electron conversion efficiency and amplification gain are different. The overall result is that individual PMTs Q_{t2t-i} and $A_{Q_{t2t-i}}$ carry part of the event information. For this reason, it comes naturally to define the grouped integrated charge and maximum amplitude as the sum of the three PMTs contributions

$$Q_{\text{gr}} = \sum_{i=1}^3 Q_{t2t-i}, \quad A_{\text{gr}} = \sum_{i=1}^3 A_{t2t-i}, \quad (2.6)$$

Triple coincidence tuning

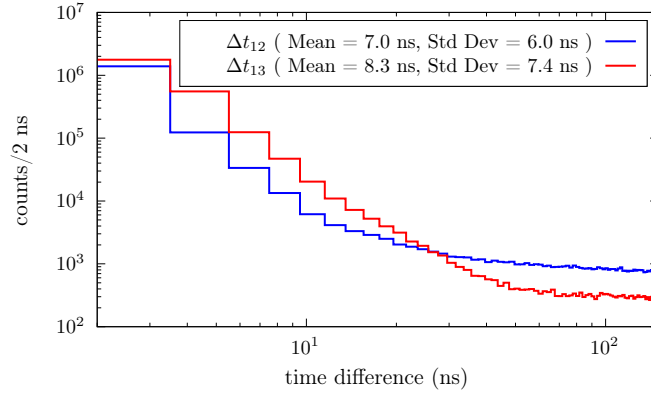


Figure 2.7: Time distribution of second (Δt_{12}) and third (Δt_{13}) events inside coincidence groups. The time is measured with respect to the absolute time of the first event.

Data grouping with FASTER can be executed in real-time or offline after the data taking. In either case, it is convenient to set a reasonable time length τ_{group} for the coincidences window. While a too large window would lead to a high pile-up probability, a too short one might miss actual coincidences with long time delays. Three physical processes involved in the UCN detection are considered in order to estimate an initial guess for τ_{group} . They are the reaction products stopping times, the lifetime of the CF_4 excited states, and the travel time of light inside the gas chamber. The first of these parameters is roughly calculated from the ranges (R) and kinetic energies (K) of proton and tritium as

$$t_{\text{stop}} \approx \frac{R}{v} = \frac{R}{\sqrt{2K/m}} \sim 2 \text{ ns}. \quad (2.7)$$

The CF_4^* lifetime $\tau_{\text{CF}_4^*} \approx 6 \text{ ns}$ was already measured and reported in [23], and the gas-chamber

crossing time of light is conservatively estimated from the chamber diameter as

$$t_{\text{travel}} \approx \frac{D}{c} \approx \frac{0.148 \text{ m}}{c} = 0.5 \text{ ns}. \quad (2.8)$$

Then, a window with a minimum width of 10 ns is large enough to give the three PMs the time to be triggered in coincidence. This is confirmed by the time distribution of events belonging to the same group and corresponding to a UCN detection, shown in Figure 2.7. Although the coincidence time window was adjusted to 200 ns, it can be seen that $\tau_{\text{group}} = 60$ ns is wide enough to include most ($\sim 99\%$) of the events. The remaining counts in the flat tails ($\sim 1\%$) are attributed to uncorrelated events.

2.2.2 Detector entrance window

The UCN transmission through the entrance window is one of the most decisive factors to achieve a high UCN detection efficiency in all types of detectors. Just as the reflection experienced by UCN along the transporting guides, the first layer of every detector could behave as a mirror if its Fermi potential is too large. Different materials and thicknesses have been tested to establish what entrance foil permits the largest UCN transmission. Measurements were performed at the ILL on the TEST beam line. The UCN spectrum was softened using the PSI filter [86] preceding a vertical climb of 90 cm. Then, UCN fall down 116 cm and cross the foil before reaching the detector. The largest transmission was obtained with aluminum-magnesium foils of 30 μm (see Table 2.1).

Table 2.1: UCN transmission through thin foils.

Material	Thickness (μm)	Transmission (%)
Al	100	77.40
	50	88.46
	25	91.64
$\text{Al}_{97}\text{Mg}_3$	100	81.68
	60	87.08
	30	92.94
Al_6O_6	100	78.49
Ti	50	45.03
	25	65.29
$\text{Ti}_{90}\text{Al}_6\text{V}_4$	50	49.20

In agreement with the tunnel effect, it was observed that the thinner the foil, the higher the transmission. However, in practice, foils cannot be made excessively thin without considering the pressure difference that they have to hold between the inside and outside of detectors. While UCN guides are vacuumed at pressures below 10^{-6} bar, CF_4 is fed into the chamber with pressures of about 1 bar. To resist such difference of pressure, the GADGET detector counts with a metallic grid placed on top of the foil. Currently, this grid makes possible the use of aluminum layers with thicknesses of about 15 μm as the one used in the experiments for this work (A. Leysens & J. Chen, private communication).

2.2.3 Influence of the ^3He and CF_4 pressures

The amount of ^3He and CF_4 inside the gas chamber define to a large extent the UCN detection performance with GADGET. These quantities are easily controlled through the gas factory apparatus, which feeds both gasses with adjustable pressures into the detector. Depending on the experiment, the GADGET detector can be operated with different pressures in order to optimize its detection efficiency. From one side, one would desire a high ^3He pressure ($P_{^3\text{He}}$) to ensure that all neutrons crossing the detector are absorbed within the chamber volume. Similarly, a high CF_4 pressure (P_{CF_4}) is envisaged to achieve a complete halt of the reaction products proton and tritium, thus converting most of their kinetic energy into light. Although there are secondary effects that disfavor the increase of both gasses pressures, a first estimation of the minimal values can be calculated from the ^3He absorption cross-section and the proton and tritium stopping power in CF_4 .

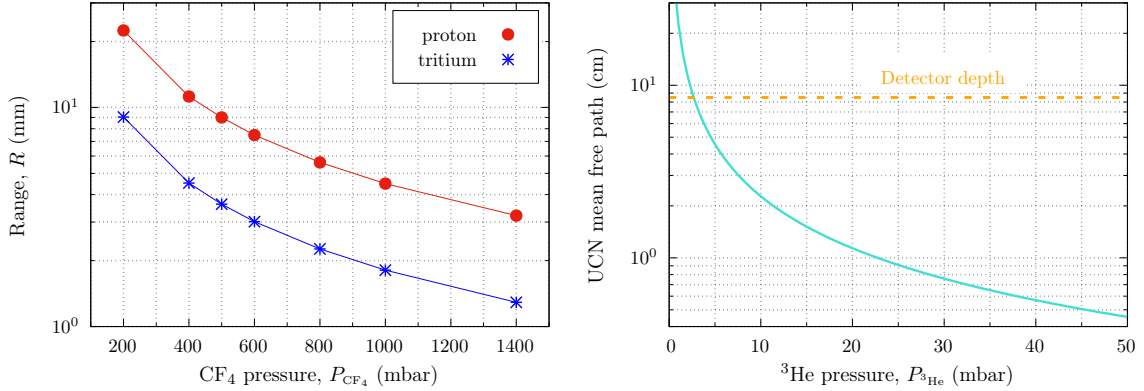


Figure 2.8: (left) Proton and tritium ranges in CF_4 calculated with SRIM at different gas pressures. (right) UCN mean free path in ^3He .

To guarantee that UCNs are absorbed before reaching the gas chamber back side, the gas pressure $P_{^3\text{He}}$ should be greater than 10 mbar. This can be seen from the UCN mean free path in ^3He as displayed in Figure 2.8 (right) as a function of the gas pressure. Since UCN entering the gas chamber with angled trajectories could reach the side walls with paths shorter than a few centimeters, the previous estimation is only valid for neutrons following trajectories parallel to the chamber axis. In general, this is not a problem given that UCNs fall through vertical guides favoring the parallel-to-axis trajectories. Nevertheless, in setups that are not arranged with the vertical UCN falling, taking $P_{^3\text{He}}$ up to 15 or 25 mbar should be considered.

The CF_4 pressure plays an important role in the pulse generation. It determines the range of proton and tritium in the gas mixture. If P_{CF_4} is too low, the reaction products could escape the chamber without producing the partial energy deposition that leads to the minimum amount of light detectable by the PMTs. Estimation of the required CF_4 pressure to ensure a complete halt of proton and tritium is done through SRIM simulations [26]. Figure 2.8 (left) shows the range computed for both particles at different CF_4 pressures with energies specified by the $\text{UCN}+^3\text{He}$ reaction. Clearly, these ranges should be measured with respect to the neutron absorption position, which mostly occurs next to the entrance foil. Given

that proton and tritium travel in opposite directions, the minimum P_{CF_4} can be set when the reaction products range equals the UCN mean free path (~ 1.5 cm at $P_{\text{He}} = 15$ mbar), i.e. $P_{\text{CF}_4} \gtrsim 400$ mbar.

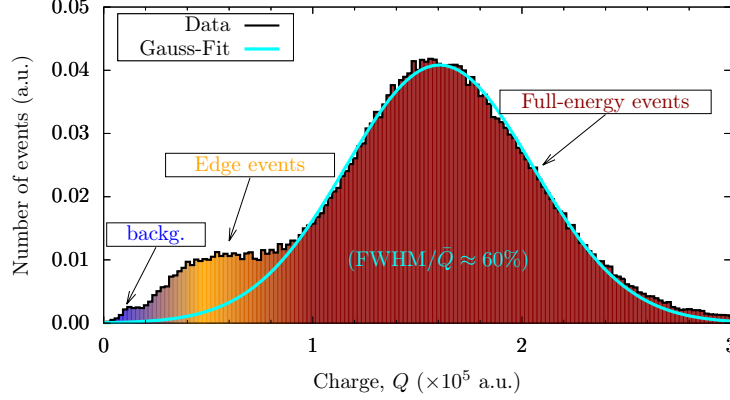


Figure 2.9: UCN charge spectrum measured by the GADGET detector. The gas chamber was filled with ^3He and CF_4 at pressures $P_{\text{He}} = 15$ mbar and $P_{\text{CF}_4} = 400$ mbar. Edge events are present at these pressures, but not dominant over the full-energy deposition events.

Since most of the UCN captures occur near the entrance window, the probability that one of the reaction products emitted from the capture reaches the window is non-zero. In those cases, the product traveling towards the window deposits part of its energy into the gas, while the rest is absorbed by the window atoms. Because only the first process induces light emission inside the gas chamber, the mean photon yield collected by the PMTs is reduced with respect to the full-energy deposition events. These partial deposition events, known as “edge events”, generate voltage pulses with shorter charges and amplitudes but are still recorded by the three PMTs. Their associated measured charge is then located at low values close to background events. Figure 2.9 shows an ordinary UCN charge spectrum measured with GADGET filled with $P_{\text{He}} = 15$ mbar and $P_{\text{CF}_4} = 400$ mbar. From small to large charges, three components of the charge spectrum are roughly identified: background, edge and full-energy events. Even though edge events add to the neutron counting, it is normally preferred to operate GADGET in conditions where they become minimal. As explained in section 2.3, edge events mimic the pulse shape of γ and β background detection in the gas, making difficult their discrimination.

2.3 Pulse Shape Analysis (PSA)

As other gaseous scintillating detectors, GADGET is sensitive to γ -rays and charged particles. Interaction of the former with CF_4 molecules liberates electrons capable of ionizing the gas and hence inducing light scintillation. Less likely, γ -rays also interact with the chamber quartz windows, leading to the emission of Cherenkov radiation. While voltage pulses raised by γ events are in general smaller than the ones corresponding to full-deposition neutron detection, Cherenkov events are characterized with fast pulses which allow their removal from the UCN counting. Charged particles, which in common experimental setups are mainly β -particles originated from the neutron activation of the detector constituents, can cross the

gas chamber and provoke scintillation on the CF_4 molecules. In this section, we perform a pulse shape analysis to identify the aforementioned processes. The technique uses the charges and amplitudes of the three PMT signals when detected in coincidences.

2.3.1 PS parameter

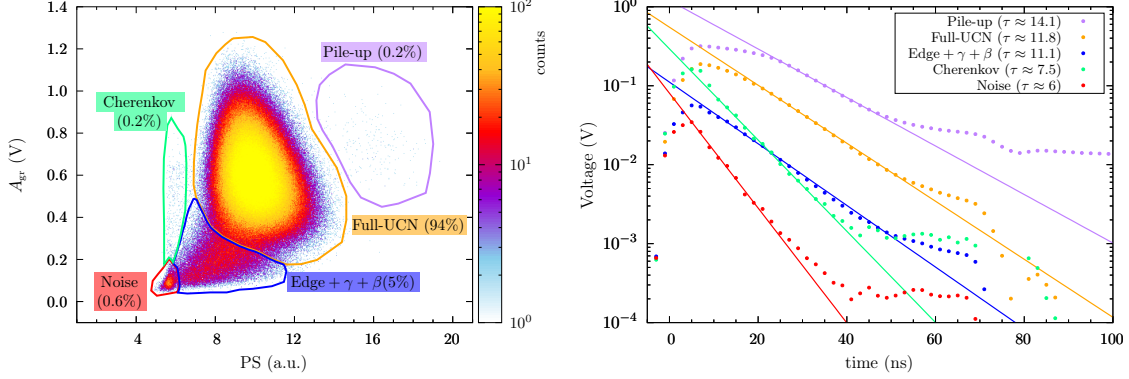


Figure 2.10: (left) PSA of UCN detection at PSI. Five initial categories are proposed to separate the main full-energy UCN events from less likely events. (right) Average pulse waveform of each category and associated exponential fit.

Both, the amplitude and integrated charge of PMT pulses are proportional to the amount of light released by the prompt emission of CF_4 . Similar to most of the organic scintillators, this gas also has a longer-lived component [87] whose contribution to the total light emission depends on the nature of the ionizing particle. This feature is used to differentiate fast from slow pulses by computing the pulse-shape (PS) parameter as

$$\text{PS} = Q_{\text{gr}}/A_{\text{gr}},$$

where Q_{gr} and A_{gr} are the grouped charges and amplitudes over the three PMTs (see Eq. (2.6)). PS, which is proportional to the time duration of pulses, allows identifying different types of events during ordinary UCN detection as shown in Figure 2.10 (left). The displayed data corresponds to UCN detection at the West-2 beam port of the UCN source at PSI (see Figure 2.21). Environmental backgrounds at this site are expected at low rates due to the large shielding between the experimental hall and the UCN source. Categories shown in the sample PS-map are simply built from visual contrast in the two-dimensional histogram. The average waveform associated to each category is presented on the right side of the same figure. The fitted decay constants of average waveforms demonstrate that events in these categories originate from diverse physical processes. Proper characterization of the proposed categories, which justifies their labeling, is thoroughly studied in the next sections.

2.3.2 Dalitz-plots

Granularity, the power to determine the interaction position of events within the sensitive volume, was not a requirement for the design of GADGET. Nevertheless, the PMTs configuration around the gas chamber allows estimating with a rather rough precision the light emission

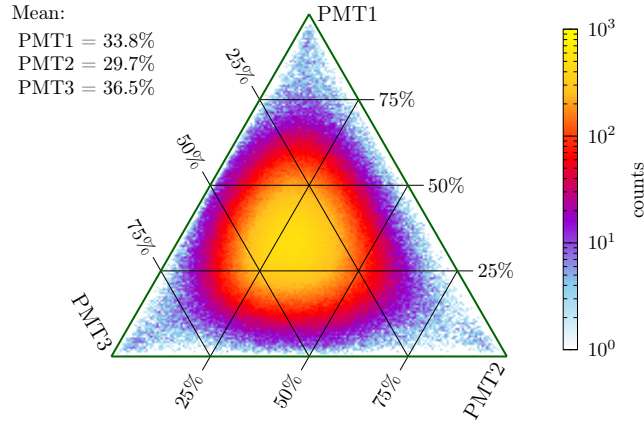


Figure 2.11: Dalitz-like plot of UCN detection constructed from the relative PMTs charges of coincidence events displayed in Figure 2.10.

position of detected events. Inherent limitations to accurately apply this technique come from the fact that solid angles formed by the light emission vertexes towards the PMTs faces are different. While PMT1 and PMT2 are placed on the curved surface, PMT3 is located on the chamber back side with respect to the entrance window (see Figure 2.4). In addition, the light reflection on the vessel inner walls adds a blurring effect to the relative PMT photon collection that complicates determining the relative distance between PMTs and the emission point.

Inspired on the Dalitz-like plots method for beta decay studies [88], we propose a graphical representation of the coincidence events where the relative integrated charges (Q_{t2t-1} , Q_{t2t-2} and Q_{t2t-3}) between the three PMTs is determined by a single point inside an equilateral triangle. The coordinates of such a point are calculated as

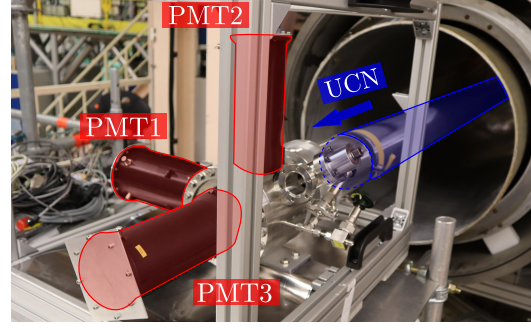
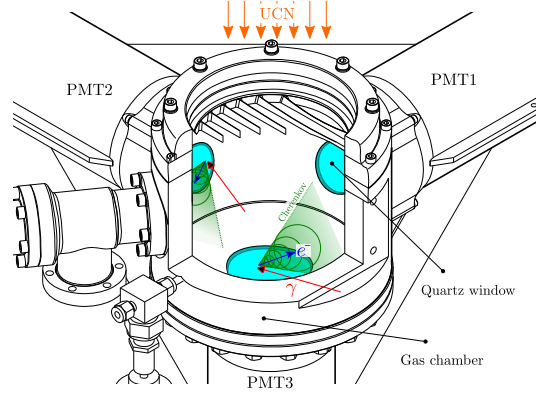
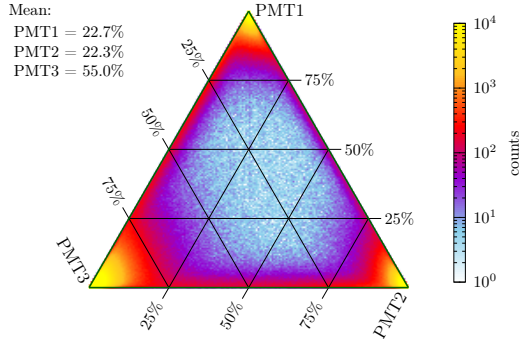
$$(x, y) = \left(\frac{1}{2} \frac{Q_{t2t-1} + 2Q_{t2t-2}}{Q_{gr}}, \frac{\sqrt{3}}{2} \frac{Q_{t2t-1}}{Q_{gr}} \right). \quad (2.9)$$

Therefore, the closer the point to one of the corners, the larger the integrated charge in one of the PMTs. In this way, coincidence events producing similar Q_{t2t} on all PMTs will populate the triangle barycenter: (PM1, PM2, PM3) = (33, 33, 33)%. In order to correct for individual signal amplifications, charges Q_{t2t-i} are normalized by the PMT gain and operating high-voltage or by its single-photo-electron peak position. As an example, the Dalitz-like plot associated to events already represented in the PS-map of Figure 2.10 is shown in Figure 2.11. The largest counting, located near (33, 33, 33)%, indicate that most of the UCN detection produce alike charges in the three PMTs. This plot allows stating that detected events originate mostly within the gas chamber with comparable distances to the PMTs. The slight deviation of the mean value from the barycenter is then attributed to differences between the effective PMT-covered solid angles.

Although this graphical technique is not entirely necessary to define a UCN category, it facilitates identifying the origin of detected events. For this reason, Dalitz-like plots are to be analyzed simultaneously along with PS-maps. In the following, four experimental setups are examined to determine the signature of background and UCN events.

Table 2.2: PMTs (type H13795-100-Y001) features.

Label	Series	Gain $\times 10^6$	Voltage (V)
PMT1	ZT8639	7.91	1750
PMT2	ZT8631	6.87	1750
PMT3	ZT7939	8.22	1750

**Figure 2.12:** PMTs experimental disposal with respect to the UCN guide at the ILL setup.**Figure 2.13:** (left) Dalitz-like plot of UCN coincidence detection with empty gas chamber. (right) Schematic view of Cherenkov light streams produced in the quartz interfaces. The conic profile explains the large event counting on the triangle corners.

2.3.3 UCN beam in empty gas chamber at ILL

Before going through the analysis of pulses created by CF_4 scintillation, it is relevant to check whether a different source of light is capable of producing coincidence events in a bare detector vessel. To this end, GADGET was vacuumed and mounted on the EDM beam port at ILL as shown in Figure 3.1. The PMT positioning with respect to the UCN beam guide and their individual features are resumed in Figure 2.12 and Table 2.2, respectively. Neutrons in this setup, whose fluxes are estimated at $\Phi_{\text{UCN}} \sim 3 \times 10^5 \text{ s}^{-1}$, can freely cross the detector gas chamber reaching the vessel walls, the quartz windows or even the PMTs. In consequence of this, the neutron absorption by the detector constituents enhances while giving place to larger γ and β backgrounds. Detected events are thus attributed to the radiation generated from the de-excitation of activated nuclei.

Electronic noise pulses due to PMT dark currents, with amplitudes of up to $\sim 5 \text{ mV}$, were discarded by setting a large voltage threshold: $V_{\text{th}} = 10 \text{ mV}$. Despite this stringent filtering, individual PMT counting rates (singles events) with empty chamber were of about 6 kHz

during UCN delivery cycles. This number reduces by a factor of 100 (60 Hz) once the 60 ns triple coincidence condition is applied (see section 2.2.1). Such great decimation demonstrates that most of the detected events are seen by a unique PMT.

Special interest is given to the 60 Hz coincidence events. Their particular distribution on the Dalitz-like plot for a two-hour measurement of UCN cycles is shown in Figure 2.13 (left). The first and most evident signature is the counting predominance near the triangle corners. They correspond to in-coincidence detection, where one of the PMTs registers a substantial charge while pulses in the other two are just above the threshold. At the same time, but less likely, coincidences where two PMTs detect similar charges while the third one is still negligible stack on the triangle sides. The number of events where the three PMTs collect alike light pulses are scarce for this detector configuration.

Since empty-chamber light pulses are mostly detected by a single PMT, the events are attributed to Cherenkov radiation emitted within the quartz interface between the chamber and the PMTs photocathodes. This radiation results from γ -background interacting with quartz atoms present in the 6-mm thick vessel light outputs and the PMTs entrance windows [89]. In fact, quartz electrons when removed by γ -rays can travel faster than the light in this medium. While moving, electrons shine light with conic streams focused along their direction of motion. In principle, these light streams could point towards one or two PMTs, but given the geometrical PMT arrangement, little light would reach the third PMT left behind the moving electron. A schematic representation of this idea is illustrated on the right side of Figure 2.13.

The contribution of each corner to the total counting in the Dalitz-like plot is approximately 16.6%, 16.8% and 66.5% for PMT1, PMT2 and PMT3, respectively. A simple explanation for such difference is based on the UCN motion when entering the gas chamber. After being transmitted through the detector entrance foil, neutrons freely cross the empty chamber with trajectories directed mainly along the UCN guide axis. Recalling that the chamber is 8.5-cm deep, one would expect a considerable fraction of the beam impinging on the PMT3 vessel side and just few neutrons hitting the PMT2 and PMT1 faces. In consequence of this, more neutron activation occurs near the PMT3 chamber, then increasing the probability of Cherenkov light on its quartz interface.

The PS-map of empty chamber detection shown in Figure 2.14 reveals that Cherenkov events spread out on a narrow region with PS parameters between 5 and 8 for coincidence and single events. On the other hand, pulse amplitudes extend over a rather large range, going from the voltage threshold up to 600 mV and 1100 mV for single and coincidence events, respectively. If comparing to other categories, the Cherenkov PS average value results short ($\overline{PS} \sim 6.4$) with respect to UCN events (see for example Figure 2.10). This is confirmed by the average pulse waveform of events in the “Cherenkov” category, which have a decay constant 40% smaller than the one computed for Full-UCN events (right side of Figure 2.10). Finally, one could also remark that the already low coincidence counting rate recorded with empty chamber further decreases after filling the gas admixture. Since neutrons are absorbed by ^3He , less activation and therefore γ -emission is available to induce the Cherenkov light.

2.3.4 γ and β (^{137}Cs source) on CF_4

One of the biggest concerns in background identification comes from the CF_4 ionization and excitation by environmental γ -rays. In addition, neutron-activated nuclei composing the

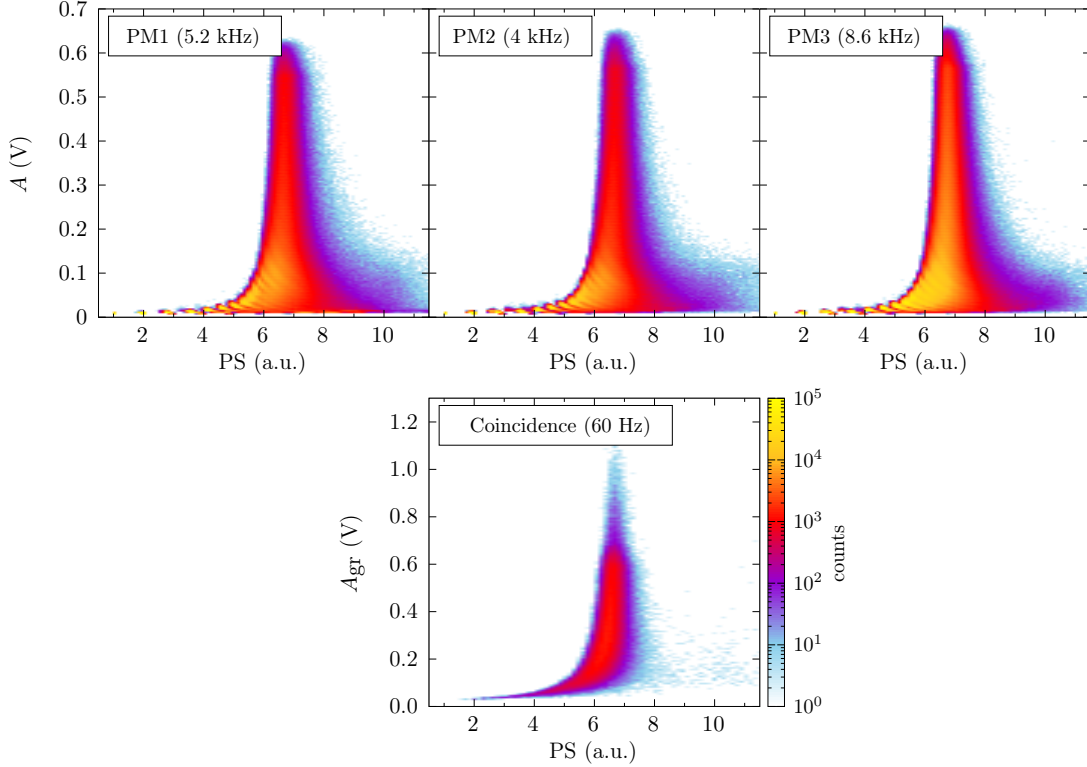


Figure 2.14: PS-maps of UCN empty chamber detection in singles (top) and coincidences (bottom). The strong rate reduction after filtering coincidence events added to the similarities between all maps supports the attribution of events to Cherenkov light.

detector entrance foil, supporting grid and UCN guides could decay through γ or β emissions that would be detected with pulses comparable to the ones of UCN edge events. To assess the signatures of these particles, a 31.79 kBq ^{137}Cs calibration source was placed on top of the detector entrance foil in an experimental room far from other human-manipulated radiation sources. This isotope emits β -particles with a maximum energy of 514 keV (94.4%) and 1175.6 keV (5.6%), the former followed by the emission of either a 662 keV γ -ray (85%) or an internal conversion electron (9.6%). When crossing the 30- μm -thick entrance foil, β -particles reduce their energies by a factor of 3% and 1% for the large and short branching ratios, respectively. On the contrary, γ -rays are almost unaltered due to their long mean free path in aluminum (~ 5 cm). Once inside the CF_4 gas, β -particles with maximum energies have ranges of 49 cm (large branching) and 141 cm (short branching) while the mean free path of γ -rays is of the order of 3.5 m. Even if γ -rays easily cross the chamber, β -particles might be totally or partially absorbed by CF_4 depending on their initial energies.

Two measurements were performed with 500 mbar of CF_4 filling. One with a 1-cm aluminum slab blocking the passage of β -particles into the detector, the second with no intermediate material. The counting rate of γ events was 5 times larger than the one recorded without the ^{137}Cs source (background events), and increased by a factor of 12 after removing

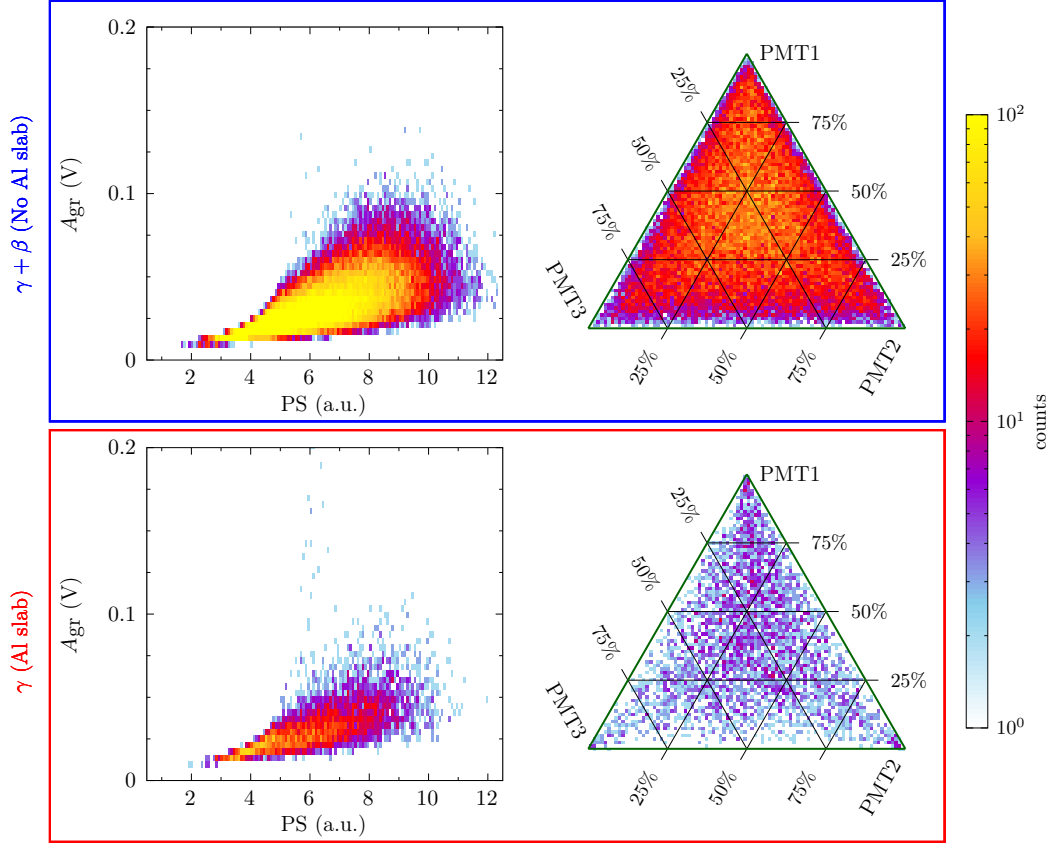


Figure 2.15: PS-maps and Dalitz-like plots measured with 500 mbar filling for $\gamma + \beta$ (top) and only γ (bottom) radiation emitted from a ^{137}Cs source. β particles in the latter were stopped by an aluminum slab placed between detector and source. Event signatures in both cases are equivalent.

the β absorber. PS-maps and Dalitz-like plots of both setups are displayed in Figure 2.15. The signature of γ and $\beta + \gamma$ detection are characterized by an almost homogeneously filled Dalitz-like plot. This is attributed to two main reasons, the low interaction probability of γ -rays and the broad trajectories of β -particles across the chamber. In both cases, the energy deposition has not a preferred location and thus counts add all along the Dalitz triangle.

The PS parameters for both measurements extend over a wide range, but the amplitudes are always lower than ~ 100 mV. PS-maps in Figure 2.15 highlight that γ and β radiations produce similar light signals. This is expected given that the interaction of 662-keV γ -rays with CF_4 occurs mainly through Compton effect, out of which the released electron provokes the scintillation. Less evident were the Cherenkov events observed with the empty chamber configuration. Although still present, their counting rate is almost negligible since most of the γ -rays mainly interact with the CF_4 molecules. This is understood if recalling that the gas volume is much larger than the quartz volume, and that the ^{137}Cs source only covers a small solid angle into the detector.

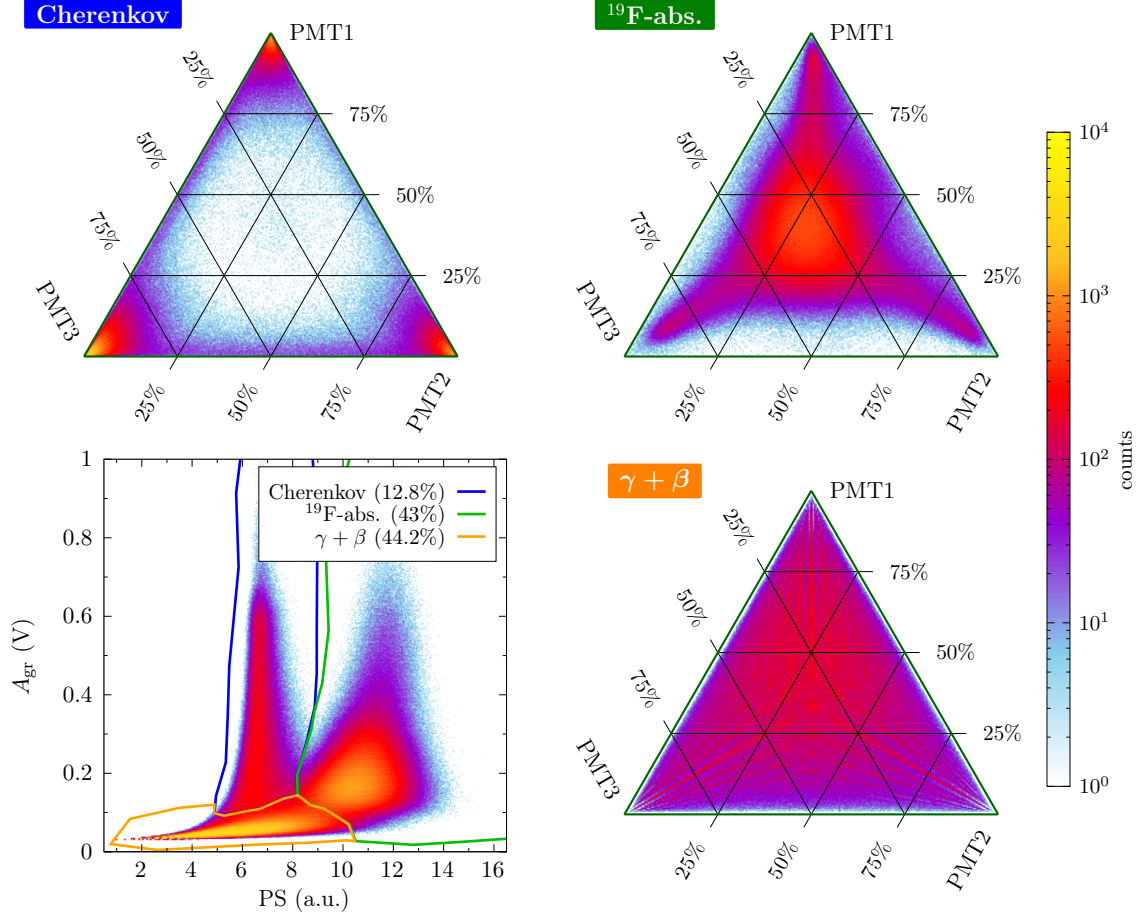
2.3.5 UCN beam on pure CF_4 

Figure 2.16: (bottom-left) PS-map of UCN detection with GADGET filled with CF_4 at 500 mbar and no ^3He . Measurement performed during 200 cycles. Top and bottom-right figures correspond to the Dalitz-like plots of categories constructed in the PS map motivated by the local maxima and the previously studied Cherenkov and $\gamma + \beta$ signatures.

This configuration combines the aforementioned events, Cherenkov, γ and β in a different setup. Here, the GADGET detector was filled with CF_4 at 500 mbar and then mounted on the ILL EDM beam port. Data was acquired during 120 UCN delivery cycles of 200 s each, resulting in a total counting of 1.6×10^7 coincidence events. The lack of ^3He gas inside the chamber contributes to the UCN interaction with CF_4 molecules or the detector walls. The number of CF_4 interactions is estimated similarly as done for the neutron absorption probability in section 2.4. The probabilities for elastic dispersion (up-scattering) and absorption in 500 mbar of CF_4 from this simplistic model yield 20% and 0.12%, respectively. According to the UCN flux, measured at ~ 300 kHz, about 60×10^6 UCN/s are lost due to up-scattering by the CF_4 molecules and about 360 UCN/s are absorbed by the fluorine in them ($\sigma_{\text{abs}}(^{19}\text{F}) \sim 3$ barn for UCN).

As previously mentioned, β -radiation could have origin on the neutron activation of the detector walls and the entrance foil. However, in this setup, it could also emerge from the neutron absorption of CF_4 . In fact, after activated ($T_{1/2} = 11$ s), ^{20}F emits β -particles with a maximum energy of 7024.5 keV. It is expected that these particles describe a particular detection signature for two reasons. First, the decaying isotope also composes the sensitive volume, making that the β ionization tracks start within the chamber. Second, there are up to 168 known γ -rays preceding the β -decay in ^{20}F [§].

Figure 2.16 (bottom-left) shows the PS-map of UCN detection with pure CF_4 filling, where three categories are defined with the help of the visible local maxima. While “Cherenkov” and “ $\gamma + \beta$ ” categories are easily recognized from direct comparison against previous Figures 2.14 and 2.15, respectively, the new “ ^{19}F -absorption” is proposed as representative of the overall light scintillation yield from the CF_4 neutron absorption. Also displayed in the same figure, the Dalitz-like plots associated to each PS category help confirming the nature of “Cherenkov” and “ $\gamma + \beta$ ” events explained in previous sections. As for the “ ^{19}F -absorption”, the spatial distribution of events appears to have origin mainly in the gas chamber center and less often in the vicinity of the quartz windows or detector inner walls. This centering in the Dalitz-like plot serves to emphasize the fact that these events are a product of the UCN interaction with CF_4 .

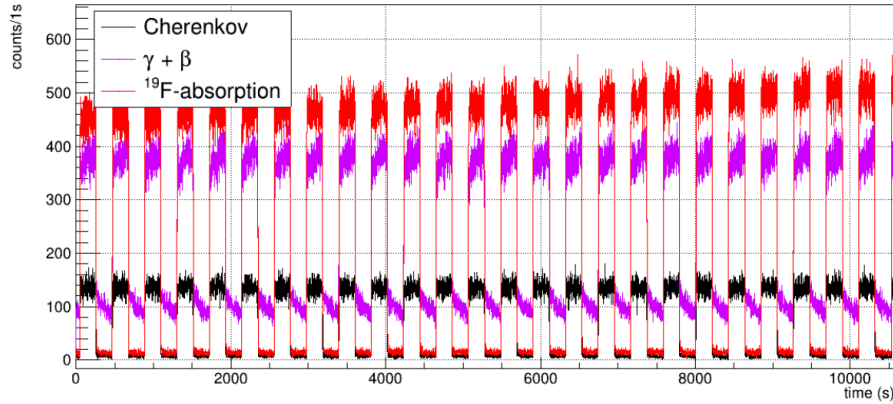


Figure 2.17: Counting rate of categories defined in Figure 2.16 as function of the time. Delivery cycles of constant UCN flux last 200 s every 400 s. 25 cycles were measured. Only ^{19}F -absorption events show a non-expected increase of the rate after several cycles.

A still unexplained feature of ^{19}F -absorption events is their counting rate evolution in time. One would expect that, as for all processes correlated to the UCN beam except for emissions from long-lived ($T_{1/2} \gtrsim \tau_{\text{cycle}} = 400$ s) neutron activated nuclei, the rate of these events remains constant during the 200 s of UCN delivery and drops to almost 0 during the next 200 s of beam sharing. Figure 2.17 compares the counting rates for the proposed categories, starting when the beam shutter was opened and stopping three hours later. During this time, “ ^{19}F -absorption” is the only category undergoing a rate variation after several cycles. This cumulative increase would be explained, for example, if the excited states in ^{20}F

[§]This characterizes the isotope as the one with the largest number of branches reported from any nuclear bound state [90].

had a life-time comparable to the cycle period. Since no evidence of such states was found in the literature, the time description of ^{19}F -absorption events is left to future works.

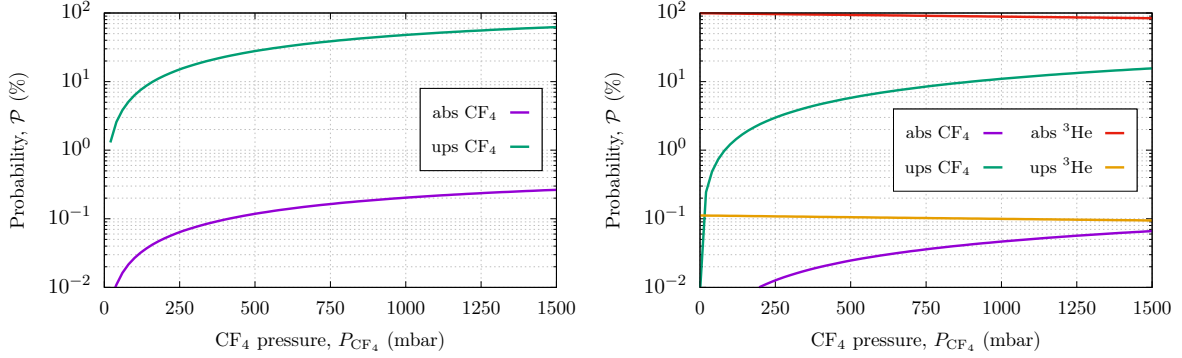


Figure 2.18: Absorption and up-scattering probabilities of UCN impinging on GADGET as a function of the CF_4 pressure from a dummy model (see next section). (left) Gas chamber filled with CF_4 only. (right) CF_4 plus 15 mbar of ^3He admixture. The neutron absorption by ^{13}C is neglected, as it represents less than 1% of the absorption in ^{19}F .

Making up the 44% of the total counting rate in this setup, ^{19}F -absorption events become negligible once ^3He is added to the gas admixture. The large absorption cross-section of ^3He dominates over the neutron mean free path. Therefore, as illustrated in Figure 2.18, the probability of ^{19}F absorption reduces from 0.12% to 0.02%, i.e. to 60 Hz assuming the same 300 kHz UCN flux. Noticing that this contribution is 10 times smaller than the statistical fluctuations, these events can be simply subtracted from the actual UCN counting without adding any significant systematic effect.

2.3.6 UCN beam on CF_4 (500 mbar) + ^3He (15 mbar) admixture

Data acquisition in this section corresponds to UCN detection recorded after filling both ^3He and CF_4 gases into GADGET's chamber. The PMTs arrangement and detector orientation with respect to the beam guide are shown in Figure 2.12. The resulting PS-map, shown in Figure 2.19, reveals that all counts spread over a continuous PS range: 2 to 18. No category completely separates from the rest since charges and amplitudes of UCN edge, full-energy deposition, $\gamma + \beta$ and pile-up events are similar between each other. This, however, does not prevent defining suitable categories to properly exclude background counting from UCN detection. A dedicated analysis of such category partitioning is presented in section 4.1.

The total counting rate during delivery cycles in this setup was of 288 kHz. Contributions from $\gamma + \beta$ background and ^{19}F -absorption were conservatively estimated from Figure 2.16 as 400 Hz (0.14%) and 58 Hz (0.02%), respectively. Since these rates are lower than the statistical fluctuations of the total counting, a large category was constructed enclosing backgrounds and UCN events, as shown in Figure 2.19 (bottom-left). “Cherenkov” and “pile-up” categories are also defined given that they are easily recognized with short and long PS parameters, respectively. Graphical cuts in this section have no purpose different from the study of their associated Dalitz plots, illustrated on the top and left sides of Figure 2.19. Although they only confirm what it was already presented in previous sections regarding Cherenkov and

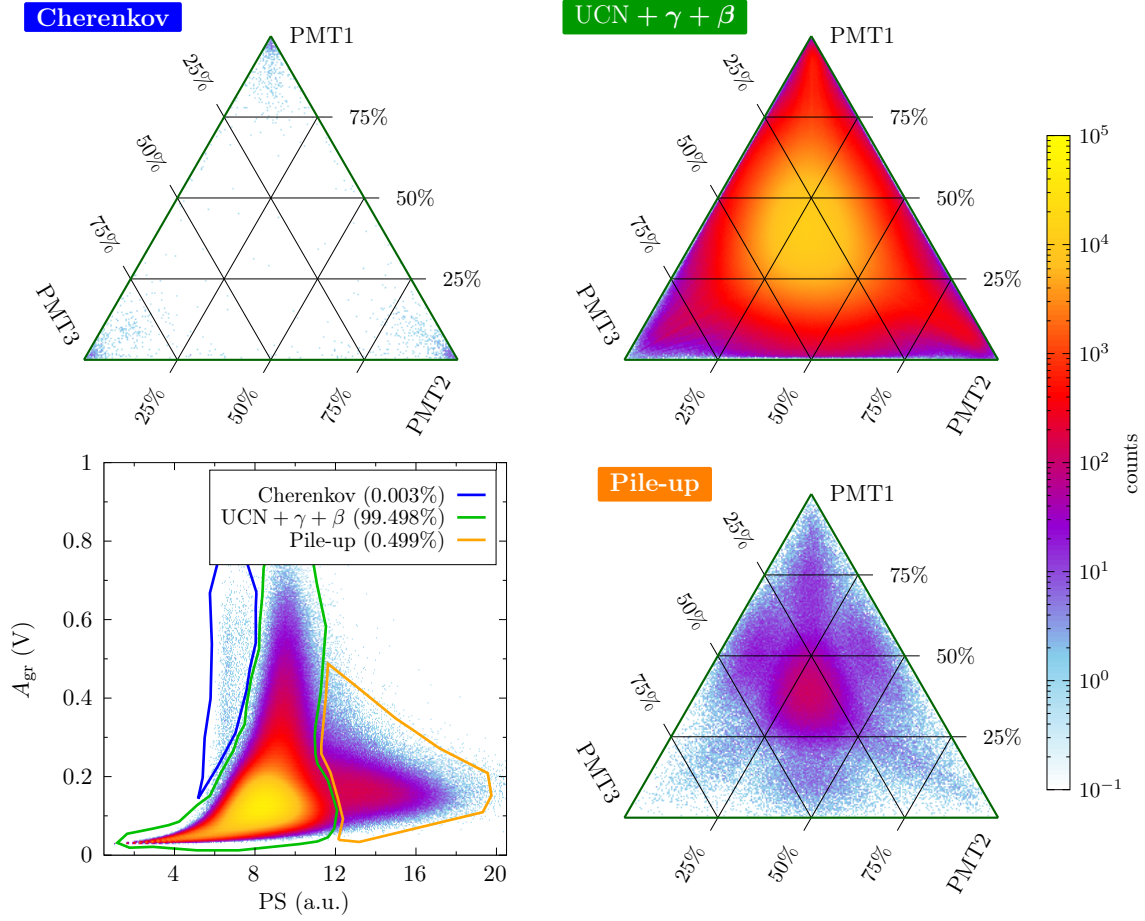


Figure 2.19: (bottom-left) PS map of events measured by GADGET during one UCN delivery cycle. The detector gas chamber was filled with 15 mbar of ^3He and 500 mbar of CF_4 . Top and bottom-right figures correspond to the Dalitz-like plots of categories constructed in the PS map. They were motivated by a previous study of Cherenkov events and the sample pulses in Figure 2.20.

UCN detection, the “pile-up” category, containing 0.5% of the total counting, requires a more detailed description.

Given the high UCN flux, the probability of double UCN detection is not negligible. The “pile-up” category is then added to include these events characterized by light pulses with amplitudes similar to single UCN detection but with almost twice their charges. A few pile-up sample voltage waveforms are depicted in Figure 2.20. We point out the fact that pile-up pulses cannot be separated at the acquisition level. The charge integration in FASTER Qt2t module (see section 2.2.1) has not a fixed window, but it rather depends on the double threshold crossing algorithm. If a second UCN produces light before the down-crossing threshold of a first UCN detection, the algorithm stores a unique event concatenating both signals. In future analyses, events in this category could be considered as double UCN counting or be safely discarded.

A summary of the main results exposed in the last four sections is found in Table 2.3. It

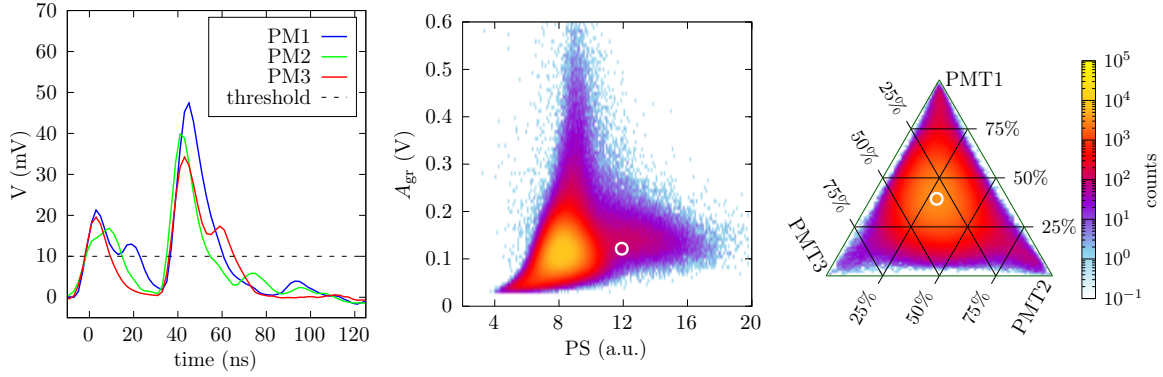


Figure 2.20: Pile up sample pulses and their corresponding map location (white circle).

Table 2.3: Event contribution to the total counting rate in different setups.

Source	GADGET	Contribution (%)					Total rate (s^{-1})
		Cherenkov	$\gamma + \beta$	^{19}F -abs.	UCN	Pile-up	
^{137}Cs	CF_4	-	100	-	-	-	192
	empty	100	-	-	-	-	60
UCN	CF_4	13	43	44	-	-	1000
	$\text{CF}_4 + ^3\text{He}$	0.003	0.14	0.02	99.338	0.499	288500

includes the relative contribution of the multiple events to the total number of counts. Even if the definition of categories remains a subjective process, the formulated conclusions are rather invariable due to the large difference between background and actual UCN rates. Most of the efforts were put on identifying the origin and physics of the detected events. Therefore, the reported numbers are just approximations to the exact real values, which are inaccessible given the categories overlapping. The main conclusion is that the predicted background contamination in the total UCN rate at the EDM beam port with GADGET detector is smaller than 1%.

2.4 Optimization of the ^3He and CF_4 gas pressures

In the previous section, we mentioned the high dependency of the neutron detection on the amount of absorbing and scintillating gases in GADGET. Two tests were carried out at the West-2 beam port of the UCN source at the PSI (see section 1.5.2) to evaluate the efficiency and optimal performance conditions of this detector. In the first (second), the CF_4 (^3He) pressure was shifted while keeping the other gas pressure constant. To reduce the sources of systematic uncertainties, all experiments were recorded with similar conditions. In order to correct for the UCN source degradation process, which leads to a reduction of the number of neutron per cycle, the UCN counting with GADGET (C_{GAD}) was normalized by a monitor counting (C_{mon}). A diagram of the experimental arrangement is shown in Figure 2.21.

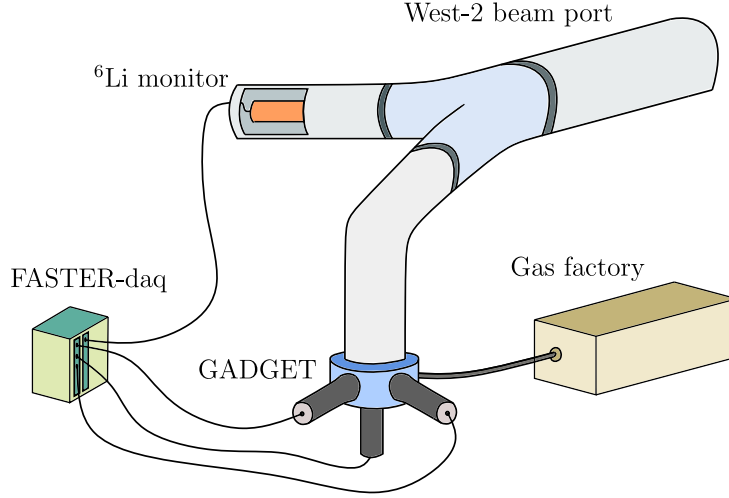


Figure 2.21: Experimental disposal of GADGET and a monitor ^6Li -based UCN detector at the West-2 beam port of the UCN source at PSI.

2.4.1 Measured signal as a function of $P_{^3\text{He}}$ and P_{CF_4}

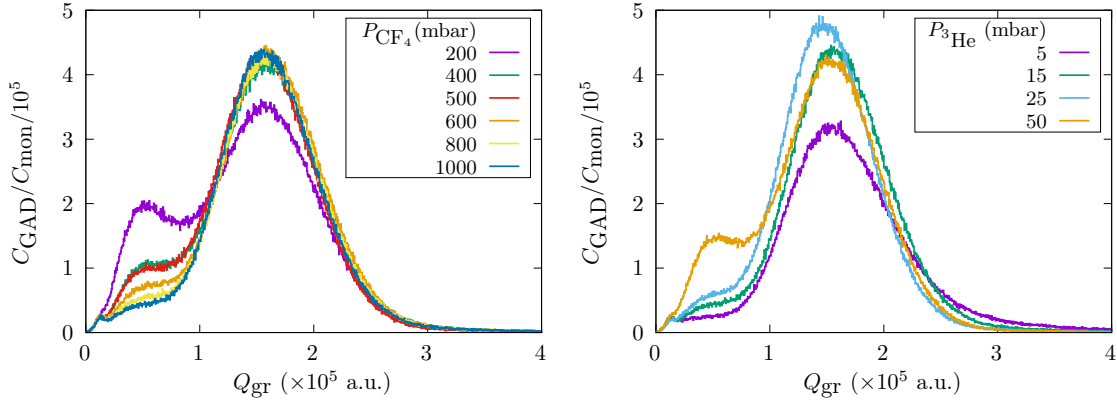


Figure 2.22: Charge spectra at different CF_4 (left) and ^3He (right) pressures. The number of edge events (left bump) become shorter as the CF_4 (^3He) pressure increases (decreases). ^3He (CF_4) pressure was kept constant at 15 mbar (1 bar).

Result of the first test, Figure 2.22 (left) shows the charge spectra obtained after varying the CF_4 pressure between 200 mbar and 1 bar while keeping ^3He at 15 mbar. The reduction of edge events at high CF_4 pressures is explained by the shortening of the proton and tritium ionizing trajectories. In particular, the drastic change between 200 mbar and 400 mbar spectra reflects the large variation of proton and tritium ranges (already reported in Figure 2.8): $2.2 \text{ cm} \rightarrow 1.1 \text{ cm}$ and $0.9 \text{ cm} \rightarrow 0.45 \text{ cm}$, respectively. Another clear behavior is the rise of the full-energy peak at large P_{CF_4} . This is expected given that events populating the ‘edge’ migrate to the ‘full-energy’ region as P_{CF_4} increases. Figure 2.22 (left) also shows that the UCN peak center is the same for the multiple measurements. Contrary to conclusions derived from the study of alpha particles detection with CF_4 [91] [J. Chen, private communication],

this result indicates constant photon yield for the tested CF_4 pressures. This difference between detection of both particles represents a proof of the quenching factor allowing larger scintillation to heavier particles. Last but not least, at very short charges and slightly less visible than the edge events, the ‘noise’ region is recognized. Its distribution, with charges $\lesssim 0.1 \times 10^5$, keeps a similar shape for all measurements and is easily removed by increasing the PMTs threshold voltage. The influence of the CF_4 pressure in the total counting rate is discussed in the next section.

The second test was carried out by shifting the ^3He pressure ($P_{^3\text{He}}$). Figure 2.22 (right) illustrates the spectra distribution obtained from runs with $P_{^3\text{He}}$ going from 5 mbar to 50 mbar, and P_{CF_4} fixed at 1 bar. Once again, edge events are more likely for few measurements. In particular, the larger the pressure, the greater the ‘edge’ region. In fact, when the helium pressure is augmented, the mean distance between the UCN absorption position and the entrance wall is shortened. In such cases, the probability for tritium and proton to escape the gas becomes higher. In contrast to what happens with CF_4 , here there is a remarkable difference between the counting rates of spectra at 5 mbar and 50 mbar. This suggests that ^3He at 5 mbar is not high enough to stop all the UCN impinging the gas chamber. Some of them find their way out after crossing it.

Table 2.4: Cross-sections of gases used in GADGET detector. σ_{up} for CF_4 reported by Seestrom *et al* [92]. Other values have been scaled from the NIST database to the UCN velocity 6.6 m/s.

	σ_{ab} (barn)	σ_{up} (barn)
^3He	1 777 667(2333)	2 000(133)
CF_4	14	3 300(660)

2.4.2 Detection efficiency as a function of $P_{^3\text{He}}$ and P_{CF_4}

It should be kept in mind that the joint contribution of edge and full-energy counts corresponds to the total UCN detection. Indeed, four main mechanisms determine the behavior of UCN after entering the gas chamber. They are the absorption and up-scattering by ^3He and CF_4 . While absorption reactions lead to light emitting processes within the gas chamber, in up-scattering reactions the UCN kinetic energy increases, thus allowing them to escape the detector.

In order to estimate the relative amount of UCN absorbed and up-scattered by both gases, we look at the *mean free path*, calculated as

$$\lambda = (\Sigma_m)^{-1} = \left(\sum n_i \sigma_i \right)^{-1}, \quad (2.10)$$

where Σ_m stands for the macroscopic cross-section accounting for all the possible interaction mechanisms with microscopic cross-section σ_i . In particular, for the processes involved in the chamber, it is written as

$$\Sigma_m = (n\sigma_{\text{up}})_{\text{CF}_4} + (n\sigma_{\text{ab}})_{\text{CF}_4} + (n\sigma_{\text{up}})_{^3\text{He}} + (n\sigma_{\text{ab}})_{^3\text{He}}, \quad (2.11)$$

with σ_{ab} and σ_{up} representing the absorption and up-scattering cross-sections, respectively. This last expression depends not only on the individual cross-sections (whose magnitudes are

resumed in Table 2.4), but also on the gas densities n_{CF_4} and $n_{^3\text{He}}$. Taking into account the operating conditions considered so far, the relative amount of gases is

$$\frac{n_{^3\text{He}}}{n_{\text{CF}_4}} = \frac{P_{^3\text{He}}}{P_{\text{CF}_4}} \approx 10^{-2}. \quad (2.12)$$

Thus, the macroscopic cross-section can be simplified to

$$\begin{aligned} \Sigma_m &\approx (n\sigma_{\text{up}})_{\text{CF}_4} + (n\sigma_{\text{ab}})_{^3\text{He}} \\ &= n_{\text{up}}\sigma_{\text{up}} + n_{\text{ab}}\sigma_{\text{ab}} \\ &= \frac{1}{K_B T} (P_{\text{CF}_4}\sigma_{\text{up}} + P_{^3\text{He}}\sigma_{\text{ab}}), \end{aligned} \quad (2.13)$$

where the ideal gas law has been used to express densities as function of pressures while adopting the subscript convention “up” referring to CF_4 and “ab” to ^3He . Note that the relative contribution to the macroscopic cross-section for double-gas-filling configurations is mainly governed by the ^3He nuclei:

$$\frac{P_{\text{CF}_4}\sigma_{\text{up}}}{P_{^3\text{He}}\sigma_{\text{ab}}} \approx 6.1\%. \quad (2.14)$$

Eq. (2.13) can be used to estimate the total absorption probability if assuming UCNs entering parallel to the chamber axis. As explained in Appendix B, the absorption probability in such simplistic scenario is given by

$$\mathcal{P}_{\text{ab}}^{\text{tot}}(P_{^3\text{He}}, P_{\text{CF}_4}) = \frac{P_{^3\text{He}}\sigma_{\text{ab}}}{P_{\text{CF}_4}\sigma_{\text{up}} + P_{^3\text{He}}\sigma_{\text{ab}}} [1 - \exp(-L/\lambda)], \quad (2.15)$$

with L the length of the gas chamber. This equation shows that while high CF_4 pressures attenuate the absorption, large ^3He pressures enhance it.

This dummy model for the neutron absorption probability can be compared against the total UCN counting of spectra in Figure 2.22. To do so, the total counting of all charges, including edge and full-energy events, is integrated and denoted as N_{tot} . For the sake of the comparison, N_{tot} and $\mathcal{P}_{\text{ab}}^{\text{tot}}$ are computed relative to their magnitude at 200 mbar when varying P_{CF_4} , and to 15 mbar when varying $P_{^3\text{He}}$. Figure 2.23 shows behaviors in both situations. The measured trends agree to a large extent with the ones predicted by the analytical model. First, one evidences that before being absorbed, some UCN are up-scattered by the CF_4 molecules. Proof of this is the 7% of counts gained when decreasing P_{CF_4} from 1000 mbar to 200 mbar. This behavior, added to the fact that the gamma-ray background is proportional to the CF_4 gas density, suggests avoiding too large P_{CF_4} . Second, raising the helium pressure from 10 to 15 mbar represents an extra 5% gain. More ^3He nuclei reduce the influence of CF_4 up-scattering. Experimentally speaking, this might also come from angled UCN trajectories that reach the wall chamber before being absorbed. The overall effect of setting both pressures properly (500 mbar CF_4 , 15 mbar ^3He) would signify an increase of 10% of the total UCN counting. That being said, low P_{CF_4} and large $P_{^3\text{He}}$ favor the predominance of edge events, which makes gamma events difficult to identify and remove from the charge spectrum. Nevertheless, it is also possible to separately measure the background spectrum, without UCN, and remove it from the measured UCN distribution.

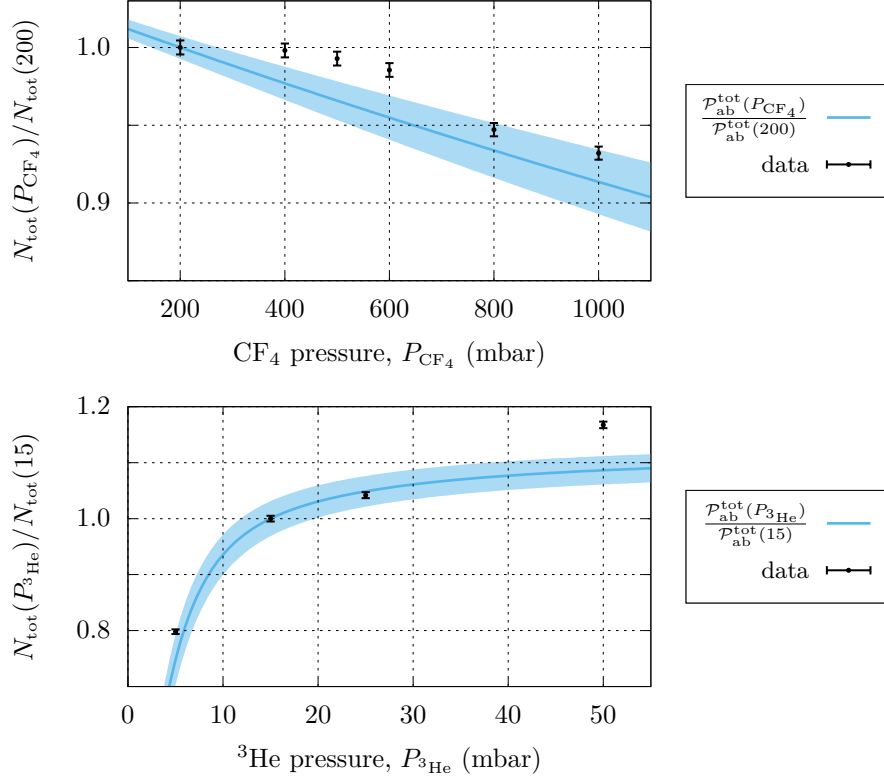


Figure 2.23: Measured counting rate as a function of the ^3He pressure with respect to 15 mbar result (bottom), and as a function of the CF_4 pressure with respect to 200 mbar result (top). The solid lines correspond to the absorption probability as determined by Eq. (2.15). The thickness of the lines represents the uncertainty propagated from σ_{ab} and σ_{up} .

2.5 Chapter conclusions

Among the several UCN detectors developed so far, GADGET proposes a fast counting while providing a simple detection mechanism which can be optimized via the gas ($^3\text{He} + \text{CF}_4$) pressures to respond to the different needs in UCN experiments. In particular, the light scintillation produced inside the mirror-polished gas chamber and the readout from the triple PMT array give place to fast voltage pulses lasting about 50 ns. Such pulses allow counting UCN in high-flux beams without leading to a significant pile-up contribution. For example, in experiments at the ILL, where the UCN detection rate could go up to 300 kHz, the pile-up rate was estimated below 0.5%.

If coupled to high-speed sampling acquisition systems such as FASTER, GADGET pulses can be analyzed for an efficient background removal. Firstly, this is done through the filtering of triple coincidences events. Pulses detected by a single or two PMTs are discarded, as most of the time they are not linked to light-emitting events generated within the gas chamber. A more rigorous Pulse Shape Analysis, constructed from the amplitude and integrated charge of each PMT pulse, has proven to separate events in at least 5 species. They are called ‘UCN events’, generated by the neutron absorption of ^3He (they can be full energy deposition if the

Table 2.5: Effect on the counting rate and number of edge events that produce increasing (\nearrow) or decreasing (\searrow) the gases pressures in GADGET.

Pressure	counting rate	edge events
CF ₄	\searrow	\searrow
³ He	\nearrow	\nearrow

reaction products are totally stopped by the scintillator gas, otherwise they are called edge events), ‘Cherenkov events’, produced by environmental γ -rays impinging on the gas chamber quartz windows and on PMT’s entrance windows, ‘ γ and β events’, due to the radiation emitted from the neutron-activated constituents of GADGET (entrance foil and inner walls), ‘pile-up events’, from multiple UCN detection within the logic coincidence time window (60 ns), and ‘¹⁹F events’, from the neutron capture by fluorine present in the scintillator molecules. Although it was not always possible to separate all species in non-overlapping PS categories, the contribution of background events was estimated below 1% at ILL.

It was also shown that, given the multiple factors affecting the detection efficiency, the optimization of both gas pressures demands a thorough study. In order to summarize the main results in this chapter concerning the gas pressure influence, we present in Table 2.5 the implications that working at high or low pressures have on the total UCN counting and edge events. In an ideal scenario with low γ background, the conclusion is straightforward, one should set low CF₄ pressure (500 mbar) to avoid up-scattering and high ³He (15 mbar) to completely absorb all neutrons. Otherwise, if experiments are to be performed in a noisy environment, an offline pulse shape analysis should be included.

Chapter 3

$n - n'$ oscillations: experimental description, data taking procedure and expected sensitivity

This chapter covers the description of the new experimental technique employed to probe $n - n'$ oscillations in UCN beams at high magnetic fields, in particular, in the range $B \in [50 - 1100] \mu\text{T}$. The magnetic field, raised by a 5 m solenoid, was applied on top of a 6 m UCN guide to induce the $n - n'$ oscillations in the high-flux UCN beam at ILL. We start the discussion by giving a technical picture of the magnetization system, UCN guiding pipes and detection system. This last one composed of the GADGET detector and FASTER acquisition system (see previous chapter). Then, the data collection technique is presented while pointing at the main assumptions on the $n - n'$ oscillation model and the UCN beam features. This is followed by the sensitivity study of the proposed method and later by a preliminary analysis, conducted to characterize the trajectories of UCN within the setup, the response of the detector to magnetic fields and the uniformity of the probing B -field.

3.1 Experimental description of the setup

The UCN delivery at PF2 is alternated among the high-flux beam ports ('EDM', 'UCN' and 'MAM') in cycles with periods defined by the users. When experiments mounted on these ports operate simultaneously, the PF2 turbine is sequentially aligned with them so that each setup profits the maximum UCN flux during its own delivery cycle. A negligible UCN flux is measured in ports not aligned with the turbine, i.e. during the 'beam sharing' periods. Previous characterizations of UCN densities at the high-flux beam ports using storage bottles [78] predicted fluxes of up to $4.2 \times 10^6 \text{ s}^{-1}$. However, these numbers are lower in specific experiments, for example approximately 10^5 UCN/s in the first-generation nEDM experiment [93]. The actual number of neutrons available in a given experimental setup is defined by the transmission of the UCN guiding system, i.e. the quality and geometrical arrangement of guides conducting UCN from the turbine to the measuring apparatus. Since there is a non-zero probability of absorption, up-scattering and transmission upon each UCN collision, too long and multiple bent guides are frequently characterized by low transmission factors. In the following, we present the UCN guide arrangement for the $n - n'$ experiment,

which is mainly shaped by the magnetization system geometry.

3.1.1 Magnetic field and UCN guide arrangement

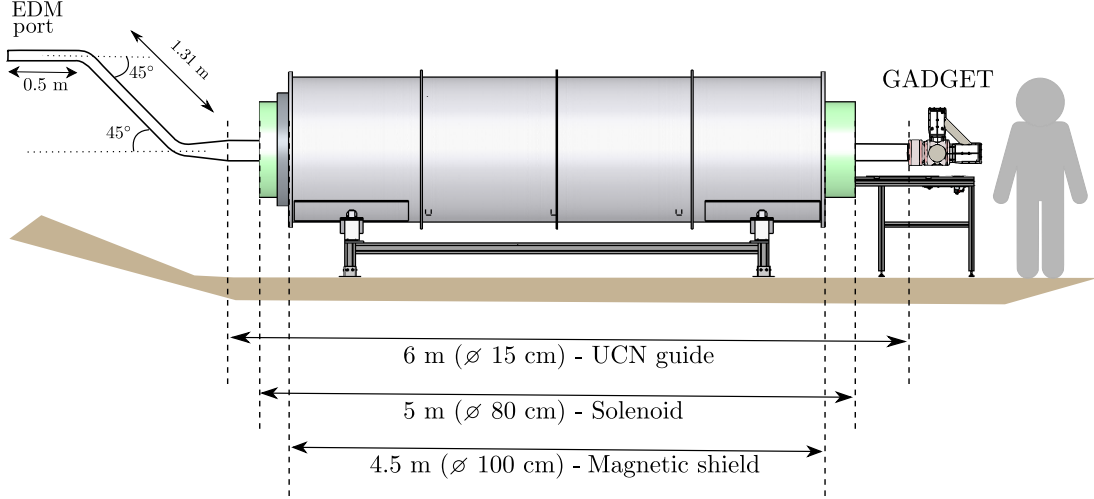


Figure 3.1: Side view of the experimental setup. The UCN beam is conducted through three straight guides and their respective turning elbows. A conic guide adaptor is used between the main $\varnothing 15$ cm and $\varnothing 8.5$ cm guides.

The magnetic field applied to UCN to lift the neutron - hidden neutron energy degeneracy $\Delta_{nn'} = \mu_n B - \delta m$ and enhance the oscillation probability (see Eq. (1.11)), was raised by a magnetization system recovered from a past work focused on the search of new forces using polarized ^3He nuclei [27]. With this system, we scanned the mass-splitting energy range $\delta m \in [3 - 66] \times 10^{-12}$ eV, corresponding to magnetic fields $B \in [50 - 1100] \mu\text{T}$. The system consists of a main solenoid, a cylindrical magnetic shielding and two compensation coils placed at the solenoid edges to increase the magnetic field uniformity. The 4.8-meters-long and 80-cm-diameter main solenoid is made of 2270 loops of $2 \times 1 \text{ mm}^2$ rectangular section copper wire around a 5-mm-thickness aluminum tube. The 25-cm-long compensation coils, with 112 loops of ~ 80 cm diameter each, are connected in series with the solenoid. The magnetic shield piece corresponds to one of the 17 segments of the cylindrical shielding in the neutron anti-neutron experiment that took place at ILL in 1994 [28]. This shield, made of mu-metal, surrounds the solenoid as shown in Figure 3.1 to increase the magnetic field uniformity at the UCN guide and expel the magnetic field lines from external sources, in particular earth's magnetic field. Its dimensions are 4.5 m length, 94.5 cm diameter and 1 mm thickness.

Given the space availability and security protocols at PF2, the magnetization system was located at a lower elevation with respect to the EDM beam port. For this reason, the arrangement of guides used to transport UCN from the port to the detector while crossing the solenoid axis included three main segments: a half-meter horizontal guide at the EDM port, a 1.31 m tilted guide and a 6 m horizontal guide. Two bent elbows were placed at the tilted guide sides and a conic guide was used to connect one of the elbows to the main 6 m guide ($\varnothing 8.5 \text{ cm} \rightarrow \varnothing 15 \text{ cm}$). The UCN GADGET detector, whose data acquisition was carried out by the FASTER system, was located at the end of the 6 m guide (75 cm from the

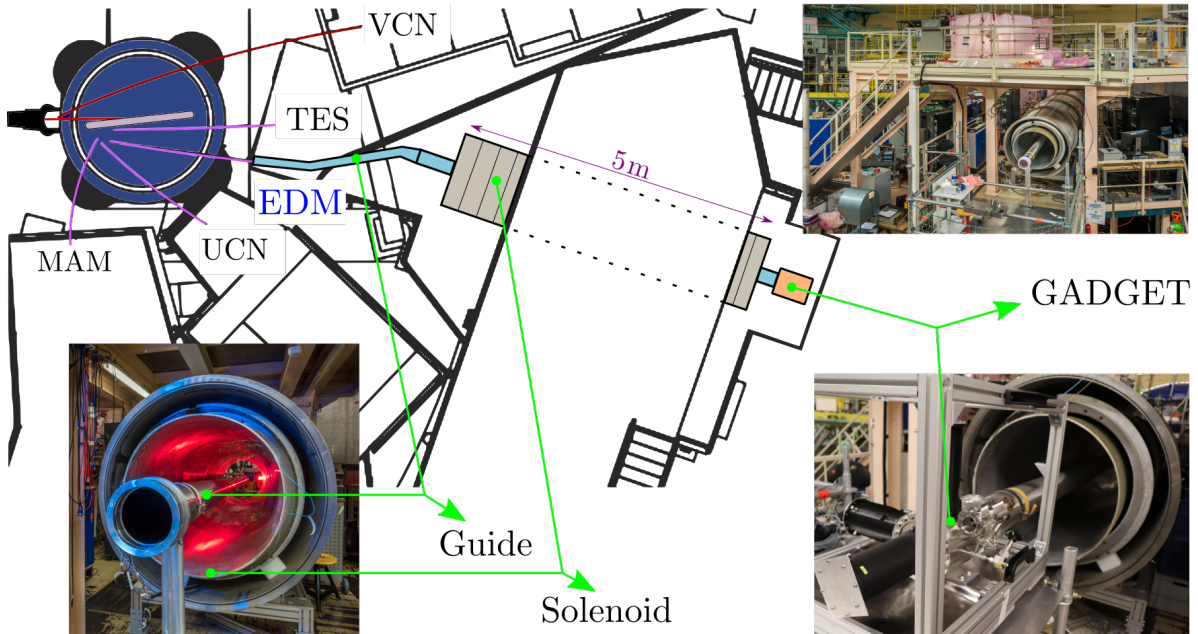


Figure 3.2: Top view of the experimental setup. The main UCN guide and magnetization system were placed below the EDM platform. Photos by Laurent Thion.

solenoid). Figure 3.2 shows a top view of the relative positioning of the setup elements with respect to the PF2 turbine and adjacent beam ports.

Detector magnetic shielding

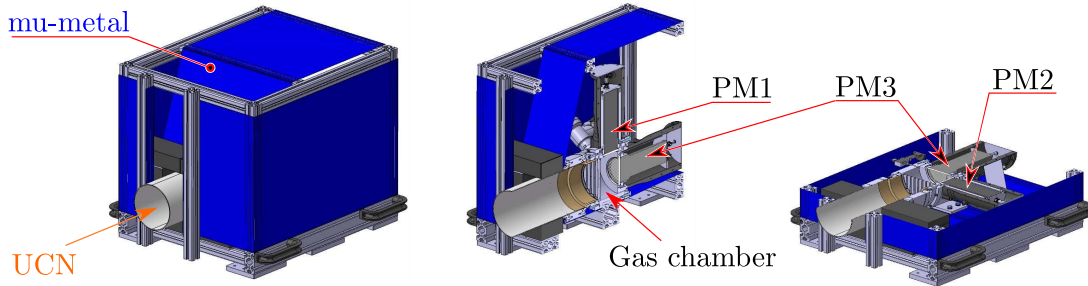


Figure 3.3: Mu-Ferro-SD magnetic shielding layers mounted on GADGET's supporting structure. The UCN guide entrance and back side remain uncovered.

It is well known that PMTs are very sensitive to magnetic fields. The focusing electrodes and electron multipliers (dynodes) within PMTs are geometrically optimized to maximize the current generated after the photon detection. If external magnetic fields modify the trajectories of the electron multiplication cascades, a different signal amplitude might be read at the PMT output or even lost if the field intensity is too large. PMTs in GADGET were manufactured by Hamamatsu with 0.5 mm thickness magnetic shielding cases made of high-permeability permalloy (Ni: 78 %, Fe, Mo and Cu : 22 %). Although the magnetic

shielding factor in the middle of such cases is of about 10^3 for magnetic fields comparable to Earth's field, it quickly falls to 1 at 5 cm from the PMT entrance window [94], thus leading to a poor shielding near the photocathode region. Therefore, given that the stray field lines, raised by a 1.1 mT solenoid magnetic field, can go up to 0.1 mT (three times larger than Earth's field) at the detector location, a second magnetic shielding was added. This was done by covering the GADGET detector with a 0.12 mm thickness Mu-Ferro-SD foil capable of shielding 0.1 mT fields with a single layer [95]. A detailed view of the shield layers can be observed in Figure 3.3. Note that no mu-metal is placed in front of the UCN guide and behind GADGET.

3.2 Data collection technique

The data taking procedure to probe $n-n'$ oscillations while scanning the applied magnetic field involves two main discussions. First, the definition of the magnetic field scanning step that guarantees a common sensitivity over the targeted mass-splitting range $\delta m \in [3 - 66] \times 10^{-12}$ eV. Second, the introduction of the analytical method through which one can conclude whether a UCN flux drop is due to oscillations. Since the latter depends on the former, we start by determining the cycle step from the resonance width of a $n - n'$ signal.

3.2.1 Resonance width & scanning step

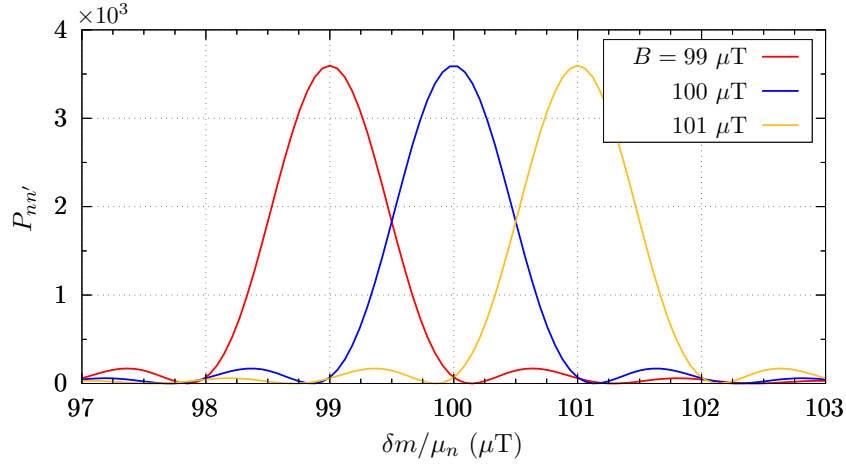


Figure 3.4: Oscillation probability as a function of the mass-splitting according to the analytical solution in Eq. (1.10). The oscillation time has been assumed $\tau_{nn'} = 1$ s and the free-flight-time corresponds to the mean value extracted from MC simulations ($\bar{t}_f = 32$ ms, see section 3.4.3). The curve overlapping suggests scanning the magnetic field with steps of 1 μ T.

Defining a reasonable step size for the magnetic field scan requires knowing the resonance width of the oscillation probability. If the step is too large, the resonance condition $\delta m = \mu_n B$ might be missed in between two steps. On the contrary, too short steps would demand a long nonviable experimental campaign. In order to establish a rough estimate of the resonance

width, we use the oscillation probability from the analytical solution of $\hat{\mathcal{H}}_{nn'}$ presented in Eq. (1.10). Figure 3.4 shows the $n - n'$ oscillation probability as a function of δm for three probing magnetic fields, where it has been assumed $\tau_{nn'} = 1$ s and $\bar{t}_f = 32$ ms*. This plot demonstrates that scans with 1 μ T steps would be sufficient to achieve an oscillation probability as large as half the in-resonance maximum probability ($\text{FWHM}(P_{nn'}) \approx 1$ μ T) within the scanned interval. Based on the probability FWHM, the probe of $n - n'$ oscillations was carried out by varying the applied magnetic field every 1 μ T. However, before describing the time sequence designed for such a scan, a few considerations on the UCN flux constancy are exposed.

3.2.2 UCN flux constancy

Following the constant-power (56 MW) operation mode of ILL's reactor, one might expect a similarly constant UCN flux at the EDM beam port. However, previous experiments on $n - n'$ oscillations with storage bottles in this facility reported fluctuations of up to 0.3% from the UCN counting over several hours [9, 96]. These fluctuations were as large as the ones described by the reactor power, but no correlation between both quantities could be established at that time. One could argue that a short-time-scale correlation between the reactor power and the UCN counting did exist, but was lost during the storage process (75 s and 150 s). In fact, such a short-time-scale correlation has been evidenced in the present work and represents the main component on the systematics analysis developed in section 4.3. Since no characterization of the UCN flux at the EDM beam port has ever been attempted at the scale of seconds, the current experiment becomes the first evaluation of the UCN flux constancy at PF2 in long time basis.

3.2.3 The ABBC measuring sequence

At the time of the $n - n'$ data taking (autumn 2020), a second experiment was operating on the neighbor 'UCN' port (see Figure 3.2). For this reason, the UCN beam from the PF2 turbine was shared with cycles of 200 s, continuously alternated between both experiments. To synchronize the UCN flux detection with the PF2 delivery cycles, a signal was sent to the FASTER acquisition system once the turbine positioning was finished. These signals were used to start and stop the UCN counting (no data was collected in the $n - n'$ setup during the beam sharing periods).

In order to complete the magnetic field scanning process, one could suggest probing a single magnetic field every delivery cycle. However, the UCN counting in that case would be sensitive to long-term variations after several cycles such as reactor drifting power, heating of the VCS, turbine slowing down or even changes in the counting efficiency of GADGET. These drifting behaviors, when correlated to the UCN source, are normally corrected in UCN storage experiments by means of a monitor detector placed at the beam port output. The present work does not adopt such a method given that the customary low detection rate in monitors add large statistical uncertainties if using their counting as normalizing factors[†]. Instead, a self-normalized measuring sequence is introduced, which is independent of long-term

*This free-flight-time corresponds to the mean \bar{t}_f extracted from Monte Carlo (MC) simulations of UCN tracks inside the 6-m-long UCN guide within the solenoid magnetic field. See section 3.4.3

[†]In case the UCN flux is divide half-and-half into the monitor and the $n - n'$ probing detector, UCN flux drifts linked to the source can be corrected while keeping low statistical uncertainties, see discussion 5.2

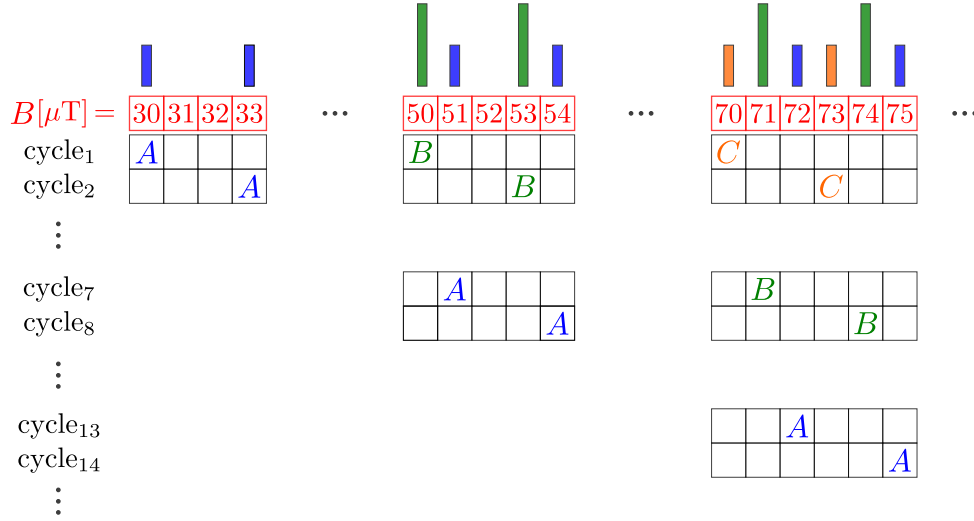


Figure 3.5: Illustration of the scanning procedure over consecutive UCN delivery cycles. The color bars on top are proportional to the time duration (sensitivity) of each evaluation window. The scanning algorithm leaves an overall B -field evaluation every 1 μT for $B \in [70 - 1080]$ μT.

variations (from one cycle to another) and also of linear drifts within the 200 s UCN cycles. A detailed explanation on how this sequence absorbs linear drifts is presented in Appendix C. The sequence divides the cycle time span (t_{cycle}) in four equivalent windows where three magnetic field values are scanned as

$$\{A, B, B, C\} = \{B - 20 \mu\text{T}, B, B, B + 20 \mu\text{T}\} \rightarrow \{44 \text{ s}, 44 \text{ s}, 44 \text{ s}, 44 \text{ s}\}. \quad (3.1)$$

The in-cycle magnetic field step of 20 μT is chosen larger than the resonance FWHM (1 μT) so that $n - n'$ oscillations can only occur at one of the field values. This way, the ratio between UCN counting at field B ($N_B + N_B$) to fields A (N_A) and C (N_C) is

$$R_{ABC} = \frac{N_B + N_B}{N_A + N_C} \begin{cases} = 1, & \text{if no oscillations} \\ < 1, & \text{if oscillations at field } B \\ > 1, & \text{if oscillations at field } A \text{ or } C. \end{cases} \quad (3.2)$$

Given that three magnetic fields are tested every cycle, the scanning step size is set such that the same field is not evaluated twice, but the 1 μT spacing required by the FWHM resonance is kept. As shown in Figure 3.5, by making the step size equal to 3 μT, which 20 μT is not a multiple of, one guarantees that all intermediate values of $B \in [70 - 1080]$ μT are covered by the scanning process with 1 μT spacing. Starting from $B = 50$ μT ($A = 30$ μT and $C = 70$ μT), the UCN flux is measured at three magnetic field values A, B and C (separated by 20 μT) within every cycle. The same measurement was repeated over multiple cycles by sweeping the three fields with a step of 3 μT until reaching $B = 1100$ μT ($A = 1080$ μT and $C = 1120$ μT). Note that, even though the scanning spacing is of 3 μT for $B \in [30 - 50]$ μT and of 2 μT for $B \in [50 - 70]$ μT, these are short ranges compared to the main 1 μT interval. The ABBC sequence in this case completes an entire scan after 350 cycles.

3.2.4 Synchronization and recording algorithm

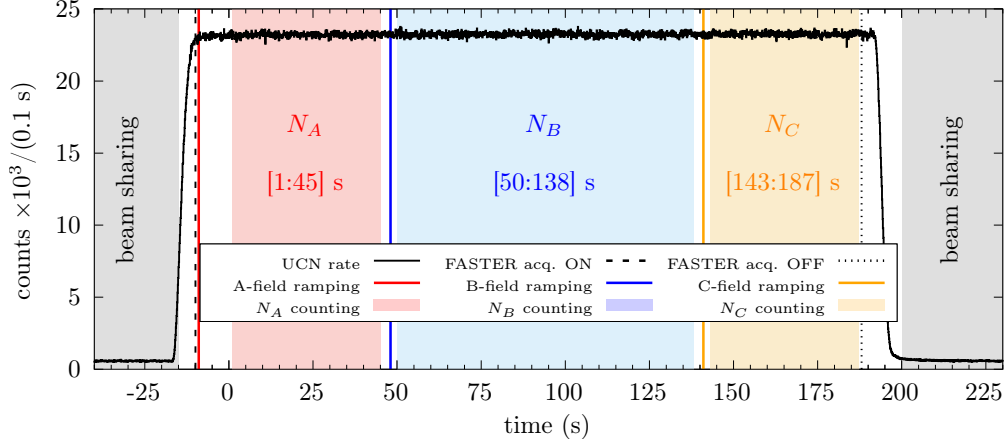


Figure 3.6: Counting rate during a typical UCN cycle. The gray and colored regions illustrate the beam sharing and UCN counting periods, respectively. The vertical lines represent the times of field ramping (2 s) and acquisition start-up.

The $\{A, B, B, C\} = \{44 \text{ s}, 44 \text{ s}, 44 \text{ s}, 44 \text{ s}\}$ integration windows presented above were conveniently defined so that the UCN delivery cycles let 24 spare to wait for an initial beam stabilization and to ramp the magnetic fields $A \rightarrow B$ and $B \rightarrow C$. The beam stabilization, which is achieved after a couple of seconds after the turbine alignment, is a physical effect due to the UCN velocity distribution and the nature of UCN reflections. While slow UCN and UCN undergoing diffusive reflections take longer times to cross the guide arrangement, fast UCN and UCN following purely specular reflections need shorter times (see Figure 3.11 in section 3.4.3). In order to avoid systematic effects related to the beam stabilization, the UCN counting starts 10 seconds after the EDM port alignment of the turbine. Regarding the field ramping, two seconds are considered for the transitions $A \rightarrow B$ and $B \rightarrow C$, although their real duration is expected faster than 1 second. In the end, the recording algorithm is structured (with $t = 0$ the synchronization time in FASTER) as

1. $t = -10 \text{ s}$: PF2 beam delivered to EDM beam line.
2. $t \approx -9 \text{ s}$: Ramp to magnetic field A .
3. $t = 0 \text{ s}$: FASTER synchronization (PF2 delayed signal).
4. $t \in [1 : 45] \text{ s}$: UCN counting at field A .
5. $t = 48 \text{ s}$: $A \rightarrow B$ ramp.
6. $t \in [50 : 138] \text{ s}$: UCN counting at field B .
7. $t = 142 \text{ s}$: $B \rightarrow C$ ramp.
8. $t \in [143 : 187] \text{ s}$: UCN counting at field C .

Therefore, by neglecting the UCN counting 2.5 seconds before and after each field ramping,

the integration periods are finally written as

$$\begin{aligned} N_A : & \quad [1 - 45] \text{ s}, \\ N_B + N_B : & \quad [50 - 138] \text{ s}, \\ N_C : & \quad [143 - 187] \text{ s}. \end{aligned} \quad (3.3)$$

Figure 3.6 shows a typical cycle where the beam sharing periods, the magnetic field ramping, the UCN recording with FASTER and the counting intervals N_i are explicitly depicted.

3.3 Expected sensitivity (ideal case)

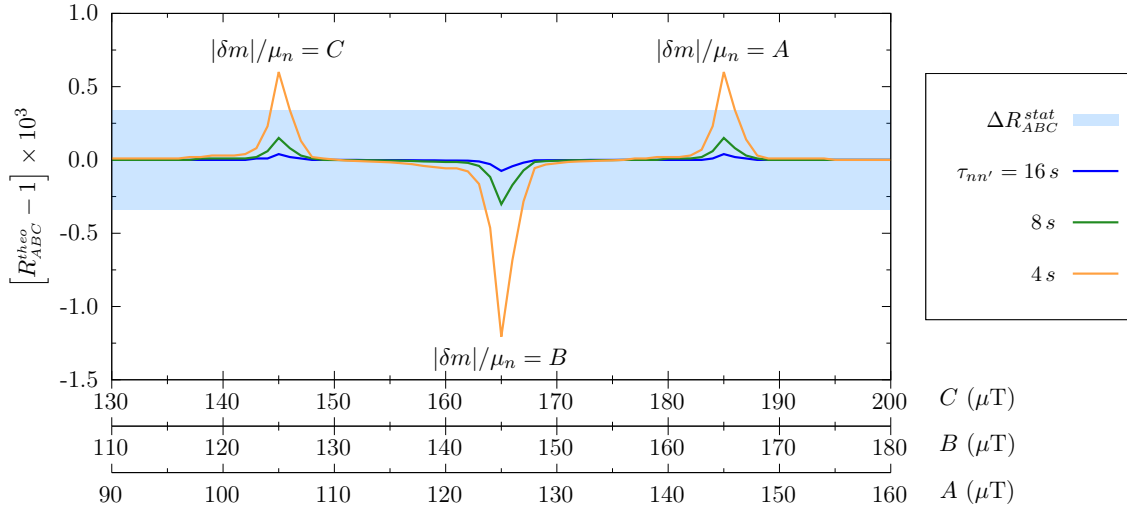


Figure 3.7: Theoretical prediction of a signal signature at $|\delta m|/\mu_m = 145 \mu\text{T}$ for three values of $\tau_{nn'}$. The larger the $\tau_{nn'}$ the lower the signal notability with respect to the statistical fluctuations (light-blue band).

According to Eq. (3.2), a $n - n'$ oscillation signal is identified when $|R_{ABC} - 1| > \zeta \Delta R_{ABC}$, with ζ a constant depending on the confidence level (CL), and ΔR_{ABC} the uncertainty of R_{ABC} . Moreover, the scanning of fields A , B and C makes the signal visible in at least three different cycles. Moving from small to large fields, the resonance condition would be firstly fulfilled by C , once again seven cycles later by B (when it has shifted $7 \times 3 \mu\text{T} \sim \Delta B$), and finally after 6 cycles more by A (when it has shifted $13 \times 3 \mu\text{T} \sim 2\Delta B$). In order to illustrate this triple-footprint feature of the resonance, we compute the theoretical prediction of R_{ABC} as

$$\begin{aligned} R_{ABC}^{\text{theo}}(\delta m, \tau_{nn'}) &= \frac{N_B^{\text{theo}}(\delta m, \tau_{nn'}) + N_C^{\text{theo}}(\delta m, \tau_{nn'})}{N_A^{\text{theo}}(\delta m, \tau_{nn'}) + N_C^{\text{theo}}(\delta m, \tau_{nn'})} \\ &= \frac{2N_0 \exp[-\mathcal{R}_B(\delta m, \tau_{nn'})t_{\sim}]}{N_0 \exp[-\mathcal{R}_A(\delta m, \tau_{nn'})t_{\sim}] + N_0 \exp[-\mathcal{R}_C(\delta m, \tau_{nn'})t_{\sim}]}, \end{aligned} \quad (3.4)$$

with $N_0 = \Phi_{\text{UCN}} \cdot 44 \text{ s}$ the UCN flux integrated over the ABBC sequence periods, $\mathcal{R}_B = \Gamma_{\beta\text{-decay}} + \Gamma_{\text{absorption}} + \Gamma_{\text{upscattering}} + \Gamma_B^{nn'}$ the total UCN lose rate of the beam during its

passage through the solenoid magnetic field, and t_{\sim} the total time to cross the field volume. Not only N_0 but also all the Γ terms corresponding to processes which are independent of the magnetic field cancel out. Therefore, taking into account that the mean number of UCN collisions within the solenoid can be expressed as $\bar{n}_{\text{coll}} = t_{\sim}/\bar{t}_f$, Eq. (3.4) rewrites

$$R_{ABC}^{\text{theo}}(\delta m, \tau_{nn'}) = \frac{2 \exp[-\bar{n}_{\text{coll}} P_{nn'}(\bar{t}_f, B, \delta m, \tau_{nn'})]}{\exp[-\bar{n}_{\text{coll}} P_{nn'}(\bar{t}_f, A, \delta m, \tau_{nn'})] + \exp[-\bar{n}_{\text{coll}} P_{nn'}(\bar{t}_f, C, \delta m, \tau_{nn'})]}, \quad (3.5)$$

where the UCN lose rate caused by $n - n'$ oscillations has been approximated to

$$\Gamma_B^{nn'} \approx \frac{1}{\bar{t}_f} P_{nn'}(\bar{t}_f, B, \delta m, \tau_{nn'}).$$

Figure 3.7 shows the $n - n'$ signals computed with Eq. (3.5) for three values of $\tau_{nn'}$ if assuming a mass-splitting $|\delta m|/\mu_n = 145 \mu\text{T}$. Whereas the average parameters \bar{n}_{coll} and \bar{t}_f are extracted from MC simulation of UCN trajectories (see section 3.4.3), the oscillation probability assumes the analytical expression given in Eq. (1.10). The triple axis labelling in this figure is used to denote the magnetic fields A , B and C , which are consistent with the values set during the scanning process. Also, displayed in light-blue, the horizontal band around 0 encloses the uncertainty interval defined by the statistical fluctuations, estimated as

$$\Delta R_{ABC}^{\text{stat}} = \sqrt{\left(\frac{\sqrt{N_B} + N_B}{N_B + N_B}\right)^2 + \left(\frac{\sqrt{N_A} + N_C}{N_A + N_C}\right)^2} \sim \sqrt{\frac{1}{N_0}} \sim 3.4 \times 10^{-4},$$

with $\Phi_{\text{UCN}} \sim 200 \text{ kHz}$ (see UCN counting rate in section 4.1).

The analytical signals in Figure 3.7 highlight two main features that are worth mentioning. Firstly, the signal is two times larger when the resonance matches the cycle central field ($|\delta m|/\mu_n = B$) than when it matches fields A and C . This is explained by the flux integration periods, which last two times longer at B than at A or C . Secondly, large values of $\tau_{nn'}$ give place to signals that hide within the statistical fluctuations band. In fact, in the limit $\tau_{nn'} \rightarrow \infty$, $R_{ABC} \rightarrow 1$ and the signal is completely confounded with the no-oscillations null hypothesis. This first estimation of R_{ABC}^{theo} shows that the sensitivity of the proposed experiment is strongly constrained by the statistical sensitivity of the counting rate measurement: with a counting rate of 200 kHz, signals faster than 8 s can still be revealed.

In the absence of a signal (no-oscillations), all measurements of $|R_{ABC} - 1|$ are contained within their uncertainties. In such case, the model parameters $\tau_{nn'}$ and δm can be bounded in the so-called parameter space. For the present work, this is done by finding the minimum $\tau_{nn'}$ at a given δm for which the predicted signal would overcome ΔR_{ABC} . Adopting the confidence interval formalism in [97] (page 131), this problem reduces to finding $\tau_{nn'}$ such that

$$\chi^2(\delta m, \tau_{nn'}) = \chi^2(\delta m, \infty) + \mathcal{N}^2, \quad (3.6)$$

with

$$\chi^2(\delta m, \tau_{nn'}) = \sum_i^{N_{\text{cycles}}} \left(\frac{R_{ABC,i}^{\text{exp}} - R_{ABC}^{\text{theo}}(\delta m, \tau_{nn'})}{\Delta R_{ABC,i}} \right)^2 \quad (3.7)$$

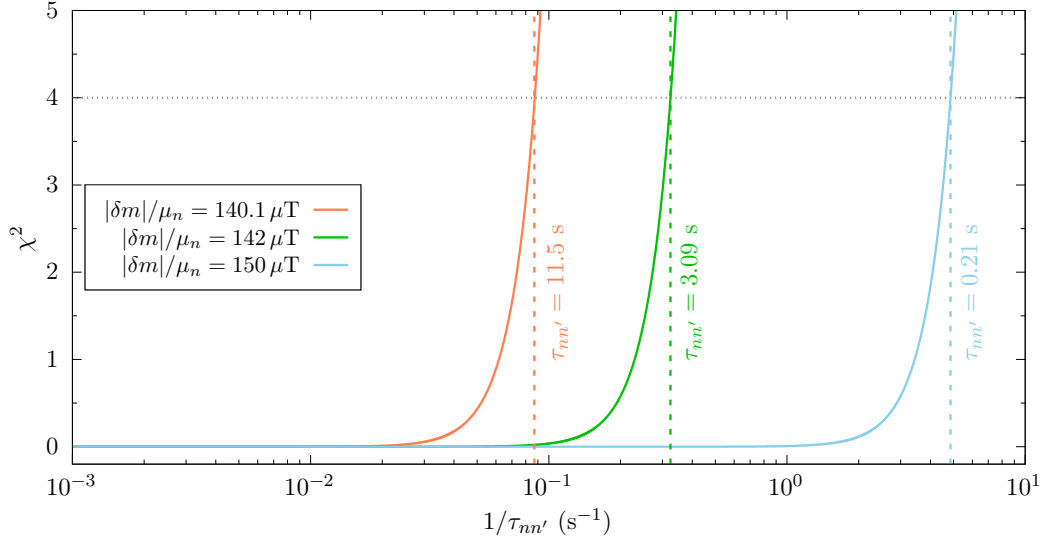


Figure 3.8: Construction of the 95% confidence intervals for $\tau_{nn'}$ exclusion. The χ^2 values were computed assuming a single cycle measurement at $B = 140 \mu\text{T}$ with no signal ($R_{ABC} = 1$). Three sample mass-splittings were tested, giving a different $\tau_{nn'}$ limit each time (vertical dashed line). The horizontal dotted line corresponds to $\chi^2(\delta m, \infty) + 2^2$.

and \mathcal{N} the number of standard deviations. Note that $\chi^2(\delta m, \infty) \rightarrow \text{NDF}$ since $\tau_{nn'} \rightarrow \infty$ coincides with the null-hypothesis.

Concerning the number of cycles (N_{cycles}) taken into account for the computation of χ^2 , there are two valid approaches which are consistent between each other. In the first one, one sets $N_{\text{cycles}} = i$ so that the $\tau_{nn'}$ boundary is constructed individually for each cycle measurement. In particular, the boundary on $\tau_{nn'}$ resulting from the i -th cycle is characterized with a large exclusion near $\delta m/\mu_n = A_i, B_i$ and C_i , and decays asymptotically far from them. Since each cycle represents an independent measurement, the multiple boundaries can be overlapped to produce an overall exclusion region. This, for example, can be determined by joining all the boundaries together. The second option consists in considering all the scan cycles simultaneously ($N_{\text{cycles}} = 350$). In such case, the boundary is computed a single time, but it contains the parameter exclusion with resonances at all the values $\delta m/\mu_n = A_i, B_i, C_i$ with $i = 1, \dots, 350$.

Out of the two approaches, the latter is chosen for one main reason: a resonant behavior affecting B_i implies resonances at A_{i-6} and C_{i+7} , and no-oscillations for the remaining cycles (see Figure 3.7). In consequence, the boundary of $\tau_{nn'}$ is constructed with more stringent requirements, thus giving place to a larger exclusion region. Although the calculation of $\chi^2(\delta m, \tau_{nn'})$ in the next chapter analysis adopts the second approach, the preliminary $n - n'$ oscillation sensitivity of this experiment is estimated with the single cycle method.

In order to illustrate the $\tau_{nn'}$ bounding process, we plot χ^2 as a function of $1/\tau_{nn'}$ for the sample magnetic field $B = 140 \mu\text{T}$. This is displayed in Figure 3.8 for three values of $|\delta m|$, where three assumptions were made

- $R_{ABC}^{\text{exp}} = 1$: the most conservative scenario with no signal detection.

- Uncertainties are purely dominated by statistical fluctuations with a UCN flux $\Phi_{\text{UCN}} \sim 200$ kHz, i.e. $\Delta R_{ABC}^{\text{stat}} \sim 3.4 \times 10^{-4}$.
- Theoretical predictions are obtained from the analytical solution in Eq. (3.5) (perfectly uniform magnetic field and average free-flight time $\bar{t}_f = 32$ ms).

The dashed vertical lines in Figure 3.8 are used to show the point of intersection with $\chi^2(\delta m, \infty) + 2^2$, where $\mathcal{N} = 2$ was chosen so to establish a confidence level of 95%. Hence, values of $1/\tau_{nn'}$ on the right of these limits are excluded from the $n - n'$ oscillation hypothesis. This dummy example shows that the larger the separation between $|\delta m|/\mu_n$ and the cycle magnetic field B , the lower the exclusion limit of $\tau_{nn'}$. Since the B -field scanning process runs over a $3 \mu\text{T}$ step, this loss of sensitivity at mass-splitting far from the applied field is recovered by other cycle measurements.

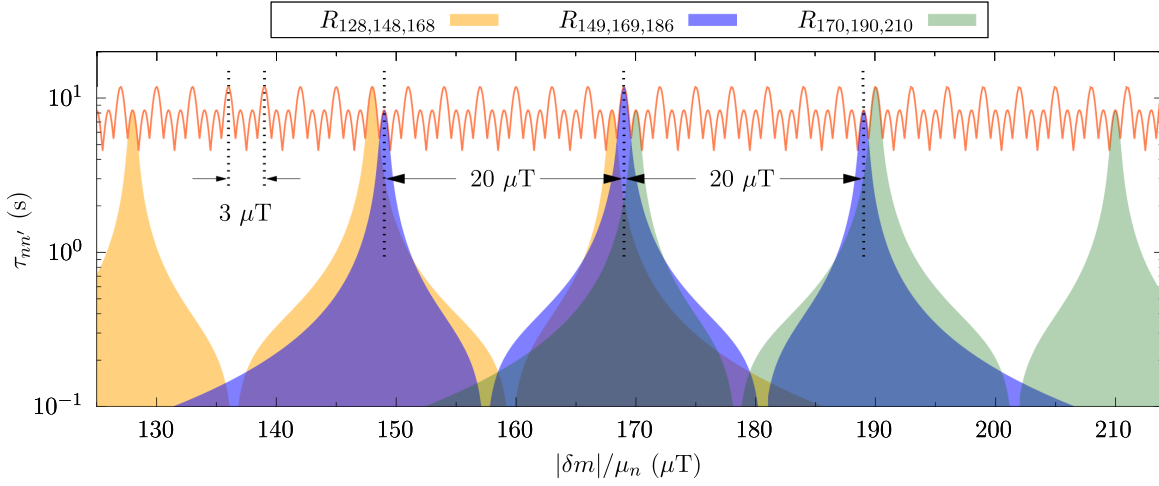


Figure 3.9: Expected sensitivity of the UCN beam experiment. The upper envelope (red line) is constructed with the 95% C.L. exclusion regions between 125 and 215 μT . Individual contributions of three cycles are displayed with colored regions to better illustrate the upper envelope shape. The same pattern extends over the full $|\delta m|/\mu_n$ range.

A general view of the parameter exclusion results from plotting the bounding $\tau_{nn'}$ as a function of $|\delta m|/\mu_n$. This construction defines the contour line separating the accepted and excluded regions in the $(\delta m, \tau_{nn'})$ space. Figure 3.9 shows the 95% C.L. parameter exclusion (colored regions) computed for three sample ‘no-signal’ cycles centered at $B_i = 148, 169$ and $190 \mu\text{T}$. This representation allows the observation of how each cycle measurement determines an exclusion pattern featuring the three maxima at $|\delta m|/\mu_n = A_i, B_i$ and C_i , with the $20 \mu\text{T}$ separation between them. In particular, we confirm the two times larger exclusion at resonances B_i with respect to those at A_i and C_i . Although we only show the exclusion derived from three cycle measurements, other intermediate and consecutive cycles generate similar exclusion patterns. In total, the same pattern shifts every $3 \mu\text{T}$ for the entire scanned range $[50 - 1100] \mu\text{T}$.

In this preliminary study of the sensitivity, the overall exclusion region is shaped by the upper envelope resulting from the superposition of all the 350 exclusion regions. The reader

can check, in Figure 3.9, that even with a scanning step of $3 \mu\text{T}$, the ABBC sequence lets to a local maximal sensitivity every $1 \mu\text{T}$. Therefore, the shortest limit of $\tau_{nn'}$, which occurs at the envelope valleys, emerges every $1 \mu\text{T}$. The value of $\tau_{nn'}$ at such valleys is regarded as the most conservative single-value limit for the entire scanned interval, i.e. the sensitivity of the present UCN beam experiment is predicted as $\tau_{nn'} \gtrsim 4 \text{ s}$ if assuming a uniform solenoid B -field.

3.4 Preliminary analysis

The discussion of $n - n'$ oscillations in the next chapter is based on three studies that were experimentally evaluated before the $n - n'$ data taking. They are the validation of the MC-simulation of UCN trajectories used to extract the free-flight-times and number of wall collisions, the influence of the solenoid magnetic field on GADGET and the magnetic field non uniformity. In the following, we briefly mention the main conclusion of each study.

3.4.1 Monte Carlo simulation of UCN tracks

The description of the $n - n'$ oscillations determined by the Hamiltonian in Eq. (1.8) involves two types of parameters. The inaccessible ones, namely the mixing parameter $\tau_{nn'}$ and the mass splitting δm , and the measurable ones, the neutron energy due to the magnetic field $\Delta E = \mu_n B$ and the free-flight time t_f . Evaluation of the first ones, which is the main objective of this work, can happen with a good knowledge of the second ones. While COMSOL magnetic field maps inside the main UCN guide (presented in the next subsection) reveal a good agreement against experimental results, we still need to determine the B -field profiles that UCN would experience during their passage through the solenoid and the free-flight-time and number of collisions distributions that characterizes the UCN bouncing in this process. Addressing these features is possible through Monte Carlo simulation (MC) of UCN tracks.

For the following, the MC based STARucn software [98] was used to simulate UCN trajectories in a geometry defined by the guide configuration presented in Figure 3.1. UCN scattering by materials and earth's gravitational force are the main interactions defining the simulated tracks. Among the input parameters fed into the simulation there are the materials, sizes and shapes of the UCN transporting guides, the initial position and velocity distributions of UCNs, and the characteristic factor accounting for the amount of diffusive reflections (d). In general, the intrinsic properties of guides, such as their Fermi potential and absorption coefficient, are well known from theory and past experiments [73]. On the contrary, UCN beam features, like the initial velocity distribution (velocity spectrum at the beam port), depend on multiple experimental factors and thus need to be measured.

Velocity spectrum validation through TOF measurements

The time-of-flight technique uses a chopper device to transform the constant beam flux into a pulsed one. It consists of a high frequency sliding shutter that cuts the UCN flux in equally separated time periods. A straight UCN guide is positioned between the chopper and the detector so that, using the time signal of the shutter t_0 and the detection time t_{det} , the time-of-flight of UCN is calculated as $\text{TOF} = t_{\text{det}} - t_0$. One possibility to correctly define the initial velocity distribution (\mathcal{V}_0) within the simulation is by comparing the TOF measurement

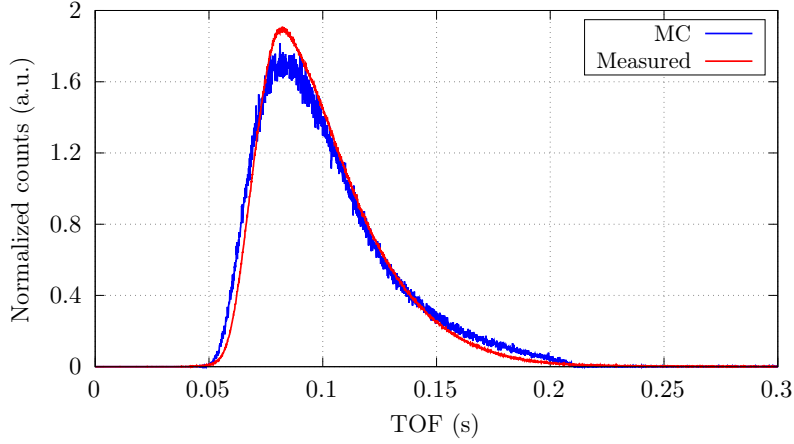


Figure 3.10: Time-of-flight from measurement at the EDM beam port and through STARucn simulation.

at the guide output to the ones obtained from simulated tracks computed with an initial guess distribution $\mathcal{V}_{0,\text{guess}}$. Fortunately, one does not need to determine the real initial distribution since even a Gaussian shape transforms, after few UCN collision in the simulation, into a more realistic Boltzmann distribution. This self-consistent shaping process derives from the physics of UCN reflections: while fast neutrons are more likely lost due to transmission through the guide walls, slow UCN are easily reflected and thus conducted until the output end. This process, which can be regarded as a velocity softening, allows reducing the degrees of freedom to fit an accurate initial distribution \mathcal{V}_0 .

Table 3.1: Input parameters for the STARucn simulation of UCN tracks.

Guide material	Steel
Fermi potential	184 neV
Diffusive reflections	1%
Absorption coefficient	5.2×10^{-4}
Detector entrance foil	$\text{Al}_{97}\text{Mg}_3$
Fermi potential	54 neV
$\cos(\theta_0)$	$[0 : 40^\circ]$
ϕ_0	$[0 : 360^\circ]$
τ_β	888 s

Figure 3.10 shows the TOF distributions obtained from measurements and through the STARucn simulation. They correspond to a setup with a single 1-m-long guide in the upper left EDM beam port (see Figure 3.1). The initial UCN velocity distribution follows a Gaussian form whose parameters (μ and σ) were optimized to minimize χ^2 with respect to the TOF measurement [99]. The resulting optimization writes

$$\mathcal{V}_0 \sim \text{Gauss}(\mu = 10 \text{ m/s}, \sigma^2 = 4^2 \text{ m}^2/\text{s}^2,) \quad (3.8)$$

with maximum and minimum velocities $v_0^{\text{max}} = 20 \text{ m/s}$ and $v_0^{\text{min}} = 0 \text{ m/s}$, respectively. The initial direction of propagation is defined by two randomly chosen angles θ_0 and ϕ_0 representing

the polar and azimuthal angles in spherical coordinates, where the zenith direction coincides with the UCN guide axis. These and other simulation parameters are resumed in Table 3.1.

UCN tracks

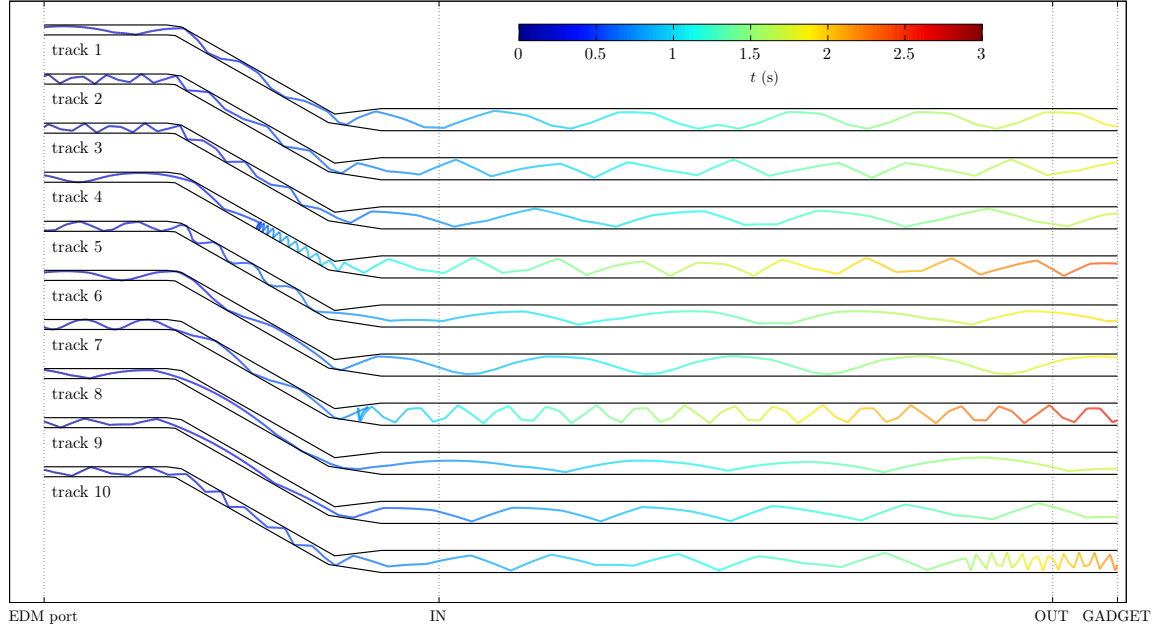


Figure 3.11: Side view of 10 simulated UCN tracks crossing the experimental setup from the EDM port to the GADGET counter. ‘IN’ and ‘OUT’ coordinates correspond to the solenoid physical boundaries. The line color represents the guide crossing time.

Using the simulation parameters above, UCN tracks were computed on the geometry defined by the UCN beam experiment. Guides and turning elbows were modelled within STARucn using the ROOT based TGeoVolume class. All the guide chunks were simulated with stainless steel material properties and perfect vacuum filling. UCN tracks were evolved until neutron absorption or transmission with a maximum number of bounces equal to 50000. Out of all the tracks, only those associated to UCN transmitted through the detector entrance window were studied. UCN which are absorbed or transmitted at the guide walls were discarded since they do not contribute to the actual detector counting.

Figure 3.11 shows the profile of ten sample tracks reaching the detector volume. The vertical axis corresponds to the y -coordinate subject to the gravitational potential. Time is represented by the color evolution of the trajectory paths, starting with blue at $t = 0$ and reaching up to a few seconds in red. It can be seen that most of the tracks are constantly directed towards the detector. This agrees with the expectations since the initial UCN momentum has no negative z component (horizontal coordinate), and the turning guide elbows have not large curvatures. However, because of the diffusive reflections represent the 1%, some tracks are deviated. In such cases, both the number of collisions and the time to reach the detector increase. Tracks 4, 7 and 10 illustrate this phenomenon.

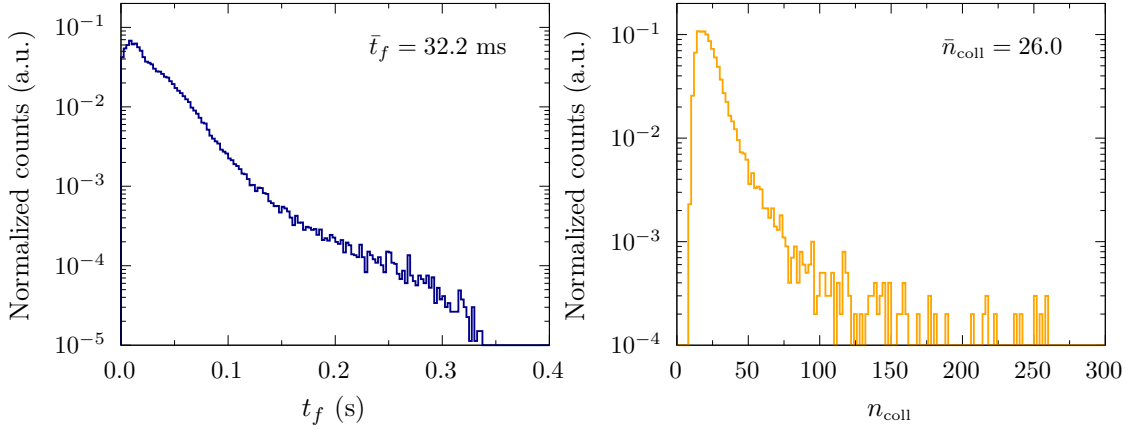


Figure 3.12: (left) Time-of-flight distribution of 10^4 MC-simulated UCN tracks. Its associated number of collisions distribution is displayed on the right-hand side.

MC simulation of UCN tracks has been the preferred method to estimate the average free-flight-time (\bar{t}_f) and the average number of collisions (\bar{n}_{coll}) in past UCN storage experiments [8] ($\bar{t}_f \sim 100$ ms and $\bar{n}_{\text{coll}} \sim 4000$). Since no $n - n'$ oscillations are expected outside the solenoid B -field volume [100], computation of these parameters for the current beam experiment consider only the trajectory steps contained within the ‘IN’ and ‘OUT’ coordinates (see Figure 3.11), i.e. free-flight segments within the solenoid volume. Figure 3.12 shows the free-flight-time and number of collisions distributions for 10^4 UCN tracks reaching the detector entrance foil. One can observe that, compared to past storage UCN experiments, $(\bar{t}_f)_{\text{storage}}/(\bar{t}_f)_{\text{beam}} \sim 3$ and $(\bar{n}_{\text{coll}})_{\text{storage}}/(\bar{n}_{\text{coll}})_{\text{beam}} \sim 150$. The former is explained by the average length of UCN trajectory steps, which is longer in UCN storage bottles, while the latter is evidently due to the fact that UCN are not stored in beam measurements. Since the validation presented above is derived from the TOF measurement along a 1-m-long guide, the UCN trajectories, along with the values of \bar{t}_f and \bar{n}_{coll} , are not fully constrained. Variations in the experimental sensitivity of $\tau_{nn'}$ produced by uncertainties on the simulation parameters are studied in section 4.4.4.

3.4.2 GADGET performance in magnetic fields

It was an important issue determining whether GADGET was sensitive to magnetic fields in the scanning range and how its neutron detection would be modified in such case. A dedicated experiment (see Appendix F) revealed that charge and amplitude PMT spectra could change in magnetic fields larger or equal to 0.3 mT. However, because of the low counting rate close to the threshold, no change in the PMT counting efficiency was observed for magnetic fields smaller than 1 mT.

Even after covering GADGET with the 0.12-mm Mu-Ferro-SD magnetic shielding layers, it was necessary to test its UCN detection efficiency as a function of the solenoid magnetic field. $n - n'$ oscillations should not be confused with a change of the detector efficiency in response to the applied B -field. To this end, the total counting of GADGET was recorded while varying B in a range covering the magnetic field magnitudes attempted in this work. No pulse shape discrimination was applied in order to check for possible spectrum shifting at all charge values. In particular, B was increased from 1 μ T to 1 mT by steps of 0.1 mT, setting

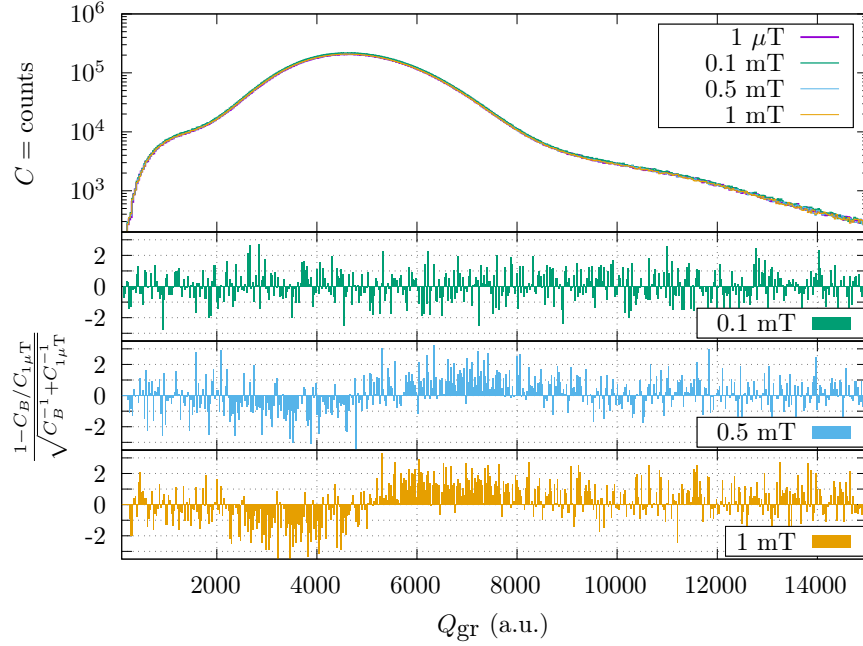


Figure 3.13: Charge spectra measured at four different B . The relative counts per bin with respect to $1 \mu\text{T}$ show a spectrum shift if the magnetic field gap is larger than 0.1 mT .

a single B -field value per UCN cycle. Note that the $B = 1 \mu\text{T}$ corresponds to the magnetic field inside the solenoid when no current is applied. In that case, the magnetic field at the detector position would correspond to the Earth's magnetic field. Figure 3.13 shows that, despite direct comparison of charge (Q_{gr}) spectra at the different solenoid magnetic fields (top side) does not reveal clear variations, when focusing at the relative counting per channel (bottom side) a systematic effect around $Q_{\text{gr}} \sim 5000$ becomes visible. This effect is clearer as the field gap between both measurements increases and, as explained in the Appendix F, it is characteristic of a horizontal-shifted charge spectrum due to improper PMT functioning. Since some solenoid stray field lines might penetrate GADGET's magnetic shielding through the UCN guide, electron cascades inside the PMTs get deviated, thus modifying the final voltage signal. We also integrated the detection rate during the entire cycle for each magnetic field and normalized by the counting at the reference field $B = 1 \mu\text{T}$. The ratios resulting from this process, displayed in Figure 3.14, reveal that in all cases the error bars contain the null hypothesis, $N_{\text{B}}/N_{1\mu\text{T}} = 1$, and that no systematics are disguised from the dispersion of points. This brief study allows asserting that the UCN detection efficiency is independent of the magnetic field produced by the solenoid in this work. In addition, given that the UCN flux is evaluated in time sequences where the B -field difference is of $0.04 \text{ mT} = 2 \times 20 \mu\text{T}$ (see Eq. (3.1)), systematic effects linked to the charge spectrum shifting can safely be ignored in the $n - n'$ analysis.

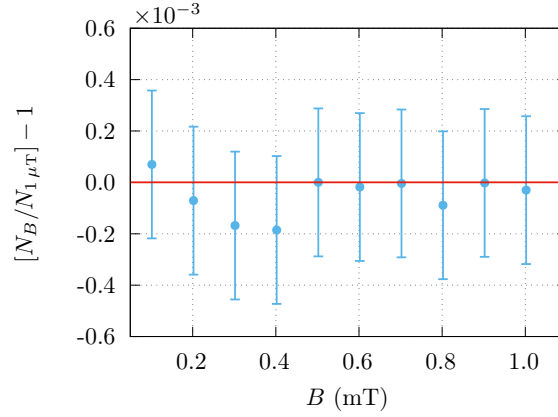


Figure 3.14: Total GADGET counting as a function of the solenoid magnetic field, relative to the solenoid with zero-current configuration. The dispersion of points and their associated Poissonian error-bars show no systematic effects.

3.4.3 Magnetic field inhomogeneities

The main objective of the magnetic field uniformity study is to establish the field profiles experienced by UCN while crossing the solenoid volume. Even if guaranteeing a high field uniformity within the 6-m-long UCN guide, all UCN experience a B -field gradient while entering and exiting the solenoid volume. These gradients have to be considered in the $n - n'$ oscillation analysis, since they modify the shape of the oscillation probability and then the sensitivity of the experiment [10]. To characterize the field profiles, we generate a magnetic field map from COMSOL simulation of the magnetization system including the main solenoid, compensation coils and magnetic shielding. This 2-dimensional model description, which is constructed by assuming azimuthal symmetry with respect to the solenoid axis, contains information of the B -field intensity and direction as a function of the solenoid current for the entire $n - n'$ beam setup volume.

Validation of COMSOL simulations

Validation of the COMSOL generated B -field map was done by comparison against measurements performed with a fluxgate probe. They were recorded at the PF2 experimental hall using a laser positioning reference before the installation of GADGET. Although the fluxgate measurements were taken for \hat{x} , \hat{y} and \hat{z} directions of the field, we report the results as a function of the cylindrical coordinates, where $\hat{r}^2 \rightarrow \hat{x}^2 + \hat{y}^2$ and \hat{z} coincides with the solenoid axis. Following this notation, Figure 3.15 shows the different components of the magnetic field over the solenoid axis ($r = 0$) obtained from COMSOL and through the fluxgate measurements. One can confirm the rather good agreement between both descriptions over the B_z , although variations of measured points at the field plateau ($z \sim [-2; 2]$ m) are larger than ones from the simulation profile. These irregularities might be due to damages in the magnetic shield or in the solenoid itself, and therefore are included in the $n - n'$ analysis (see next subsection). For technical reasons, running the compensation coil at the beam port solenoid side was not possible. This explains why one observes a ‘bump’ in B_z at $z = 2$ m but not at $z = -2$ m (the coil was also turned off within COMSOL). Regarding the perpendicular

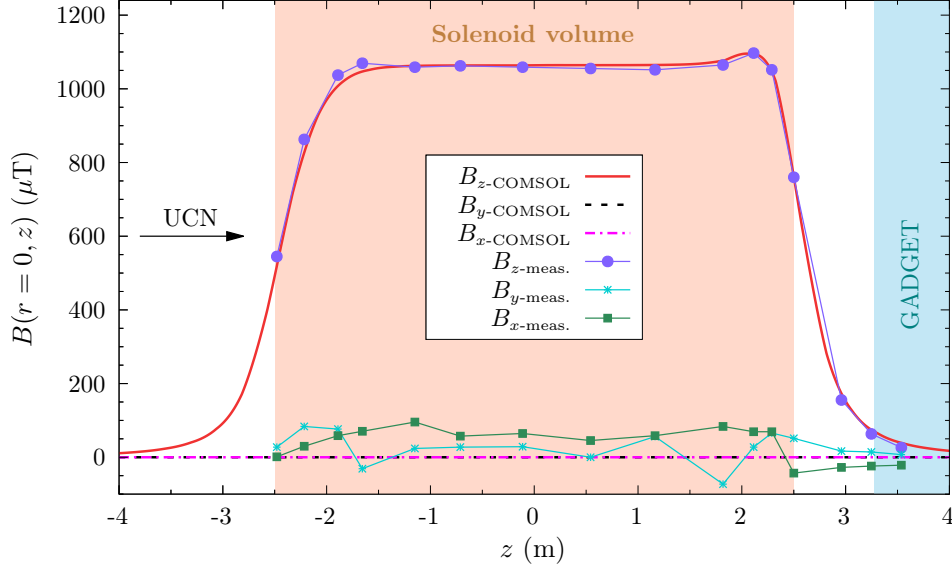


Figure 3.15: Cartesian components of the solenoid magnetic field along the solenoid axis ($r = 0$). Values computed from COMSOL generated maps are displayed with lines and fluxgate measurements with point-lines. The arrow represents the normal UCN flux from the EDM port through solenoid volume (reddish region) until the GADGET counter (light-blue region). The B -field profiles are raised with a solenoid current of 1.78 A.

magnetic field components (B_x and B_y), their mean measured values represent less than the 5% of the B -field magnitude. Such small contribution is used as first argument to neglect the radial B -fields in the $n - n'$ analysis.

Experienced magnetic field profiles

In order to determine the experienced B -field profiles, we couple the fluxgate field measurements with the COMSOL map and UCN MC tracks. Whereas the first one adds the field inhomogeneities observed withing the solenoid volume, the second one is used to correctly extrapolate the field values outside the solenoid volume and off the guide axis. In this way, we can track the B -field evolution for each UCN bouncing across the 6-m guide by means of its trajectory coordinates (r_i, z_i) . The magnetic field is updated after each time step, which for the purposes of this work is made of $10 \mu\text{s}$ (0.1 mm for UCN traveling at 10 m/s), according to the interpolation[‡]:

$$B_z(r_i, z_i) = \begin{cases} B_{z\text{-meas}}(r = 0, z_i) \frac{B_{\text{COMSOL}}(r_i, z_i)}{B_{\text{COMSOL}}(r=0, z_i)}, & \text{inside the solenoid} \\ B_{z\text{-COMSOL}}(r_i, z_i), & \text{outside the solenoid.} \end{cases} \quad (3.9)$$

$$B_r(r_i, z_i) = B_{r\text{-COMSOL}}(r_i, z_i) \quad (3.10)$$

Note that at $r = 0$ we recover the measured field profile.

[‡]To guarantee a soft evolution of the magnetic field profile, we implement a bicubic interpolation of COMSOL maps.

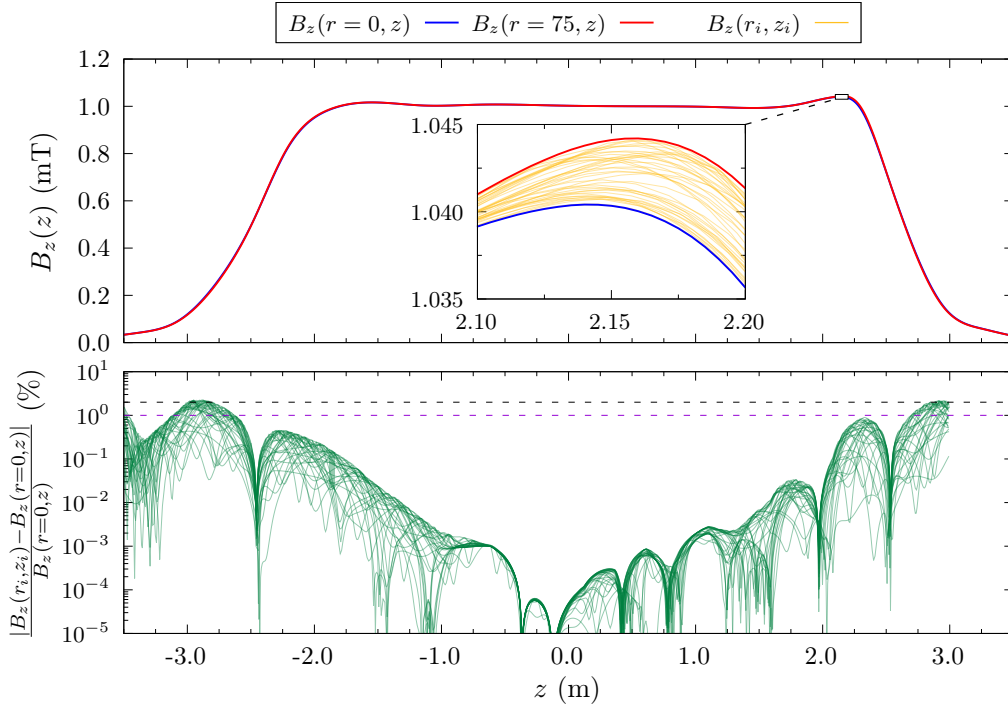


Figure 3.16: (Top) B_z field profiles as a function of z computed from 100 UCN tracks through the interpolation in Eq. (3.10). The multiple yellow lines, corresponding to the realistic trajectories, are bounded by the blue and red curves associated to the reference profiles at $r = 0$ and $r = 75$ mm, respectively. (Bottom) Relative difference between realistic B_z profiles to the reference on-axis profile $B_z(r = 0, z)$. The horizontal dashed lines are used to illustrate 1% and 2% limits.

The top side of Figure 3.16 shows the evolution of B_z for 100 UCN tracks as a function of the horizontal coordinate z (generally, z increases with time. See Figure 3.11). The yellow lines, which indicate the $(B_{z,i}, z_i)$ paths of all UCN tracks confounded, are enveloped by the reference field profiles for ideal straight trajectories along the solenoid axis ($r = 0$) and on top of the UCN guide wall ($r = 75$ mm). The bottom side of Figure 3.16, which displays the absolute relative separation between $B_z(r_i, z_i)$ and $B_z(r = 0, z)$, demonstrates that all UCN field profiles deviate up to 2% from the axis-of-symmetry field profile. Such small differences, which are even lower than 1% at the B -field plateau, reveal the low radial gradient of the axial magnetic field, i.e.

$$\nabla_r B_z \sim 0.$$

An important consequence of this is that the $n - n'$ analysis can be safely constructed by assuming a unique field profile: $B_z(r_i, z_i) = B_z(r = 0, z_i)$. That being said, computation of the $n - n'$ oscillation probability still has to account for the field gradient $\nabla_z B$, especially at the entrance and exit of the solenoid.

Before finishing this chapter, we examine the experienced B -field distributions obtained by projecting the pairs $(B_{z,i}, z_i)$ of Figure 3.16 on the vertical B_z axis. This is done for both the axial B_z and radial B_r components using the same 100 UCN tracks. The output distributions,

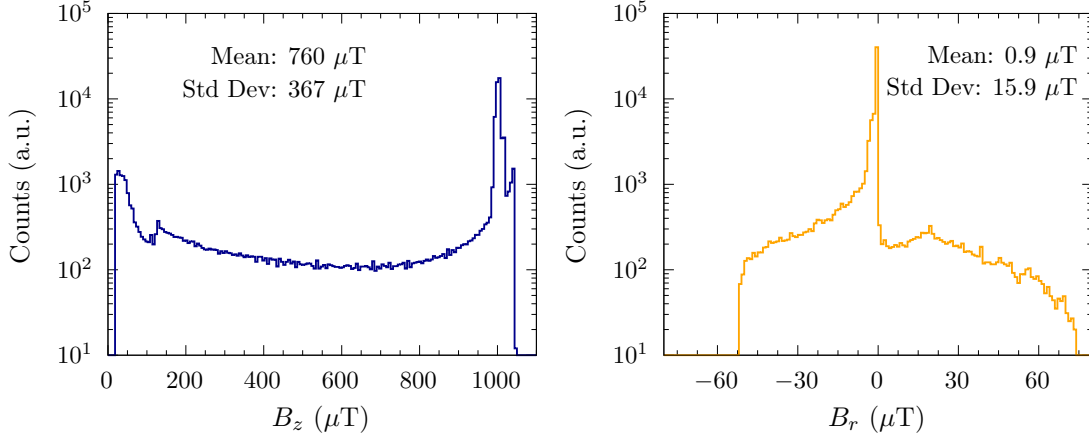


Figure 3.17: Frequency histograms of the experienced B_z (left) and B_r (right) field components. The histograms are constructed with the interpolated values $B(r_i, z_i)$ extracted from 100 UCN MC trajectories.

shown in Figure 3.17, illustrate the magnetic field values that are more frequently experienced by UCN if setting a solenoid B -field of 1 mT. For example, one can observe that UCN feel B_z values all along the range $[0 - 1045] \mu\text{T}$, but the main contribution is due to the field plateau at $B_z \sim 1000 \mu\text{T}$. In particular, the second peak at $B_z \sim 1040 \mu\text{T}$ is built when UCN travel through the ‘field bump’ mentioned above (see Figure 3.15). Also, the right-side distribution in Figure 3.17 allows verifying the negligible magnitude of B_r with respect to B_z ($< 1\%$), thus indicating that $n - n'$ analyses can be based on magnetic fields purely described by the B_z component.

3.5 Chapter conclusions

To probe for $n - n'$ oscillations in UCN beams, one requires experimental setups as simple as the ones constructed in past UCN storage bottles [7–11]. Oscillations in both cases are induced by matching the neutron energy due to an external B -field ($\mu_n B$) and the hidden neutron energy $\Delta E'$ (δm in the most generic approach). The main differences between both techniques are found in the size of the oscillation volume, which for the present work is a 6-m-long UCN guide, and the number of UCN counts per second, which went up to 200 kHz at the EDM beam port at ILL. The latter being the reason for including a UCN detector with high-counting rate efficiency (GADGET).

The data collection technique was designed such that the scanning over magnetic fields $B \in [50 - 1100] \mu\text{T}$ lead to a common sensitivity on $\tau_{nn'}$ within the entire interval $\delta m \in [3 - 66] \times 10^{-12}$. The scanning field step of $3 \mu\text{T}$, was determined from the probability resonance FWHM and the ABBC measuring sequence, which targets at the probe of three magnetic field values (A, B and C , separated by $20 \mu\text{T}$) every UCN delivery cycle (200 s). By normalizing the number of detected UCN during the counting at each field magnitude as $R_{ABC} = (N_B + N_C)/(N_A + N_C)$, one can test for signals in the three field values (see Eq. (3.2)) while removing linear drifts on the UCN flux within the cycles and avoiding long-term variations on the UCN counting in between cycles.

Preliminary analyses on the proposed approach revealed an experimental sensitivity, governed by the counting statistics $\Delta R_{ABC}^{\text{stat}} \sim 3.4 \times 10^{-4}$, written as $\tau_{nn'} \gtrsim 4s$, if assuming a uniform solenoid B -field. The computation of this value is constructed from the ABBC ratio equation and from MC simulations (validated by experimental TOF measurements) of UCN tracks. The MC simulation plays an important role as it used to estimate the magnitude of the free-flight-times and the number of collisions that characterize the UCN trajectories while traveling inside the magnetic field. In addition, they allowed determining the B -field profiles experienced by UCN while crossing the solenoid volume. In particular, it was found that such profiles are mostly defined by the z component of the axial field, i.e. $B \approx B_z(r=0, z)$.

Chapter 4

$n - n'$ oscillations: Data analysis

After describing the phenomenology (chapter 1) and the experimental technique to probe $n - n'$ oscillations with UCN beams (chapter 3), the following discussion is dedicated to the analysis of data collected at the PF2's EDM beam port at ILL during autumn 2020. In the first part, the UCN detection with GADGET is examined to define a category in the pulse shape (PS) map fulfilling both, a high UCN counting rate and a negligible background contribution. Using this event selection, a brief summary of the collected data is given while indicating the time sequence followed for its acquisition. Then, in the third part, an exhaustive characterization of the UCN flux fluctuations which affect the entire UCN counting data set is performed. In particular, this section is relevant for the final conclusions since it explains the sources of systematics. In the fourth part, the data fitting and parameter exclusion of $n - n'$ signals are exposed, first in the generic double-model scenario and later allowing hidden magnetic fields. At the end, the perspectives for future experiments are presented.

4.1 UCN category selection

Analyses in this chapter look for a signal confirming the neutron disappearance from the ILL UCN beam. To do so, two main assumptions were made beforehand. First, the UCN flux is constant or drifts linearly in time. This is necessary to correctly normalize the number of neutrons per cycle. Second, any fluctuating behavior in the normalized counting is purely attributed to UCN events, i.e. there are no background events with time structures at the scale of the UCN delivery period affecting the measurements.

Previous discussions on background analysis revealed the presence of non UCN events in the counting of GADGET at the EDM beam port. Although they represent a small fraction (see Table 2.3), these events might have time structures that could induce systematic errors in the normalized counts. For example, the well known $\gamma + \beta$ background produced from neutron activation of elements at the experimental site already showed a non-linear increasing (decreasing) pattern during the UCN delivery (sharing) time. This can be seen in Figure 2.17, where the counting rate of the $\gamma + \beta$ category follows a cumulative exponential behavior during the delivery cycles and an exponential decay elsewhere.

In order to avoid systematic effects of this kind, the detection PS map was partitioned into 5 categories to isolate the UCN counting from spurious events. These categories were defined after a parallel comparison of background (UCN beam on CF_4) and double-gas-filling

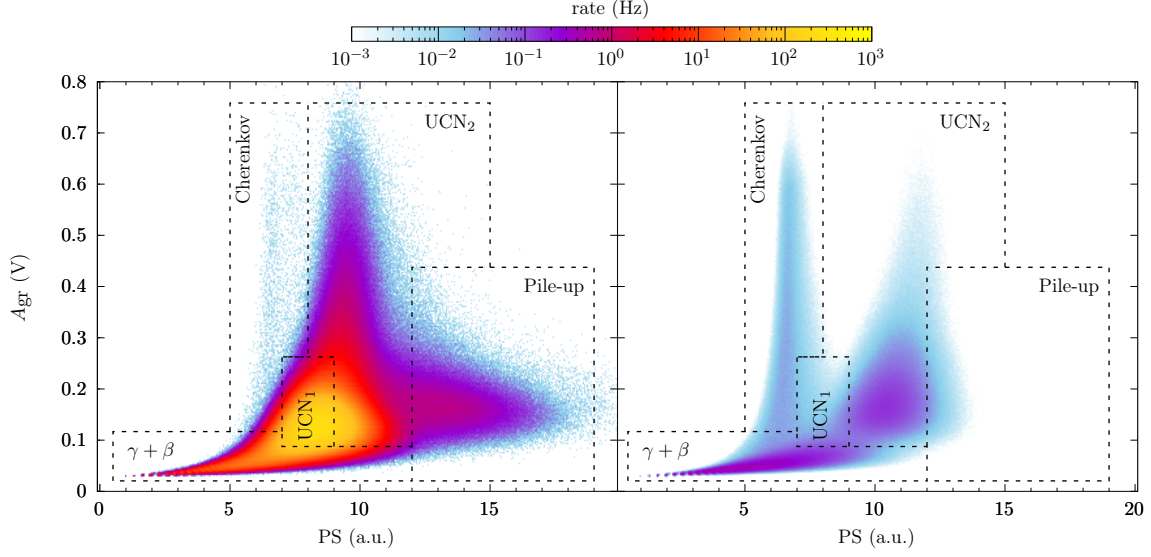


Figure 4.1: PS maps categories. The partitions are motivated by the signatures of events detection in background (CF_4 on the right) and double-gas-filling ($\text{CF}_4 + {}^3\text{He}$ on the left) setups. For a quantitative description, see Table 4.1.

Table 4.1: Categories contribution to the total counting in background (CF_4) and double-gas-filling ($\text{CF}_4 + {}^3\text{He}$) setups. Amount of saturated pulses (Sat.) are also reported.

Gas filling	Rate (kHz)	Category contribution (%)					
		$\gamma + \beta$	Cherenkov	UCN ₁	UCN ₂	Pile-up	Sat.
$\text{CF}_4 + {}^3\text{He}$	288.5	13.454	0.773	62.18	23.09	0.48	0.003
CF_4	~ 1	43.33	12.77	7.65	29.35	2.62	4.28

UCN (UCN beam on $\text{CF}_4 + {}^3\text{He}$ admixture) measurements, as shown in Figure 4.1. The reasons to define such category partitioning are the following:

- **$\gamma + \beta$ category** spans over the large horizontal cloud visible in the background measurement. Since γ and β detection events are contained in this category, even if they represent a small number, they must be excluded.
- **Cherenkov category** encloses most of the Cherenkov events in both measurements 2.3.3.
- **UCN₁ category** hosts most of the UCN counts, while excluding the regions of maximum ${}^{19}\text{F}$ -absorption (see section 2.3.5) and $\gamma + \beta$ events. Cherenkov and pile-up contamination is negligible.
- **UCN₂ category** includes the maximum of ${}^{19}\text{F}$ -absorption events in background conditions. It contains a large fraction of UCN which could be safely added to UCN₁ since most of the ${}^{19}\text{F}$ -absorption events transform into ${}^3\text{He}$ -absorption when adding this second gas to the admixture.

- **Pile-up category** keeps part of the UCN pile-up and ^{19}F -absorption. Their scarce contribution justifies excluding them from the UCN counting.

A quantitative description supporting these statements is presented in Table 4.1, where the most populated categories are highlighted in gray. While the category with maximum contribution in the double-gas-filling PS map (UCN_1) corresponds to the ^3He absorption, the most populated category ($\gamma + \beta$) in the background map is due to γ and β events. If one wants to estimate the amount of the total background contained within the UCN_1 category in double-gas-filling conditions, in addition to the percent contributions, the relative rates need to be taken into account:

$$\begin{aligned}
 (\text{background})_{\text{UCN}_1} &= \frac{[\text{rate} * (\text{contribution})_{\text{UCN}_1}]_{\text{background}}}{[\text{rate} * (\text{contribution})_{\text{UCN}_1}]_{\text{double-gas-filling}}} \\
 &\approx \frac{1000 * 7.65\%}{288500 * 62.18\%} \\
 &= 0.04\%.
 \end{aligned}$$

Note that not only this final number is extremely low, but it also corresponds to a very conservative approximation: most of the UCN absorption by ^{19}F is transformed into ^3He -absorption when operating with double-gas-filling. According to Figure 2.18, the ^{19}F -absorption reduces by a factor of 6 in double-gas-filling and therefore the background in UCN_1 becomes $\sim 0.007\%$, i.e. 10 Hz. For that reason, subsequent analyses on neutron hidden neutron oscillations constructed with the neutron counting in the UCN_1 category can be safely said “background-free”.

4.2 Acquired data summary

In our experiment, the UCN flux was recorded during 3794 cycles while scanning the solenoid magnetic field from $B = 30$ to $1100 \mu\text{T}$ with steps of $3 \mu\text{T}$ (this corresponds to a total of 350 cycles). Once a scan was finished, i.e. an entire sweep of the magnetic field range, a new one was automatically started from the top down while keeping the same step size. Ramp-up and ramp-down scans were continuously performed until manual halt from the user control system. After achieving a few scans, the run was stopped and the solenoid current was reversed to probe negative magnetic fields within the same range. In total, 9 scans were initiated with $+B$ and 5 with $-B$ polarities, although not all of them completed the 350 cycles. The exact number of cycles per scan for the whole experiment is summarized in Table 4.2.

Computation of R_{ABC} was done for all cycles using the UCN counting in GADGET’s UCN_1 category. Even if the contribution of this category to the total detection is of 62%, its counting is large enough to significantly conclude on the oscillation analysis while avoiding any spurious systematic effects produced by background counts. To see this, one could for example calculate the ratio $R_{ABC} = (N_B + N_{\bar{B}})/(N_A + N_C)$, assuming the resonance at the central B -field. Eq. (3.4) would then be rewritten as

$$\frac{N_B + N_{\bar{B}}}{N_A + N_C} = \frac{2N_0(e^{-\bar{n}_{\text{coll}}\langle P_{nn'} \rangle})}{N_0 + N_0} \approx 1 - \bar{n}_{\text{coll}}\langle P_{nn'} \rangle = 1 - \bar{n}_{\text{coll}} \left(\frac{\bar{t}_f}{\tau_{nn'}} \right)^2,$$

Table 4.2: Data collection summary.

Run	B -field polarity	Scan number	Cycles in scan	Cycles in run
1	+	0	320	320
2	+	0	147	147
3	+	0	163	163
4	+	0	331	331
5	+	0	350	1212
		1	350	
		2	350	
		3	162	
6	-	0	350	1490
		1	350	
		2	350	
		3	350	
7	+	4	90	131
		0	131	

or equivalently

$$\tau_{nn'} = t_f \sqrt{n_{\text{coll}} \left(1 - \frac{N_B + N_B}{N_A + N_C}\right)^{-1}}. \quad (4.1)$$

Therefore, in the limiting case where the deviation of $N_B + N_B$ with respect to $N_A + N_C$ is due to purely statistical fluctuations, i.e.

$$\frac{N_B + N_B}{N_A + N_C} = \frac{N_0 - \sqrt{N_0}}{N_0} = 1 - N_0^{-1/2},$$

a positive signal should be greater than

$$\tau_{nn'} = t_f \sqrt{n_{\text{coll}} \sqrt{N_0}}. \quad (4.2)$$

One can thus see that by restricting the counting to the UCN_1 category, the limit on $\tau_{nn'}$ is shortened to a $\sqrt{\sqrt{62\%}} = 89\%$. In other words, we reduce the experimental sensitivity by 11%.

4.3 Systematics: UCN flux fluctuations

Analyses posterior to data collection revealed the presence of non-statistical fluctuations in the UCN flux linked to the reactor power variations. This can be proven by direct comparison of both data sets: the UCN flux detection with GADGET and the reactor power obtained from ILL's neutron detectors at the reactor core. However, before reaching that point, a detailed characterization of the detected UCN flux and evaluation of possible extra less-relevant sources of non-statistical fluctuations in R_{ABC} are presented.

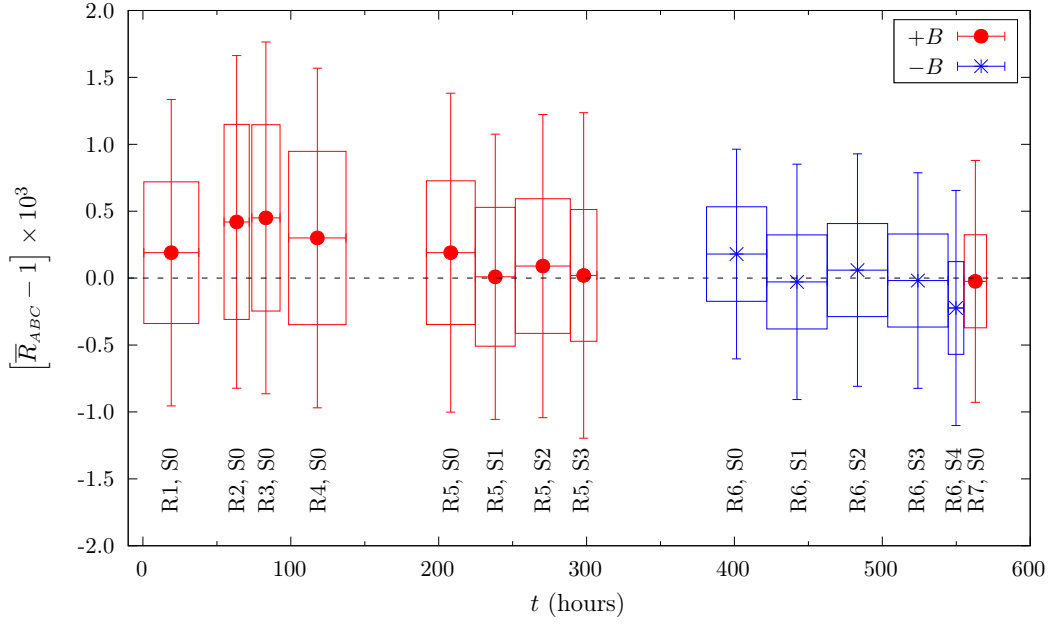


Figure 4.2: Mean R_{ABC} computed on complete or incomplete B -scans (S) for the 7 runs (R) composing the total collected data. Vertical boxes and lines represent the uncertainty expected from statistical fluctuations and data dispersion, respectively. Horizontal sizes show the time duration of each scan.

4.3.1 Flux stability within hours (scan level)

In section 3.3 it was explained that a $n - n'$ oscillation signal would be observed in one or two cycle measurements along an entire scan since the resonance width is comparable to the experimental sensitivity resolution ($\sim 1 \mu\text{T}$). For such a reason, even if a true positive signal is comprehended in the data, the mean R_{ABC} over the 350 cycles is expected to be consistent with the null hypothesis: $\bar{R}_{ABC} = 1$. This is illustrated in Figure 4.2 where \bar{R}_{ABC} is computed for the 14 experimental scans and plotted as a function of the recording time. The different scans were discriminated within runs in order to specify which of them are employed in next higher-resolution fluctuation analysis. The horizontal box sizes represent the time duration of each scan, and the vertical sizes the uncertainties of \bar{R}_{ABC} expected from counting statistics only. It is then normal that wider boxes have shorter uncertainties as they include more cycle measurements. Also shown in the same figure with vertical lines are the 1σ -dispersion of data points. Their greater magnitude with respect to statistical uncertainties suggest a systematic effect in the data for both $+B$ and $-B$ configurations. In fact, these non-statistical fluctuations seem to be present in the whole data set, with alike participation in all scans.

4.3.2 Flux stability within minutes (cycles level)

One possible approach to fluctuations identification is the search for periodic time structures in quantities which are expected to be constant. It was already suggested that no evidence of such time patterns was found in \bar{R}_{ABC} at the scale of several days (Figure 4.2). In fact, since calculation of \bar{R}_{ABC} results from the average over up to 350 cycles recorded during ~ 35

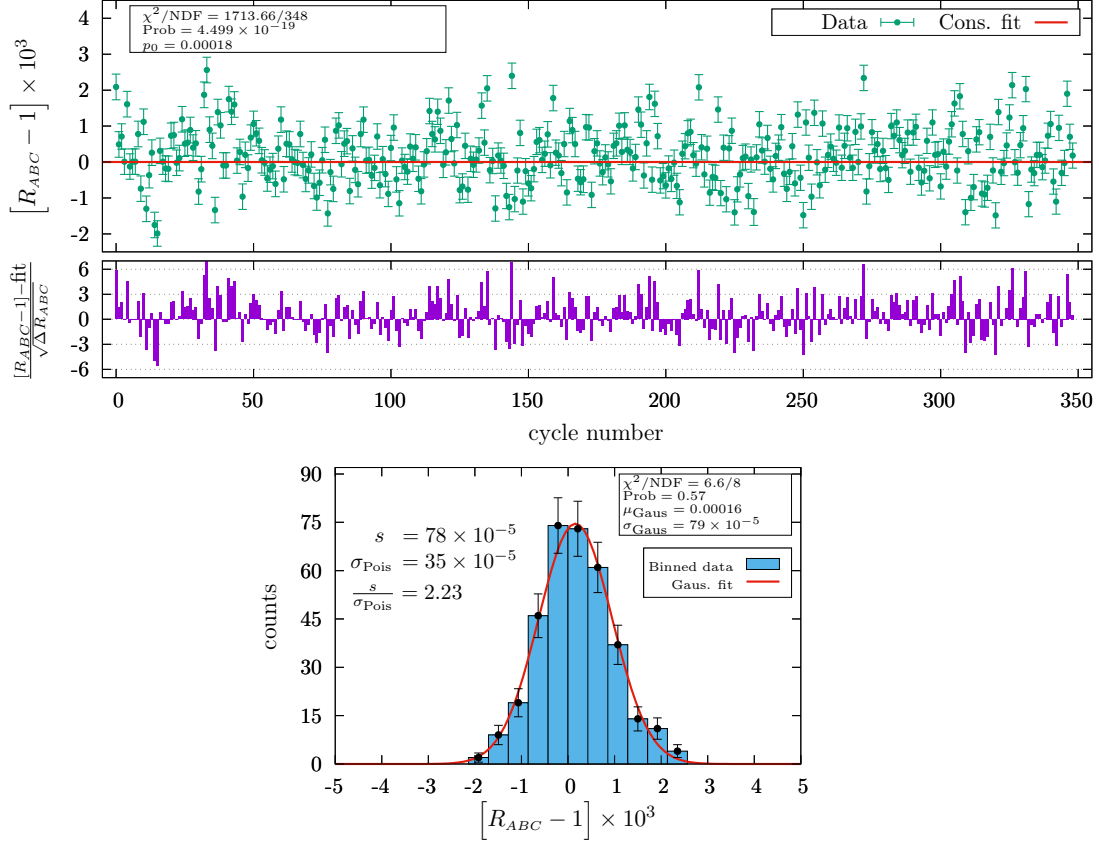


Figure 4.3: (Top) R_{ABC} as a function of the scan cycle number. (Middle) The normalized residuals show multiple non-statistical fluctuations all along the scan, thus suggesting systematic effects with shorter time scales. (Bottom) The data dispersion is not totally explained by statistical fluctuations, but follows a Gaussian distribution.

hours, time structures at shorter scales are not visible.

In order to increase the time resolution for fluctuations identification, the top side of Figure 4.3 presents the individual values of R_{ABC} as a function of the cycle number for the first scan of run 6 (R6-S0). One can observe that non-statistical fluctuations appear all along the scan, with no particular correlation to the time nor the magnetic field (both linearly proportional to the cycle number). Considering that the time between two consecutive cycles is about 8 minutes, and that error bars are purely computed from counting statistics, the source of non-statistical fluctuations are predicted at time scales even shorter than the cycle span.

The normalized residuals with respect to the constant fit, shown in the bottom of Figure 4.3, verify that about 50 out of the 350 points lay beyond the $\pm 3\sigma$. Clearly, this issue cannot be explained by the look-elsewhere effect. However, the frequency histogram of $[R_{ABC} - 1]$ points, on the bottom side of the same figure, demonstrates that even if the data dispersion,

computed as

$$s = \sqrt{\sum_{i=1}^{N_{\text{cycles}}} \frac{(R_{ABC,i} - \bar{R}_{ABC})^2}{N_{\text{cycles}} - 1}}, \quad (4.3)$$

is 2.23 times greater than the prediction from counting (Poisson) statistics

$$\sigma_{\text{Pois}} = \sqrt{N_{\text{cycles}} / \left(\sum_{i=1}^{N_{\text{cycles}}} (\Delta R_{ABC,i})^{-2} \right)}, \quad (4.4)$$

with

$$\Delta R_{ABC,i} = R_{ABC,i} \sqrt{\frac{1}{N_{B,i} + N_{B,i}} + \frac{1}{N_{A,i} + N_{C,i}}}, \quad (4.5)$$

where we have assumed no correlation between N_A , N_B and N_C , the data distribution follows a Gaussian form: $\mu_{\text{Gaus}} = 0.00016$, $\sigma_{\text{Gaus}} \approx s$ and $\chi^2/\text{NDF} = 6.6/8$. In the end, given that the observed nature of the non-statistical fluctuations support the fact that all cycles are subject to the same systematic effects, a common scaling factor equals to $(s/\sigma_{\text{Pois}})_{R_{ABC}} = 2.23$ can be safely applied on each R_{ABC} error bar. It was noted that this scaling factor is equivalent to the one obtained from the zeroth polynomial goodness of fit, computed as $\sqrt{\chi^2/(\text{NDF} - 1)} = \sqrt{1713.66/348} \approx 2.22$ [68].

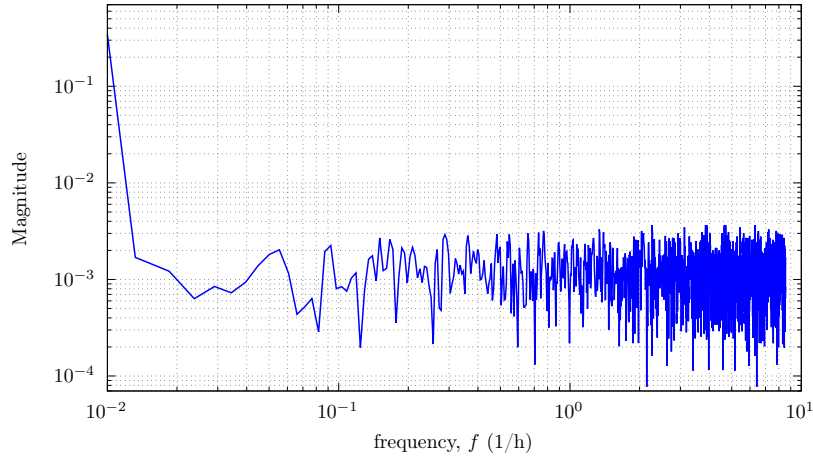


Figure 4.4: FFT of R_{ABC} during run 6. No relevant modulation is perceived within the displayed frequency range. The 8 minutes data sampling corresponds to the cycle time span.

For the sake of completeness, before looking for non-statistical fluctuations at shorter time scales, the Fast-Fourier Transform (FFT) of R_{ABC} points during the longest run R6 composed of almost 5 entire scans is presented. Figure 4.4 shows the FFT computed using a Hann window over the 1490 consecutive cycles that translate into 186 hours, i.e. 1 point every 8 minutes. This result shows no evident periodic phenomena modulating the measurement of R_{ABC} in the displayed frequency range. In particular, no modulation with frequency $f \approx 1/24\text{h}$ indicates that $n - n'$ signals are disfavored in the ‘solar system-static hidden

magnetic field' scenario explained in section 4.5. Conclusions from this study on R_{ABC} in R6 are extended to the rest of the UCN data set.

4.3.3 Flux stability within seconds (within cycles)

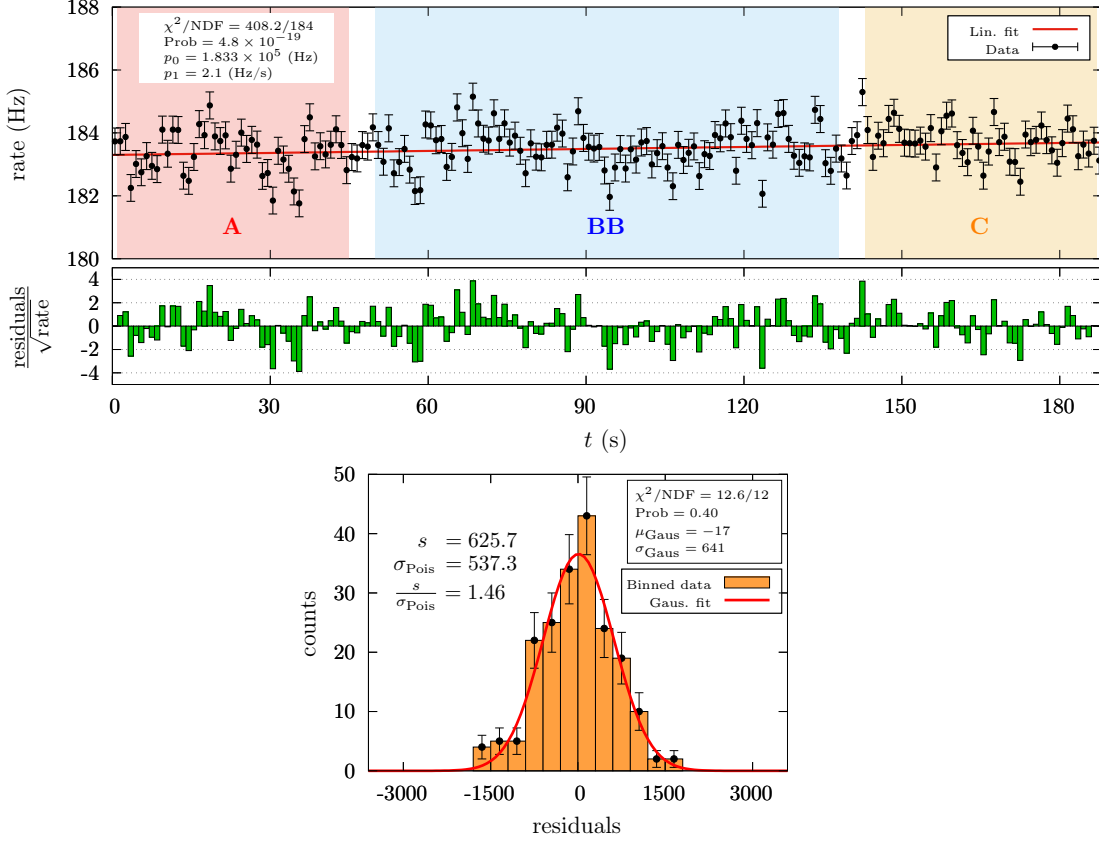


Figure 4.5: (Top) Total UCN rate as a function of the time within one sample cycle. (Middle) The normalized residuals show multiple non-statistical fluctuations all along the cycle with no predominance at A , B or C . (Bottom) The data dispersion is not totally explained by statistical fluctuations, but follows a Gaussian distribution.

Given that the construction of R_{ABC} is done from the flux integration over 200 s, the search for non-statistical fluctuations at the order of seconds cannot be done through this quantity. Instead, one can look at the UCN counting rate within delivery cycles. To do so, linear fits are performed on the detected flux of each cycle as

$$\text{rate} = p_0 + p_1 \cdot t, \quad (4.6)$$

with p_0 and p_1 the fitted parameters. A sample cycle rate and its associated normalized residuals with respect to the fit are shown in Figure 4.5 (top). Non-statistical fluctuations appear in the flux measurement during the entire time interval, with no evident predominance

at a particular time. The UCN rate, which is constructed by binning the time-of-detection signals achieved with the 2 ns resolution of the FASTER acquisition system, is computed every second starting from (ending in) the initial (final) time of N_A (N_C) counting. After constructing the frequency histogram of residuals (bottom side of Figure 4.5) and computing the expected data dispersion from Poisson statistics, one concludes that the extra systematics have to be added to the rate error bars in order to explain the ratio $(s/\sigma_{\text{Pois}})_{\text{rate}} = 1.46$. Since this scaling factor is shorter than the one obtained for R_{ABC} data points, $(s/\sigma_{\text{Pois}})_{R_{ABC}} = 2.23$, one can predict that the non-statistical fluctuations build-up at the scale of seconds to minutes. Similarly, as for R_{ABC} , the rate residuals dispersion follows a Gaussian distribution with $\chi^2/\text{NDF} = 12.6/12$.

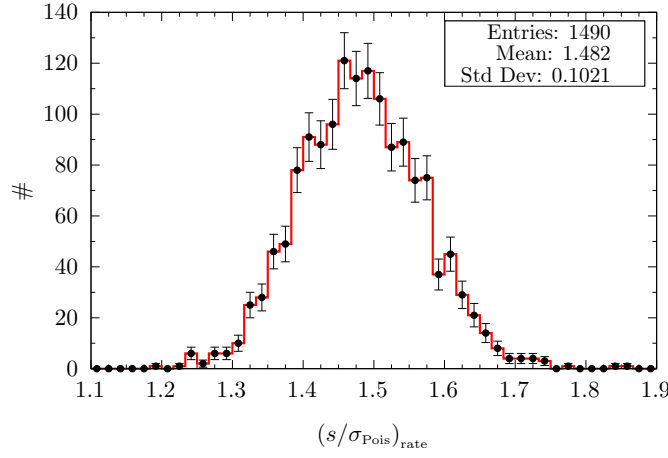


Figure 4.6: Observed-to-Poisson predicted dispersion of residuals of the rates in all cycles of run 6.

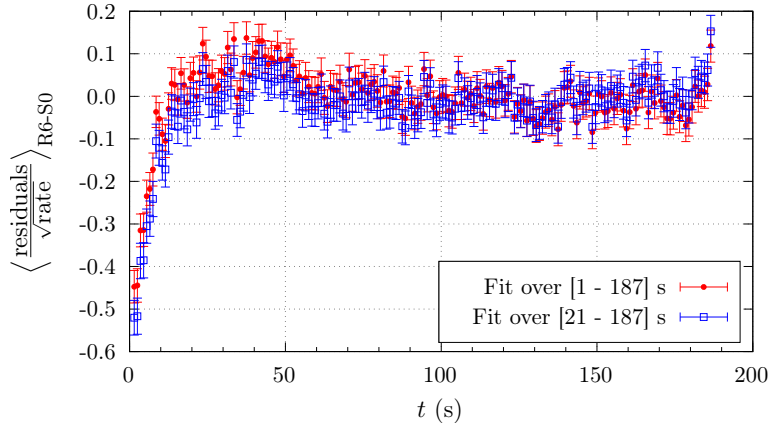


Figure 4.7: Average normalized counting rate residuals in all cycles of R6-S0. The residuals are calculated with respect to the linear fit of each cycle rate. In red, the fitting range corresponds to the initial ABBC integration interval. In order to avoid the residual beam ramping-up, the first 20 seconds are neglected in the fitting procedure of empty-blue-squares data.

Conclusions from the previous paragraph are extended over all cycles in this experiment. The distribution of $(s/\sigma_{\text{Pois}})_{\text{rate}}$ resulting from the linear fit of UCN cycles in run 6, displayed in Figure 4.6, shows that the rate error bars are underestimated with a mean $\langle (s/\sigma_{\text{Pois}})_{\text{rate}} \rangle = 1.482$. We point out that the entire distribution lays below $(s/\sigma_{\text{Pois}})_{R_{ABC}}$ thus confirming that non-statistical fluctuations show up at the scale of seconds.

Comparison of the counting rate from multiple cycles is not possible. The long-term drift of the UCN flux prevents computing any statistics on direct values of the rate. However, this limitation is removed if calculating the normalized rate residuals, which are obtained with respect to the linear fit of the UCN counting in each cycle (Eq. (4.6)). Figure 4.7 shows the average shape of these residuals computed over all the cycles in R6 as a function of time. Two cases displayed: in red the fitting range is the made equal to the ABBC integration interval $[1 - 187]$ s, and in blue the first 20 s are neglected, $[21 - 187]$ s. In both cases, one observes a decreasing defect on the average residuals during the first 20 s, which is attributed to the UCN beam ramping-up produced by the PF2 turbine alignment with the EDM beam port. Although the turbine alignment lasts about 2 seconds, its ramping-up effect might be noticeable at the detector event at 10 or 15 seconds, caused by the long-lasting trajectories of slow neutrons or of those undergoing multiple diffusive reflections.

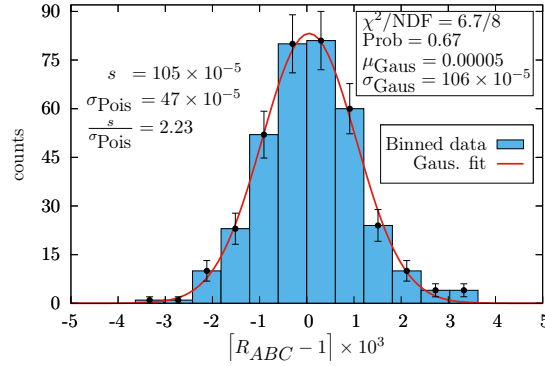


Figure 4.8: R_{ABC} data points dispersion and statistics after reducing the counting intervals according to Eq. (4.7). Comparison against Figure 4.3 reveal similar non-statistical fluctuations.

In order to avoid any systematics induced by the residual beam ramping-up effect, the R_{ABC} integration intervals are modified. In particular, the first 20 seconds counting of each cycle are removed, thus shrinking N_A to almost half its original size. In addition, to maintain the ABBC symmetry needed to absorb linear drifts, the N_B and N_C integration intervals are also resized. These new intervals, which are kept for subsequent fluctuations and $n - n'$ analyses, are rewritten as

$$\begin{aligned}
 N_A : & \quad [1 - 45] \text{ s} \rightarrow [20 - 45] \text{ s}, \\
 N_B + N_B : & \quad [50 - 138] \text{ s} \rightarrow [69 - 119] \text{ s}, \\
 N_C : & \quad [143 - 187] \text{ s} \rightarrow [143 - 168] \text{ s}.
 \end{aligned} \tag{4.7}$$

After such a redefinition, the reduced counting statistics makes R_{ABC} error bars $\sim \sqrt{2}$ larger (see Eq. (4.5)) while the sensitivity is expected to decrease to a $\sim \sqrt{\sqrt{50\%}} \approx 84\%$ (see

Eq. (4.2)). Nevertheless, as shown by the residuals frequency histogram of R_{ABC} points after the redefinition in Eq. (4.7), in Figure 4.8, the weight of non-statistical fluctuations remain unchanged. Since the scaling factor $(s/\sigma_{\text{Pois}})R_{ABC}$ results exactly the same as the one reported with the original 44 s integration windows, it can be concluded that the non-statistical fluctuations were not linked to the beam ramping-up.

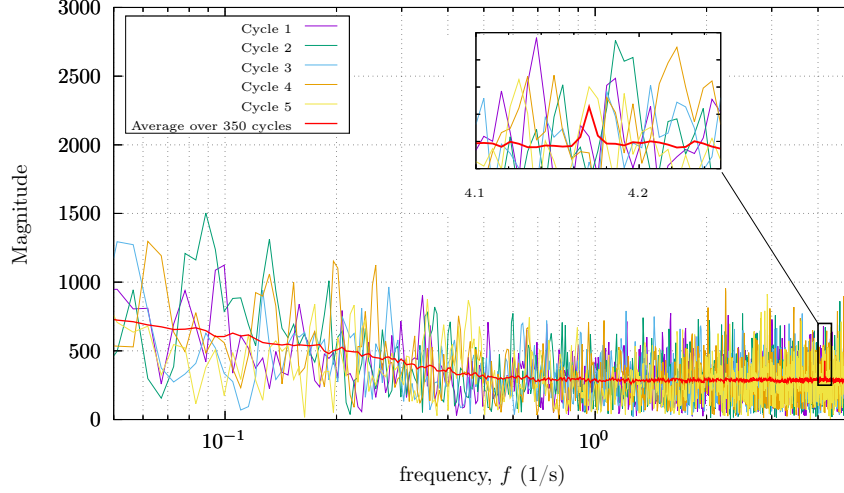


Figure 4.9: FFT of 5 sample UCN rate histograms and average FFT over all cycles in R0-S6. Besides the habitual white noise at low frequency, the average graph shows a short periodic signal with frequency similar to the PF2 turbine ($\sim 4 \text{ s}^{-1}$). This result excludes significant periodic parasite signals on the UCN detection within cycles.

Last but not least, the FFT computed over the counting rate of a single cycle is compared to the average FFT over all cycles in scan 0 of run 6 (see Figure 4.9). These plots show that no significant periodic patterns are evident on individual FFTs. However, after averaging over multiple runs, one observes a short signal with frequency $f = 4.17 \text{ s}^{-1}$ which is directly linked to the PF2 turbine rotation speed ($240 \text{ rpm} \approx 4 \text{ s}^{-1}$). Although explanation of this phenomenon can be cumbersome, it is concluded that its correlation to the non-statistical fluctuations on single UCN counting cycles is negligible. The fast rotation frequency of the turbine cannot explain the large fluctuations appearing every few seconds.

4.3.4 Flux stability within milliseconds

Another approach to study the non-statistical fluctuations of the UCN detection rate is based on the computation of the Allan Deviation (σ_{Allan}) [101]. The principle of this technique is to look at the fluctuations between consecutive averages of the counting rate as a function of the averaging time window (τ). Although this quantity is mostly employed to quantify the stability of variables which are assumed constant, its determination could eventually lead to noise identification. To do so, counting time histograms are constructed with 10 ms bin size so that the averaging time τ can be made as small as 20 ms. By denoting Y_j the UCN

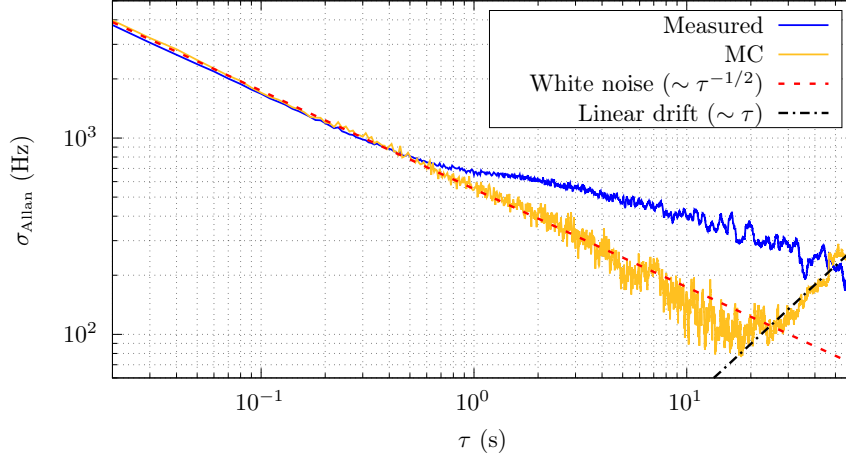


Figure 4.10: Average Allan deviation computed over 10 cycles measurement and on a non-statistical fluctuations free MC dummy rate spectrum. While MC reproduces the expected white noise (statistical fluctuation) and slow linear drift, the measurement deviates from the white noise at $\tau \sim 0.5$ s.

counting in bin j , the Allan deviation reads

$$\sigma_{\text{Allan}}(\tau) = \sqrt{\frac{1}{2(M-1)} \sum_i^{M-1} (\bar{Y}_{i+1,\tau} - \bar{Y}_{i,\tau})^2}, \quad (4.8)$$

with

$$\bar{Y}_{i,\tau} = \frac{1}{[\tau/10 \text{ ms}]} \sum_j^{[\tau/10 \text{ ms}]} Y_j \quad (4.9)$$

and $M = [200 \text{ s}/\tau]$ the number of time partitions for a given τ .

Using Eq. (4.8), the Allan deviation is computed as a function of τ for 10 UCN cycles chosen randomly from run 6. Figure 4.10 shows the average Allan deviation shape associated to these measurements next to the Allan deviation of a reference MC-generated counting spectrum. The MC spectrum is simulated by assuming purely statistical fluctuations on top of a slow linear drift of the rate. After direct comparison of the measured against MC simulation, one sees that the former deviates from statistical fluctuations (white noise) around $\tau = 0.5$ s. This is compatible with analyses in the next section (4.3.5) where it is demonstrated that the non-statistical fluctuations are negligible at time scales as small as a couple μs but become relevant at the order of few seconds (see section 4.3.3). In principle, if such fluctuations happen to be proportional to the UCN flux, they accumulate in the neutron counting. Hence, the longer the counting intervals, the larger the non-statistical fluctuations. In fact, this is the reason why $(s/\sigma_{\text{Pois}})_{R_{ABC}} = 2.23$ and $(s/\sigma_{\text{Pois}})_{\text{rate}} = 1.689$. While the former derives from UCN counting during 44 s periods, the latter corresponds to 1 s binning. A detailed demonstration of this cumulative process of non-statistical fluctuations is presented in Appendix D.

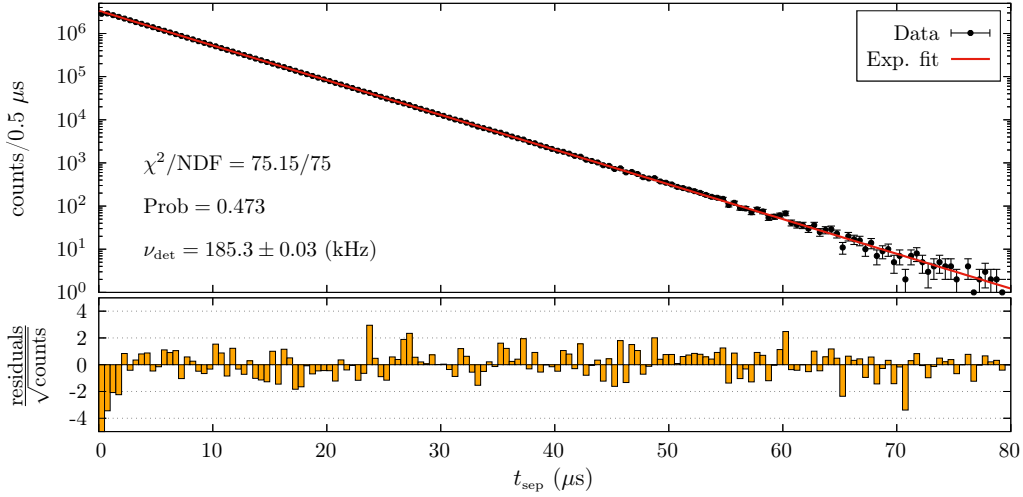


Figure 4.11: Event-to-event time separation distribution. Data corresponds to 35 million detection in a sample cycle measurement. The exponential fit according to Eq. (4.10) reveals no systematic uncertainties at these time scales. The counting defect in the first bin is due to pile-up events contain inside the coincidence time window of 50 ns.

4.3.5 Flux stability within microseconds

The high resolution in time of UCN detection with FASTER allows performing a detailed analysis of the flux fluctuations. Another approach to evaluate the flux constancy is to look at the time separation between UCN events. In fact, if the detection rate (ν_{det}) is constant, the probability to find two consecutive events separated by t_{sep} seconds is given by

$$P(t_{\text{sep}}) = \nu_{\text{det}} e^{-\nu_{\text{det}} t_{\text{sep}}}. \quad (4.10)$$

This expression is used to fit the time separation distribution constructed from a single UCN cycle (see Figure 4.11). The fitting, $[1.5 - 40] \mu\text{s}$, range was chosen smaller than the histogram span so to ignore the first bin (500 ns), whose counting is underestimated due to pile-up events, and bins with low statistics at large t_{sep} . The counting defect on the first bin is explained by the 50 ns coincidence time window programmed within FASTER to group the PMT signals. Events separated by times shorter than this window are detected as a single one and thus add as a pile-up. Using Eq. (4.10) and the fitted ν_{det} , the pile-up probability is estimated as

$$P_{\text{pile-up}} = \int_0^{50 \text{ ns}} P(t) dt = 1 - e^{-\nu_{\text{det}} * 50 \text{ ns}} \approx 1\%, \quad (4.11)$$

which is consistent with the ‘pile-up’ category counting reported in section 2.3.6. The normalized residuals, shown in the bottom side of Figure 4.11, confirm a good agreement between data and Eq. (4.10) on the entire range besides the first bin. Such congruity is also reflected on the fitting χ^2/NDF ($= 75.15/75$), demonstrating that the non-statistical fluctuations cannot be perceived at the μs scale.

4.3.6 Data correction from reactor power fluctuations

It has been proved that the R_{ABC} error bars were underestimated due to a systematic effect producing non-statistical fluctuations on the detected UCN flux at the scale of seconds. This fluctuating phenomenon appears all along the UCN delivery cycles without a fixed periodic time structure. A simple homogeneous scaling of the rate error bars equal to $S_{\text{rate}} = 1.689$ would be sufficient to completely adjust the UCN counting rate per second at each cycle to linear functions. Likewise, taking into account the accumulation of fluctuations, a homogeneous scaling of R_{ABC} error bars of $S_{R_{ABC}} = 2.23$ makes the whole data set consistent with the null-hypothesis of no $n - n'$ oscillations. In the following, we argue how this scaling can be safely be applied by attributing the non-statistical fluctuations to the reactor power variations.

Long term variations ($t > t_{\text{cycle}}$)

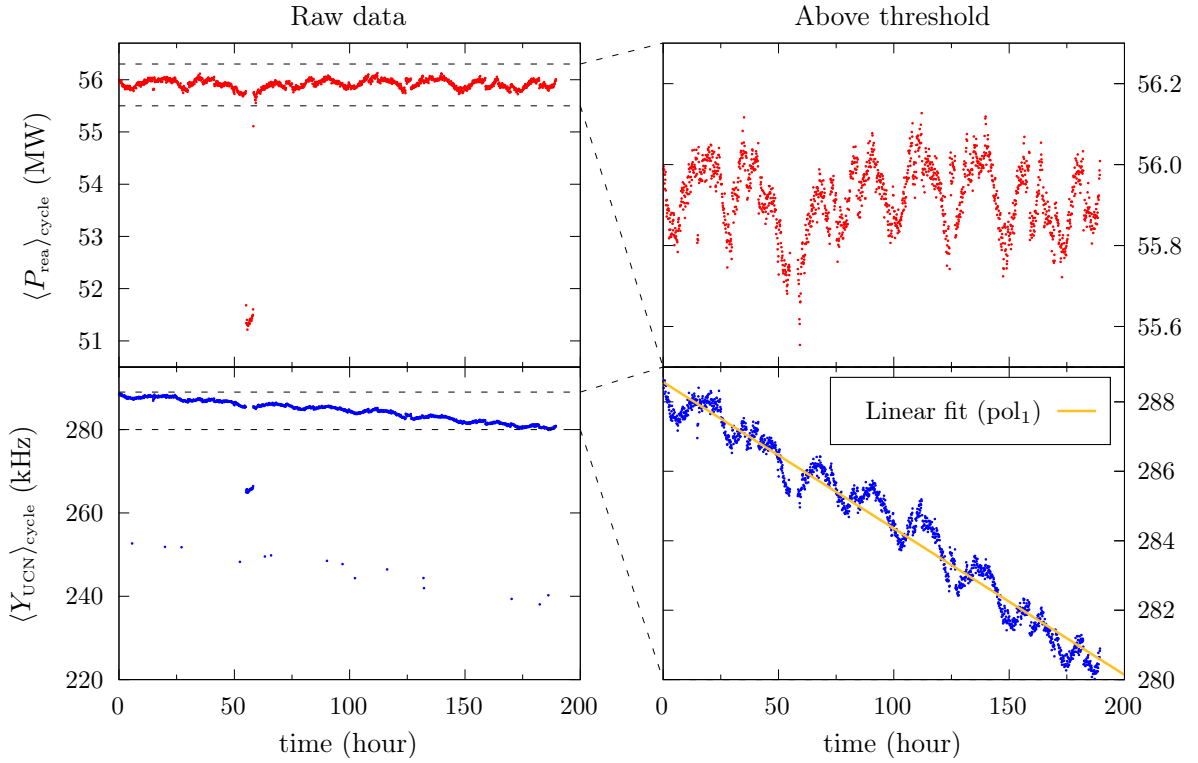


Figure 4.12: Average UCN rate and reactor power per cycle as a function of time. Right-side plots result from the data cleansing performed for correlation studies. The linear fit is used to compute the residuals on the average UCN rate according to Eq. (4.12).

Access to the reactor power data was only possible after the $n - n'$ experimental campaign. Since computation of the power is managed by the ILL operators to control and survey the reactor performing, the algorithm for its calculation remains private. The data set consists of the reactor nominal power with 1-second resolution, sampled during the entire 2020 reactor cycle. Given that both the power and the UCN detection were recorded with different clock

systems, there is a time offset between them. Assuming this offset is negligible*, a first estimate of the correlation between the UCN rate and the power is computed by looking at their average values per cycle, $\langle Y_{\text{UCN}} \rangle_{\text{cycle}}$ and $\langle P_{\text{rea}} \rangle_{\text{cycle}}$, respectively. The left side of Figure 4.12 shows these averages as a function of time during runs 6 and 7, where several remarks can be mentioned. First, besides the 5-hours drop of $\langle P_{\text{rea}} \rangle_{\text{cycle}}$ at $t \approx 55$ h, it keeps about 56 MW for the whole time interval. In contrast, $\langle Y_{\text{UCN}} \rangle_{\text{cycle}}$ decreases continuously from 288 kHz to 280 kHz in the same period. This long-term drift is attributed to the ILL's vertical cold source (VCS) decreasing efficiency, which might be linked to a possible heating of the liquid D₂ (see Figure 1.6). Also, multiple quick drops on $\langle Y_{\text{UCN}} \rangle_{\text{cycle}}$ seem to be independent of the reactor power. They could be related to changes at the level of the PF2 turbine or the acquisition system. In order to exclude these spurious points, we limit the correlation analysis to data points above convenient thresholds (lower horizontal dashed lines). Once the undesired drops are removed, the progressive falling of $\langle Y_{\text{UCN}} \rangle_{\text{cycle}}$ is adjusted to a linear function pol_1 , which allows defining the average UCN rate residuals as

$$\langle Y_{\text{UCN}}^{\text{res}} \rangle_{\text{cycle}} = \langle Y_{\text{UCN}} \rangle_{\text{cycle}} - \text{pol}_1. \quad (4.12)$$

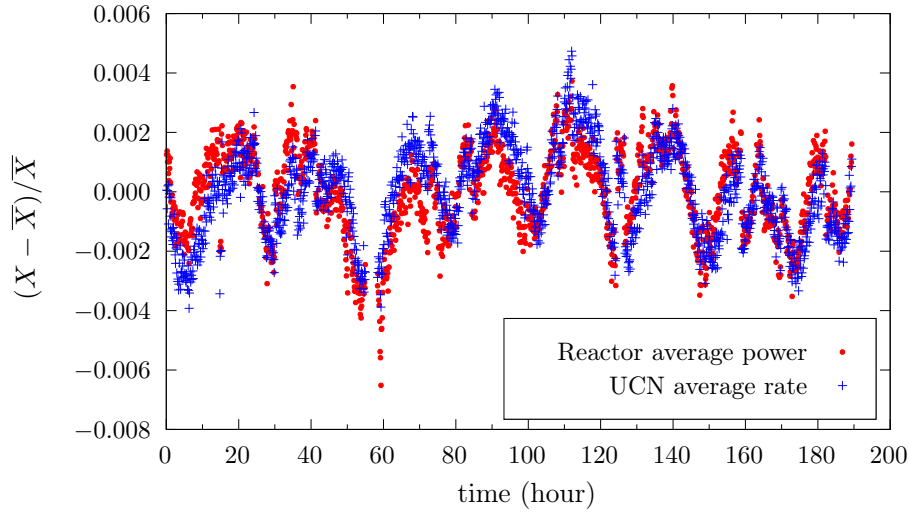


Figure 4.13: Long-term variation of average UCN counting rate and reactor power. The point sampling corresponds to the cycle period 400 s. The large correlation coefficient (0.76) explains the slow UCN rate variations.

Figure 4.13 shows the superposition of $\langle Y_{\text{UCN}}^{\text{res}} \rangle_{\text{cycle}}$ and $\langle P_{\text{rea}} \rangle_{\text{cycle}}$ after centering and normalizing with respect to their respective mean values. This comparative description permits looking, for the first time, the matching between ILL's reactor power and the UCN counting at the PF2 EDM beam port. The visible correlation in Figure 4.13 (characterized by a Pearson correlation coefficient $\rho_{\text{pea}} \approx 0.76$) allows assigning the long-term (larger than 400 s) variations of the UCN flux to the reactor power fluctuations. One could think on correcting the long-term fluctuations of $\langle Y_{\text{UCN}} \rangle_{\text{cycle}}$, for example, by dividing them by $\langle P_{\text{rea}} \rangle_{\text{cycle}}$. However, since the self-normalized construction of the ratio R_{ABC} does compensate for the long-term variations

* t_{offset} should not be larger than the cycle period (400 s).

($t > t_{\text{cycle}}$), it is important to establish whether the non-statistical short-term fluctuations ($t < t_{\text{cycle}}$) affecting the dispersion of R_{ABC} points can be corrected through the reactor data.

Short term variations and correction of R_{ABC} ($t < t_{\text{cycle}}$)

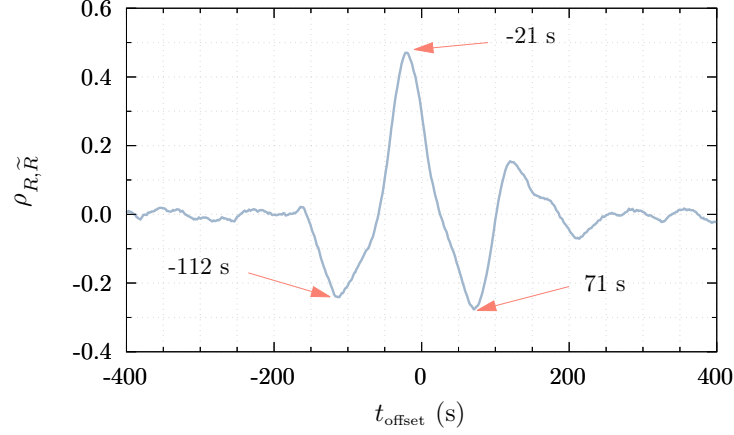


Figure 4.14: Correlation coefficient between UCN counting and reactor power ratios (Eq. (3.2) and (4.13)) as a function of the time offset.

To evaluate the possibility of correcting R_{ABC} points at the scale of seconds, an equivalent quantity is computed from the reactor's power data:

$$\tilde{R}_{\text{pow}} = \frac{P_{B-\text{pow}} + P_{B-\text{pow}}}{P_{A-\text{pow}} + P_{C-\text{pow}}}, \quad (4.13)$$

where P_i^{pow} represents the average power during the UCN counting N_i (see Eq. (3.2)). As R_{ABC} , this reactor power ratio is also insensitive (unless non-statistical fluctuations) to linear drifts at time scales comparable to t_{cycle} and to any long-term variation. Before attempting the correction of R_{ABC} with \tilde{R}_{pow} , we conduct a time synchronization between both data sets by finding the time offset (t_{offset}) for maximum correlation. Figure 4.14 shows the correlation after shifting the power reference time in steps of 1 second. The resulting behavior depicts a maximum at $t_{\text{offset}} = -21\text{s}$, which is used to calibrate the data set, and also two minima at -112s and 71s . The maximum correlation time offset contains information on the time delay between both acquisition system clocks. However, it is also affected by physical processes such as the time for neutron transport from the reactor core to the UCN detector. Nevertheless, distinguishing each contribution is irrelevant for the synchronization purpose. Concerning the position of minimum correlation, we notice that their time difference matches the UCN cycle time span (180 s), and their middle point the maximum correlation. As one would expect, no correlation is found when the time offset exceeds t_{cycle} .

In virtue of the large correlation $\rho_{R, \tilde{R}}$ after data synchronization, one would naively think that the R_{ABC} points could be corrected by compensating for the reactor power variations as

$$R_{ABC}^{\text{correc}} = \frac{N_B + N_B}{(N_A + N_C) \frac{P_B + P_B}{P_A + P_C}} = \frac{R_{ABC}}{\tilde{R}_{\text{pow}}}. \quad (4.14)$$

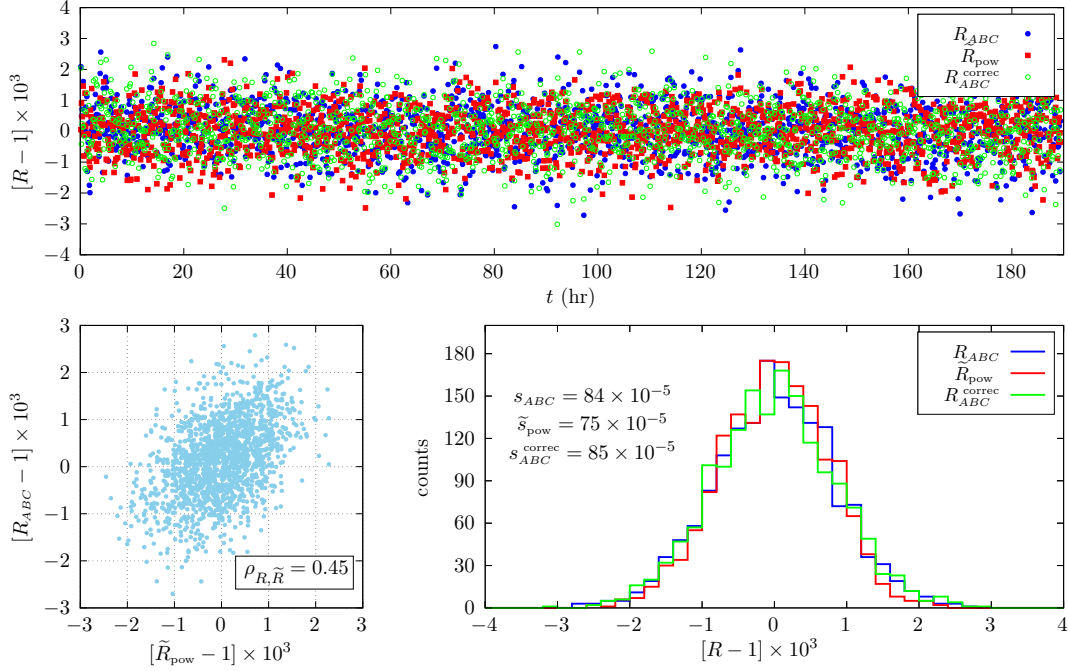


Figure 4.15: Comparison of UCN counting and reactor power normalized ratios per cycle as a function of time (top) and in frequency histograms (bottom-right). Both plots include the UCN points corrected as $R_{ABC}^{\text{correc}} = R_{ABC}/\tilde{R}_{\text{pow}}$. Also shown (bottom-left) the correlation of both data sets.

However, one has to take into account that, in order to perform a profitable correction, the correlation coefficient has to fulfill

$$\rho_{R, \tilde{R}} > \frac{1}{2} \frac{\tilde{s}_{\text{pow}}}{s_{ABC}}, \quad (4.15)$$

with s_{ABC} and \tilde{s}_{pow} the standard deviations of R_{ABC} and \tilde{R}_{pow} , respectively. Eq. (4.15) can be derived by recalling that the purpose after the correction is to narrow the R_{ABC} distribution so that the point dispersion gets closer to the prediction from statistical fluctuations, i.e. $s_{ABC} \rightarrow \sigma_{\text{Pois}}$ (Eq. (4.3) and (4.4)). Hence, using the definition in Eq. (4.14), the narrowing requirement is written as

$$\begin{aligned} s_{ABC} > s_{ABC}^{\text{correc}} &= |R_{ABC}^{\text{correc}}| \sqrt{\left(\frac{s_{ABC}}{R_{ABC}}\right)^2 + \left(\frac{\tilde{s}_{\text{pow}}}{\tilde{R}_{\text{pow}}}\right)^2 - 2\rho_{R, \tilde{R}} \frac{s_{ABC} \tilde{s}_{\text{pow}}}{R_{ABC} \tilde{R}_{\text{pow}}}} \\ &\Leftrightarrow s_{ABC}^2 > s_{ABC}^2 + \tilde{s}_{\text{pow}}^2 - 2\rho_{R, \tilde{R}} s_{ABC} \tilde{s}_{\text{pow}} \\ &\Leftrightarrow 0 > \tilde{s}_{\text{pow}} - 2\rho_{R, \tilde{R}} s_{ABC} \end{aligned} \quad (4.16)$$

where we have safely assumed $R_{ABC}^{\text{correc}} = R_{ABC} = \tilde{R}_{\text{pow}} \approx 1$. This last expression, which is equivalent to Eq. (4.15), demonstrates that the larger the \tilde{s}_{pow} the greater the correlation has to be to conveniently correct R_{ABC} . In our case, when looking at the experimental data, it occurs

that both R_{ABC} and \tilde{R}_{pow} present similar dispersion $s_{ABC} \approx \tilde{s}_{\text{pow}}$, thus requiring $\rho_{R, \tilde{R}} > 0.5$. However, since the actual measured correlation after synchronization is $\rho_{R, \tilde{R}} = 0.45$, the reactor power data cannot be used for the desired correction[†]. In particular, the distribution of R_{ABC}^{correc} exhibits a dispersion comparable to that of R_{ABC} and \tilde{R}_{pow} . Figure 4.15 resumes the three ratio distributions as a function of time next to frequency histograms that allow a visual comparison of the dispersion after correction.

Even if no correction can be applied, the main result in the analysis above is that the reactor fluctuations are as large as the UCN detection ones: $s_{ABC} \approx \tilde{s}_{\text{pow}}$. Hence, one can simply argue that the non-statistical fluctuations have origin at the reactor power. As a consequence of this, we can safely scale the error bars ΔR_{ABC} with factors as big as the ones displayed in Figure 4.8 ($(s/\sigma_{\text{Pois}})_{R_{ABC}} = 2.23$).

4.4 Probing oscillations as a function of δm ($B' = 0$)

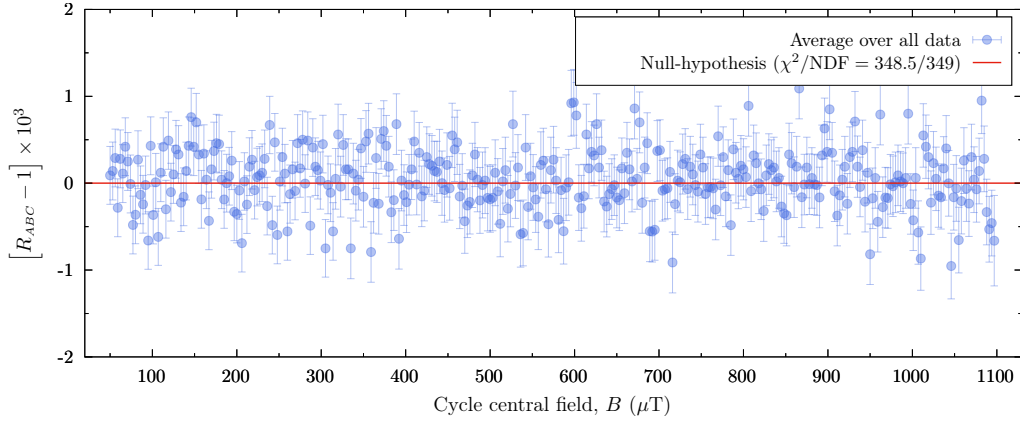


Figure 4.16: Average R_{ABC} over all measured scans as a function of the central field of the ABBC sequence. Error bars scaling is performed according to Eq. (4.20).

Analyses in this section are built within the scenario of non-zero neutron-hidden neutron mass splitting ($\delta m \neq 0$) and vanishingly small hidden magnetic fields $B' = 0$, i.e. $n - n'$ oscillations can be described by the double-parameter model in Eq. (1.10). In this model, the spin is conserved during oscillations and the resonance condition $\Delta_{nn'} = \mu_n B - \delta m = 0$ is only fulfilled for one of the spin states. This can be easily seen from the Hamiltonian in Eq. (1.8), written as

$$\hat{\mathcal{H}}_{nn'} = \begin{pmatrix} \mu_n B & 0 & \epsilon_{nn'} & 0 \\ 0 & -\mu_n B & 0 & \epsilon_{nn'} \\ \epsilon_{nn'} & 0 & \delta m & 0 \\ 0 & \epsilon_{nn'} & 0 & \delta m \end{pmatrix}, \quad (4.17)$$

[†]Note that in the ideal scenario, with $\rho_{R, \tilde{R}} = 1$, Eq. (4.16) gives a perfect correction: $s_{ABC}^{\text{correc}} = 0$

leading to the spin-up and spin-down resonances

$$\begin{aligned}\mu_n B = \delta m & : n_{\uparrow} \rightarrow n'_{\uparrow} \\ -\mu_n B = \delta m & : n_{\downarrow} \rightarrow n'_{\downarrow}.\end{aligned}$$

Therefore, provided $\delta m > 0$, n_{\uparrow} oscillates into n'_{\uparrow} for $+B$ resonant fields and n_{\downarrow} oscillates into n'_{\downarrow} for $-B$ resonant fields. However, this is not relevant for the analysis, since the UCN beam used in this experiment is made of 50% n_{\uparrow} and 50% n_{\downarrow} (not polarized). We can thus average over the R_{ABC} measurements available from all scans (see Table 4.2) regardless of the applied B -field orientation (+ or -). The number of neutrons disappearing from the beam due to $n - n'$ oscillations is the same for both magnetic field directions. Note that, under these circumstances, the asymmetry $A_{\uparrow\downarrow}$ in Eq. (1.17) is expected to be zero: $N_B = N_{-B}$, i.e. the asymmetry channel is not sensitive to $n - n'$ oscillations. That would not be the case for a polarized beam (see discussion in sec 5.2).

Based on the above reasoning, the weighted averages and their uncertainties for every B_i -field step using the $R_{ABC,i,j}$ points available from the multiple j scans were computed as

$$R_{ABC,i} = \frac{\frac{1}{N_{\text{scans}}} \sum_{j=1}^{N_{\text{scan}}} \frac{R_{ABC,i,j}}{\Delta R_{ABC,i,j}^2}}{\sum_{j=1}^{N_{\text{scan}}} \frac{1}{\Delta R_{ABC,i,j}^2}}, \quad (4.18)$$

and

$$\Delta R_{ABC,i} = \sqrt{\frac{1}{N_{\text{scans}} \sum_{j=1}^{N_{\text{scan}}} \frac{1}{\Delta R_{ABC,i,j}^2}}}. \quad (4.19)$$

Whereas the input uncertainties $\Delta R_{ABC,i,j}$ only include poissonian statistics, the output weighted uncertainties $\Delta R_{ABC,i}$ are scaled after the average calculation. In this case, the scaling factor obtained from the dispersion of averaged values is comparable to the one already validated by the reactor power fluctuations (2.23):

$$\left(\frac{s}{\sigma_{\text{Pois}}} \right)_{R_{ABC,i}} = \frac{34 \times 10^{-5}}{15 \times 10^{-5}} = 2.25. \quad (4.20)$$

One can confirm that, although the $R_{ABC,i}$ points dispersion is reduced after the averaging, $s = 105 \times 10^{-5} \rightarrow s = 34 \times 10^{-5}$, the scaling factor remains the same. Such invariability is consistent with our procedure, since Eq. (4.18) and (4.19) only consider poissonian uncertainties. Thus, it is normal that σ_{Pois} also shortens as we average over several scan measurements.

Figure 4.16 shows the average $R_{ABC,i}$ points as a function of the central magnetic B_i -field. We observe that, even after the error bars scaling, there is a slight difference between the null-hypothesis χ_{null}^2 and the number of degree-freedom NDF. This is expected because the scaling factor is computed throughout the R_{ABC} points dispersion (Eq. (4.20)) rather than through the expression $\sqrt{\chi_{\text{null}}^2 / (\text{NDF} - 1)}$. While the former involves the sum $\sum (R_{ABC,i} - \bar{R}_{ABC})^2$, the latter computes $\sum (R_{ABC,i} - 1)^2$.

There are two general approaches for probing $n - n'$ oscillations as a function of the solenoid magnetic field. They both propose a fitting function to describe the measured R_{ABC} . The first one assumes a homogeneous solenoid B -field, thus providing an analytical expression for the oscillation probability $P_{nn'}^{\text{Anal}}$. The second one implements the numerical solution for the Hamiltonian, where the magnetic field is interpolated from the COMSOL - measurement model as UCN move along the STARucn simulated tracks. For comparison purposes as well as for defining the sensitivity and accuracy of the conclusions derived here, both approaches are simultaneously followed in next sections.

4.4.1 Oscillation probability: Numerical and analytical solutions

In section 3.2.1, we evaluated the oscillation probability FWHM through the analytical solution of $\hat{\mathcal{H}}_{nn'}$ in Eq. (1.10). In that example, the resonance behavior, plotted as a function of δm , was described by a sinc^2 -like pattern with axis of symmetry at $\Delta_{nn'} = 0$. However, the use of such a simplistic image is only valid in highly homogeneous B -fields with negligible gradients $\nabla_{\vec{r}}\vec{B} = 0$. For the present work this is not true given that the B -field profiles that UCN experience while crossing the 6-m guide do not fulfill $\nabla_z B_z = 0$; although $\nabla_r B_z \sim 0$ and $B_r \sim 0$ (see section 3.4.3). In order to fully expose the dynamics of $n - n'$ oscillations, we compare the oscillation probability determined from the analytical solution, with $\nabla_{\vec{r}}\vec{B} = 0$, and through the numerical solution accounting for the field gradient $\nabla_z B_z$.

Whether the magnetic field is assumed uniform or its simulated and measured inhomogeneities are included, the $n - n'$ oscillation probability, $P_{nn'}$, depends on the multiple trajectory steps followed by UCN within the solenoid volume. In particular, the oscillation probability at the trajectory's i -th step (P_i) is determined by the free-flight-time

$$t_{f,i} = t_i^{\text{coll}} - t_{i-1}^{\text{coll}} \quad (4.21)$$

and the magnetic field profile experienced between both wall collisions. Since detected neutrons in the experiment are regarded as neutrons surviving $n - n'$ oscillations after all the trajectory steps, computation of $P_{nn'}$ is made by selecting the STARucn tracks that end up at the detector entrance window. Other UCN lost via β -decay, up-scattering, absorption or transmission at the guide walls do not contribute to the analysis.

To define the fitting function for the experimental points R_{ABC} , we have first to compute the total probability for a UCN to escape the setup as consequence of $n - n'$ oscillations. For a UCN describing n_{coll} wall collisions, this probability is written as

$$\begin{aligned} P_{nn'} &= P_1 + (1 - P_1)P_2 + (1 - P_1)(1 - P_2)P_3 + \cdots + \left(\prod_{i=1}^{n_{\text{coll}}-1} (1 - P_i) \right) P_{n_{\text{coll}}}, \\ &\approx P_1 + P_2 + P_3 + \cdots + P_{n_{\text{coll}}}. \end{aligned} \quad (4.22)$$

Non-linear terms in the latter expression can be safely neglected given that, even at resonance, the oscillation probability is at the most

$$P_{\text{max}} \sim (\bar{t}_f / \tau_{nn'})^2 = (0.032/1)^2 = 1.37 \times 10^{-5},$$

if assuming an oscillation time $\tau_{nn'} = 1$ s and $\bar{t}_f = 32$ ms (see Fig. 3.12).

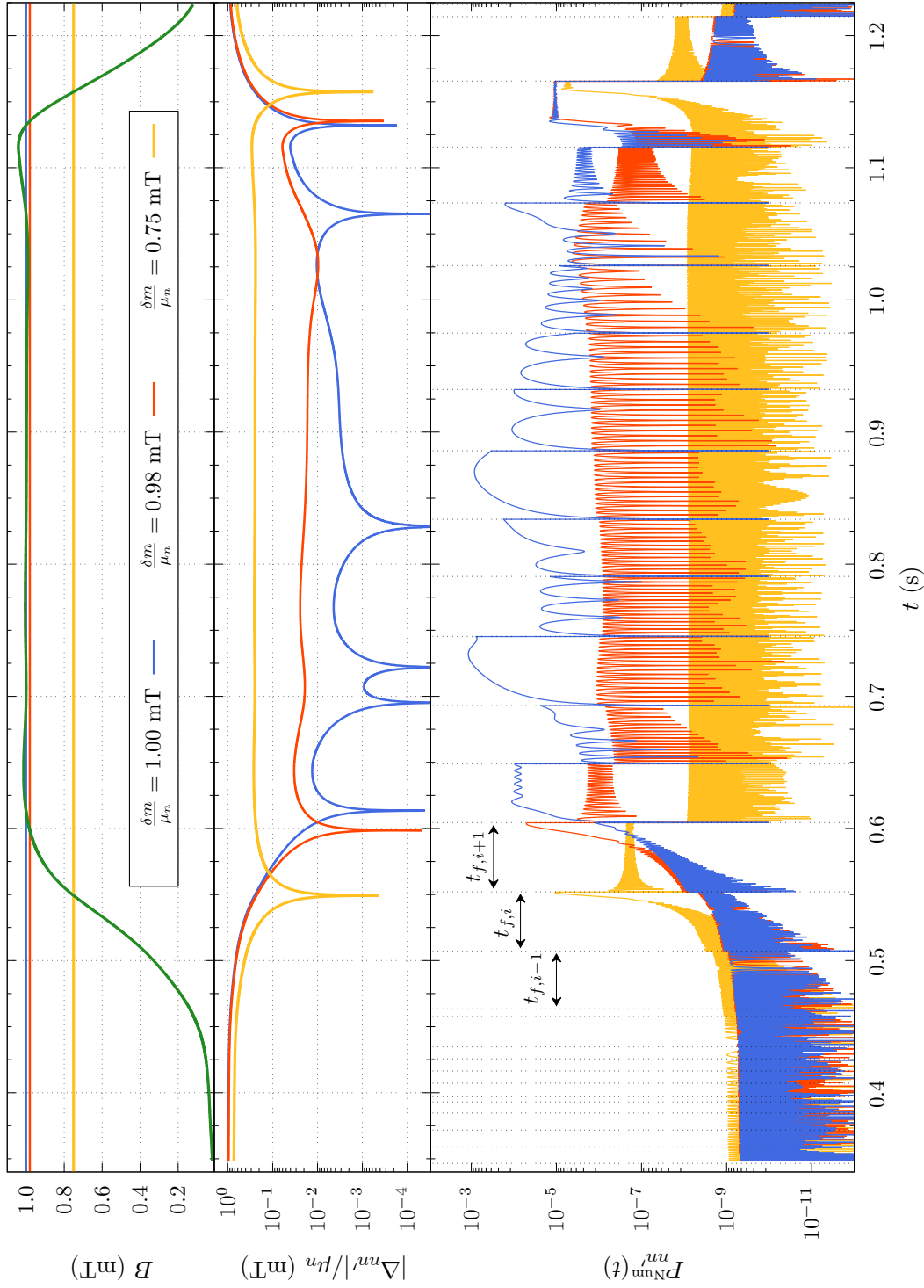


Figure 4.17: (bottom) Time evolution of the oscillation probability (numerical estimation) in an ordinary simulated UCN trajectory for three probing δm values and $\tau_{nn'} = 1$ s. The vertical dashed lines indicate the collision times when the hidden component of the wave function is reset to neutron state $\psi_{n'} = 0$. The top and center plots represent the experienced B -field and the energy degeneracy factor $\Delta_{nn'} = \mu_n B - \delta m$, respectively.

Eq. (4.22) represents the bifurcating point for the analytical and numerical approaches. In the former, the i -th step probability is obtained by evaluating the expression in Eq. (1.10) at the free-flight-time $t_{f,i}$ and characteristic field B_i as

$$P_i^{\text{Anal}} = \frac{4\epsilon_{nn'}^2}{4\epsilon_{nn'}^2 + (\mu_n B_i - \delta m)^2} \sin^2 \left(\frac{1}{2} \sqrt{(\mu_n B_i - \delta m)^2 + 4\epsilon_{nn'}^2} t_{f,i} \right), \quad (4.23)$$

where the free-flight-times are extracted from STARucn tracks, and B_i can be replaced by the average B -field over the step segment or simply be considered as the mean solenoid field \overline{B} . In the latter approach, the numerical solution provides a more realistic description of the $n - n'$ oscillations as it takes into account the magnetic field variations. The probability from this approach is logged at the wall collisions of UCN MC tracks as

$$P_i^{\text{Num}} = |\psi_{n'}(t_i^{\text{coll}})|^2,$$

where the hidden neutron state $\psi_{n'}$ is determined by

$$i \frac{d}{dt} \begin{pmatrix} \psi_n(t) \\ \psi_{n'}(t) \end{pmatrix} = \begin{pmatrix} \mu_n B(z(t)) & 1/\tau_{nn'} \\ 1/\tau_{nn'} & \delta m \end{pmatrix} \begin{pmatrix} \psi_n(t) \\ \psi_{n'}(t) \end{pmatrix}, \quad (4.24)$$

with $B(z(t))$ the solenoid magnetic field evaluated at the UCN horizontal position $z(t)$. A complete description of the numerical technique is resumed in Appendix E.

Every evaluation of $P_{nn'}$ implies fixing both model parameters $\tau_{nn'}$ and δm . Fortunately, the average oscillation probability per UCN computed over several trajectories is proportional to $1/\tau_{nn'}^2$. This is advantageous from a computational point of view since definition of the average $\langle P_{nn'}(\tau_{nn'}, \delta m) \rangle$ only requires scanning δm for a single $\tau_{nn'}$, e.g. 1 s. The resulting $P_{nn'}$ shape can be thus extrapolated to any $\tau_{nn'}$ by making

$$\langle P_{nn'}(\tau_{nn'}, \delta m) \rangle = \left(\frac{1 \text{ s}}{\tau_{nn'}} \right)^2 \langle P_{nn'}(1 \text{ s}, \delta m) \rangle. \quad (4.25)$$

Although each UCN trajectory determines a unique $n - n'$ oscillation pattern, looking at the time evolution of $P_{nn'}^{\text{Num}}$ for a sample trajectory allows verifying the wave function behavior as UCN travel across the solenoid. This is shown in Figure 4.17 next to the magnetic field profile experienced by the UCN and the energy degeneracy factor $\Delta_{nn'}$ (see Eq. (1.11)). The oscillation probability and $\Delta_{nn'}$ are displayed for three probing δm values, which are conventionally chosen at the resonance (blue), 10 μT off the resonance (red), and 250 μT far from the resonance (yellow). Several remarks can be made out of this $n - n'$ tracking sample:

- If $\delta m/\mu_n$ is lower than the B -field plateau ($B_{\text{plat.}}$), the exact energy degeneracy lifting $\Delta_{nn'} = 0$ is achieved twice, at the solenoid entrance and exit (red and yellow lines). If $\delta m/\mu_n \approx B_{\text{plat.}}$, the lifting happens several times inside the solenoid caused by the field inhomogeneities (blue line).
- Independently of δm , $P_{nn'}^{\text{Num}}$ monotonically increases when $\delta m/\mu_n$ approaches the magnetic field B , i.e. $\Delta_{nn'} \rightarrow 0$. This growth, which approximately follows $(t/\tau_{nn'})^2$, reaches a maximum shortly after $\Delta_{nn'} = 0$.

- When $\Delta_{nn'}$ stays constant during the entire step, i.e. uniform B -field, $P_{nn'}^{\text{Num}}$ oscillates according to Eq. (4.23), which can be written as

$$P_{nn'}(t) = \frac{4\epsilon_{nn'}^2}{4\epsilon_{nn'}^2 + \Delta_{nn'}^2} \sin^2 \left(\frac{1}{2} \sqrt{\Delta_{nn'}^2 + 4\epsilon_{nn'}^2} t \right) \quad (4.26)$$

(This can be checked, for example, at $t \sim 0.9$ s, where the oscillation amplitude is proportional to $1/\Delta_{nn'}^2$ and the frequency to $\Delta_{nn'}$.)

- Even after collisions, $P_{nn'}^{\text{Num}}$ quickly recovers its previous amplitude if $\Delta_{nn'}$ remains unchanged. This generally happens while traversing the B -field plateau.
- At the end of the sample trajectory, the total oscillation probability, computed from Eq. (4.22) gives

$$P_{nn'}^{\text{Num}} = \begin{cases} 1.7 \times 10^{-3}, & \text{for } \delta m/\mu_n = 1.00 \text{ mT} \\ 6.8 \times 10^{-5}, & \text{for } \delta m/\mu_n = 0.98 \text{ mT} \\ 1.5 \times 10^{-5}, & \text{for } \delta m/\mu_n = 0.75 \text{ mT.} \end{cases}$$

Whereas the total oscillation probability $P_{nn'}^{\text{Num}}$, for a resonant δm , is mostly built at the B plateau, for off-resonance mass splittings it is mainly due to the two $\Delta_{nn'} = 0$ crossing points at the entrance and exit of the solenoid volume.

The former analysis, based on a single $n - n'$ tracking trajectory, can be extrapolated to all of them. Small variations appear when UCN undergo diffusive scattering that reverse the traveling path towards the beam port. In those cases ($< 1\%$), UCN cross several times the solenoid volume, thus making the total trajectory time and total oscillation probability slightly larger. In order to illustrate the mean behavior of $n - n'$ oscillations, the cumulative oscillation probability (abscissa) is plotted against time (ordinate) for 30 UCN trajectories in Figure 4.18. The distribution of points, which are vertically projected into the upper histograms, represents the total oscillation probability obtained at the end of 10^3 trajectories. Given that these $n - n'$ tracks are evaluated for the same δm probing parameters as before, this result contains the sample trajectory studied in Figure 4.17.

In particular, Figure 4.18 points two major features. First, the time required by UCN to reach the detector's entrance window describes a wide distribution, ranging from 0.5 s to 2 s. This, however, includes the idle time spent while traveling from the EDM port to the solenoid magnetic field volume, where no-oscillations are expected [11]. Second, independently of δm , distributions of the oscillation probability at the end of the trajectories present a large spreading: Mean/StdDev ~ 2 . In posterior $n - n'$ oscillations analyses, we assume $P_{nn'}$ equal to the mean value of such distributions.

To construct the mean oscillation probability per UCN, the numerical method has to be run $N_{\text{UCN}} \times N_B \times N_{\delta m}$ times, with N_{UCN} the number of trajectories, N_B the number of applied magnetic fields and $N_{\delta m}$ the number of probing δm parameters. Whereas N_B in this experiment is 1053 (for all A, B and C values combined) and $N_{\delta m}$ is conventionally chosen to have a good resolution near the resonance, the definition of N_{UCN} has to deal with a compromise between the computational time per UCN track and the error on the mean $\langle P_{nn'}^{\text{Num}} \rangle$ associated to its rate of convergence. By simulating 5×10^4 $n - n'$ tracks at a resonant δm parameter, we found that $\langle P_{nn'}^{\text{Num}} \rangle$ deviates about $\sim 4\%$ ($\sim 2\%$) with respect to the 5×10^4

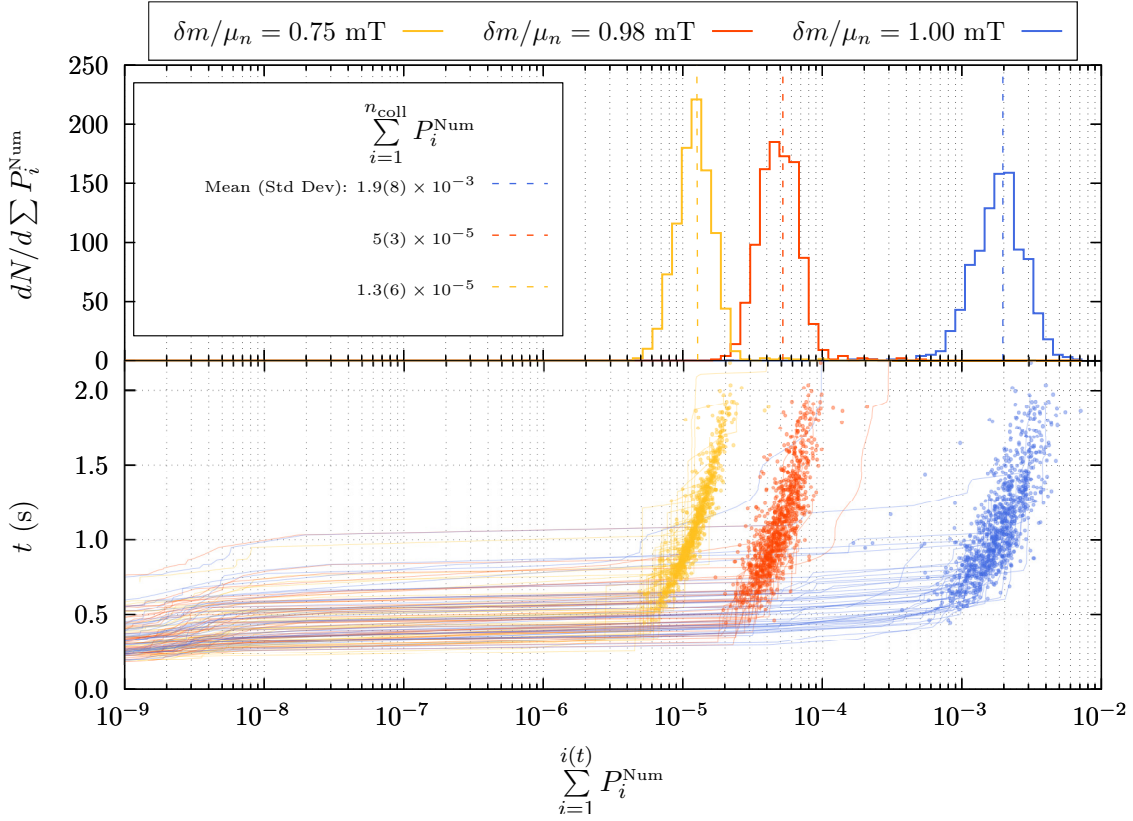


Figure 4.18: Lines: Cumulative oscillation probability as a function of the time for 30 sample $n - n'$ tracks. Dots: Total time and oscillation probability at the end of 10^3 tracks. Histograms: Projection of dots on the horizontal axis. All the tracks are constructed considering a solenoid with $\bar{B} \sim 1$ mT and evaluated for three probing δm parameters.

estimation if averaging over 10^2 (10^3) tracks. Therefore, according to the robustness analysis in section 4.4.4, we set $N_{\text{UCN}} = 10^2$ and keep conservative 5% error bars on $\langle P_{nn'}^{\text{Num}} \rangle$.

Figure 4.19 shows the mean oscillation probability per UCN obtained from the process described above, explicitly computed as

$$\langle P_{nn'}^{\text{Num}}(t_i^{\text{coll}}) \rangle = \frac{1}{N_{\text{UCN}}} \sum_{i=1}^{N_{\text{UCN}}} \sum_{j=1}^{n_{\text{coll},i}} |\psi_{n'}(t_{i,j}^{\text{coll}}; B, \delta m, \tau_{nn'})|^2, \quad (4.27)$$

and compares it to the probabilities derived from the analytical approach, all built for a solenoid field of $1000 \mu\text{T}$. In particular, the analytical solution is plotted for two scenarios. In yellow, the oscillation probability per UCN collision determined by Eq. (4.23) is evaluated at the mean free-flight-time and multiplied by the mean number of collisions:

$$\bar{n}_{\text{coll}} P_{nn'}^{\text{Anal}}(\bar{t}_f) = \bar{n}_{\text{coll}} P_{nn'}^{\text{Anal}}(\bar{t}_f; 1000 \mu\text{T}, \delta m, \tau_{nn'}) \quad (4.28)$$

with

$$\bar{n}_{\text{coll}} = \frac{1}{N_{\text{UCN}}} \sum_{i=1}^{N_{\text{UCN}}} \frac{1}{n_{\text{coll},i}} \sum_{j=1}^{n_{\text{coll},i}} 1 \quad (4.29)$$

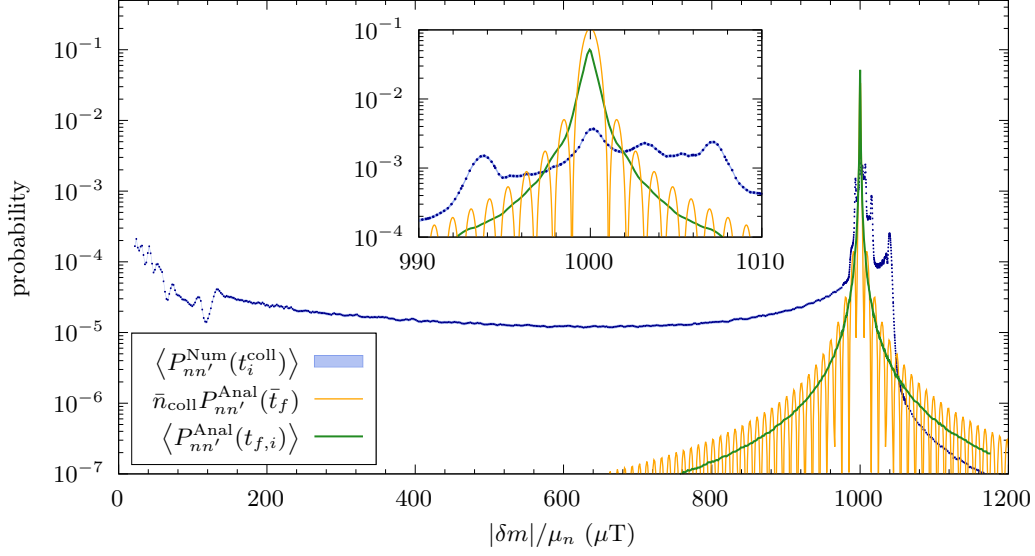


Figure 4.19: Mean oscillation probability as a function of δm for a solenoid field with $\bar{B} \sim 1$ mT. The average values are computed over 10^2 UCN trajectories for both the numerical and analytical approaches. The former is characterized with a wider spreading, which is caused by the B -field gradient experienced by UCN. The color band in the numerical solution represents the 5% convergence error discussed in the text.

and

$$\bar{t}_f = \frac{1}{N_{\text{UCN}}} \sum_{i=1}^{N_{\text{UCN}}} \frac{1}{n_{\text{coll},i}} \sum_{j=1}^{n_{\text{coll},i}} t_{f,i}. \quad (4.30)$$

In green, we compute its average value over the multiple UCN tracks

$$\langle P_{nn'}^{\text{Anal}}(t_{f,i}) \rangle = \frac{1}{N_{\text{UCN}}} \sum_{i=1}^{N_{\text{UCN}}} \sum_{j=1}^{n_{\text{coll},i}} P_{nn'}^{\text{Anal}}(t_{f,i}; 1000 \mu\text{T}, \delta m, \tau_{nn'}), \quad (4.31)$$

where each trajectory step contributes with the oscillation probability associated to the step free-flight-time $t_{f,i}$. This last calculation is included to demonstrate how the wiggling pattern of the analytical solutions is washed out after averaging over the tracks with different t_f and n_{coll} . Among the several differences observed between the curves, we note that the numerical solution does not show a symmetric shape. This is due to the fact that the magnetic field experienced by UCN along their paths is not symmetric about $1000 \mu\text{T}$ (see frequency histograms in Figure 3.17). This effect is also responsible for the maximum probability decrease and widening of the FWHM. Since UCN in the numerical solution spend less time at the solenoid field plateau, the oscillation probability at this value is reduced. In compensation, a higher $P_{nn'}$ is built around $1000 \mu\text{T}$ thus provoking the widening of the resonance. One would then expect a reduced experimental sensitivity at the central cycle values A, B and C , but an improved sensitivity for δm in between them.

Although not displayed here, we computed the 1053 $\langle P_{nn'}^{\text{Num}}(\delta m) \rangle$ curves, one for each B value, with $N_{\delta m} = 300$ out of which 200 points were centered around the resonance $\delta m \approx \bar{B}$. These are then used to estimate the expected ABBC ratio as

$$\begin{aligned} R_{ABC}^{\text{theo}}(\delta m, \tau) &= \frac{N_0(1 - \langle P_{nn'}^{\text{Num}}(B, \delta m, \tau) \rangle) + N_0(1 - \langle P_{nn'}^{\text{Num}}(B, \delta m, \tau) \rangle)}{N_0(1 - \langle P_{nn'}^{\text{Num}}(A, \delta m, \tau) \rangle) + N_0(1 - \langle P_{nn'}^{\text{Num}}(C, \delta m, \tau) \rangle)}, \\ &= \frac{2(1 - \langle P_{nn'}^{\text{Num}}(B, \delta m, \tau) \rangle)}{2 - \langle P_{nn'}^{\text{Num}}(A, \delta m, \tau) \rangle - \langle P_{nn'}^{\text{Num}}(C, \delta m, \tau) \rangle}, \end{aligned} \quad (4.32)$$

where N_0 represents the integrated UCN flux in case of no-oscillations (see Eq. (3.4)). In next sections, we use this last expression to find the level of agreement between the measured R_{ABC}^{exp} and the numerical solution as a function of δm and $\tau_{nn'}$.

4.4.2 Looking for resonances

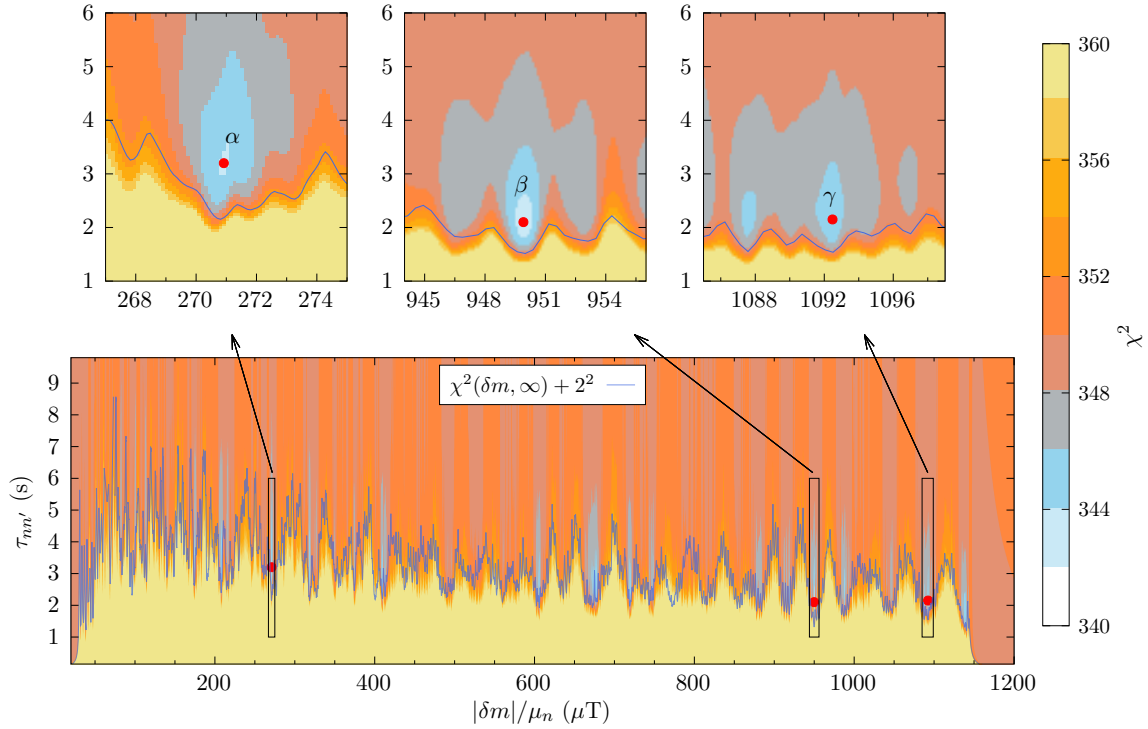


Figure 4.20: χ^2 (Eq. (4.33)) evaluated within the parameter space. The color box range is adjusted to stress the contrast of local minima near the null hypothesis $\chi_{\text{null}}^2/\text{NDF} = 348.5/349$. Zoomed regions in the top side enclose the three lowest values α, β and γ detailed in Table 4.3.

The most simplistic method to establish whether $n - n'$ resonances can be evidenced from the measured R_{ABC}^{exp} points is through the calculation of

$$\chi^2(\delta m, \tau_{nn'}) = \sum_i^{N_{\text{cycles}}} \left(\frac{R_{ABC, i}^{\text{exp}} - R_{ABC}^{\text{theo}}(\delta m, \tau_{nn'})}{\Delta R_{ABC, i}} \right)^2, \quad (4.33)$$

Table 4.3: Lowest χ^2 per degree of freedom within the $(\delta m, \tau_{nn'})$ parameter space of Figure 4.20. The shape of the predicted signals for each minimum is displayed in Figure 4.21.

Local minimum	$ \widehat{\delta m} /\mu_n$ (μT)	$\widehat{\tau}_{nn'}$ (s)	χ^2/NDF
α	271.1	3.2	343.9/348
β	949.9	2.1	343.2/348
γ	1092.5	2.2	344.1/348

where i runs over all the cycle steps in the magnetic field scan (see discussion in section 3.3).

One could initially propose minimizing χ^2 within the parameter space $(\delta m, \tau_{nn'})$, but given that the null-hypothesis already matches the R_{ABC}^{exp} points (see Figure 4.16), any minimizing pair $\widehat{\delta m}, \widehat{\tau}_{nn'}$ difficulty fulfills

$$\frac{\chi_{\widehat{\delta m}, \widehat{\tau}_{nn'}}^2}{\text{NDF}} \ll \frac{\chi_{\text{null}}^2}{\text{NDF}}.$$

In other words, the large compatibility between the null-hypothesis and data can lead to several χ^2 local minima in the parameter space with

$$\frac{\chi_{\widehat{\delta m}, \widehat{\tau}_{nn'}}^2}{\text{NDF}} \sim \frac{\chi_{\text{null}}^2}{\text{NDF}}.$$

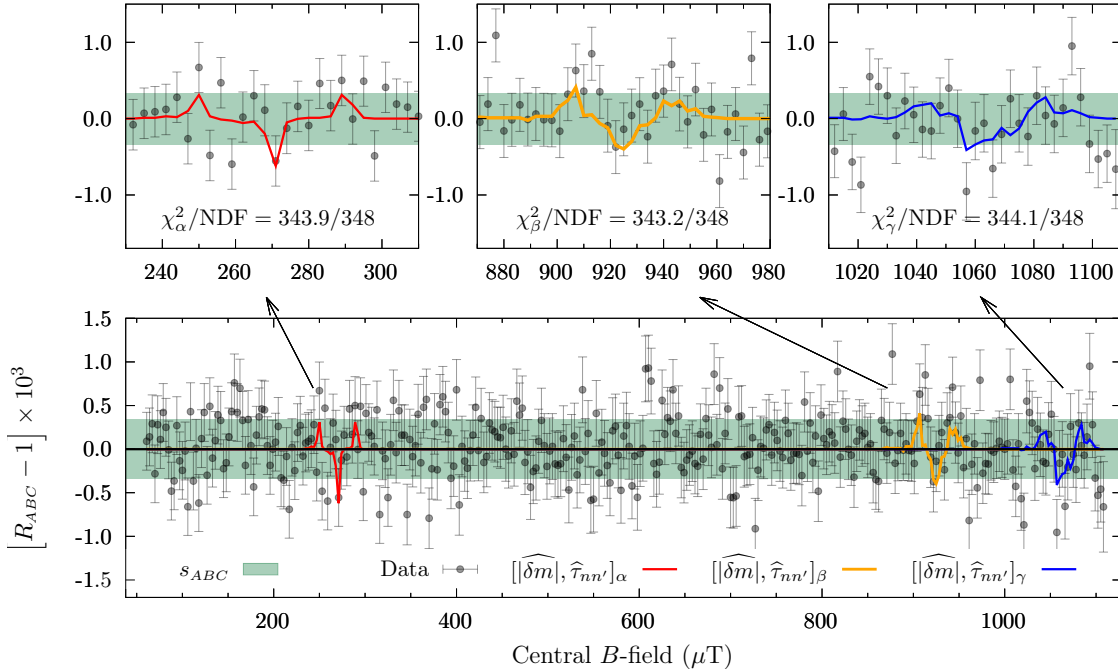


Figure 4.21: R_{ABC} theoretical prediction for the three parameters combination α, β and γ giving the lowest χ^2 in the map of Figure 4.20. The signals raised in all cases are contained within the null-hypothesis fluctuations band s_{ABC} .

This phenomenon is displayed in the bottom side of Figure 4.20, where χ^2 has been computed using the numerical approach to $P_{nn'}$, for $\delta m \in [20 - 1200] \mu\text{T} \cdot \mu_n$ and $\tau_{nn'} \in [0 - 10] \text{s}$. The exhaustive evaluation of χ^2 , which includes $N_{\delta m} \times N_{\tau_{nn'}} = 10^4 \times 10^2$ parameter combinations, reveals multiple local minima with $343 < \chi^2 < 350$, all located above $\tau_{nn'} = 1.5 \text{s}$. Clearly, they cannot be regarded as potential signals, but instead they suggest that the data set does not witness any $n - n'$ signal. To see this, we focus on the parameter space regions near the three lowest points of χ^2 , labeled as α, β and γ (top side of Figure 4.20). The coordinates of such points and their associated χ^2 are reported in Table 4.3. We corroborate that in the three cases, the χ^2 per degree of freedom is comparable to the null hypothesis $\chi^2_{\text{null}}/\text{NDF} = 348.5/349$. In addition, as illustrated in Figure 4.21, when plotting $R_{ABC}^{\text{theo}}(\widehat{\delta m}, \widehat{\tau}_{nn'})$ as a function of the cycle central B -field for the minimizing parameters (α, β and γ), the hypothetical signals in the three cases are contained within the fluctuations band s_{ABC} (green horizontal band). Hence, since none of these minimizing parameter pairs gives place to a potential signal beyond $1.2s_{ABC}$, we attribute all the local minima observed within the parameter space for this experiment to background fluctuations, i.e, they are explained by the look else where effect.

The reader might remark that the theoretical predictions of R_{ABC} , illustrated in Figure 4.21, present the expected symmetric triple-footprint shape at low magnetic fields, but it is progressively deformed as the field increases (see ideal case in Figure 3.7). This change in form is caused by the magnetic field inhomogeneities, which are amplified when setting a large B -field. Such feature is only taken into account within the numerical solution $\langle P_{nn'}^{\text{Num}} \rangle$ and is responsible for the parameter exclusion boundary shaping.

4.4.3 Parameter exclusion

Although the acquired data does not contain a significant signal, we can set a new boundary to the $n - n'$ model parameters. As explained in section 3.3, such bounding values are constructed through the calculation of the $\chi^2(\delta m, \infty) + 2^2$ contour line (Eq. (3.6)) that defines the 95% C.L. exclusion region. This limit, which is displayed on top of the χ^2 map in Figure 4.20, shows various peaks and valleys going from $\tau_{nn'} = 1 \text{s}$ to $\tau_{nn'} \sim 8 \text{s}$. By recalling the preliminary sensitivity analysis of Figure 3.9, we link this wavy pattern to the exclusion maxima and minima achieved at the resonances $\delta m/\mu_n = B_i$ and at the intermediate magnetic fields skipped between cycles, respectively. One can see that fixing a single $\tau_{nn'}$ limit for the entire scanned interval in this experiment becomes a cumbersome task if one wants to profit the maximum exclusion at each δm . Nevertheless, in order to present the result in a simplified way, the limiting $\tau_{nn'}$ is chosen as the lowest valley of the 95% contour line:

$$\tau_{nn'} > 1 \text{s for } |\delta m| \in [30 - 1143] \mu\text{T} \cdot \mu_n \text{ (95\% C.L.)}, \quad (4.34)$$

or equivalently, in energy units

$$\tau_{nn'} > 1 \text{s for } |\delta m| \in [2 - 69] \times 10^{-12} \text{eV (95\% C.L.)}. \quad (4.35)$$

The result above has been derived from the boundary contour computed by means of the numerical solution of the $n - n'$ oscillation probability $P_{nn'}^{\text{Num}}$. It is then natural to wonder what the conclusion would have been if we had considered the more simplistic approach, which assumes a uniform magnetic field and uses the analytical solution $P_{nn'}^{\text{Anal}}$. This question is firstly

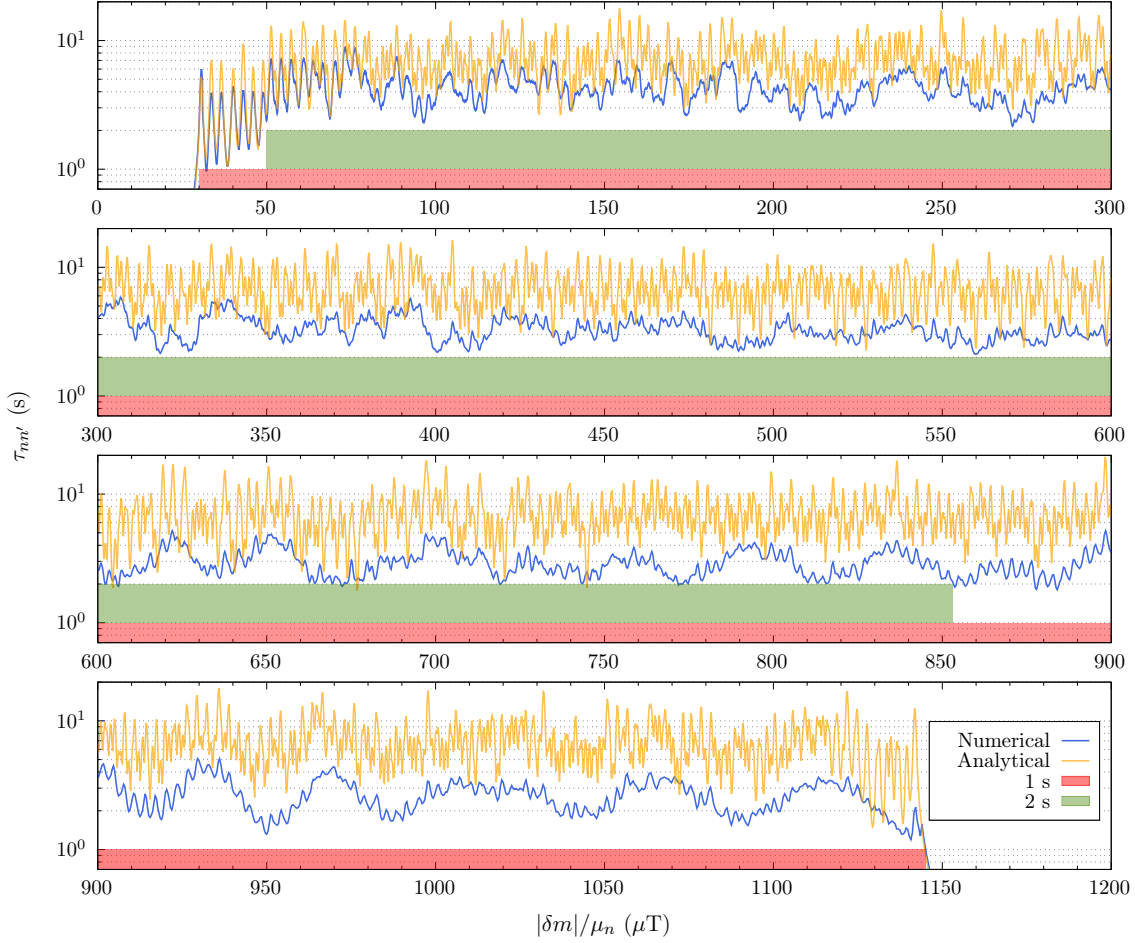


Figure 4.22: Numerical and analytical contour lines corresponding to the 95% C.L. exclusion boundaries. ‘1 s’ and ‘2 s’ regions (colored) show the ranges for which the limits hold.

examined by comparing the exclusion boundaries raised from both approaches (see Figure 4.22). The depicted contours, which extend all along the parameter space, allow highlighting two main differences. First, the separation between maxima and minima are less pronounced for the numerical result in the entire δm range. Second, there is a slight decrease on the numerical exclusion as δm increases. Both of these behaviors are induced by the magnetic field inhomogeneities affecting the calculation of $P_{nn'}^{\text{Num}}$. Given that these inhomogeneities are more significant when setting a large solenoid field,

$$\left. \frac{\delta B}{\overline{B}} \right|_{\text{large } B} > \left. \frac{\delta B}{\overline{B}} \right|_{\text{small } B}, \quad (4.36)$$

it is reasonable to obtain a lower and wider oscillation resonance curve (Figure 4.19) at large values of δm . In consequence, the contour line, which reproduces the shapes of the multiple resonances, features lower and wider exclusion peaks as δm increases. That being

Table 4.4: Parameters exclusion intervals at 95% C.L. for $n - n'$ oscillations assuming $\delta m \neq 0$. The two intervals are given in magnetic field and energy units.

$\tau_{nn'}$	$ \delta m $	
	$(\mu\text{T} \cdot \mu_n)$	$(\times 10^{-12} \text{ eV})$
$> 1 \text{ s}$	30 – 1143	2 – 69
$> 2 \text{ s}$	50 – 852	3 – 51

said, the lowest common limit of $\tau_{nn'}$ for the entire scanned interval is almost the same in both scenarios. Besides the few analytical contour valleys going below the numerical line, the exclusion regions are defined using the conservative ‘1 s’ and ‘2 s’ bands in Figure 4.22. The exclusion ranges for both time limits are resumed in Table 4.4.

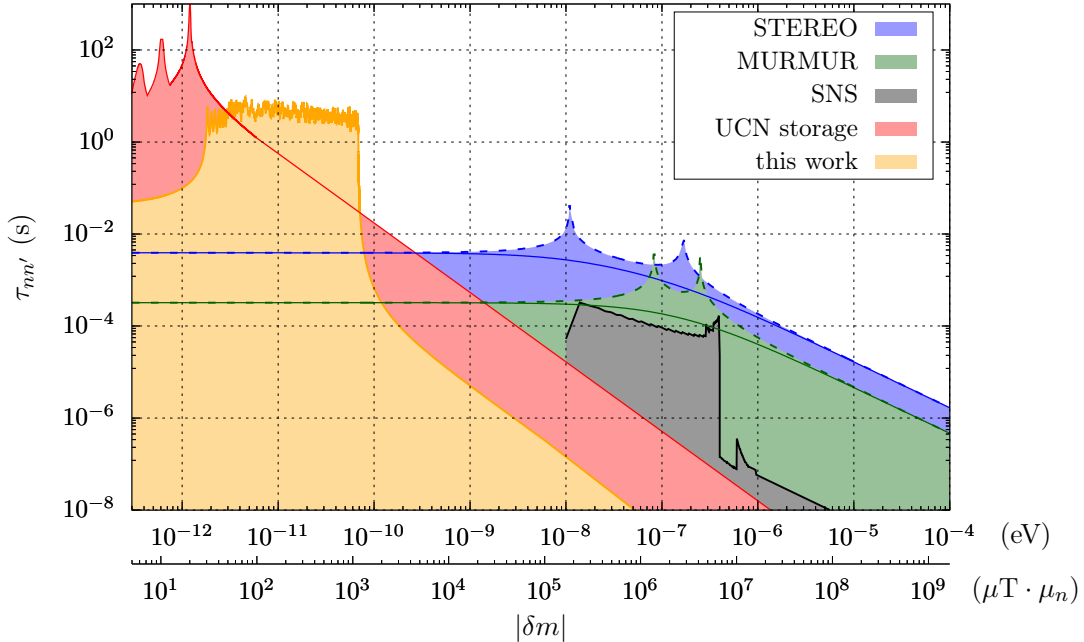


Figure 4.23: Exclusion of the $n - n'$ parameter space including all experimental results up to August 2022.

Because of its more realistic description, the exclusion boundary derived from the numerical approach is used to contrast the contribution of this work to the general view of $n - n'$ oscillations alongside with past measurements (see section 1.4). Using a color selection compatible with the last published comparison [14], the updated parameter space is presented in Figure 4.23. The exclusion region emerging from this work becomes thus the first measurement probing $n - n'$ oscillations with mass splittings values located between UCN storage and passing-through-wall experiments. Even if our sensitivity is about one order of magnitude shorter than that of UCN storage measurements, the experimental technique introduced with this work allows efficiently scanning a wide range of δm values. While the most sensitive UCN storage experiment [11] dedicated 40 days to test $n - n'$ oscillations at two magnetic field magnitudes, we achieved scanning more than one thousand fields with an experimental

campaign lasting 25 days. The sensitivity of this new result is not negligible if taking into account that the most sensitive measurement in passing-through-wall experiments lays below $\tau_{nn'} = 10$ ms. One fact to keep in mind if visualizing a future UCN beam experiment to scan larger δm is that the resonance width ($\sim 1 \mu\text{T} \cdot \mu_n$) and the scanning step are not expected to change drastically. Therefore, in order to contribute with a considerable exclusion region at $\delta m > 10^3 \mu\text{T} \cdot \mu_n$, the experiment has to improve the counting statistics to maintain the same $\tau_{nn'} \sim 1$ s sensitivity.

4.4.4 Robustness of the results

In the previous section, we presented the exclusion boundary variations introduced by the numerical and analytical solutions of $P_{nn'}$. However, given that the former includes a more realistic estimation of the magnetic field inhomogeneities we opted for the numerical solution to report our final result. Even if both approaches led to similar conclusions on the large scale ('1 s' and '2 s' bands in Figure 4.22), the numerical method was preferred as it gives a more detailed description of $n - n'$ oscillations near the resonances. Independently of the chosen theoretical approach, there is an extra source of uncertainties affecting the final exclusion region in this work: the simulated UCN trajectories. In section 3.4.1, it was demonstrated that STARucn input parameters were calibrated to reproduce the time-of-flight measurement. Although the calibration of parameters resulted from a χ^2 optimization process, the yield spectrum might suffer from overfitting given the large number of inaccessible STARucn input parameters (Table 3.1). In order to study the systematic uncertainties added by these “flexible” parameters, several UCN trajectories sets were generated while varying the parameters that do not largely alter the time-of-flight calibration, i.e. the number of diffusive reflections (d) and the initial velocity distribution (v_0). In the following, we quantify the final sensitivity variations using a single cycle measurement.

Amount of diffusive reflections

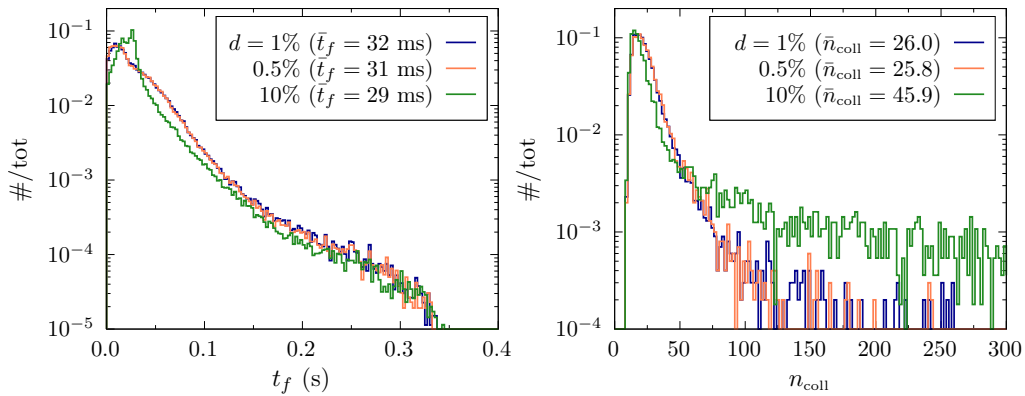


Figure 4.24: Time-of-flight (left) and number of collision within the solenoid magnetic field (right) distributions extracted from MC simulations of UCN trajectories. Three independent runs consider different values of the number of diffusive reflections d .

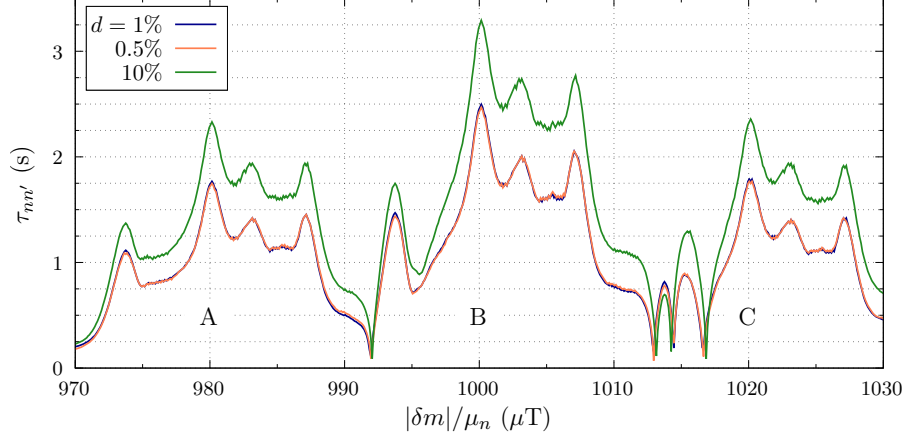


Figure 4.25: 95% C.L. boundaries obtained from the single cycle measurement ($B = 1000 \mu\text{T}$) assuming different numbers of the diffusive reflections d . The boundaries correspond to the MC event distributions depicted in Figure 4.24.

Experimental setups with $d < 1\%$, i.e. highly smooth and clean UCN guides, are technically difficult to achieve. On the contrary, it might happen that improper guide commissioning and mounting affect the UCN interactions against the guide inner walls, allowing numerous diffusive reflections $d \sim 5\%$. Considering the UCN guide arrangement of this work, one would expect that $d > 1\%$ favors UCN trajectories where the direction of propagation is reversed. In such cases, neutrons spend longer times within the solenoid magnetic field and the average $n - n'$ oscillation probability increases. In the end, this augmentation of the oscillation probability converts into a larger theoretical signal that extends the 95% C.L. bounding of $\tau_{nn'}$ if no oscillations are observed. Under the same reasoning, for $d < 1\%$, UCN would mostly travel towards the detector without bouncing back through the guide. This continuous forward flowing makes the oscillation probability to be merely defined by the average free-flight-time \bar{t}_f of specular reflections and the average number of collision to cross the setup. The exclusion boundary in this case remains unchanged. To demonstrate these behaviors, independent STARucn simulations are run by making $d = 0.5\%, 1\%$ and 10% . The free-flight-time and number of collisions distributions obtained from each run are displayed in Figure 4.24. Note that whereas \bar{t}_f keeps almost the same for the three values of d , \bar{n}_{coll} drastically increases for $d = 10\%$. This, as mentioned above, echoes on the 95% C.L. exclusion boundaries, which for the sake of simplicity are computed and plotted for a single cycle measurement with central field $B = 1000 \mu\text{T}$ in Figure 4.25. One can then confirm that scenarios with high d give place to more sensitive discriminations of $\tau_{nn'}$. In the current example, going from $d \leq 1\%$ to $d = 10\%$ implies a gain on the sensitivity of 30%. Although the magnitude of d cannot be experimentally established, the key point of this brief analysis is that $d = 1\%$ corresponds to an optimistic assumption producing a conservative conclusion. Then, the uncertainty in the final exclusion region induced by d is negligible.

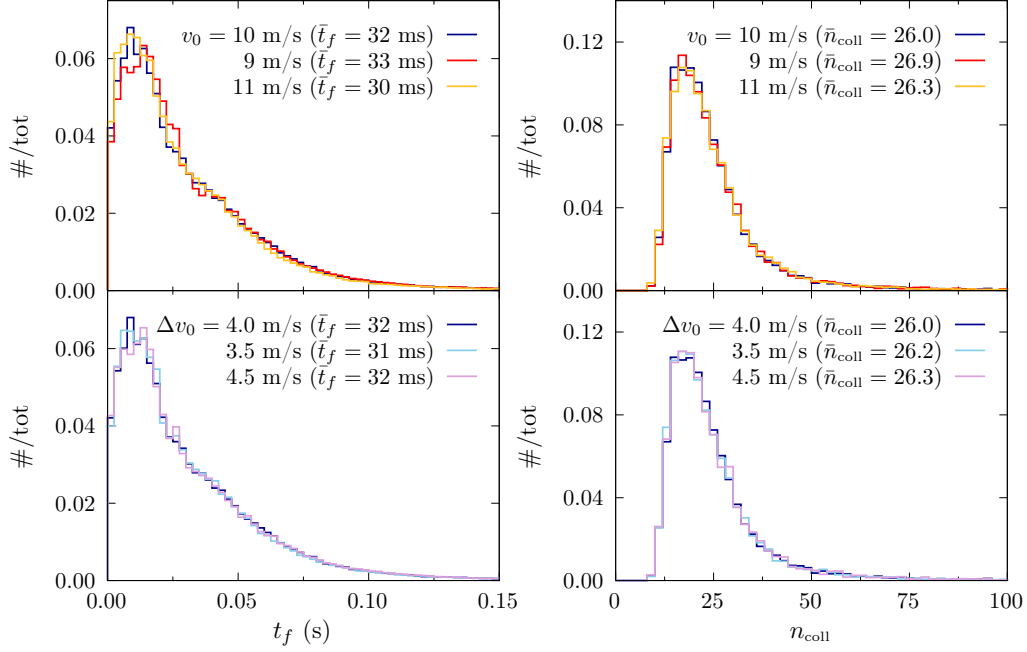


Figure 4.26: Time-of-flight (left) and number of collision within the solenoid magnetic field (right) distributions extracted from MC simulations of UCN trajectories. Independent runs consider different v_0 (top) and Δv_0 (bottom).

Initial velocity distribution

UCN initial velocities in previous sections were randomly chosen from a Gaussian distribution whose parameters (mean $v_0 = 10$ m/s and standard deviation $\Delta v_0 = 4$ m/s) were optimized to reproduce the TOF measurement presented in section 3.4.1. The UCN velocities measurement was obtained with a beam chopper device positioned at the end of the 0.5 m horizontal UCN guide at the level of the EDM beam port. However, since UCN spectrum deformations produced by the guide bents and the 6 m guide are not taken into account in the TOF optimization, the simulation validation might not be completely accurate. Therefore, in order to establish whether the conclusions reported in the previous section are sensitive to spectrum variations, independent STARucn simulations are run by making $v_0 = 9, 10, 11$ m/s and $\Delta v_0 = 3.5, 4, 4.5$ m/s. The time-of-flight and number of collisions distributions resulting from all these cases are shown in Figure 4.26. Opposite to the changes observed after varying the number of diffusive reflections d , variations in t_f and n_{coll} distributions after modifying v_0 (10%) and Δv_0 (12%) are almost imperceptible: \bar{t}_f and \bar{n}_{coll} change less than 6% and 3%, respectively. In addition, these small variations have a negligible impact on the exclusion boundaries. As shown in Figure 4.27 whereas the boundary is enlarged by a 5% if setting $v_0 = 9$ m/s, it remains unchanged for $v = 11$ m/s and for all the tested values of Δv_0 . One can explain the sensitivity augmentation by recalling that soft spectra ($v_0 < 10$ m/s) imply larger free-flight-times, which in turns increase the $n - n'$ oscillation probability. On the contrary, hard spectra ($v_0 > 10$ m/s) are more strongly shifted towards slow velocities since fast UCN easily escape the guides, then leading to similar sensitivities. Once again, it occurs

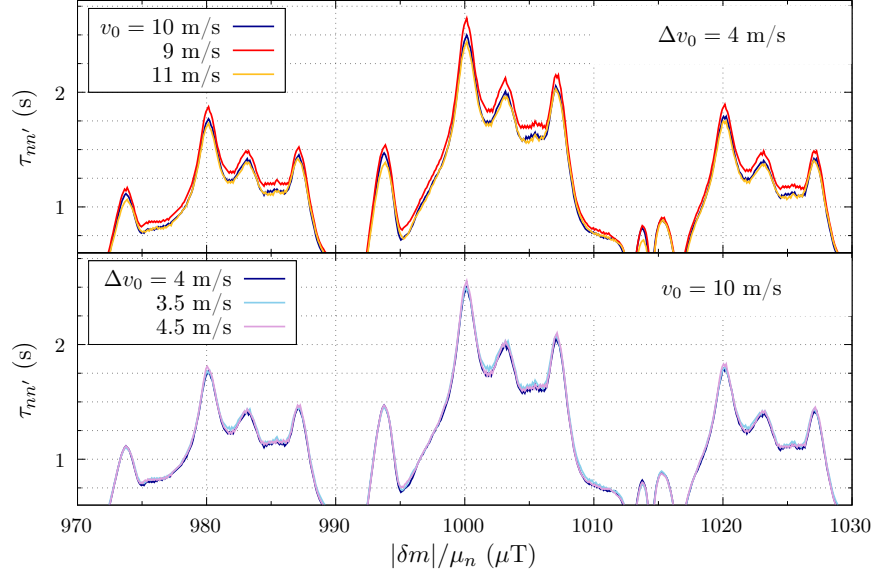


Figure 4.27: 95% C.L. boundaries for a single cycle measurements assuming different values of v_0 (top) and Δv_0 (bottom). The reported lines correspond to the events distributions depicted in Figure 4.26

that the velocity parameters used to extract the main result are the most consistent ones (they result from an optimization process) and also correspond to a conservative scenario. We can thus conclude that no major uncertainties on the results reported in this work, in particular the 95% C.L. limits, are due to the MC simulation of UCN trajectories.

4.5 Oscillations in presence of hidden magnetic fields ($\delta m = 0$)

In this section, $n - n'$ oscillations are studied while considering a hidden magnetic field present at the experimental site and a negligible mass splitting, i.e. $\Delta E' = \mu_n B' \gg \delta m$. In such scenario, the $n - n'$ Hamiltonian and the oscillation probability depend on the angle formed by the ordinary and hidden magnetic fields β . The analytical solution to this problem, presented in section 1.3.3, demonstrates that the oscillation probability $P_{nn'}^{\text{Anal}}(\tau_{nn'}, B')$ in the presence of hidden B' -fields is modulated by the factor $1 + \cos \beta$. Since information of β is not accessible, its influence on the collected data is estimated by separating runs with positive and negative B -field orientations (see Table 4.2). Note that while maximum mixing occurs at $\beta = 0^\circ$, it is practically zero for $\beta = 180^\circ$. For the following, we assume β to be constant during the data taking. This is consistent with the theoretical arguments presented in [17], where hidden magnetic fields as large as hundreds μT cannot be explained by the low density dark matter around the solar system, but rather to dark matter trapped by earth's gravity.

4.5.1 Numerical solution

Unlike past UCN storage experiments where the neutron counting at positive, negative and zero B -fields is used to compute the parameter exclusion in the spaces $(B', \tau_{nn'}/\sqrt{\cos \beta})$ and

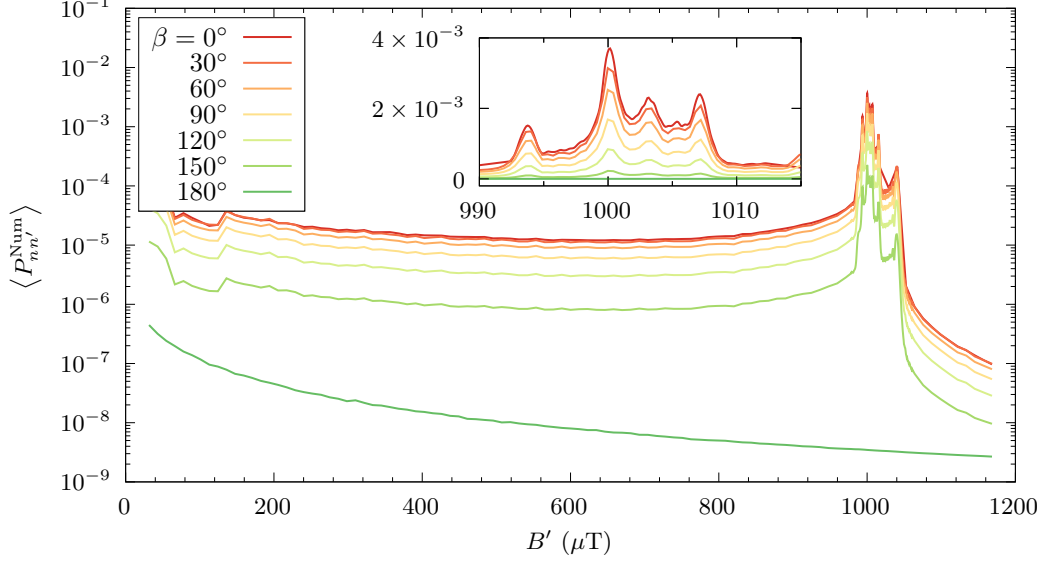


Figure 4.28: Mean oscillation probability for a single B -field as a function of the hidden magnetic field B' computed from the numerical solution of Eq. (4.37).

($B', \tau_{nn'}$) (asymmetry and ratio channels, respectively [17]), the construction of the observable R_{ABC} prevents defining an analytical expression such that β can be factorized or canceled. This does not represent a real issue given that we target instead a numeric approach where the magnetic field inhomogeneities are taken into account in the calculation of $P_{nn'}$. To do so, we introduce the Liouville-Neumann equation [102]

$$\frac{\partial}{\partial t} \hat{\rho} = -i[\hat{\mathcal{H}}, \hat{\rho}] = -i\hat{\mathcal{H}}\hat{\rho} + i\hat{\rho}\hat{\mathcal{H}}^\dagger, \quad (4.37)$$

where

$$\hat{\mathcal{H}}_{nn'} = \begin{pmatrix} \mu_n B & 0 & 1/\tau_{nn'} & 0 \\ 0 & -\mu_n B & 0 & 1/\tau_{nn'} \\ 1/\tau_{nn'} & 0 & \mu_n B' \cos \beta & \mu_n B' \sin \beta \\ 0 & 1/\tau_{nn'} & \mu_n B' \sin \beta & -\mu_n B' \cos \beta \end{pmatrix} \quad (4.38)$$

$$= \begin{pmatrix} 2\omega & 0 & 1/\tau_{nn'} & 0 \\ 0 & -2\omega & 0 & 1/\tau_{nn'} \\ 1/\tau_{nn'} & 0 & 2\omega' \cos \beta & 2\omega' \sin \beta \\ 0 & 1/\tau_{nn'} & 2\omega' \sin \beta & -2\omega' \cos \beta \end{pmatrix} \quad (4.39)$$

is the Hamiltonian in a medium in presence of ordinary B and hidden B' magnetic fields, and $\hat{\rho}$ is the 4×4 density matrix in the basis $(\psi_n^+, \psi_n^-, \psi_{n'}^+, \psi_{n'}^-)$ describing the quantum state composed of neutrons and hidden neutrons. Note that the diagonal terms of $\hat{\rho}$ represent the

probabilities of observing spin-up and spin-down neutrons and hidden neutrons according to

$$\begin{aligned} \text{spin-up neutron: } P_n^+ &= \rho_{11}, \\ \text{spin-down neutron: } P_n^- &= \rho_{22}, \\ \text{spin-up hidden neutron: } P_{n'}^+ &= \rho_{33}, \\ \text{spin-down hidden neutron: } P_{n'}^- &= \rho_{44}, \end{aligned}$$

while fulfilling $\text{Tr}(\hat{\rho}) = 1$. Following this notation, the system collapse into pure neutron state produced at wall collisions is manually included in the tracking simulation by making

$$\hat{\rho}_n = \begin{pmatrix} 0.5 & 0 & 0 & 0 \\ 0 & 0.5 & 0 & 0 \\ 0 & 0 & 0 & 0 \\ 0 & 0 & 0 & 0 \end{pmatrix}, \quad (4.40)$$

where equal probabilities are given to ψ_n^+ and ψ_n^- . In this way, the average $n - n'$ oscillation probability per neutron is computed from the third and fourth diagonal elements of $\hat{\rho}$ as

$$\langle P_{nn'}^{\text{Num}} \rangle = \frac{1}{N_{\text{UCN}}} \sum_{i=1}^{N_{\text{UCN}}} \sum_{j=1}^{N_{\text{coll}, i}} [\rho_{33} + \rho_{44}]_{t_{i,j}^{\text{coll}}}, \quad (4.41)$$

with $t_{i,j}^{\text{coll}}$ the j -th collision time of the i -th UCN trajectory.

Numerical implementation of Eq. (4.37) is a cumbersome task since it deals with 16 coupled complex equations. Computationally speaking, it takes almost two times longer than the numerical solution of $n - n'$ oscillations with $\delta m \neq 0$ presented in previous sections. The detailed explanation of the employed method is left to the Appendix E.

Before starting the data analysis within the hidden magnetic field scope, we show in Figure 4.28 the average oscillation probabilities derived from the Liouville-Neumann numerical solution for a single magnetic field. This sample plot depicts the resonance curves as a function of B' for different β between 0 and 180°. Even though the resonance shape remains almost unchanged, it is straightforwardly confirmed that $P_{nn'}$ decreases as $\beta \rightarrow 180^\circ$. This is true for all angles except $\beta = 180^\circ$, where no resonance peak is observed at any B' . These features are easily validated by the analytical solution (Eq. (1.16)) which gives

$$\begin{aligned} P_{nn'}(\beta = 0^\circ) &\xrightarrow{B' \rightarrow B} \frac{\sin^2[(\omega - \omega')t]}{\tau_{nn'}^2(\omega - \omega')^2}, \\ P_{nn'}(\beta = 90^\circ) &\xrightarrow{B' \rightarrow B} \frac{\sin^2[(\omega - \omega')t]}{2\tau_{nn'}^2(\omega - \omega')^2}, \\ P_{nn'}(\beta = 180^\circ) &= \frac{\sin^2[(\omega + \omega')t]}{\tau_{nn'}^2(\omega + \omega')^2}, \end{aligned}$$

thus explaining the factor 2 between the maximum probabilities at $\beta = 0^\circ$ and 90° , and the monotonic decreasing behavior at $\beta = 180^\circ$.

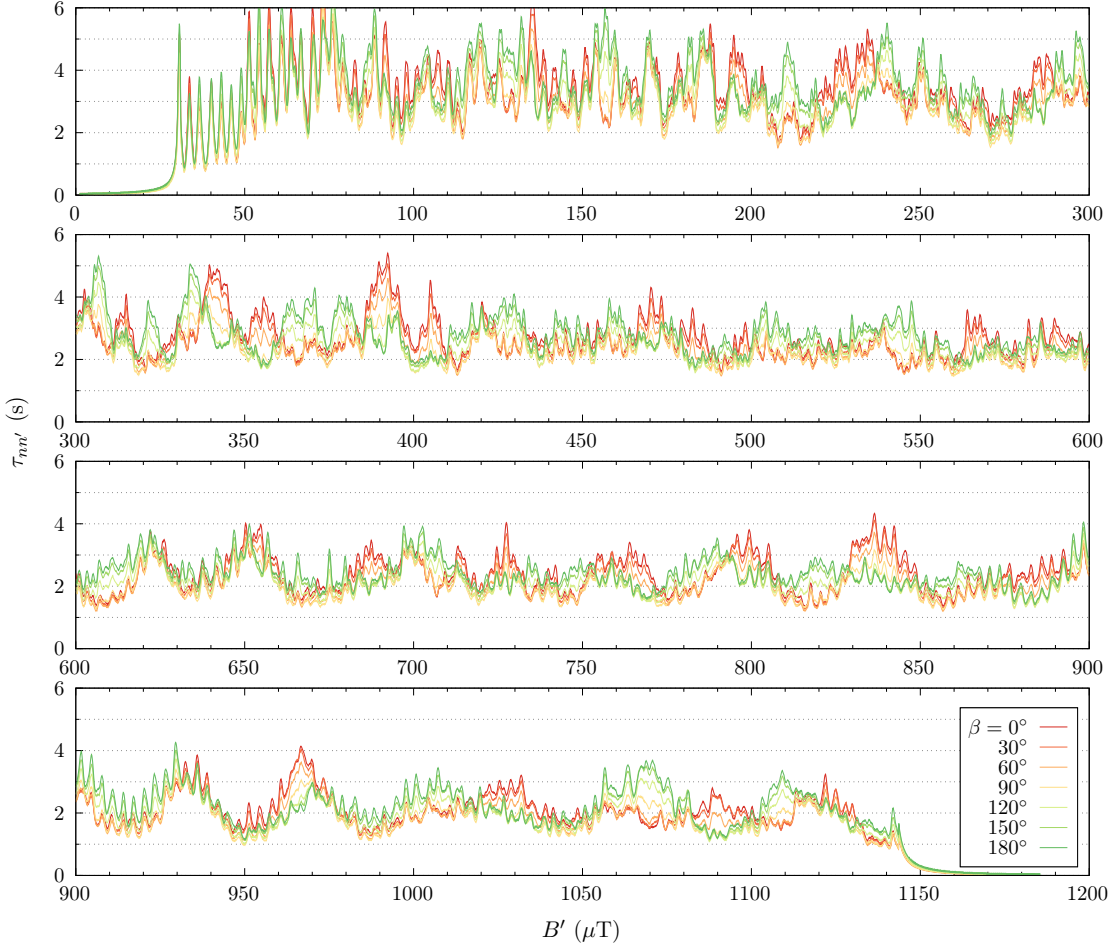


Figure 4.29: 95% exclusion boundaries computed as a function of B' for various values of β . The general picture allows stating that $\tau_{nn'} > 1$ s for $B' \in [50 - 1130]$ μT .

4.5.2 Parameter exclusion

All scanned magnetic fields in this work were measured with positive and negative orientations. This allows us to compute the average $R_{+ABC,i}$ and $R_{-ABC,i}$ with $i = 1, \dots, 350$, so to end up with a single data set composed of 700 points. One could fear that the angle β during data taking was close to 180° thus reducing the oscillation probability and the experimental sensitivity (see Figure 4.28). However, even if $+B$ measurements were recorded with a $\beta_+ = 180^\circ$, only those data points would be affected by a low sensitivity. The remaining R_{ABC} ratios, recorded with inverted $-B$ field, would profit the maximum sensitivity given that β is also reversed in this configuration: $\beta_- = 180^\circ - \beta_+ = 0^\circ$. Therefore, independently of the actual value of β , the complementary measurements at $+B$ and $-B$ lead to a non-negligible sensitive analysis if fitting all 700 points simultaneously.

Following a process similar to the one in section 4.4, we compute the 95% exclusion regions in the parameter space $(B', \tau_{nn'})$ by means of the χ^2 statistics. The main difference in this

case is found on the double summing factor that includes data and predictions at both B -field directions:

$$\chi^2_{\tau_{nn'}, B', \beta} = \sum_i^{350} \left[\left(\frac{R_{+ABC, i}^{\text{exp}} - R_{ABC}^{\text{theo}}(\tau_{nn'}, B', \beta)}{\Delta R_{+ABC, i}} \right)^2 + \left(\frac{R_{-ABC, i}^{\text{exp}} - R_{ABC}^{\text{theo}}(\tau_{nn'}, B', \pi - \beta)}{\Delta R_{-ABC, i}} \right)^2 \right]. \quad (4.42)$$

To work around the ignorance of β , we compute the average oscillation probability for all tested magnetic fields assuming $\beta = 0^\circ, 30^\circ, 60^\circ, 90^\circ, 120^\circ, 150^\circ$ and 180° . These probabilities are then feed into Eq. (4.42) to produce the 95% exclusion region of each case. The superposition of the different exclusion boundaries, depicted in Figure 4.29, allows demonstrating that, in the large picture, the values of B' where the exclusion is maximal at $\beta = 0^\circ$ correspond to the minimal exclusion at $\beta = 180^\circ$ and vice versa. Boundaries associated to intermediate angles are contained within these envelope curves all along the scanned interval. This behavior is expected given that, as explained above, whereas the $+B$ subset gains sensitivity at $\beta = 0^\circ$, the $-B$ subset reaches the minimal sensitivity at $\beta = 180^\circ$. In particular, if $\beta = 90^\circ$, equal sensitivities are attributed to both field directions subsets.

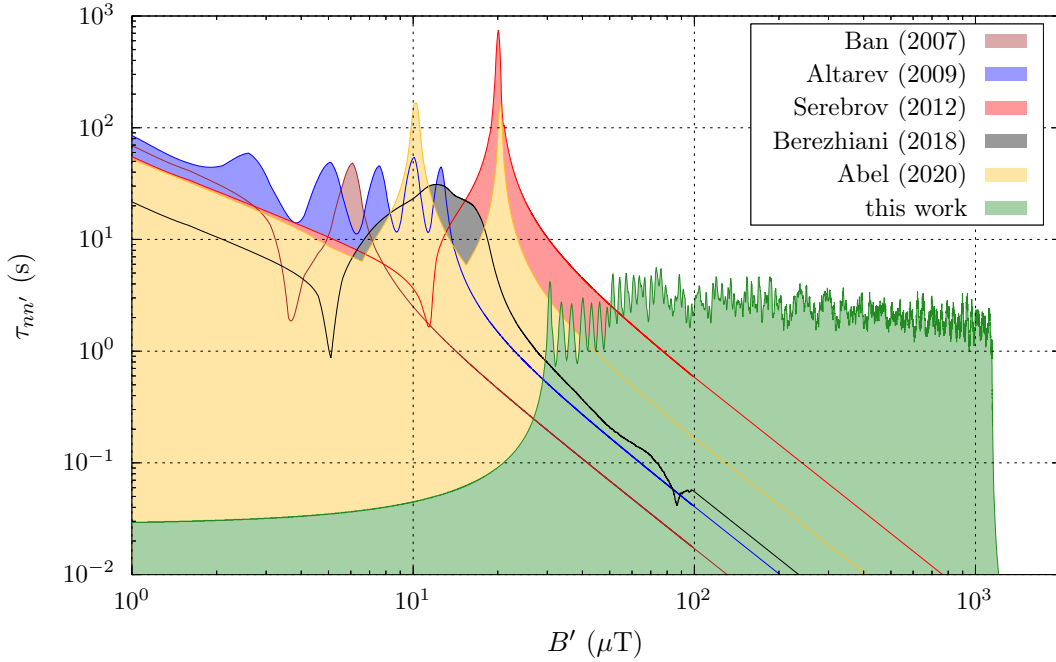


Figure 4.30: $n - n'$ space parameter within the hidden magnetic field hypothesis.

Even if the real value of β cannot be determined, the exclusion boundaries reported in Figure 4.29 show that a general conservative exclusion can be defined by the lower envelope, which is common for all values of β . In such case, rather than fitting or canceling the influence of β , the exclusion limit assumes the worst scenario for each B' . The lower envelope resulting from this analysis is plotted in Figure 4.30 next to all reported exclusions from past UCN storage experiments. For a detailed description of previous exclusions, the reader is referred to [100]. We focus on the exclusion achieved in this work, which can be written in a simplified

way as

$$\tau_{nn'} > 1 \text{ s for } B' \in [50 - 1130] \mu\text{T (95\% C.L.)}. \quad (4.43)$$

In particular, this result is important for two main reasons. First, $n - n'$ oscillations are discarded at large hidden magnetic fields, thus confirming that the 5σ anomaly at high hidden magnetic fields (region c) reported in [54] (2012) is not any more present [10]. Note that all experimental efforts so far targeted the anomaly at short B' . Second, we proved the high efficiency of UCN beams to scan $n - n'$ oscillations in a wide interval of hidden magnetic fields. Although not discussed in detail, the uncertainty analysis of the aforementioned limit is analogous to the one exposed in section 4.4.4. This is true given that the STARucn simulation employed for the construction of exclusion regions in this section is the same as the one in the δm study. The main difference is that, whereas R_{ABC} were averaged over the 14 scans to test δm , R_{+ABC} and R_{-ABC} shared the same scans to test B' . This explains the overall reduction on the sensitivity observed in the latter approach (the ‘2s’ band cannot be drawn in Figure 4.29).

4.6 Chapter conclusions

The UCN detection performance of GADGET has demonstrated being stable and reliable. Even if the PSA developed here does not suggest a UCN category entirely free of background, we could establish an event selection with large UCN counting (~ 180 kHz) and a background contribution far below statistical fluctuations ($\sim 0.007\%$, i.e. 10 Hz). The $n - n'$ experimental campaign in 2020 at ILL and its data analysis reported in this chapter position GADGET as the benchmark of high rate UCN counters. In fact, this successful test supports the inclusion of GADGET detectors in the future nEDM measurements at PSI [103].

The high counting rate capabilities of GADGET allowed the characterization of the UCN flux at the PF2’s EDM beam port. Using the 2 ns resolution and the Qt2t pulse shape parameters featuring the acquisition with FASTER, we could evaluate the time fluctuations of the UCN flux at the scales of hours, minutes, seconds, milliseconds and microseconds. Correlation analyses demonstrated that non-statistical fluctuations of the UCN rate, which become significant at periods ~ 0.5 seconds (see 4.10), are mostly caused by the reactor power fluctuations. This permitted the resize of data error bars and revealed the nature of the systematics that caused their initial underestimation.

We did not observe any significant signal in the R_{ABC} data, but instead constructed a new boundary on the $(\delta m, \tau_{nn'})$ parameter space. The common limit for the entire scanned region is written as

$$\tau_{nn'} > 1 \text{ s for } |\delta m| \in [2 - 69] \times 10^{-12} \text{ eV (95\% C.L.)}. \quad (4.44)$$

Such a result appears as the most sensitive probe at intermediate effective mass-splitting between previous exclusions from UCN storage experiments, mainly focused on small δm [7–10, 100], and regeneration experiments, whose resonance peaks show at higher δm [13–15]. Since this is the first time that a UCN beam experiment is used to test $n - n'$ oscillations, the results presented above confirm the effectiveness of the proposed technique.

By considering non-negligible hidden B' -fields and $\delta m = 0$, the same UCN data set was used to define a new boundary in the $(B', \tau_{nn'})$ parameter space. Given that the self-normalized UCN counting sequence $\{A, B, B, C\}$ evaluates three magnetic fields simultaneously, the data

could only be compared to previous parameter exclusions through the ratio channel (Eq. (1.20)); the asymmetry channel would have been achievable if measuring the UCN beam flux with sequences such as $\{B, -B, -B, B\}$. Nevertheless, the limit for the scanned interval of B' is written as

$$\tau_{nn'} > 1 \text{ s for } B' \in [50 - 1130] \mu\text{T (95\% C.L.)}. \quad (4.45)$$

When compared to past UCN experiments, results in this work demonstrate a superior sensitivity at large hidden magnetic fields. However, the parameter space regions still compatible with the latest reported signals $[10, 100]$ were not excluded. That being said, our limit can be used to confirm the exclusion of the already disfavored 5σ signal contained within the region c in [54]. This portion of the parameter space, which was consistent with the 5σ anomaly initially reported in [54], was removed after including the magnetic field inhomogeneities in the analysis [10].

Chapter 5

Overview and perspectives

The main focus of this work, the probe of $n - n'$ oscillations at large magnetic fields ($B \in [50 - 1100] \mu\text{T}$), allowed the development of several parallel studies. In particular, the optimization and characterization of the novel UCN detector GADGET and the evaluation of the ILL's UCN beam constancy at the level of seconds.

5.1 Overview

The theoretical fundamentals and state of the art concerning the mixing of matter with hidden sectors have been introduced in the first part. It was shown how diverse BSM interactions could be added to the SM Lagrangian to include the swapping of ordinary neutral particles into undetectable hidden states. Either such processes correspond to oscillations between ordinary particles and new-sector particles, including mirror universes where each known particle would have one or multiple (up to 10^{32}) mirror twins, or they are associated to transitions in a high-dimensional bulk, where each slice (brane) determines a different universe, the mixing phenomenology is described by the same set of equations. The introduction of such BSM leads to a simple mathematical treatment of a rich theory capable of shedding some light into yet unsolved problems in physics, such as the origin of dark matter and the nature of processes producing baryogenesis.

Great efforts have been made to evaluate the existence of new hidden sectors with dedicated low energy particle physics experiments. Starting from 2007, this has been done by looking at the neutron disappearance in UCN storage bottles in at least five different setups [7–11]. More recently, since 2015, experiments at reactor facilities have measured the probability of neutron regeneration outside the biological shielding of reactor cores [12–14]. A third method, whose results were published during the production of this work, used VCN beams to probe the regeneration probability after impinging a VCN beam in a high-density neutron stopper [15]. Analysis by Berezhiani *et al.* [54] reported a 5σ anomaly in the asymmetry channel of UCN experiments, which motivated extra searches using magnetic fields of about $10 - 20 \mu\text{T}$. Posterior works with UCN bottles updated the analysis and stated extra 2.5σ and 3.1σ signals [10]. Although the parameter space regions favored from such signals have been largely constrained [11], there are still unexplored portions that are targeted by new measurements [57, 60]. Also, since the parameter exclusion has been mostly bounded at low mass-splitting ($\tau_{nn'} \gtrsim 10 \text{ s}$ for $\delta m < 10^{-12} \text{ eV}$) in UCN storage experiments, and less efficiently

($\tau_{nn'} \gtrsim 10^{-1}$ s) at large mass-splitting (up to $\delta m \approx 10^{-8}$ eV) in regeneration setups, there is a growing interest on probing $n - n'$ oscillations at the scale of seconds at large mass-splitting.

To achieve such a sensitive test at large mass-splitting, a fourth experimental technique was designed with UCN beams and large magnetic fields. Originally conceived for the n2EDM project [103], the novel UCN gaseous detector GADGET played an important role in the success of the new beam technique. Given the high flux of UCN beams (up to 300 kHz at the EDM port at ILL), incorporating a high-rate detector such as GADGET was crucial. During this work, characterization of the detection properties of GADGET and its optimization were both deeply studied. From PSA based on conventional amplitude vs. PS parameter maps and through the Dalitz-like representation of PMT pulses, it has been shown that GADGET detected events can be separated in at least 5 species. In order of relevance, starting from the largest contribution one can identify

- **UCN events**, generated by the neutron absorption of ^3He . If the reaction products of $n + ^3\text{He}$ are totally stopped by the scintillator gas, they are called full-energy deposition events, otherwise they are called edge events.
- **γ and β events**, due to the radiation emitted from the neutron-activated constituents of GADGET, in particular the entrance foil and gas chamber inner walls.
- **Pile-up events**, from multiple UCN detection within the logic coincidence time window (60 ns).
- **^{19}F events**, from the neutron capture by the fluorine nuclei present in the scintillator CF_4 molecules.
- **Cherenkov events**, produced by environmental γ -rays impinging on the gas chamber quartz windows and on the PMT's entrance windows.

Although it was not always possible to separate all the species in non-overlapping PS categories, the contribution of background events was estimated below 1% at ILL. The optimization of both gas pressures in GADGET, revealed multiple factors affecting the detection efficiency. However, in an ideal scenario with low γ background, one should operate with low CF_4 pressure (500 mbar) to avoid neutron up-scattering and high ^3He (15 mbar) to completely absorb all neutrons crossing the gas chamber. On the contrary, if experiments are to be performed in a noisy environment, an offline pulse shape analysis should be included.

The UCN beam setup was quite simple as it only required a magnetization system to lift the $n - n'$ energy degeneracy and a set of guides to transmit the UCN beam from the EDM port at PF2 to GADGET. Since no storage stage was attempted, the oscillations were prompted during the UCN crossing of a 6-m-long and 75-mm-diameter guide surrounded by a 5-m-long solenoid. The magnetic field produced within the solenoid was isolated from external sources with the help of a cylindrical mu-metal shielding and shaped at the solenoid edges via compensation coils. After corroborating that GADGET was insensitive to the magnetic fields produced by such a magnetization system, the beam flux was recorded while scanning $B \in [50 - 1100]$ μT with steps of 3 μT . The data collection technique, constructed as a function of the UCN delivery cycles at PF2 (200 s of delivery every 400 s), evaluated the UCN flux at three magnetic field values A, B and C according to $\{A, B, B, C\} \rightarrow \{44 \text{ s}, 44 \text{ s}, 44 \text{ s}, 44 \text{ s}\}$. By normalizing the number of UCN detected during the counting intervals as $R_{ABC} = (N_B + N_B)/(N_A + N_C)$,

one can test for signals in the three field values, remove linear drifts on the UCN flux within the cycles and avoid long-term variations on the UCN counting in between cycles. The combination of COMSOL simulations of the magnetization system, fluxgate measurements of the magnetic field along the solenoid axis and MC simulations of UCN tracks demonstrated that the B -field profiles experienced by UCN can be safely described by the axial component B_z as a function of the axial coordinate z along the solenoid axis of symmetry ($r = 0$). Evaluation of the oscillation probability can thus assume $\nabla_r B = 0$ but should include the field gradient $\nabla_z B_z$, especially at the solenoid edges.

The data collected for testing $n - n'$ oscillations in the UCN beam at PF2's EDM port also allowed a high-resolution time study of the UCN flux constancy. In fact, while looking for $n - n'$ signals, the data revealed non-statistical fluctuations appearing on the UCN counting during the entire experimental campaign. The 2 ns sampling resolution of FASTER was used to quantify these fluctuations at the scale of hours, minutes, seconds, milliseconds and microseconds. The non-statistical fluctuations influence on the normalized fluxes was found to be shorter as the analyzing window was reduced till the scale of seconds. At milliseconds and microseconds time scales, all the fluctuations were described by the counting statistics. In post data collection analyses, the comparison of the UCN detection against the ILL reactor power demonstrated equivalent dispersion and a large correlation between both data sets ($\rho_{R, \tilde{R}} = 0.45$) at the scale of seconds. Such a result proved that, although no profitable data correction can be applied to the UCN data set ($\rho_{R, \tilde{R}}$ should be larger than 0.5 for a beneficial correction), the non-statistical fluctuations can be completely attributed to the reactor power fluctuations. The error bars on the UCN ratios R_{ABC} could then be safely enlarged by the factor $(s/\sigma_{\text{Pois}})_{R_{ABC}} = 2.23$.

Once error bars were resized to account for the reactor power fluctuations, the search for $n - n'$ did not point at any potential signal. First, by assuming a negligible contribution from hidden magnetic fields to the energy degeneracy $\Delta_{nn'}$, the oscillations were probed as a function of the mass splitting δm . Since the dynamics are not expected to change by inverting the applied magnetic field, all the measurements were averaged over the several scans with + and - field directions. To precisely bound the $(\delta m, \tau_{nn'})$ parameter space, a numerical solution to the oscillation Hamiltonian $\hat{\mathcal{H}}_{nn'}$ was implemented. Within this approach, one achieves a more realistic estimation of the oscillation probability as the magnetic field gradients experienced by UCN crossing the solenoid are taken into account. A consequence of this, the sensitivity is reduced at the resonance values $\delta m = \mu_n B$ but enlarged in between the field steps values. In the end, by computing the contour line associated to the exclusion region with 95% C.L., the overall limit resulting from this work is written as

$$\tau_{nn'} > 1 \text{ s for } |\delta m| \in [30 - 1143] \mu\text{T} \cdot \mu_n \text{ (95\% C.L.)}, \quad (5.1)$$

or equivalently, in energy units

$$\tau_{nn'} > 1 \text{ s for } |\delta m| \in [2 - 69] \times 10^{-12} \text{ eV (95\% C.L.)}. \quad (5.2)$$

By considering non-negligible hidden B' -fields and $\delta m = 0$, the same collected data set was used to define a new boundary in the $(B', \tau_{nn'})$ parameter space. While assuming a constant hidden magnetic field, the measured points R_{ABC} and R_{-ABC} were analyzed as a function of the angle β contained between applied and hidden magnetic fields. After computing the 95% C.L. limits for $\beta \in [0^\circ - 180^\circ]$ with steps of 30° , the overall boundary line was constructed

from the most conservative result at each value of B' . The common limit after such operation is written as

$$\tau_{nn'} > 1 \text{ s for } B' \in [50 - 1130] \mu\text{T (95\% C.L.)}. \quad (5.3)$$

The aforementioned limits have been proved robust as they correspond to the most conservative estimations under several circumstances. In particular, after running MC simulations of UCN tracks with different but yet reasonable input parameters (number of diffusive reflections and initial velocity distribution), no significant change was found on the exclusion boundaries.

Using the mean UCN free-flight-time ($\bar{t}_f = 32.2 \text{ ms}$), mean number of wall collisions ($\bar{n}_{\text{coll}} = 26$), detected flux ($\Phi_{\text{UCN}} = 288 \text{ kHz}$) and integration time window ($T_{\text{int}} = 44 \text{ s}$), the experimental sensitivity of $\tau_{nn'}$ reached in this work was initially estimated from Eq. (4.2) as

$$\tau_{nn'} = t_f \sqrt{n_{\text{coll}} \sqrt{T_{\text{int}} \Phi_{\text{UCN}}}} = t_f \sqrt{n_{\text{coll}} \sqrt{N_0}} \sim 10 \text{ s}. \quad (5.4)$$

However, after the multiple stages of data treatment during the analysis, such sensitivity dropped to the final reported values due to the following reasons:

1. **Category selection:** The UCN counting was reduced to the UCN_1 category to avoid any background systematics. The contribution of this category to the total counting is $C_{\text{UCN-1}} = 62.18\%$
2. **Beam ramping-up cutoff:** The initial 44 s integration windows were resized to 25 s to remove the residual beam ramping up observed on the UCN counting rate inside cycles. This time interval reduction is denoted as $C_{\text{wind}} = 57\%$.
3. **R_{ABC} error bars scaling:** It was included to account for the non-statistical fluctuations linked to the reactor power variations. This scaling reduces the term $\sqrt{N_0}$ by $C_{\text{scale}} = 1/2.23 = 45\%$.
4. **Averaging over multiple scans:** The repeated measurements of R_{ABC} make its error bar to shorten after averaging as $\Delta R_{\text{ABC}} \rightarrow \Delta R_{\text{ABC}} / \sqrt{n_{\text{scan}}}$, with n_{scan} the total number of measurements. Since almost 14 scans were performed, this factor increases the term $\sqrt{N_0}$ by $C_{\text{scan}} = 3.7$.
5. **B -field inhomogeneities (∇B):** Their contribution to the parameter exclusion was the decrease of the $\tau_{nn'}$ limit of about 2 s.
6. **Exclusion limit valleys:** The single $\tau_{nn'}$ limit was constructed with the lowest points (valleys) of the exclusion contour lines in both parameter spaces. A factor of 5 (20%) was found between the sensitivity at the peaks (resonances) and valleys.

Note that the first four of these effects can be included in Eq. (5.4) as

$$\tau_{nn'} = t_f \sqrt{n_{\text{coll}} C_{\text{scale}} C_{\text{scan}} \sqrt{C_{\text{UCN-1}} C_{\text{wind}} N_0}}. \quad (5.5)$$

However, since establishing an analytical expression for the contribution of the last two effects to the $\tau_{nn'}$ sensitivity is a cumbersome task, they are not explicitly accounted in the equation above. Table 5.1 resumes all the described effects while showing their influence on the sensitivity of $\tau_{nn'}$.

Table 5.1: Summary of the main effects changing the experimental sensitivity. The column on the right shows the cumulative effect on $\tau_{nn'}$.

Effect	Affects (by)	Sensitivity change	Cumulative
-	-	-	$\tau_{nn'} \sim 10$ s
$C_{\text{UCN-1}}$	N_0 (62.18%)	89%	~ 8.9 s
C_{wind}	N_0 (57%)	87%	~ 7.7 s
C_{scale}	$\sqrt{N_0}$ (45%)	67%	~ 5.2 s
C_{scan}	$\sqrt{N_0}$ (3.7)	192%	~ 10 s
∇B	$\tau_{nn'}$ (+2 s)	+2 s	~ 12 s
Valleys	$\tau_{nn'}$ (20%)	20%	~ 2.4 s

5.2 Perspectives

The large sensitivity to $n - n'$ oscillation of UCN storage experiments has shown to efficiently bound the $(\delta m, \tau_{nn'})$ parameter space at short mass-splitting ranges. One would then expect that future works constructed with this technique ascertain the yet-favored regions from past anomalies. However, in case there is no confirmation of the signals, the evaluation of $n - n'$ oscillation should focus on the large mass-splitting domain ($\delta m > 10^{-12}$ eV). While next generation neutron-sensitive neutrino setups and VCN experiments could contribute to such a search through regeneration measurements for δm up to 10^{-6} eV, neutron disappearance in UCN beams could be used to probe the interval $\delta m \in [10^{-12} - 10^{-10}]$ eV with improved sensitivities. For the latter, a few modifications to the beam setup presented in this work are worth to be evaluated:

- The use of a wider beam guide to allow larger UCN trajectories with longer free-flight-times. As expressed in Eq. (4.2), the sensitivity of $\tau_{nn'}$ at the exact resonance $\Delta_{nn'}$ is proportional to t_f . However, this has to be improved while guarantying a uniform magnetic field.
- The inclusion of a high efficient monitor detector to correct for the beam non-statistical fluctuations caused by the reactor power variations. For example, if separating the UCN beam into two symmetric sides, one for $n - n'$ oscillations probing and the other for flux monitoring, the sensitivity on $\tau_{nn'}$ at the resonance is reduced to a $\sqrt{\sqrt{50\%}} \approx 84\%$, but the reactor power systematics that enlarge the R_{ABC} error bars by a factor of 2.23 are suppressed. Such a monitor detector should be placed just before the magnetic field volume to assure a large correlation with the principal counter (see Eq. (4.15)).

Since data collected according to the self-normalized $\{A, B, B, C\}$ sequence cannot be used to probe $n - n'$ oscillations through Berezhiani's asymmetry channel (Eq. (1.19)), provided that future UCN beam experiments include a beam monitor, sequences with patterns $\{B, -B, -B, B\}$ should be considered in order to examine the asymmetry anomalies. Nevertheless, given that $A_{\uparrow\downarrow}$ is predicted zero within the $n - n'$ generic approach with $\delta m \neq 0$ and $B' = 0$ for non-polarized beams, next generation UCN beam experiments could be designed with spin analyzers (as the one* presented in the Appendix G). In such a scenario, because

*This model corresponds to the next U-Shape Spin Analyzer for the n2EDM project, which was modeled using COMSOL simulations in this work.

the resonance condition $\Delta_{nn'} = \mu_n B - \delta m = 0$ is only fulfilled for spin-up neutrons (the degeneracy is not lifted for spin-down neutrons: $\Delta_{nn'} = -\mu_n B - \delta m$), the ratio between the UCN counting of both spin components would be proportional to

$$\frac{N_{\text{spin-up}}}{N_{\text{spin-down}}} \approx 1 - n_{\text{coll}} \left(\frac{t_f}{\tau_{nn'}} \right)^2. \quad (5.6)$$

This additional channel for probing $n - n'$ oscillations by differentiating the spin components has never been attempted.

Appendices

Appendix A

From mirror to hidden neutrons

Although the mirror and hidden $n - n'$ oscillation models incorporate different interactions, the observable E_0 measured in UCN experiments can be used to conclude in both contexts. In particular, exclusion bounds in $(B', \tau_{nn'})$ can be directly transformed into the space $(\delta m, \tau_{nn'})$. To see this, let us recall the definition of the ratio E_0 , constructed with the neutron counting in positive (N_B), negative (N_{-B}) and zero (N_0) magnetic fields as

$$1 + E_0 = \frac{2N_0}{N_B + N_{-B}} = \frac{2e^{-n_s P_0}}{e^{-n_s P_B} + e^{-n_s P_{-B}}} \quad (\text{A.1})$$

$$= \frac{\exp[-n_s(P_0 - (P_B + P_{-B})/2)]}{\cosh[n_s(P_B - P_{-B})/2]}, \quad (\text{A.2})$$

where n_s is the number of neutron wall collisions, and $P_{\pm B}$ and P_0 the oscillation probabilities in $\pm B$ and zero magnetic fields. Independently of the oscillation model, these probabilities are small and therefore allow the approximation

$$\frac{E_0}{n_s} \approx \frac{1}{2}(P_B + P_{-B}) - P_0. \quad (\text{A.3})$$

Notice that, up to now, no specific form of P_B has been established. Indeed, the differences between the exclusion limits on the spaces $(B', \tau_{nn'})$ and $(\delta m, \tau_{nn'})$ have origin in this last expression. Whereas the oscillation probability for uniform magnetic fields within the mirror neutron model is written as

$$P_B(t; B', \tau_{nn'}, \beta) = \frac{\sin^2[(\omega - \omega')t]}{2\tau_{nn'}^2(\omega - \omega')^2}(1 + \cos \beta) + \frac{\sin^2[(\omega + \omega')t]}{2\tau_{nn'}^2(\omega + \omega')^2}(1 - \cos \beta), \quad (\text{A.4})$$

with $2\omega^{(\prime)} = \mu_n B^{(\prime)}$, in the hidden neutron model it gives

$$P_B(t; \delta m, \tau_{nn'}) = \frac{\sin^2[(\omega - \tilde{\omega})t]}{\tau_{nn'}^2(\omega - \tilde{\omega})^2}, \quad (\text{A.5})$$

with $2\tilde{\omega} = \delta m$. One can corroborate that the latter coincides with the former's particular case for $\beta = 0$, and that $P_B(t; \delta m, \tau_{nn'}) = P_{-B}(t; \delta m, \tau_{nn'})$ provided that the analyzed neutrons are not polarized. Using these oscillation probabilities, Eq. (A.3) can be rewritten as

$$\tau_{nn'}^2 = \begin{cases} \frac{n_s}{E_0} \left(\frac{1}{2} \left[\frac{S(\omega - \omega')}{(\omega - \omega')^2} + \frac{S(\omega + \omega')}{(\omega + \omega')^2} \right] - \frac{S(\omega')}{\omega'^2} \right), & \text{for mirror neutrons,} \\ \frac{n_s}{E_0} \left(\frac{S(\omega - \tilde{\omega})}{(\omega - \tilde{\omega})^2} - \frac{S(\tilde{\omega})}{\tilde{\omega}^2} \right), & \text{for hidden neutrons,} \end{cases} \quad (\text{A.6})$$

with $S(\omega) = \langle \sin^2(\omega t) \rangle$ as introduced in Eq. (6) of [10].

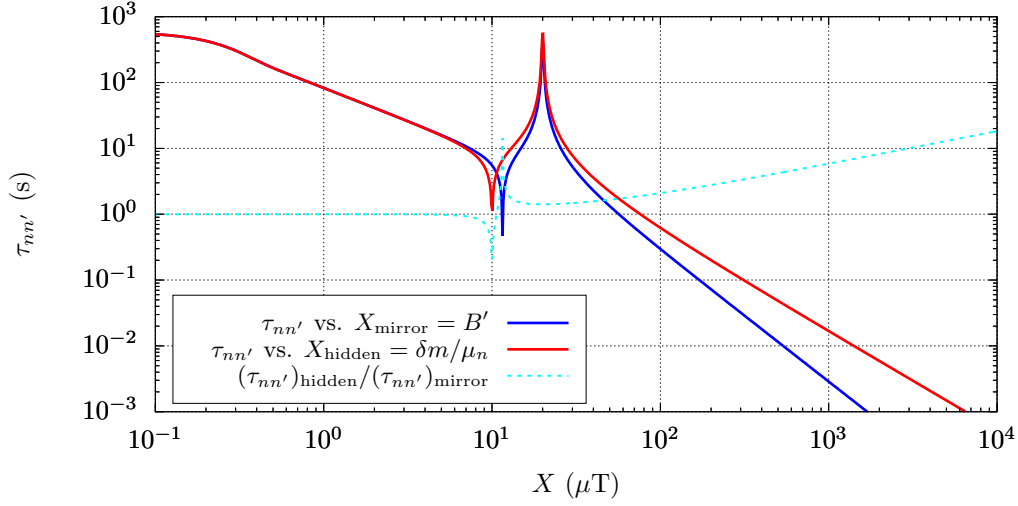


Figure A.1: 95% C.L. exclusion boundary for the mirror (blue) and hidden (red) contexts (Eqs. A.6) computed from experimental results of UCN storage reported in [104]. The dashed line corresponds to the ratio between both limits.

A graphical comparison of these two cases is depicted in Figure A.1, where the boundary is constructed from the experimental results in [104] as reported in [54]. As expected, the hidden neutron approach yields to a larger $\tau_{nn'}$ exclusion given that in general

$$\frac{S(\omega - \omega')}{(\omega - \omega')^2} > \frac{S(\omega + \omega')}{(\omega + \omega')^2}. \quad (\text{A.7})$$

Although the difference is almost negligible close and below the resonance ($B = 20 \mu\text{T}$), it grows as $X \rightarrow \infty$. This effect, illustrated by the dashed cyan curve can be analytically quantified by simple calculation of the ratio $(\tau_{nn'})_{\text{hidden}}/(\tau_{nn'})_{\text{mirror}}$ from Eqs. A.6. To do so, let us recall that, if assuming $\langle \sin^2(\omega t) \rangle \approx 1/2$, the ratio channel in the mirror neutron model can also be expressed as [17]

$$(\tau_{nn'})_{\text{mirror}}^2 = \frac{n_s}{E_0} \frac{\eta^2(3 - \eta^2)}{2\omega'^2(1 - \eta^2)^2}. \quad (\text{A.8})$$

with $\eta = \omega/\omega'$. By following a similar procedure, the ratio channel in the hidden neutron approach yields

$$(\tau_{nn'})_{\text{hidden}}^2 = \frac{n_s}{E_0} \frac{2\tilde{\eta} - \tilde{\eta}^2}{2\tilde{\omega}^2(1 - \tilde{\eta})^2}. \quad (\text{A.9})$$

with $\tilde{\eta} = \omega/\tilde{\omega}$. Hence, the factor to transform a mirror neutron boundary into a hidden neutron one is

$$C_{m \rightarrow h} = \frac{(\tau_{nn'})_{\text{hidden}}}{(\tau_{nn'})_{\text{mirror}}} = \frac{(2 - \tilde{\eta})(1 + \tilde{\eta})^2}{\tilde{\eta}(3 - \tilde{\eta}^2)} \quad (\text{A.10})$$

if making $\omega' \rightarrow \tilde{\omega}$, i.e. $\mu_n B' \rightarrow \delta m$. The accuracy of this procedure is displayed in Figure A.2, where the mirror neutron boundary presented in Figure A.1 has been transformed into the hidden neutron context (dashed green line).

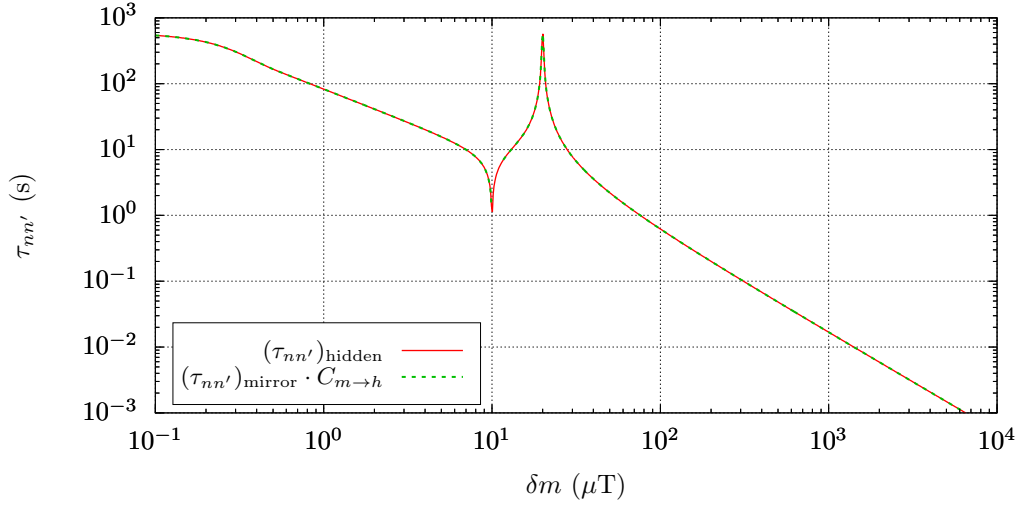


Figure A.2: 95% C.L. exclusion boundary for the hidden context. The dashed line corresponds to the mirror neutron limit converted to a hidden neutron one through Eq. A.10.

This result proves that no extra analysis has to be done on previous UCN experiments to conclude on the hidden neutron hypothesis, it is sufficient to apply the aforementioned transformation. That being said, since the conversion factor $C_{m \rightarrow h}$ depends on the applied field B , the proposed method can only be used on mirror neutron boundaries derived from a single magnetic field magnitude.

Appendix B

Absorption probability

UCN traveling in a gaseous mixture composed of CF_4 and ^3He can undergo up-scattering and absorption from either gas, ^3He absorption and CF_4 up-scattering being the most probable processes. The following dummy model allows estimating the overall absorption probability for UCN impinging normally (\hat{x}) on a gas chamber of length L filled with a gas admixture of CF_4 and ^3He .

On the one hand, the probability for a UCN to not interact after crossing a distance x inside the gas is written as

$$\mathcal{P}_{\text{sur}}(x) = \exp(-x/\lambda), \quad (\text{B.1})$$

with λ the UCN *mean free path*, calculated as

$$\lambda = \frac{1}{\sum_i n_i \sigma_i} = \frac{1}{n_{\text{up}} \sigma_{\text{up}} + n_{\text{ab}} \sigma_{\text{ab}}} \quad (\text{B.2})$$

where n_{ab} and n_{up} are the densities of nuclei responsible for the absorption (^3He) and up-scattering (CF_4), and σ_{ab} and σ_{up} their corresponding cross-sections. On the other hand, the UCN absorption probability in an infinitesimal layer of thickness dx is given expressed as

$$\mathcal{P}_{\text{ab}} = n_{\text{ab}} \sigma_{\text{ab}} dx. \quad (\text{B.3})$$

Therefore, the probability for absorption between x and $x + dx$, once the UCN has reached x , is calculated as

$$\mathcal{P}_{\text{ab}}(x) = \mathcal{P}_{\text{sur}}(x) \cdot \mathcal{P}_{\text{ab}} \quad (\text{B.4})$$

$$= \exp(-x/\lambda) \cdot (n_{\text{ab}} \sigma_{\text{ab}} dx), \quad (\text{B.5})$$

whose integral, between $x = 0$ and $x = L$, represents the total absorption probability in the chamber:

$$\mathcal{P}_{\text{ab}}^{\text{tot}} = \int_0^L \exp(-x/\lambda) n_{\text{ab}} \sigma_{\text{ab}} dx \quad (\text{B.6})$$

$$= n_{\text{ab}} \sigma_{\text{ab}} \lambda [1 - \exp(-L/\lambda)] \quad (\text{B.7})$$

$$= \frac{n_{\text{ab}} \sigma_{\text{ab}}}{n_{\text{up}} \sigma_{\text{up}} + n_{\text{ab}} \sigma_{\text{ab}}} [1 - \exp(-L/\lambda)]. \quad (\text{B.8})$$

Appendix C

ABBC and linear drifts

Normally, when experimentalist want to test the influence of a given experimental configuration on a controlled quantity, for example, the influence of applying a magnetic field (B) on the UCN counting after storage (N_B), a deep knowledge of the controlled quantity (the UCN counting without magnetic fields, N_0) is required. Taking the example above, to carry out the experiment, one could simply propose performing one measurement after the other, e.g. N_0 followed by N_B ($\{0, B\}_{\text{simple}}$), and then test the hypothesis by looking at the deviations of

$$R_{\text{simple}} = \frac{N_B}{N_0} \quad (\text{C.1})$$

with respect to 1. This approach is valid provided that the initial number of UCN filled into the bottle is the same for both measurements. However, if that is not the case and the UCN source production efficiency drifts in time, one would misinterpret the difference between N_B and N_0 as an influence of the applied magnetic field.

One possible solution to work around time drifts is by repeating N_0 and N_B measurements in equally separated cycles with alternating sequences. For example, if counting UCN according to the sequence $\{0, B, B, 0\}_{\text{seq1}}$, the ratio

$$R_{\text{seq1}} = \frac{N_B^{2\text{nd}} + N_B^{3\text{rd}}}{N_0^{1\text{st}} + N_0^{4\text{th}}} \quad (\text{C.2})$$

is insensitive to linear drifts. To see this, let us first assume that there are not time drifts and that the counting N_B is indeed affected by the B -field:

$$N_B = N_0 - \gamma, \quad (\text{C.3})$$

with γ the neutron deficit due to the physical influence of B . The ratio in Eq. (C.2) then reads

$$\begin{aligned} R_{\text{seq1}} &= \frac{(N_0 - \gamma) + (N_0 - \gamma)}{N_0 + N_0} \\ &= 1 - \frac{\gamma}{N_0}. \end{aligned} \quad (\text{C.4})$$

Now, if on top of the influence of B , the UCN source describes a linear drift in time, i.e. the zero-field counting is proportional to the experiment cycle i :

$$N_{0,i} = N_0 + \rho i, \quad (\text{C.5})$$

with ρ a constant, whereas the ratio obtained from the former sequence $\{0, B\}_{\text{simple}}$ yields

$$\begin{aligned} R_{\text{simple}} &= \frac{N_0 - \gamma + \rho(i+1)}{N_0 + \rho i} \\ &\approx 1 - \frac{\gamma - \rho}{N_0}, \end{aligned} \tag{C.6}$$

the ratio from the sequence $\{0, B, B, 0\}_{\text{seq1}}$ results

$$\begin{aligned} R_{\text{seq1}} &= \frac{[N_0 - \gamma + \rho(i+1)]_{\text{2nd}} + [N_0 - \gamma + \rho(i+2)]_{\text{3rd}}}{[N_0 + \rho i]_{\text{1st}} + [N_0 + \rho(i+3)]_{\text{4th}}} \\ &= 1 - \frac{2\gamma}{2N_0 + \rho(2i+3)} \\ &\approx 1 - \frac{\gamma}{N_0}, \end{aligned} \tag{C.7}$$

which happens to be equal to the no-drift ratio in Eq. (C.4). In conclusion, the linear drift constant ρ has been removed. Following a similar procedure, it can be shown that the sequence $\{0, B, B, 0, B, 0, 0, B\}$ removes time shifts with quadratic component.

Appendix D

From rate to R_{ABC} non-statistical fluctuations

Similarly to random walk processes, where the walker's position after many random steps describes a normal distribution with variance proportional to the elapsed time ($\sigma^2 \propto t$), when integrating the UCN flux (N) whose magnitude depends on the reactor power fluctuations, the number of non-statistical fluctuations increases as the integration interval enlarges. To see this, let us write the non-statistical fluctuations proportional to UCN the flux

$$\Phi = \Phi_0(1 + \rho), \quad (\text{D.1})$$

with ρ a random variable following a normal distribution $\mathcal{N}(0, \Delta\rho^2)$ and Φ_0 the average flux. Following this notation, the integrated flux after T seconds is

$$N = \Phi_0 T(1 + \rho). \quad (\text{D.2})$$

One can then compute the expected value and variance of this new random variable:

$$\mathbb{E}[N] = \langle N \rangle = \phi_0 T \quad (\text{D.3})$$

$$\begin{aligned} \text{Var}[N] &= \Delta N^2 \\ &= \langle N \rangle \left(1 + \Delta\rho^2(1 + \langle N \rangle) \right) \\ &\approx \langle N \rangle \left(1 + \Delta\rho^2 \langle N \rangle \right), \end{aligned} \quad (\text{D.4})$$

Therefore, the ratio between the dispersion of N over multiple UCN cycles normalized to the expected dispersion from counting statistics (Poisson statistics) is

$$\begin{aligned} \left(\frac{s}{\sigma_{\text{Pois}}} \right) &= \frac{\sqrt{\left(\frac{\Delta N}{N} \right)_{\text{non-st}}^2}}{\sqrt{\left(\frac{\Delta N}{N} \right)_{\text{Pois}}^2}} = \frac{\sqrt{\frac{1 + \langle N \rangle \Delta\rho^2}{\langle N \rangle}}}{\sqrt{\frac{1}{\langle N \rangle}}} \\ &= \sqrt{1 + \langle N \rangle \Delta\rho^2} \\ &= \sqrt{1 + \Phi_0 \Delta\rho^2 T}. \end{aligned} \quad (\text{D.5})$$

Note that the previous ratio, which is used in this work to scale the error bars ΔR_{ABC} , is proportional to the square root of the integration interval T . This explains why the amount of non-statistical fluctuations is different if computed over the UCN counting rate $((s/\sigma_{\text{Pois}})_{\text{rate}} = 1.689)$ or from the R_{ABC} points dispersion $((s/\sigma_{\text{Pois}})_{R_{ABC}} = 2.23)$. Whereas the former corresponds to a sampling rate of 1 second, the latter is based on the 44 s integration periods.

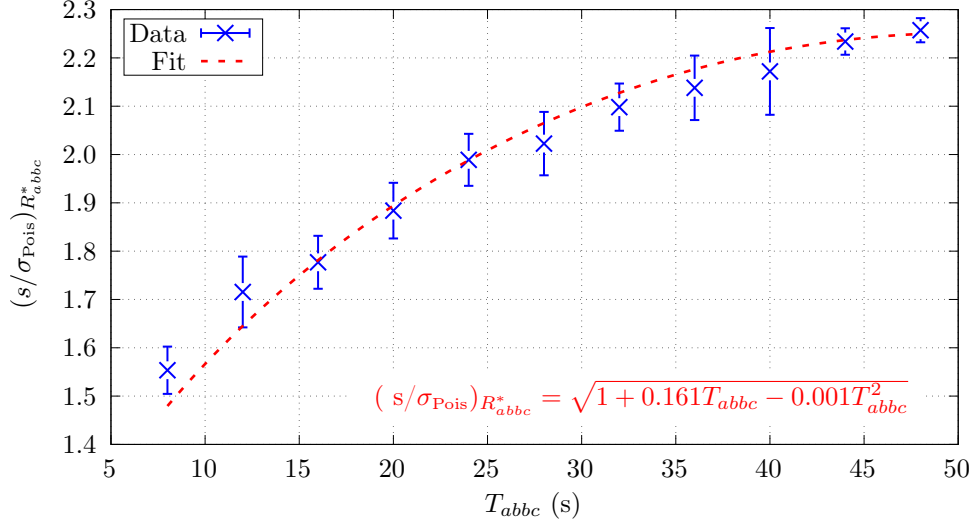


Figure D.1: Dispersion of R^*_{abbc} points normalized by the expected statistical fluctuations as a function of the integration period T_{abbc} . The error bars correspond to the 1σ dispersion from repeated R^*_{abbc} calculation along the cycle span (when permitted by T_{abbc}). The fitted function is included to test the validity of Eq. (D.5).

In order to corroborate that the description of the reactor power fluctuations above is valid, a resized R^*_{abbc} was computed as a function of the integration periods, now denoted as T_{abbc} . Forgetting that the magnetic field is ramped as ABBC within the cycles, the resized ratio is defined as

$$R^*_{abbc} = \frac{N_b + N_c}{N_a + N_c} \quad (\text{D.6})$$

with N_a, N_b and N_c the UCN counting rate integrated during $T_{abbc}/4$ seconds according to the sequence $\{N_a, N_b, N_b, N_c\}$. Starting from $T_{abbc} = 8$ s, which corresponds to the sequence $\{2 \text{ s}, 2 \text{ s}, 2 \text{ s}, 2 \text{ s}\}$, the ratios R^*_{abbc} were calculated for all the Run-6 cycles. The resulting $(s/\sigma_{\text{Pois}})R^*_{abbc}$ is plotted as a function of T_{abbc} in Figure D.1. One can finally confirm that the scaling factor increases almost proportional to $\sqrt{T_{abbc}}$, just as the random walk variance evolution.

Appendix E

Numerical solution of $\mathcal{H}_{nn'}$

Solution to quantum mechanics problems via numerical algorithms need special attention. The truncation error inherent to any numerical method should not modify the physical properties, such as the normalization of quantum states linked to the continuity equation and the probability conservation. The numerical solution to the $n - n'$ oscillation model within the mass-splitting approach ($B' = 0$) is different from the one within the hidden magnetic field scenario ($\delta m = 0$). The latter requires the definition of an extra parameter: the angle formed by the ordinary and hidden magnetic fields β . In the following, we present the numerical algorithms used to solve to calculate the oscillation probability in both scenarios.

E.1 Mass-splitting scenario

The solution to the 2×2 Hamiltonian, written as

$$\hat{\mathcal{H}}_{nn'} = \begin{pmatrix} \Delta E & \epsilon_{nn'} \\ \epsilon_{nn'} & \delta m \end{pmatrix}, \quad (\text{E.1})$$

is proposed through two different approaches. First, using the method derived by Biondi [105], which is used to compute the $n - n'$ oscillation probability in [10]. Second, by means of the Liouville-Neumann equation [102].

E.1.1 Biondi's method

By making $2a = \delta m - \Delta E$ and $2b = \delta m + \Delta E$, the oscillation Hamiltonian can be rewritten as

$$\hat{\mathcal{H}}_{nn'} = \begin{pmatrix} b - a & \epsilon_{nn'} \\ \epsilon_{nn'} & b + a \end{pmatrix} = \begin{pmatrix} b & 0 \\ 0 & b \end{pmatrix} + \begin{pmatrix} -a & \epsilon_{nn'} \\ \epsilon_{nn'} & a \end{pmatrix}, \quad (\text{E.2})$$

out of which the first term $b\mathbb{I}_{2 \times 2}$ can be dropped out as it does not change the dynamics. Therefore, the Schrödinger, expressed as

$$i \frac{d}{dt} \begin{pmatrix} \psi_n(t) \\ \psi_{n'}(t) \end{pmatrix} = \begin{pmatrix} -a & \epsilon_{nn'} \\ \epsilon_{nn'} & a \end{pmatrix} \begin{pmatrix} \psi_n(t) \\ \psi_{n'}(t) \end{pmatrix} \quad (\text{E.3})$$

leads to the discretized equation

$$\begin{aligned} \begin{pmatrix} \psi_n(t_{i+1}) \\ \psi_{n'}(t_{i+1}) \end{pmatrix} &= \begin{pmatrix} \psi_n(t_i) \\ \psi_{n'}(t_i) \end{pmatrix} - i\Delta t \begin{pmatrix} -a_i & \epsilon_{nn'} \\ \epsilon_{nn'} & a_i \end{pmatrix} \begin{pmatrix} \psi_n(t_i) \\ \psi_{n'}(t_i) \end{pmatrix} \\ &= \begin{pmatrix} [1 + i\Delta t a_i] \psi_n(t_i) - i\Delta t \epsilon_{nn'} \psi_{n'}(t_i) \\ [1 - i\Delta t a_i] \psi_{n'}(t_i) - i\Delta t \epsilon_{nn'} \psi_n(t_i) \end{pmatrix}, \end{aligned} \quad (\text{E.4})$$

which can be conventionally rewritten as

$$\begin{aligned} \psi_n(t_{i+1}) &= \cos(\tilde{a}_{i+1,i}\Delta t) \psi_n(t_i) \\ &\quad - i \sin(\tilde{a}_{i+1,i}\Delta t) \cos(2\theta_{i+1,i}) \psi_{n'}(t_i) \\ &\quad - i \sin(\tilde{a}_{i+1,i}\Delta t) \sin(2\theta_{i+1,i}) \psi_{n'}(t_i) \end{aligned} \quad (\text{E.5})$$

$$\begin{aligned} \psi_{n'}(t_{i+1}) &= \cos(\tilde{a}_{i+1,i}\Delta t) \psi_{n'}(t_i) \\ &\quad + i \sin(\tilde{a}_{i+1,i}\Delta t) \cos(2\theta_{i+1,i}) \psi_{n'}(t_i) \\ &\quad - i \sin(\tilde{a}_{i+1,i}\Delta t) \sin(2\theta_{i+1,i}) \psi_n(t_i) \end{aligned} \quad (\text{E.6})$$

with

$$\begin{aligned} \tilde{a}_{i+1,i} &= \sqrt{a_{i+1,i}^2 + \epsilon_{nn'}^2} \\ a_{i+1,i} &= (\delta m - (\Delta E_{i+1} + \Delta E_i)/2)/2 \\ \sin(2\theta_{i+1,i}) &= \epsilon_{nn'}/\tilde{a}_{i+1,i} \\ \cos(2\theta_{i+1,i}) &= a_{i+1,i}/\tilde{a}_{i+1,i}. \end{aligned}$$

The $n - n'$ oscillation probability is then computed as

$$P_{nn'}(t) = |\psi_{n'}(t)|^2.$$

E.1.2 Liouville-Neumann equation

An alternative to the Biondi's approach is the numerical solution of the Liouville-Neumann equation. In this case, the oscillation probability is directly linked to the diagonal terms of the density matrix $\hat{\rho}$, which evolves in time according to

$$\frac{\partial}{\partial t} \hat{\rho} = -i[\hat{\mathcal{H}} \cdot \hat{\rho}] = -i\hat{\mathcal{H}}\hat{\rho} + i\hat{\rho}\hat{\mathcal{H}}^\dagger, \quad (\text{E.7})$$

explicitly written for the Hamiltonian in Eq. (E.1) as

$$\begin{aligned} \frac{d}{dt} \begin{pmatrix} \rho_{11} & \rho_{12} \\ \rho_{21} & \rho_{22} \end{pmatrix} &= -i \left[\begin{pmatrix} \Delta E & \epsilon_{nn'} \\ \epsilon_{nn'} & \delta m \end{pmatrix} \begin{pmatrix} \rho_{11} & \rho_{12} \\ \rho_{21} & \rho_{22} \end{pmatrix} - \begin{pmatrix} \rho_{11} & \rho_{12} \\ \rho_{21} & \rho_{22} \end{pmatrix} \begin{pmatrix} \Delta E & \epsilon_{nn'} \\ \epsilon_{nn'} & \delta m \end{pmatrix} \right] \\ &= -i \begin{pmatrix} \epsilon_{nn'}(\rho_{21} - \rho_{12}) & -\epsilon_{nn'}(\rho_{11} - \rho_{22}) - (\delta m - \Delta E)\rho_{12} \\ \epsilon_{nn'}(\rho_{11} - \rho_{22}) + (\delta m - \Delta E)\rho_{21} & \epsilon_{nn'}(\rho_{12} - \rho_{21}) \end{pmatrix}. \end{aligned} \quad (\text{E.8})$$

By recalling that $\rho_{12} = \rho_{21}^*$ and that $\text{Tr}(\hat{\rho}) = \rho_{11} + \rho_{22} = 1$, the matrix elements in the last expression can be written as

$$\begin{aligned}\dot{\rho}_{11} &= -2\epsilon_{nn'}\text{Im}(\rho_{12}) \\ \dot{\rho}_{12} &= i[\epsilon_{nn'}(2\rho_{11} - 1) + (\delta m - \Delta E)\rho_{12}] \\ \dot{\rho}_{21} &= \dot{\rho}_{12}^* \\ \dot{\rho}_{22} &= -\dot{\rho}_{11}.\end{aligned}\tag{E.9}$$

Therefore, out of the initial 8 equations for the real and imaginary parts of each ρ_{ij} , there are only three independent equations:

$$\begin{aligned}\dot{\rho}_1 &= -2\epsilon_{nn'}I_2 \\ \dot{R}_2 &= (\Delta E - \delta m)I_2 \\ \dot{I}_2 &= -(\Delta E - \delta m)R_2 + \epsilon_{nn'}(2\rho_1 - 1),\end{aligned}\tag{E.10}$$

where we have defined $\rho_1 = \rho_{11}$, $R_2 = \text{Re}(\rho_{12})$ and $I_2 = \text{Im}(\rho_{12})$. This set of equations completely determines the evolution of the neutron and hidden neutron states, where the oscillation probability is given by

$$P_{nn'}(t) = \rho_{22}(t) = 1 - \rho_{11}(t).\tag{E.11}$$

E.2 Hidden magnetic field scenario

By including a hidden magnetic field (B') forming an angle β with respect to the applied magnetic field (B), the $n - n'$ model requires considering the neutron spins states. If defining the quantization axis along the ordinary field direction, the neutron and hidden neutron energies are given by

$$\begin{aligned}\Delta E &= \mu_n \cdot \vec{B} = 2\omega\hat{\sigma}_z \\ \Delta E' &= \mu_n \cdot \vec{B}' = 2\omega'\vec{\sigma} = 2\omega'(\sin\beta\hat{\sigma}_x + \cos\beta\hat{\sigma}_z),\end{aligned}\tag{E.12}$$

respectively. In these last equations, we have defined the resonances $2\omega = \mu_n B$ and $2\omega' = \mu_n B'$. Also, without loss of generality, B' has been placed in the xz -plane.

The $n - n$ oscillations are thus described by the Hamiltonian

$$\hat{\mathcal{H}}_{nn'} = \begin{pmatrix} 2\omega & 0 & \epsilon_{nn'} & 0 \\ 0 & -2\omega & 0 & \epsilon_{nn'} \\ \epsilon_{nn'} & 0 & 2\omega'\cos\beta & 2\omega'\sin\beta \\ 0 & \epsilon_{nn'} & 2\omega'\sin\beta & -2\omega'\cos\beta \end{pmatrix},\tag{E.13}$$

where $\hat{\rho}$ is now the 4×4 matrix:

$$\hat{\rho} = \begin{pmatrix} \rho_{11} & \rho_{12} & \rho_{13} & \rho_{14} \\ \rho_{21} & \rho_{22} & \rho_{23} & \rho_{24} \\ \rho_{31} & \rho_{32} & \rho_{33} & \rho_{34} \\ \rho_{41} & \rho_{42} & \rho_{43} & \rho_{44} \end{pmatrix}.\tag{E.14}$$

Therefore, the Liouville-Neumann equation represents a set of $2(4 \times 4) - 4 = 28$ (the factor 2 comes from the real and imaginary parts of the non-diagonal terms) coupled equations, which should fulfill $\rho_{ij} = \rho_{ji}^*$ and $\text{Tr}(\hat{\rho}) = \rho_{11} + \rho_{22} + \rho_{33} + \rho_{44} = 1$. Following a process similar to the one used to derive Eq. (E.10), the set of independent equations in this approach are written as

$$\begin{aligned}
\dot{R}_{11} &= -2\epsilon_{nn'} I_{13} \\
\dot{R}_{12} &= -\epsilon_{nn'} (I_{23} + I_{14}) + 4I_{12}\omega \\
\dot{I}_{12} &= -\epsilon_{nn'} (R_{23} + R_{14}) - 4I_{12}\omega \\
\dot{R}_{13} &= -2I_{14} + 2I_{13}(\omega - \omega' \cos \beta) \\
\dot{I}_{13} &= -\epsilon_{nn'} (R_{33} - R_{11}) + 2R_{14}\omega' \sin \beta - 2R_{13}(\omega - \omega' \cos \beta) \\
\dot{R}_{14} &= \epsilon_{nn'} (I_{34} - I_{12}) - 2(I_{13}\omega' \sin \beta - I_{14}(\omega + \omega' \cos \beta)) \\
\dot{I}_{14} &= -\epsilon_{nn'} (R_{34} - R_{12}) + 2(R_{13}\omega' \sin \beta - R_{14}(\omega + \omega' \cos \beta)) \\
\dot{R}_{22} &= -2\epsilon_{nn'} I_{24} \\
\dot{R}_{23} &= -\epsilon_{nn'} (I_{34} - I_{12}) - 2(I_{24} + I_{23}(\omega + \omega' \cos \beta)) \\
\dot{I}_{23} &= -\epsilon_{nn'} (R_{34} - R_{12}) + 2(R_{24} + R_{23}(\omega + \omega' \cos \beta)) \\
\dot{R}_{24} &= -2(I_{23}\omega' \sin \beta + I_{24}(\omega - \omega' \cos \beta)) \\
\dot{I}_{24} &= -\epsilon_{nn'} (1 - R_{11} - R_{33} - 2R_{22}) + 2(R_{23}\omega' \sin \beta + R_{24}(\omega - \omega' \cos \beta)) \\
\dot{R}_{33} &= 2(\epsilon_{nn'} I_{13} - 2I_{34}\omega' \sin \beta) \\
\dot{R}_{34} &= \epsilon_{nn'} (I_{14} + I_{23}) + 4I_{34}\omega' \cos \beta \\
\dot{I}_{34} &= -\epsilon_{nn'} (R_{14} - R_{23}) - 2(2R_{34}\omega' \cos \beta + (1 - R_{11} - R_{22} - 2R_{33})\omega' \sin \beta),
\end{aligned}$$

where we have defined $R_{ij} = \text{Re}(\rho_{ij})$ and $I_{ij} = \text{Im}(\rho_{ij})$. The oscillation probability over both spin components is

$$P_{nn'}(t) = \rho_{33}(t) + \rho_{44}(t) = 1 - \rho_{11}(t) - \rho_{22}(t). \quad (\text{E.15})$$

Appendix F

PMT inside magnetic fields

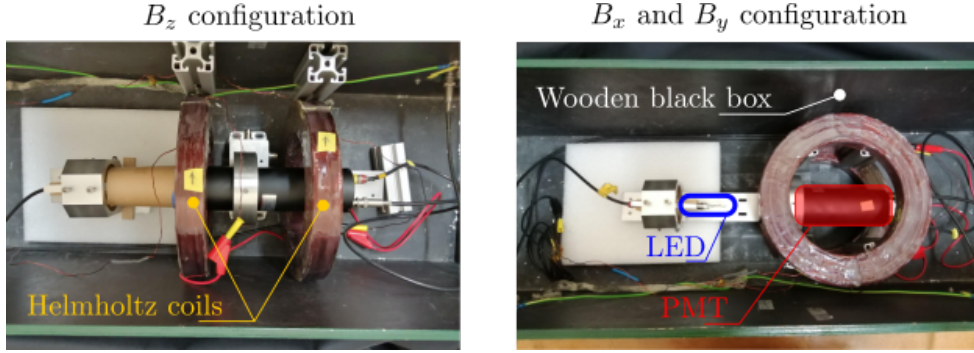


Figure F.1: Helmholtz setup for testing the influence of magnetic fields on GADGET PMTs. The applied field coincides with the axial PMT direction (B_z) in the left configuration and with the radial direction (B_x and B_y) in the right configuration. The same elements are used for both configurations.

A dedicated test to probe the influence of magnetic fields on GADGET PMTs took place at the *dark room* at LPC. The setup consisted of an LED placed in front of one of GADGET's 2" PMTs (type H13795-100-Y001), a 20-cm-diameter Helmholtz coil providing a uniform magnetic field of up to 1 mT, and a wooden black box within which the setup was installed. In order to apply the Helmholtz central magnetic field to different regions of the PMT (the PMT length is about the coil diameter), the PMT readout was recorded while shifting its position within the Helmholtz coil. A top view of the arrangement is displayed in Figure F.1. Whereas magnetic fields pointing in the PMT radial direction are denoted as B_x and B_y (B_x is obtained from B_y by rotating the PMT 90° about its axis), magnetic fields along PMT's axial direction are denoted as B_z . The LED pulses were controlled from a signal generator that provided voltage pulses of 50 ns width with a frequency of 2 kHz. Variation of the voltage in the LED circuit are estimated in 0.2%.

The power supplied to the LED was adjusted so to produce a charge distribution in the PMT readout much larger than the electronic noise. Such charge distributions were recorded for magnetic fields in the three directions with intensities as large as 1 mT (negative values correspond to backwards flow of the current). The charge distribution centroids, obtained from Gaussian fits of each magnetic field configuration, were compared relative to the zero

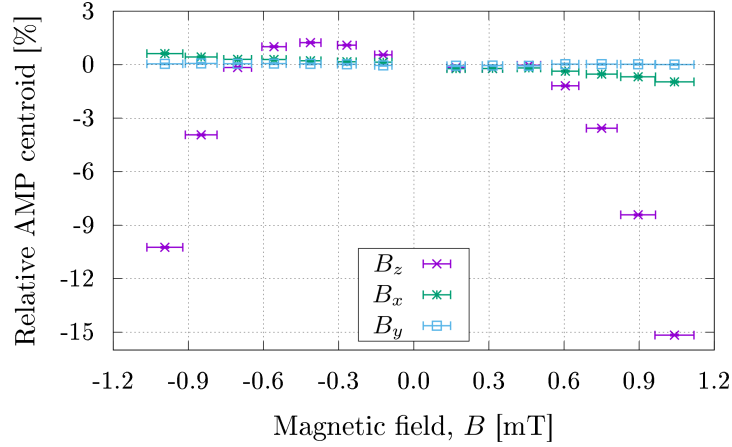


Figure F.2: Magnetic field influence on the GADGET PMTs readout.

magnetic field configuration. The results, plotted in Figure F.2, show that the most significant variation are generated by B -fields applied along the PMT's axial direction (B_z). On the other hand, radial fields B_x and B_y in the tested range show little deviations from the zero-field configuration. This is consistent with the expectations since the PMT electron cascades travel in trajectories perpendicular to B_z (see linear-focused PMTs in [94]), thus making the Lorentz force ($\propto \vec{v}_{\text{UCN}} \times \vec{B}$) somewhat bigger. Although the pulse counting rate did not change for the magnetic fields reported here, given the observed charge spectra deviations, PMTs should not be operated in environments with magnetic fields larger than 0.6 mT.

Appendix G

The n2EDM spin-sensitive counter

Many times, UCN experiments are concerned with the polarization of neutrons. For instance, the very precise measurement of the UCN precession frequency in the EDM measurement rely on the counting of spin-up and spin-down populations [103]. Given that the energy released by the capture reactions in neutron detectors is independent of their polarization, determination of its spin state is usually not performed at the detection stage*. Instead, an extra module composed of a spin-flipper and an analyzing foil has been included in several UCN setups [71, 100, 107]. This appendix is dedicated to expose the COMSOL model of the next n2EDM U-Shape-Spin-Analyzer (USSA) system.

G.1 Working principle

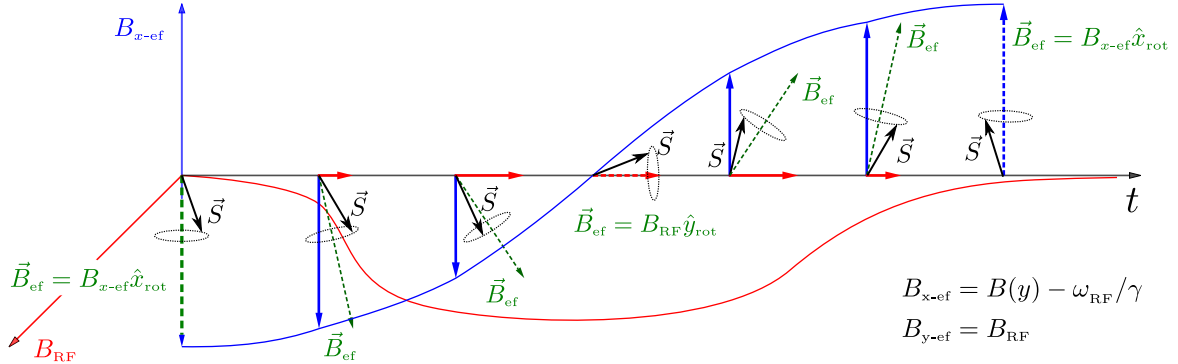


Figure G.1: Illustration of the spin-flipping process in a reference frame moving with the UCN and rotating about $\hat{x} = \hat{x}_{\text{rot}}$ with frequency ω_{RF} . The spin-flip is achieved as the UCN travels (along $y(t)$) within the static field $B(y)$ (with gradient $\nabla_y B(y(t)) > 0$) and the perpendicular RF-field B_{RF} . If the adiabatic condition is fulfilled (Eq. (G.2)), the UCN precessing spin is capable of following the \vec{B}_{ef} field inversion. The red axis is used to represent the magnitude of B_{RF} , but not its direction. The latter is indicated by the red arrows.

Spin sensitive systems are of basic construction. Their functioning is explained by the

*A ^3He -based spin sensitive filter is for example described in [106]

simultaneous operation of two modules, a spin-flipper, capable of reversing the polarization of UCN, and a spin-filter (or spin analyzer), responsible for the reflection and transmission of UCN depending on their polarization. Whereas the latter blocks the passage of UCN with a spin down component, the former prepares neutrons in either polarization state.

A spin analyzer consists of a thin foil ($\sim 10 \mu\text{m}$) made of a material with low Fermi potential (aluminum is normally the case: $V_{\text{Fermi}} = 54 \text{ neV}$) covered by a finer magnetic layer. Iron is often the most preferred option ($V_{\text{Fermi}} = 210 \text{ neV}$). If applying an external magnetic field so to fully magnetize the finer layer (larger than 60 mT for iron), added to the Fermi potential, UCN experience a magnetic potential U_{mag} (see section 1.5.1). When reaching the foil, UCN would then observe a potential barrier equals to

$$U_{\text{tot}} = V_{\text{Fermi}} \pm U_{\text{mag}} = (210 \pm 120) \text{ neV}, \quad (\text{G.1})$$

where the sign ‘+’ (‘-’) goes for spin-down (spin-up) UCN and the numerical values correspond to the materials mentioned above. In this way, whereas spin-up UCN see a 90 neV barrier, spin-down UCN experience a barrier of 330 neV. Provided that UCN kinetic energies are contained within this range, all spin-down (spin-up) UCN are reflected of (transmitted through) the analyzing foil. With such a total barrier, one can determine the number of spin-up neutrons by counting the UCN behind the analyzing foil. On the other hand, to determine the number of spin-down neutrons, a spin-flipper is added in the setup just before the spin analyzer. If it is activated, UCN finding their way through the analyzer are those with initial spin-down polarization.

Similar to the RF pulses used to invert spin states in Rabi oscillations, a spin-flipper employs an RF field to adiabatically change the polarization of UCN. This process, illustrated in Figure G.1, requires a positive static magnetic field ($\vec{B}_{\text{static}} = B_{\text{static}}\hat{x}$) perpendicular to a RF field ($\vec{B}_{\text{RF}} = B_{\text{RF}}(\cos(\omega_{\text{RF}})\hat{y} + \sin(\omega_{\text{RF}})\hat{z})$) and featuring a positive gradient in the direction of UCN propagation (here chosen \hat{y}), i.e. $\vec{B}_{\text{static}} = B(y)\hat{x}$ with $\nabla_y B(y) > 0$. To see how the combination of \vec{B}_{static} and \vec{B}_{RF} induce a spin-flip, let us move to the UCN reference frame rotating with frequency ω_{RF} around $\hat{x} = \hat{x}_{\text{rot}}$. In such a frame, the effective magnetic experience by the UCN is

$$\begin{aligned} B_{x\text{-ef}} &= B(y) - \omega_{\text{RF}}/\gamma \\ B_{y\text{-ef}} &= B_{\text{RF}} \\ B_{z\text{-ef}} &= 0, \end{aligned}$$

with γ the neutron gyro-magnetic ratio. Note that in this frame, the RF-field is static along \hat{y}_{rot} and according to the transformation rules of rotating frames, an additional field $-\omega_{\text{RF}}/\gamma$ appears along \hat{x}_{rot} . One can then see that, as UCN travel towards \hat{y} through the RF-field, the effective field $B_{x\text{-ef}}$ goes from $-\omega_{\text{RF}}/\gamma$, far from the static field source ($y \rightarrow -\infty$), to $B_{x\text{-ef}} \approx B(y)$ after crossing the field gradient. UCN spins precessing around the total effective field follow this $B_{x\text{-ef}}$ field inversion, provided that the $B_{x\text{-ef}}$ rate of change is much smaller than the Larmor precession frequency. Such condition, referred to as the adiabatic condition, reads [108]:

$$k = \frac{\gamma_n B_{\text{ef}}^3}{d(B_{x\text{-ef}})/dt \cdot B_{\text{RF}}} \gg 1. \quad (\text{G.2})$$

G.2 Past USSA and new version requirements

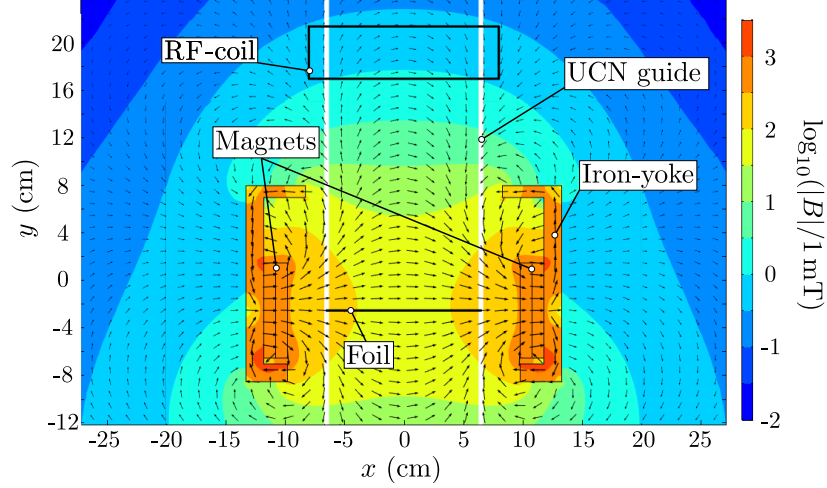


Figure G.2: Side view of the static magnetic fields of the nEDM magnetization system generated from COMSOL simulations. If using 130-mm-diameter UCN guides, the perpendicularity between \vec{B}_{RF} and \vec{B}_{static} need for a correct spin flipping within the RF-coil is not fulfilled at the guide edges. UCN flux goes from top to bottom. A 3D view can be grasped from similar USSA versions in Figure G.5.

The former USSA design, used in the nEDM experiment [109], consists of a UCN beam separating piece connected to two symmetric arms. Each arm, dedicated to the counting of one of the spin components, counts with an RF-coil placed about 20 cm above an analyzing foil (see a cross-section view of one of the arms in Figure G.2). An iron yoke hosts a set of permanent magnets which enclose both arms at the level of the analyzing foils. Whereas the RF-coils produce an alternating field along the UCN guide axis (\hat{y}), the yoke and magnets provide the static magnetic field gradient necessary for the spin-flip and to fully magnetize the analyzing foils. The color map and field arrows in Figure G.2 represent the static field generated by the permanent magnets and shaped by the yoke obtained from COMSOL simulations.

Previous tests with this USSA and the new n2EDM UCN guides, revealed a low spin-flipping efficiency: $\sim 73\%$ (private communication, J. Chen). The reason for such a poor functioning is explained by the static field lines. As stated above, a correct spin-flipping process is achieved by totally perpendicular RF and static fields. However, this perpendicularity is not always fulfilled by the small nEDM yoke mounted on the wider n2EDM guides. In nEDM the UCN guide side (squared cross-section) was 80 mm while in n2EDM, the UCN guide diameter (circular cross-section) is 130 mm. One can corroborate in Figure G.2 that the static field arrows do not always point in the \hat{x} direction. Instead, they have a large vertical component (B_y) next to the n2EDM guide edges. Because of this bad coupling between nEDM's USSA and the new wider UCN guides, the n2EDM project requires the construction of an updated spin analyzing system (especially the yoke).

G.3 Modeling the n2EDM USSA

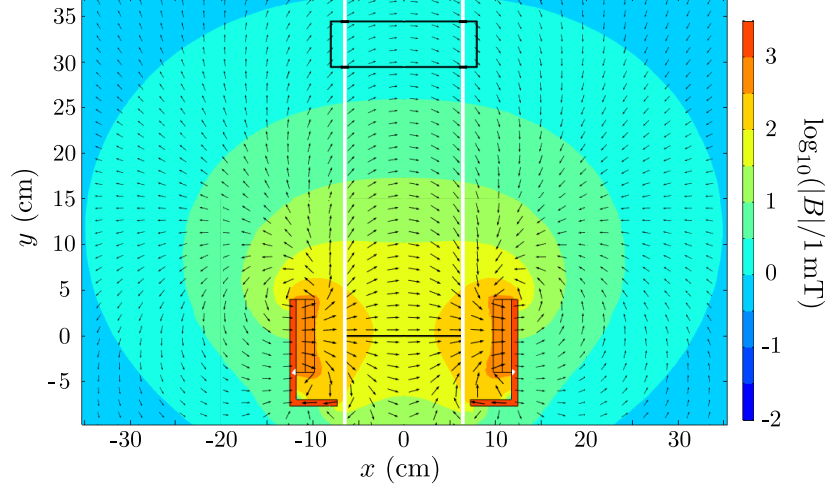


Figure G.3: Side view of the static magnetic fields of the n2EDM magnetization system generated from COMSOL simulations. Compared to the previous version, the yoke top flanges are removed so to fix the field horizontality at the RF-coil (green box).

The new USSA design takes as reference the nEDM version presented above. First, in order to fix the non-perpendicularity at the guide edges, the yoke top flanges are removed from the geometry and the RF-coil is displaced by 10 cm upwards (see Figure G.3). Note that the static field is mostly horizontal at the new RF-coil position. Although the yoke top flanges were initially installed to reduce the field intensity at the RF-coil position, their removal does not represent a big problem. In fact, since the larger the static field, the higher the RF frequency has to be so to guarantee a zero-crossing point in $B_{x\text{-ef}} = B(y) - \omega_{\text{RF}}/\gamma$, the top flange suppression translates into larger RF-frequencies. Whereas the static field was of about 0.7 mT at the RF-coil (whose operation frequency was set to 20 kHz) in nEDM's USSA, the model presented in Figure G.3 suggest placing the RF-coil at $y = 33.5 \text{ cm}^\dagger$ where the static field is of 1.4 mT with a gradient of 0.14 mT/cm. Such a factor 2 between both static field magnitudes is compensated by a two times larger RF-frequency in the new model: $\sim 42 \text{ kHz}$.

Magnetization foil

A side effect of removing the yoke top flanges is the reduction of the static field intensity in the middle plane between the magnets. Since the spin-analyzer foils are located within this region, one has to check that field strength does not go below the minimum value required to magnetize the thin foil up to saturation (60 mT). To compensate for the static field weakening at $y = 0$ and because the UCN guides are guider, the new USSA model adds more magnets along the \hat{z} direction. Figure G.4 shows a top view of the magnetic field strength within

[†]This distance corresponds to the separation between the analyzing foil and the RF-coil center. More details of the RF-coil geometry are resumed in G.2

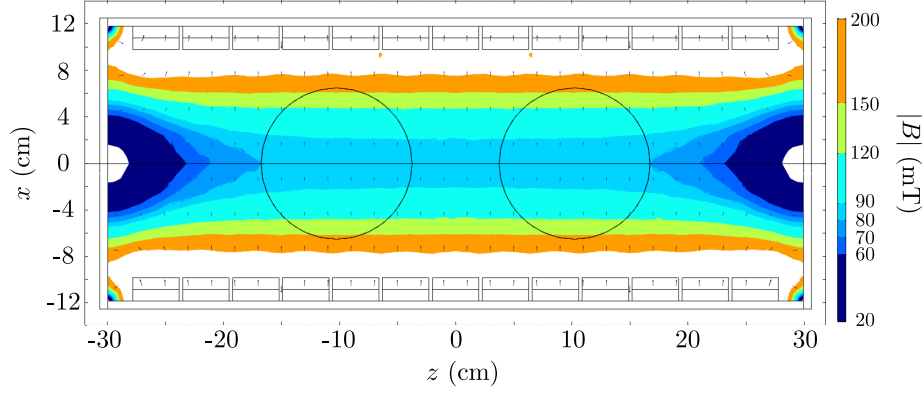


Figure G.4: Static field intensity on the $y = 0$ plane. The small squares represent the permanent magnets and the circles the position of the analyzing foils.

the magnetization system at $y = 0$. One can corroborate that by gathering 13 columns of magnets, the minimum static field at the foils (black circles) is of ~ 80 mT and are located at the outermost sides of the yoke ($z = \pm 17$ cm). Provided that the analyzing foils are kept within these limits, their full magnetization should be attained.

Yoke stray field at the level of the GADGET detector

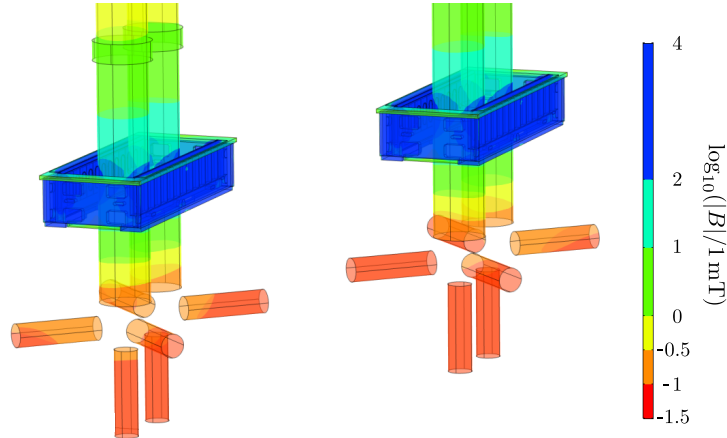


Figure G.5: 3-dimensional representation of the magnetic field strength on top of both n2EDM USSA surfaces. The relative position between both USSA is the one of the n2EDM setup.

GADGET will also be used as UCN counter in the n2EDM project. Therefore, it is essential to consider the magnetic field constraints required for a correct GADGET performance. Detailed discussions on the sensitivity of GADGET to magnetic fields were already presented in section 3.4.2 and in the Appendix F. Results obtained in these studies, are used to shape the new USSA model within COMSOL simulations. In particular, the yoke bottom flanges are wider than in the previous USSA version to enclose the field lines within the yoke and therefore to have a stray field with a lower intensity at the GADGET PMTs level. Also, given

that the n2EDM project employs two USSA next to each other, it is necessary to guarantee that the superposition from both magnetization systems does not produce a magnetic field too large at the PMTs position. Figure G.5 shows a 3-dimensional view of both COMSOL simulated USSAs, where the color surfaces indicate the magnetic field strength. This color map results from a geometry with 30 cm between the analyzing foil and the detector entrance window. Note that the yellow-to-orange boundaries, that correspond to 0.3 mT, leaves PMTs outside magnetic fields larger than 0.3 mT. Operating the PMTs at such field intensities does not provoke a change on the counting rate, but might slightly ($\sim 1\%$, see Figure F.1) deviate the charge spectra. This is not crucial for the n2EDM setup as the position of GADGET is not expected to change during the data taking.

G.3.1 Shaping the RF-field

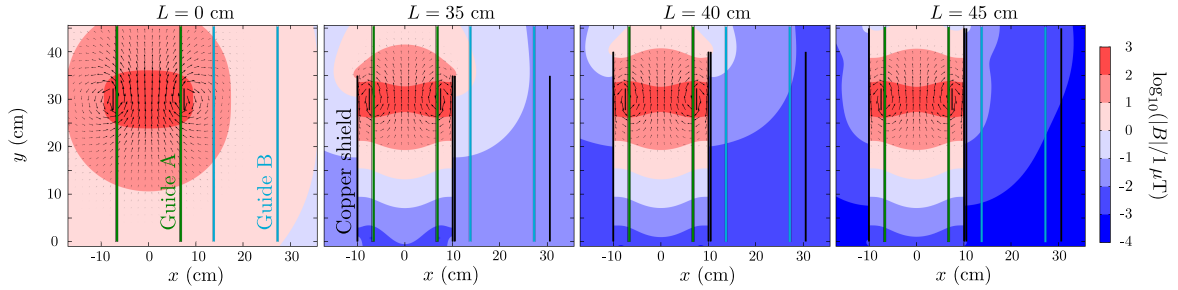


Figure G.6: Influence of a cylindrical RF-shielding with height L on the field strength along the opposite USSA arm.

One last feature to be evaluated for the new USSA model is the cross-talk between the spin-flippers in both USSA arms: the RF-field in one arm should not induce a spin-flip of UCN going through the opposite arm. To isolate the RF fields, copper shields are placed around the USSA arms. These shields, designed with cylindrical shapes, should not be too close to the RF-coils so that the magnetic fields raised by the Lenz effect in the shield are negligible. Also, they cannot be too large due to space constraints. By leaving a distance between the UCN guide and the RF-coil of 5 mm and between the RF-coil and the shielding of 25 mm, each arm shield is free of significant Lenz fields for RF currents of up to 1 A. Optimization of the shield height (L) is determined by estimating the RF-field generated by one arm (let us call it Guide A) in the opposite arm (Guide B). Figure G.6 shows the RF-field intensities on the plane $z = 0$ for different L . By making $L = 40$ cm, the parasite RF-field in Guide B is lower than $0.1 \mu\text{T}$, i.e. 3 orders of magnitude lower than the intensity needed for correct spin-flipping. The validation of this shield height is presented in the next subsection.

G.3.2 Efficiency estimation from spin tracking algorithms

A first characterization of the new USSA model can be made from spin tracking algorithms which take into account the COMSOL magnetic field maps. A toy simulation of the spin state of UCN crossing the USSA volume is implemented by solving numerically the spin-evolution equation

$$\frac{d\vec{S}}{dt} = \gamma [\vec{S} \times \vec{B}], \quad (\text{G.3})$$

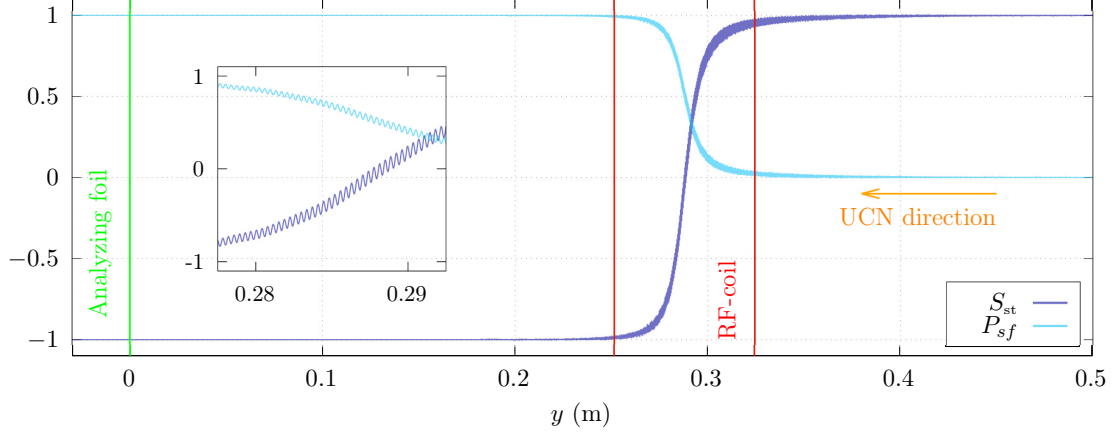


Figure G.7: Sample spin track trajectory obtained from the numerical solution of Eq. (G.3). The displayed trajectory corresponds to an RF placed at $y = 0.29$ m. The spin-flipping probability (P_{sf}) is computed from the spin projection on the static field S_{st} through Eq. (G.9).

equivalently written as

$$\begin{pmatrix} \dot{S}_x \\ \dot{S}_y \\ \dot{S}_z \end{pmatrix} = \gamma \begin{pmatrix} B_z S_y - B_y S_z \\ B_x S_z - B_z S_x \\ B_y S_x - B_x S_y \end{pmatrix}. \quad (\text{G.4})$$

This system of coupled differential equations is solved through the Runge-Kutta-4 algorithm while updating the magnetic field after each time step. In order to guarantee that the numerical truncation error does not change the spin magnitude by more than 1/10000, i.e. $\delta|\vec{S}| < 0.01\%$, the time step size is conventionally chosen much smaller than the Larmor precession period: $\Delta t = T_{\text{Larmor}}/500$. Regarding the magnetic field description, it includes the RF-field and the static field as

$$\vec{B} = \vec{B}_{\text{RF}} + \vec{B}_{\text{static}} \quad (\text{G.5})$$

$$= B_{\text{RF}}(\vec{r}) \begin{pmatrix} 0 \\ \sin(\omega_{\text{RF}} t) \\ \cos(\omega_{\text{RF}} t) \end{pmatrix} + \begin{pmatrix} B_x(\vec{r}) \\ B_y(\vec{r}) \\ B_z(\vec{r}) \end{pmatrix}_{\text{static}}, \quad (\text{G.6})$$

where $B_{\text{RF}}(\vec{r})$ and $\vec{B}_{\text{static}}(\vec{r})$ are interpolated from the COMSOL simulated maps at each spatial step $\vec{r}_{i+1} = \vec{r}_i + \Delta\vec{r}$, with $\Delta\vec{r} = \vec{v}_{\text{UCN}}\Delta t$. To keep a simple algorithm, the UCN trajectories are all constructed by assuming entirely straight paths: $\vec{v}_{\text{UCN}} = v_y \hat{y} = -5 \text{ m/s } \hat{y}$. UCN initial positions are defined as $\vec{r}_0 = (x_0, 0.5 \text{ m}, z_0)$, with x_0 and z_0 randomly chosen within the UCN guide section:

$$x_0^2 + z_0^2 < R_{\text{guide}}^2, \quad (\text{G.7})$$

with $R_{\text{guide}} = 65 \text{ mm}$ the guide radius.

Since UCN in the n2EDM setup are expected to be immersed in an external magnetic field which drives the spin polarization from the precession chambers to the USSA (see [16]), the initial spin polarization within the spin tracking algorithm is determined by the static

field direction at \vec{r}_0 . The spin polarization is then written as

$$S_{\text{st}} = \vec{S} \cdot \frac{\vec{B}_{\text{static}}}{\|\vec{B}_{\text{static}}\|}. \quad (\text{G.8})$$

Figure G.7 shows an ordinary UCN spin track obtained from the implemented algorithm as a function of the y -coordinate. One can evidence how the spin projection onto the static field direction is inverted as the UCN crosses the RF-coil volume: $S_{\text{st}} = 1$ at $\vec{r}_0 = 0.5 \text{ m } \hat{y}$ ($t = 0$) becomes $S_{\text{st}} = -1$ at the analyzing foil $\vec{r} = 0$ ($t = 0.5 \text{ m}/(5 \text{ m/s}) = 0.1 \text{ s}$). The wiggling pattern depicted in the zoomed plot illustrates the precession movement of the spin about the magnetic field direction. Using the magnitude of S_{st} , the spin-flipping probability computed as [110]

$$P_{sf} = \frac{1}{2}(1 - S_{\text{st}}). \quad (\text{G.9})$$

is also plotted in Figure G.7 in light-blue. Note that, for the sample track, the flipping probability is zero at $t = 0$, but becomes almost 1 once the UCN crosses the RF-field. Therefore, if the analyzing foil is fully magnetized, such a spin down UCN would be reflected from the magnetic barrier.

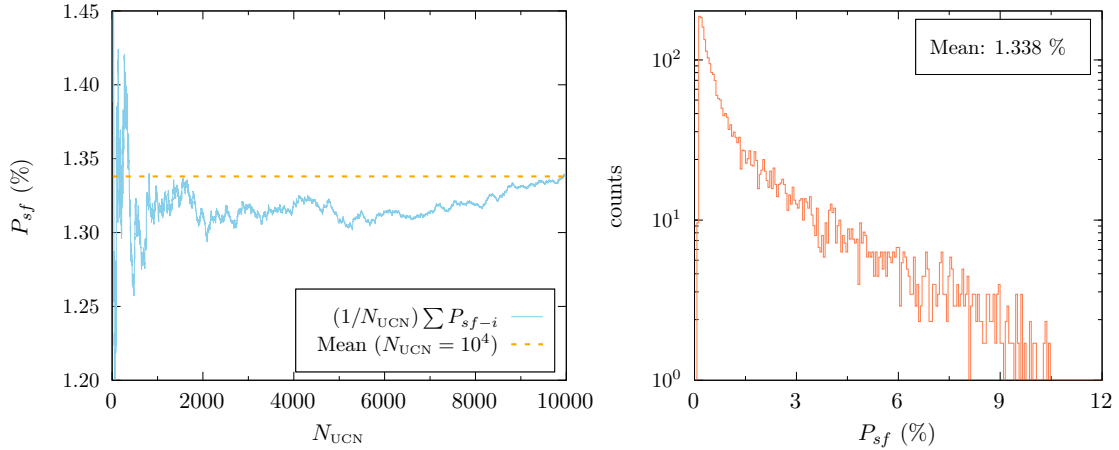


Figure G.8: Spin-flipping probability due to the cross-talk between USSA arms if no RF-shield is included. The left side plot shows the probability as a function of the number of simulated UCN tracks. The total distribution is illustrated on the histogram of the right side.

The spin tracking algorithm was used as validation tool at each USSA model modification, where the simulation of $N_{\text{UCN}} = 10^4$ UCN tracks was required to yield a large spin-flipping probability ($\bar{P}_{sf} > 99\%$). Although this spin-flipping study is not reported here for all the USSA model construction stages, it is presented for the last modification: the RF shielding length L optimization (see previous section). For example, Figure G.8 shows the spin-flipping probability of UCN going through the Guide B due to the RF-coil of Guide A if no RF shielding is used. One can see that after many UCN tracks, the mean spin-flipping is not negligible (it converges to $\sim 1.33\%$), i.e. there is a parasite cross-talk between both USSA

Table G.1: Spin flipping probability generated from cross-talk between USSA arms for different RF-shield lengths.

Shield length (cm)	Mean flipping probability (%)
45	10^{-5}
40	3×10^{-5}
35	0.35
30	0.53
0 (no shield)	1.33

arms[‡]. To determine the shield length necessary to suppress this behavior, the mean spin-flipping probability was evaluated as a function of L . The output from the several simulations is resumed in Table G.1. It was concluded that a good shielding was achieved with a shield of 40 cm.

G.3.3 Summary

Table G.2: First n2EDM USSA model summary.

Yoke	Magnets	4 rows of 13 magnets each Magnetization: 900 kA/m Size: $80 \times 40 \times 10$ mm ³
	Iron layers	Thickness: 7 mm Large side: 110×559 mm ² Small side: 110×250 mm ² Bottom flange: 52×559 mm ²
RF-coil		Diameter: 150 mm Current: 1 A Frequency: 42 kHz No. turns: 25 Wire diameter: 1.8 mm Position: 335 mm (from analyzing foil)
B at the RF-coil center	Static	$B_{\text{static}} : 1.44$ mT $\nabla_y B_{x\text{-static}} : 0.14$ mT/cm
	RF	$B_{\text{RF}} : 122$ μ T
RF-shield		Length: 400 mm Diameter: 200 mm Thickness: 1 mm
GADGET		Entrance window: > 300 mm below the foil

The spin flipping efficiency of the USSA COMSOL model presented in this section was larger than 99.9% with a cross-talk effect estimated in $3 \times 10^{-5}\%$. Such features are good enough for finishing this first prototype model, whose main dimensions and most relevant

[‡]This result was the one that motivated the inclusion of the copper shield.

quantities are resumed in Table G.2. The yoke system and RF-coils were already commissioned and experimentally tested at PSI in June 2022. The results will be published in the upcoming months.

Bibliography

- [1] Gia Dvali and Michele Redi. Phenomenology of 10^{32} dark sectors. *Physical Review D*, 80(5), sep 2009.
- [2] R. Foot, H. Lew, and R. R. Volkas. Possible consequences of parity conservation. *Modern Physics Letters A*, 07(28):2567–2574, 1992.
- [3] Michaël Sarrazin and Fabrice Petit. Equivalence between domain walls and “noncommutative” two-sheeted spacetimes: Model-independent matter swapping between branes. *Physical Review D*, 81(3), feb 2010.
- [4] Zurab Berezhiani, Denis Comelli, and Francesco L. Villante. The early mirror universe: inflation, baryogenesis, nucleosynthesis and dark matter. *Physics Letters B*, 503(3):362–375, 2001.
- [5] S. V. Demidov, D. S. Gorbunov, and A. A. Tokareva. Positronium oscillations to mirror world revisited. *Physical Review D*, 85(1), jan 2012.
- [6] Sebastian Böser, Christian Buck, Carlo Giunti, Julien Lesgourgues, Livia Ludhova, Susanne Mertens, Anne Schukraft, and Michael Wurm. Status of light sterile neutrino searches. *Progress in Particle and Nuclear Physics*, 111:103736, 2020.
- [7] G. Ban, K. Bodek, M. Daum, R. Henneck, S. Heule, M. Kasprzak, N. Khomutov, K. Kirch, S. Kistryn, A. Knecht, P. Knowles, M. Kuźniak, T. Lefort, A. Mtchedlishvili, O. Naviliat-Cuncic, C. Plonka, G. Quémener, M. Rebetez, D. Rebreyend, S. Roccia, G. Rogel, M. Tur, A. Weis, J. Zejma, and G. Zsigmond. Direct experimental limit on neutron–mirror-neutron oscillations. *Physical Review Letters*, 99(16), oct 2007.
- [8] A.P. Serebrov, E.B. Aleksandrov, N.A. Dovator, S.P. Dmitriev, A.K. Fomin, P. Geltenbort, A.G. Kharitonov, I.A. Krasnoschekova, M.S. Lasakov, A.N. Murashkin, G.E. Shmelev, V.E. Varlamov, A.V. Vassiljev, O.M. Zhrebtssov, and O. Zimmer. Experimental search for neutron–mirror neutron oscillations using storage of ultracold neutrons. *Physics Letters B*, 663(3):181–185, 2008.
- [9] I. Altarev, C. A. Baker, G. Ban, K. Bodek, M. Daum, P. Fierlinger, P. Geltenbort, K. Green, M. G. D. van der Grinten, E. Gutsmedl, P. G. Harris, R. Henneck, M. Horras, P. Iaydjiev, S. Ivanov, N. Khomutov, K. Kirch, S. Kistryn, A. Knecht, P. Knowles, A. Kozela, F. Kuchler, M. Kuźniak, T. Lauer, B. Lauss, T. Lefort, A. Mtchedlishvili, O. Naviliat-Cuncic, S. Paul, A. Pazgalev, J. M. Pendlebury, G. Petzoldt, E. Pierre, C. Plonka-Spehr, G. Quémener, D. Rebreyend, S. Roccia, G. Rogel, N. Severijns,

- D. Shiers, Yu. Sobolev, R. Stoepler, A. Weis, J. Zejma, J. Zenner, and G. Zsigmond. Neutron to mirror-neutron oscillations in the presence of mirror magnetic fields. *Physical Review D*, 80(3), aug 2009.
- [10] Z. Berezhiani, R. Biondi, P. Geltenbort, I. A. Krasnoshchekova, V. E. Varlamov, A. V. Vassiljev, and O. M. Zhrebtsov. New experimental limits on neutron – mirror neutron oscillations in the presence of mirror magnetic field. *The European Physical Journal C*, 78(9), sep 2018.
- [11] C. Abel, N.J. Ayres, G. Ban, G. Bison, K. Bodek, V. Bondar, E. Chancel, P.-J. Chiu, C. Crawford, M. Daum, R.T. Dinani, S. Emmenegger, P. Flaux, L. Ferraris-Bouchez, W.C. Griffith, Z.D. Grujić, N. Hild, K. Kirch, H.-C. Koch, P.A. Koss, A. Kozela, J. Krempel, B. Lauss, T. Lefort, A. Leredde, P. Mohanmurthy, O. Naviliat-Cuncic, D. Pais, F.M. Piegsa, G. Pignol, M. Rawlik, D. Rebreyend, I. Rienäcker, D. Ries, S. Rocchia, D. Rozpedzik, P. Schmidt-Wellenburg, N. Severijns, J. Thorne, A. Weis, E. Wursten, J. Zejma, and G. Zsigmond. A search for neutron to mirror-neutron oscillations using the nedm apparatus at psi. *Physics Letters B*, 812:135993, 2021.
- [12] Michaël Sarrazin, Guillaume Pignol, Jacob Lamblin, Fabrice Petit, Guy Terwagne, and Valery V. Nesvizhevsky. Probing the braneworld hypothesis with a neutron-shining-through-a-wall experiment. *Physical Review D*, 91(7), apr 2015.
- [13] Coraline Stasser, Guy Terwagne, Jacob Lamblin, Olivier Méplan, Guillaume Pignol, Bernard Coupé, Silva Kalcheva, Steven Van Dyck, and Michaël Sarrazin. Probing neutron-hidden neutron transitions with the MURMUR experiment. *The European Physical Journal C*, 81(1), jan 2021.
- [14] H. Almazán, L. Bernard, A. Blanchet, A. Bonhomme, C. Buck, P. del Amo Sanchez, I. El Atmani, L. Labit, J. Lamblin, A. Letourneau, D. Lhuillier, M. Licciardi, M. Lindner, T. Materna, O. Méplan, H. Pessard, G. Pignol, J.-S. Réal, J.-S. Ricol, C. Roca, R. Rogly, T. Salagnac, M. Sarrazin, V. Savu, S. Schoppmann, T. Soldner, A. Stutz, and M. Vialat. Searching for hidden neutrons with a reactor neutrino experiment: Constraints from the stereo experiment. *Phys. Rev. Lett.*, 128:061801, Feb 2022.
- [15] L. J. Broussard, J. L. Barrow, L. DeBeer-Schmitt, T. Dennis, M. R. Fitzsimmons, M. J. Frost, C. E. Gilbert, F. M. Gonzalez, L. Heilbronn, E. B. Iverson, A. Johnston, Y. Kamyshev, M. Kline, P. Lewiz, C. Matteson, J. Ternullo, L. Varriano, and S. Vavra. Experimental search for neutron to mirror neutron oscillations as an explanation of the neutron lifetime anomaly. *Phys. Rev. Lett.*, 128:212503, May 2022.
- [16] N. J. Ayres, G. Ban, L. Bienstman, G. Bison, K. Bodek, V. Bondar, T. Bouillaud, E. Chancel, J. Chen, P.-J. Chiu, B. Clément, C. B. Crawford, M. Daum, B. Dechenaux, C. B. Doorenbos, S. Emmenegger, L. Ferraris-Bouchez, M. Fertl, A. Fratangelo, P. Flaux, D. Goupillière, W. C. Griffith, Z. D. Grujic, P. G. Harris, K. Kirch, P. A. Koss, J. Krempel, B. Lauss, T. Lefort, Y. Lemièrre, A. Leredde, M. Meier, J. Menu, D. A. Mullins, O. Naviliat-Cuncic, D. Pais, F. M. Piegsa, G. Pignol, G. Quémener, M. Rawlik, D. Rebreyend, I. Rienäcker, D. Ries, S. Rocchia, K. U. Ross, D. Rozpedzik, W. Saenz, P. Schmidt-Wellenburg, A. Schnabel, N. Severijns, B. Shen, T. Stapf, K. Svirina,

- R. Tavakoli Dinani, S. Touati, J. Thorne, R. Viot, J. Voigt, E. Wursten, N. Yazdandoost, J. Zejma, and G. Zsigmond. The design of the n2edm experiment. *The European Physical Journal C*, 81(6), jun 2021.
- [17] Zurab Berezhiani. More about neutron–mirror neutron oscillation. *The European Physical Journal C*, 64(3), 2009.
- [18] Ya. B. Zeldovich. *Sov.Phys.JETP*, 9:1389–90, 1959.
- [19] A. Steyerl. Measurements of total cross sections for very slow neutrons with velocities from 100 m/sec to 5 m/sec. *Physics Letters B*, 29(1):33–35, 1969.
- [20] Rabindra N. Mohapatra and Shmuel Nussinov. Constraints on mirror models of dark matter from observable neutron-mirror neutron oscillation. *Physics Letters B*, 776:22–25, jan 2018.
- [21] William Saenz. A gaseous detector for ultracold neutrons in the n2EDM project. Master’s thesis, University of Caen - Normandie, 2019.
- [22] A. Kaboth, J. Monroe, S. Ahlen, D. Dujmic, S. Henderson, G. Kohse, R. Lanza, M. Lewandowska, A. Roccaro, G. Sciolla, N. Skvorodnev, H. Tomita, R. Vanderspek, H. Wellenstein, R. Yamamoto, and P. Fisher. A measurement of photon production in electron avalanches in cf4. *Nuclear Instruments and Methods in Physics Research Section A: Accelerators, Spectrometers, Detectors and Associated Equipment*, 592(1):63–72, 2008.
- [23] G. Lehaut, S. Salvador, J.-M. Fontbonne, F.-R. Lecolley, J. Perronnel, and Ch. Vandamme. Scintillation properties of n2 and cf4 and performances of a scintillating ionization chamber. *Nuclear Instruments and Methods in Physics Research Section A: Accelerators, Spectrometers, Detectors and Associated Equipment*, 797:57–63, 2015.
- [24] Gwendal Rogel. *Développement de détecteurs de neutrons ultra-froids et d’un système d’analyse de polarisation pour la mesure de l’EDM du neutron*. PhD thesis, 2009.
- [25] Faster qt2t mnm user manual. <http://faster.in2p3.fr/index.php/documentation?download=24:faster-qt2t-mnm-user-manual-pdf>. Accessed: 2022-01-02.
- [26] James F. Ziegler, M.D. Ziegler, and J.P. Biersack. Srim – the stopping and range of ions in matter (2010). *Nuclear Instruments and Methods in Physics Research Section B: Beam Interactions with Materials and Atoms*, 268(11):1818–1823, 2010. 19th International Conference on Ion Beam Analysis.
- [27] Mathieu Guigue. *À la recherche de nouvelles forces avec l’hélium 3 polarisé*. PhD thesis, Université de Grenoble, 2015.
- [28] M. Baldo-Ceolin, P. Benetti, T. Bitter, F. Bobisut, E. Calligarich, R. Dolfini, D. Dubbers, P. El-Muzeini, Massimo Genoni, D. Gibin, A. Berzolari, K. Gobrecht, A. Guglielmi, Jürgen Last, Marco Laveder, W. Lippert, F. Mattioli, F. Mauri, Mauro Mezzetto, and L. Visentin. A new experimental limit on neutron-antineutron oscillations. *Zeitschrift für Physik C Particles and Fields*, 63:409–416, 09 1994.

- [29] T. D. Lee and C. N. Yang. Question of parity conservation in weak interactions. *Phys. Rev.*, 104:254–258, Oct 1956.
- [30] Lev B Okun'. Mirror particles and mirror matter: 50 years of speculation and searching. *Physics-Uspekhi*, 50(4):380–389, apr 2007.
- [31] C. S. Wu, E. Ambler, R. W. Hayward, D. D. Hoppes, and R. P. Hudson. Experimental test of parity conservation in beta decay. *Phys. Rev.*, 105:1413–1415, Feb 1957.
- [32] J. H. Christenson, J. W. Cronin, V. L. Fitch, and R. Turlay. Evidence for the 2π decay of the K_2^0 meson. *Phys. Rev. Lett.*, 13:138–140, Jul 1964.
- [33] R. Foot. Mirror dark matter: Cosmology, galaxy structure and direct detection. *International Journal of Modern Physics A*, 29(11n12):1430013, 2014.
- [34] G. Dvali. Black holes and large n species solution to the hierarchy problem. *Fortschritte der Physik*, 58(6):528–536, apr 2010.
- [35] Michaël Sarrazin and Fabrice Petit. Brane matter, hidden or mirror matter, their various avatars and mixings: many faces of the same physics. *The European Physical Journal C*, 72(11), nov 2012.
- [36] R. Foot, A.Yu. Ignatiev, and R.R. Volkas. Physics of mirror photons. *Physics Letters B*, 503(3-4):355–361, mar 2001.
- [37] R. Bernabei, P. Belli, V. Caracciolo, R. Cerulli, V. Merlo, F. Cappella, A. d’Angelo, A. Incicchitti, C. J. Dai, X. H. Ma, X. D. Sheng, F. Montecchia, and Z. P. Ye. The dark matter: Dama/libra and its perspectives, 2021.
- [38] C. E. Aalseth, P. S. Barbeau, J. Colaresi, J. I. Collar, J. Diaz Leon, J. E. Fast, N. E. Fields, T. W. Hossbach, A. Knecht, M. S. Kos, M. G. Marino, H. S. Miley, M. L. Miller, J. L. Orrell, and K. M. Yocum and. Cogent: A search for low-mass dark matter using p-type point contact germanium detectors. *Physical Review D*, 88(1), jul 2013.
- [39] Z. Berezhiani. *Through the looking-glass: Alice’s adventures in mirror world*, pages 2147–2195.
- [40] Robert Foot, Archil Kobakhidze, and Raymond R. Volkas. ATLAS and CMS hints for a mirror higgs boson. *Physical Review D*, 84(9), nov 2011.
- [41] Wen sheng Li, Peng fei Yin, and Shou hua Zhu. Detecting $h \rightarrow hh$ in the mirror model at the cern large hadron collider. *Physical Review D*, 76(9), nov 2007.
- [42] Z. Chacko, Hock-Seng Goh, and Roni Harnik. Natural electroweak breaking from a mirror symmetry. *Physical Review Letters*, 96(23), jun 2006.
- [43] Zackaria Chacko, David Curtin, Michael Geller, and Yuhsin Tsai. Direct detection of mirror matter in twin higgs models. *Journal of High Energy Physics*, 2021(11), nov 2021.

- [44] G. Mention, M. Fechner, Th. Lasserre, Th. A. Mueller, D. Lhuillier, M. Cribier, and A. Letourneau. Reactor antineutrino anomaly. *Physical Review D*, 83(7), apr 2011.
- [45] A. P. Serebrov, R. M. Samoilov, V. G. Ivochkin, A. K. Fomin, V. G. Zinoviev, P. V. Neustroev, V. L. Golovtsov, S. S. Volkov, A. V. Chernyj, O. M. Zherebtsov, M. E. Chaikovskii, A. L. Petelin, A. L. Izhutov, A. A. Tuzov, S. A. Sazontov, M. O. Gromov, V. V. Afanasiev, M. E. Zaytsev, A. A. Gerasimov, and V. V. Fedorov. Search for sterile neutrinos with the neutrino-4 experiment and measurement results. *Phys. Rev. D*, 104:032003, Aug 2021.
- [46] Jeffrey M. Berryman, Pilar Coloma, Patrick Huber, Thomas Schwetz, and Albert Zhou. Statistical significance of the sterile-neutrino hypothesis in the context of reactor and gallium data. *Journal of High Energy Physics*, 2022(2), feb 2022.
- [47] A. P. Serebrov, R. M. Samoilov, I. A. Mitropolsky, and A. M. Gagarsky. Neutron lifetime, dark matter and search for sterile neutrino, 2018.
- [48] Zurab Berezhiani. Neutron lifetime puzzle and neutron–mirror neutron oscillation. *The European Physical Journal C*, 79(6), jun 2019.
- [49] Zurab Berezhiani and Luís Bento. Neutron–mirror-neutron oscillations: How fast might they be? *Physical Review Letters*, 96(8), feb 2006.
- [50] D. L. Shepelyansky I. B. Khriplovich. Capture of dark matter by the solar system. *International Journal of Modern Physics D*, 18(12):1903–1912, nov 2009.
- [51] Mark G. Wolfire, Christopher F. McKee, David Hollenbach, and A. G. G. M. Tielens. Neutral atomic phases of the interstellar medium in the galaxy. *The Astrophysical Journal*, 587(1):278–311, apr 2003.
- [52] Zurab Berezhiani. Neutron lifetime and dark decay of the neutron and hydrogen. *Letters in High Energy Physics*, 2(1), 2019.
- [53] Zurab Berezhiani, Riccardo Biondi, Yuri Kamyshev, and Louis Varriano. On the neutron transition magnetic moment. *Physics*, 1(2):271–289, 2019.
- [54] Zurab Berezhiani and Fabrizio Nesti. Magnetic anomaly in ucn trapping: Signal for neutron oscillations to parallel world? *The European Physical Journal C*, 72(4), 2012.
- [55] Yu.N. Pokotilovski. On the experimental search for neutron \rightarrow mirror neutron oscillations. *Physics Letters B*, 639(3-4):214–217, aug 2006.
- [56] Zurab Berezhiani, Matthew Frost, Yuri Kamyshev, Ben Rybolt, and Louis Varriano. Neutron disappearance and regeneration from a mirror state. *Physical Review D*, 96(3), aug 2017.
- [57] N. J. Ayres, Z. Berezhiani, R. Biondi, G. Bison, K. Bodek, V. Bondar, P. J. Chiu, M. Daum, R. T. Dinani, C. B. Doorenbos, S. Emmenegger, K. Kirch, V. Kletzl, J. Krempel, B. Lauss, D. Pais, I. Rienaecker, D. Ries, N. Rossi, D. Rozpedzik, P. Schmidt-Wellenburg, K. S. Tanaka, J. Zejma, N. Ziehl, and G. Zsigmond. Improved search for

neutron to mirror-neutron oscillations in the presence of mirror magnetic fields with a dedicated apparatus at the psi ucn source, 2021.

- [58] C.A. Baker, Y. Chibane, M. Chouder, P. Geltenbort, K. Green, P.G. Harris, B.R. Heckel, P. Iaydjiev, S.N. Ivanov, I. Kilvington, S.K. Lamoreaux, D.J. May, J.M. Pendlebury, J.D. Richardson, D.B. Shiers, K.F. Smith, and M. van der Grinten. Apparatus for measurement of the electric dipole moment of the neutron using a cohabiting atomic-mercury magnetometer. *Nuclear Instruments and Methods in Physics Research Section A: Accelerators, Spectrometers, Detectors and Associated Equipment*, 736:184–203, 2014.
- [59] Prajwal MohanMurthy. *A Search for Neutron to Mirror-Neutron Oscillations*. PhD thesis, 2020.
- [60] A Addazi, K Anderson, S Ansell, K S Babu, J L Barrow, D V Baxter, P M Bentley, Z Berezhiani, R Bevilacqua, R Biondi, C Bohm, G Brooijmans, L J Broussard, J Cedercäll, C Crawford, P S B Dev, D D DiJulio, A D Dolgov, K Dunne, P Fierlinger, M R Fitzsimmons, A Fomin, M J Frost, S Gardiner, S Gardner, A Galindo-Uribarri, P Geltenbort, S Girmohanta, P Golubev, E Golubeva, G L Greene, T Greenshaw, V Gudkov, R Hall-Wilton, L Heilbronn, J Herrero-Garcia, A Holley, G Ichikawa, T M Ito, E Iverson, T Johansson, L Jönsson, Y-J Jwa, Y Kamyshkov, K Kanaki, E Kearns, Z Kokai, B Kerbikov, M Kitaguchi, T Kittelmann, E Klinkby, A Kobakhidze, L W Koerner, B Kopeliovich, A Kozela, V Kudryavtsev, A Kupsc, Y T Lee, M Lindroos, J Makkinje, J I Marquez, B Meirose, T M Miller, D Milstead, R N Mohapatra, T Morishima, G Muhrer, H P Mumm, K Nagamoto, A Nepomuceno, F Nesti, V V Nesvizhevsky, T Nilsson, A Oskarsson, E Paryev, R W Pattie, S Penttil, H Perrey, Y N Pokotilovski, I Potashnikovav, K Ramic, C Redding, J-M Richard, D Ries, E Rinaldi, N Rizzi, N Rossi, A Ruggles, B Rybolt, V Santoro, U Sarkar, A Saunders, G Senjanovic, A P Serebrov, H M Shimizu, R Shrock, S Silverstein, D Silvermyr, W M Snow, A Takibayev, I Tkachev, L Townsend, A Tureanu, L Varriano, A Vainshtein, J de Vries, R Wagner, R Woracek, Y Yamagata, S Yiu, A R Young, L Zanini, Z Zhang, and O Zimmer. New high-sensitivity searches for neutrons converting into antineutrons and/or sterile neutrons at the HI-BEAM/NNBAR experiment at the european spallation source. *Journal of Physics G: Nuclear and Particle Physics*, 48(7):070501, jun 2021.
- [61] Michaël Sarrazin, Guillaume Pignol, Fabrice Petit, and Valery V. Nesvizhevsky. Experimental limits on neutron disappearance into another braneworld. *Physics Letters B*, 712(3):213–218, jun 2012.
- [62] Schmidt. U. An experimental limit on neutron mirror-neutron oscillation. Proceedings of BNLV International Workshop 2007. 13. Berkeley, CA, U.S.A, 2007.
- [63] L. J. Broussard, K. M. Bailey, W. B. Bailey, J. L. Barrow, B. Chance, C. Crawford, L. Crow, L. DeBeer-Schmitt, N. Fomin, M. Frost, A. Galindo-Uribarri, F. X. Gallmeier, L. Heilbronn, E. B. Iverson, Y. Kamyshkov, C. Y. Liu, I. Novikov, S. I. Penttillä, A. Ruggles, B. Rybolt, M. Snow, L. Townsend, L. J. Varriano, S. Vavra, and A. R. Young. New search for mirror neutrons at hfir, 2017.
- [64] N. Allemandou, H. Almazán, P. del Amo Sanchez, L. Bernard, C. Bernard, A. Blanchet, A. Bonhomme, G. Bosson, O. Bourrion, J. Bouvier, C. Buck, V. Caillot, M. Chala,

- P. Champion, P. Charon, A. Collin, P. Contrepolis, G. Coulloux, B. Desbrières, G. Deleglise, W. El Kanawati, J. Favier, S. Fuard, I. Gomes Monteiro, B. Gramlich, J. Haser, V. Helaine, M. Heusch, M. Jentschel, F. Kandzia, G. Konrad, U. Köster, S. Kox, C. Lahonde-Hamdoun, J. Lamblin, A. Letourneau, D. Lhuillier, C. Li, M. Lindner, L. Manzanillas, T. Materna, O. Méplan, A. Minotti, C. Monon, F. Montanet, F. Nunio, F. Peltier, Y. Penichot, M. Pequignot, H. Pessard, Y. Piret, G. Prono, G. Quémener, J.-S. Real, C. Roca, T. Salagnac, V. Sergeyeva, S. Schoppmann, L. Scola, J.-P. Scordilis, T. Soldner, A. Stutz, D. Tourres, C. Vescovi, and S. Zsoldos. The STEREO experiment. *Journal of Instrumentation*, 13(07):P07009–P07009, jul 2018.
- [65] Matheus Hostert, David McKeen, Maxim Pospelov, and Nirmal Raj. Dark sectors in neutron-shining-through-a-wall and nuclear absorption signals, 2022.
- [66] Philipp Schmidt-Wellenburg. *Production of ultracold neutrons in superfluid helium under pressure*. PhD thesis, 2009.
- [67] NIST. Codata internationally recommended 2018 values of the fundamental physical constants.
- [68] Particle Data Group, P A Zyla, R M Barnett, J Beringer, O Dahl, D A Dwyer, D E Groom, C J Lin, K S Lugovsky, E Pianori, D J Robinson, C G Wohl, W M Yao, K Agashe, G Aielli, B C Allanach, C Amsler, M Antonelli, E C Aschenauer, D M Asner, H Baer, Sw Banerjee, L Baudis, C W Bauer, J J Beatty, V I Belousov, S Bethke, A Bettini, O Biebel, K M Black, E Blucher, O Buchmuller, V Burkert, M A Bychkov, R N Cahn, M Carena, A Ceccucci, A Cerri, D Chakraborty, R Sekhar Chivukula, G Cowan, G D’Ambrosio, T Damour, D de Florian, A de Gouvêa, T DeGrand, P de Jong, G Dissertori, B A Dobrescu, M D’Onofrio, M Doser, M Drees, H K Dreiner, P Eerola, U Egede, S Eidelman, J Ellis, J Erler, V V Ezhela, W Fetscher, B D Fields, B Foster, A Freitas, H Gallagher, L Garren, H J Gerber, G Gerbier, T Gershon, Y Gershtein, T Gherghetta, A A Godizov, M C Gonzalez-Garcia, M Goodman, C Grab, A V Gritsan, C Grojean, M Grünewald, A Gurtu, T Gutsche, H E Haber, C Hanhart, S Hashimoto, Y Hayato, A Hebecker, S Heinemeyer, B Heltsley, J J Hernández-Rey, K Hikasa, J Hisano, A Höcker, J Holder, A Holtkamp, J Huston, T Hyodo, K F Johnson, M Kado, M Karliner, U F Katz, M Kenzie, V A Khoze, S R Klein, E Klempt, R V Kowalewski, F Krauss, M Kreps, B Krusche, Y Kwon, O Lahav, J Laiho, L P Lellouch, J Lesgourgues, A R Liddle, Z Ligeti, C Lippmann, T M Liss, L Littenberg, C Lourenço, S B Lugovsky, A Lusiani, Y Makida, F Maltoni, T Mannel, A V Manohar, W J Marciano, A Masoni, J Matthews, U G Meißner, M Mikhasenko, D J Miller, D Milstead, R E Mitchell, K Mönig, P Molaro, F Moortgat, M Moskovic, K Nakamura, M Narain, P Nason, S Navas, M Neubert, P Nevski, Y Nir, K A Olive, C Patrignani, J A Peacock, S T Petcov, V A Petrov, A Pich, A Piepke, A Pomarol, S Profumo, A Quadt, K Rabbertz, J Rademacker, G Raffelt, H Ramani, M Ramsey-Musolf, B N Ratcliff, P Richardson, A Ringwald, S Roesler, S Rolli, A Romaniouk, L J Rosenberg, J L Rosner, G Rybka, M Ryskin, R A Ryutin, Y Sakai, G P Salam, S Sarkar, F Sauli, O Schneider, K Scholberg, A J Schwartz, J Schwiening, D Scott, V Sharma, S R Sharpe, T Shutt, M Silari, T Sjöstrand, P Skands, T Skwarnicki, G F Smoot, A Soffer, M S Sozzi, S Spanier, C Spiering, A Stahl, S L Stone, Y Sumino, T Sumiyoshi, M J Syphers,

- F Takahashi, M Tanabashi, J Tanaka, M Taševský, K Terashi, J Terning, U Thoma, R S Thorne, L Tiator, M Titov, N P Tkachenko, D R Tovey, K Trabelsi, P Urquijo, G Valencia, R Van de Water, N Varelas, G Venanzoni, L Verde, M G Vinciter, P Vogel, W Vogelsang, A Vogt, V Vorobyev, S P Wakely, W Walkowiak, C W Walter, D Wands, M O Wascko, D H Weinberg, E J Weinberg, M White, L R Wiencke, S Willocq, C L Woody, R L Workman, M Yokoyama, R Yoshida, G Zanderighi, G P Zeller, O V Zenin, R Y Zhu, S L Zhu, F Zimmermann, J Anderson, T Basaglia, V S Lugovsky, P Schaffner, and W Zheng. Review of Particle Physics. *Progress of Theoretical and Experimental Physics*, 2020(8), 08 2020. 083C01.
- [69] A. T. Yue, M. S. Dewey, D. M. Gilliam, G. L. Greene, A. B. Laptev, J. S. Nico, W. M. Snow, and F. E. Wietfeldt. Improved determination of the neutron lifetime. *Phys. Rev. Lett.*, 111:222501, Nov 2013.
- [70] Stephan Paul. The puzzle of neutron lifetime. *Nuclear Instruments and Methods in Physics Research Section A: Accelerators, Spectrometers, Detectors and Associated Equipment*, 611(2):157–166, 2009. Particle Physics with Slow Neutrons.
- [71] Kim Ulrike Roß. *Towards a high precision measurement of the free neutron lifetime with τ SPECT*. PhD thesis, 2021.
- [72] R. W. Pattie, N. B. Callahan, C. Cude-Woods, E. R. Adamek, L. J. Broussard, S. M. Clayton, S. A. Currie, E. B. Dees, X. Ding, E. M. Engel, D. E. Fellers, W. Fox, P. Geltenbort, K. P. Hickerson, M. A. Hoffbauer, A. T. Holley, A. Komives, C.-Y. Liu, S. W. T. MacDonald, M. Makela, C. L. Morris, J. D. Ortiz, J. Ramsey, D. J. Salvat, A. Saunders, S. J. Seestrom, E. I. Sharapov, S. K. Sjue, Z. Tang, J. Vanderwerp, B. Vogelaar, P. L. Walstrom, Z. Wang, W. Wei, H. L. Weaver, J. W. Wexler, T. L. Womack, A. R. Young, and B. A. Zeck. Measurement of the neutron lifetime using a magneto-gravitational trap and in situ detection. *Science*, 360(6389):627–632, may 2018.
- [73] Robert Golub, Steve Keith Lamoreaux, and David J. Richardson. *Ultra-cold neutrons*. Hilger, 1991.
- [74] H. Becker, G. Bison, B. Blau, Z. Chowdhuri, J. Eikenberg, M. Fertl, K. Kirch, B. Lauss, G. Perret, D. Reggiani, D. Ries, P. Schmidt-Wellenburg, V. Talanov, M. Wohlmuther, and G. Zsigmond. Neutron production and thermal moderation at the psi ucn source. *Nuclear Instruments and Methods in Physics Research Section A: Accelerators, Spectrometers, Detectors and Associated Equipment*, 777:20–27, 2015.
- [75] T. Brys, M. Daum, P. Fierlinger, A. Foelske, M. Gupta, R. Henneck, S. Heule, M. Kasprzak, K. Kirch, M. Kuzniak, T. Lippert, M. Meier, A. Pichlmaier, and U. Straumann. Diamond-like carbon coatings for ultracold neutron applications. *Diamond and Related Materials*, 15(4):928–931, 2006. Diamond 2005.
- [76] G. Bison, M. Daum, K. Kirch, B. Lauss, D. Ries, P. Schmidt-Wellenburg, G. Zsigmond, T. Brenner, P. Geltenbort, T. Jenke, O. Zimmer, M. Beck, W. Heil, J. Kahlenberg, J. Karch, K. Ross, K. Eberhardt, C. Geppert, S. Karpuk, T. Reich, C. Siemenssen,

- Y. Sobolev, and N. Trautmann. Comparison of ultracold neutron sources for fundamental physics measurements. *Phys. Rev. C*, 95:045503, 4 2017.
- [77] F. Atchison, B. van den Brandt, T. Brys, M. Daum, P. Fierlinger, P. Hautle, R. Henneck, S. Heule, M. Kasprzak, K. Kirch, J. A. Konter, A. Michels, A. Pichlmaier, M. Wohlmuther, A. Wokaun, K. Bodek, U. Szerer, P. Geltenbort, J. Zmeskal, and Y. Pokotilovskiy. Production of ultracold neutrons from a cold neutron beam on a $^2\text{H}_2$ target. *Phys. Rev. C*, 71:054601, May 2005.
- [78] A. Steyerl, H. Nagel, F.-X. Schreiber, K.-A. Steinhauser, R. Gähler, W. Gläser, P. Ageron, J.M. Astruc, W. Drexel, G. Gervais, and W. Mampe. A new source of cold and ultracold neutrons. *Physics Letters A*, 116(7):347–352, 1986.
- [79] G. Ban, G. Bison, K. Bodek, Z. Chowdhuri, P. Geltenbort, W. C. Griffith, V. Hélaine, R. Henneck, M. Kasprzak, Y. Kermaidic, K. Kirch, S. Komposch, P. A. Koss, A. Kozela, J. Krempel, B. Lauss, T. Lefort, Y. Lemièrre, A. Mtchedlishvili, M. Musgrave, O. Naviliat-Cuncic, F. M. Piegsa, E. Pierre, G. Pignol, G. Quémener, M. Rawlik, D. Ries, D. Rebreyend, S. Roccia, G. Rogel, P. Schmidt-Wellenburg, N. Severijns, E. Wursten, J. Zejma, and G. Zsigmond. Ultracold neutron detection with 6li-doped glass scintillators. *The European Physical Journal A*, 52(10), oct 2016.
- [80] Martin Klein and Christian J. Schmidt. Cascade, neutron detectors for highest count rates in combination with asic/fpga based readout electronics. *Nuclear Instruments and Methods in Physics Research Section A: Accelerators, Spectrometers, Detectors and Associated Equipment*, 628(1):9–18, 2011. VCI 2010.
- [81] F. M. Piegsa, M. Fertl, S. N. Ivanov, M. Kreuz, K. K. H. Leung, P. Schmidt-Wellenburg, T. Soldner, and O. Zimmer. New source for ultracold neutrons at the institut laue-langevin. *Phys. Rev. C*, 90:015501, Jul 2014.
- [82] S. Imajo, K. Mishima, M. Kitaguchi, Y. Iwashita, N. L. Yamada, M. Hino, T. Oda, T. Ino, H. M. Shimizu, S. Yamashita, and R. Katayama. Pulsed ultra-cold neutron production using a Doppler shifter at J-PARC. *Progress of Theoretical and Experimental Physics*, 2016(1), 01 2016. 013C02.
- [83] A Saunders, J.M Anaya, T.J Bowles, B.W Filippone, P Geltenbort, R.E Hill, M Hino, S Hoedl, G.E Hogan, T.M Ito, K.W Jones, T Kawai, K Kirch, S.K Lamoreaux, C.-Y Liu, M Makela, L.J Marek, J.W Martin, C.L Morris, R.N Mortensen, A Pichlmaier, S.J Seestrom, A Serebrov, D Smith, W Teasdale, B Tipton, R.B Vogelaar, A.R Young, and J Yuan. Demonstration of a solid deuterium source of ultra-cold neutrons. *Physics Letters B*, 593(1):55–60, 2004.
- [84] Fast acquisition system for nuclear research. <https://faster.in2p3.fr/>. Accessed: 2022-01-02.
- [85] G. Ban, G. Bison, K. Bodek, Z. Chowdhuri, P. Geltenbort, W. C. Griffith, V. HÉlaine, R. Henneck, M. Kasprzak, Y. Kermaidic, K. Kirch, S. Komposch, P. A. Koss, A. Kozela,

- J. Krempel, B. Lauss, T. Lefort, Y. Lemi re, A. Mtchedlishvili, M. Musgrave, O. Naviliat-Cuncic, F. M. Piegsa, E. Pierre, G. Pignol, G. Qu m ner, M. Rawlik, D. Ries, D. Rebreyend, S. Roccia, G. Rogel, P. Schmidt-Wellenburg, N. Severijns, E. Wursten, J. Zejma, and G. Zsigmond. Ultracold neutron detection with ^6Li -doped glass scintillators, NANOSC: a fast ultracold neutron detector for the nEDM experiment at the Paul Scherrer Institute. *European Physical Journal A*, 52:326, 2016. 14 pages, 12 figures, regular article submitted for publication.
- [86] M. Daum, A. Frei, P. Geltenbort, E. Gutsmedl, P. H bel, H.-C. Koch, A. Kraft, T. Lauer, A.R. M ller, S. Paul, and G. Zsigmond. A low-pass velocity filter for ultracold neutrons. *Nuclear Instruments and Methods in Physics Research Section A: Accelerators, Spectrometers, Detectors and Associated Equipment*, 675:103–111, 2012.
- [87] James E. Hesser and Kurt Dressler. Radiative lifetimes of ultraviolet emission systems excited in bf_3 , cf_4 , and sif_4 . *The Journal of Chemical Physics*, 47(9):3443–3450, 1967.
- [88] R.H. Dalitz. Cxii. on the analysis of τ -meson data and the nature of the τ -meson. *The London, Edinburgh, and Dublin Philosophical Magazine and Journal of Science*, 44(357):1068–1080, 1953.
- [89] G. Mavromanolakis. Quartz fiber calorimetry and calorimeters, 2004.
- [90] S. Raman, E. K. Warburton, J. W. Starner, E. T. Jurney, J. E. Lynn, P. Tikkanen, and J. Keinonen. Spectroscopy of ^{20}F levels. *Phys. Rev. C*, 53:616–646, 2 1996.
- [91] A. Morozov, M.M.F.R. Fraga, L. Pereira, L.M.S. Margato, S.T.G. Fetal, B. Guerard, G. Manzin, and F.A.F. Fraga. Photon yield for ultraviolet and visible emission from cf_4 excited with α -particles. *Nuclear Instruments and Methods in Physics Research Section B: Beam Interactions with Materials and Atoms*, 268(9):1456–1459, 2010.
- [92] S. J. Seestrom, E. R. Adamek, D. Barlow, L. J. Broussard, N. B. Callahan, S. M. Clayton, C. Cude-Woods, S. Currie, E. B. Dees, W. Fox, P. Geltenbort, K. P. Hickerson, A. T. Holley, C.-Y. Liu, M. Makela, J. Medina, D. J. Morley, C. L. Morris, J. Ramsey, A. Roberts, D. J. Salvat, A. Saunders, E. I. Sharapov, S. K. L. Sjue, B. A. Slaughter, B. VornDick, P. L. Walstrom, Z. Wang, T. L. Womack, A. R. Young, and B. A. Zeck. Upscattering of ultracold neutrons from gases. *Phys. Rev. C*, 92:065501, 12 2015.
- [93] K. Kirch, B. Lauss, P. Schmidt-Wellenburg, and G. Zsigmond. Ultracold neutrons—physics and production. *Nuclear Physics News*, 20(1):17–23, 2010.
- [94] Hamamatsu photonics.
- [95] Holland Shielding Systems BV | Leader in EMI/RFI shielding gaskets and solutions. Mu-ferro shielding foil.
- [96] Marcin Ku niak. *The Neutron Electric Dipole Moment Experiment: Research and Development for the New Spectrometer*. PhD thesis, 2008.
- [97] G. Cowan. *Statistical data analysis*. Oxford University Press, USA, 1998.

- [98] Benoit Clement. Starucn (simulation of transmission, absorption and reflection of ultracold neutrons).
- [99] Baptiste Perriolat. Search for the mirror world with ultra-cold neutrons. Master's thesis, Grenoble-Alpes University, 2020.
- [100] C. Abel, S. Afach, N. J. Ayres, C. A. Baker, G. Ban, G. Bison, K. Bodek, V. Bondar, M. Burghoff, E. Chanel, Z. Chowdhuri, P.-J. Chiu, B. Clement, C. B. Crawford, M. Daum, S. Emmenegger, L. Ferraris-Bouchez, M. Fertl, P. Flaux, B. Franke, A. Fratangelo, P. Geltenbort, K. Green, W. C. Griffith, M. van der Grinten, Z. D. Grujić, P. G. Harris, L. Hayen, W. Heil, R. Henneck, V. Hélaine, N. Hild, Z. Hodge, M. Horras, P. Iaydjiev, S. N. Ivanov, M. Kasprzak, Y. Kermaidic, K. Kirch, A. Knecht, P. Knowles, H.-C. Koch, P. A. Koss, S. Komposch, A. Kozela, A. Kraft, J. Krempel, M. Kuźniak, B. Lauss, T. Lefort, Y. Lemièrre, A. Leredde, P. Mohanmurthy, A. Mtchedlishvili, M. Musgrave, O. Naviliat-Cuncic, D. Pais, F. M. Piegsa, E. Pierre, G. Pignol, C. Plonka-Spehr, P. N. Prashanth, G. Quémener, M. Rawlik, D. Rebreyend, I. Rienäcker, D. Ries, S. Roccia, G. Rogel, D. Rozpedzik, A. Schnabel, P. Schmidt-Wellenburg, N. Severijns, D. Shiers, R. Tavakoli Dinani, J. A. Thorne, R. Viro, J. Voigt, A. Weis, E. Wursten, G. Wyszynski, J. Zejma, J. Zenner, and G. Zsigmond. Measurement of the permanent electric dipole moment of the neutron. *Phys. Rev. Lett.*, 124:081803, 2 2020.
- [101] D.W. Allan. Statistics of atomic frequency standards. *Proceedings of the IEEE*, 54(2):221–230, 1966.
- [102] Heinz-Peter Breuer and Francesco Petruccione. *The Theory of Open Quantum Systems*. Oxford University Press, 01 2007.
- [103] Abel, C., Ayres, N. J., Ban, G., Bison, G., Bodek, K., Bondar, V., Chanel, E., Chiu, P.-J., Clement, B., Crawford, C., Daum, M., Emmenegger, S., Flaux, P., Ferraris-Bouchez, L., Griffith, W.C., Grujić, Z.D., Harris, P.G., Heil, W., Hild, N., Kirch, K., Koss, P.A., Kozela, A., Krempel, J., Lauss, B., Lefort, T., Lemièrre, Y., Leredde, A., Mohanmurthy, P., Naviliat-Cuncic, O., Pais, D., Piegsa, F.M., Pignol, G., Rawlik, M., Rebreyend, D., Ries, D., Roccia, S., Ross, K., Rozpedzik, D., Schmidt-Wellenburg, P., Schnabel, A., Severijns, N., Thorne, J., Viro, R., Voigt, J., Weis, A., Wursten, E., Zejma, J., and Zsigmond, G. The n2edm experiment at the paul scherrer institute. *EPJ Web Conf.*, 219:02002, 2019.
- [104] A.P. Serebrov, E.B. Aleksandrov, N.A. Dovator, S.P. Dmitriev, A.K. Fomin, P. Geltenbort, A.G. Kharitonov, I.A. Krasnoschekova, M.S. Lasakov, A.N. Murashkin, G.E. Shmelev, V.E. Varlamov, A.V. Vassiljev, O.M. Zhrebtsov, and O. Zimmer. Search for neutron–mirror neutron oscillations in a laboratory experiment with ultracold neutrons. *Nuclear Instruments and Methods in Physics Research Section A: Accelerators, Spectrometers, Detectors and Associated Equipment*, 611(2):137–140, 2009. Particle Physics with Slow Neutrons.
- [105] Riccardo Biondi. Monte carlo simulation for ultracold neutron experiments searching for neutron–mirror neutron oscillation. *International Journal of Modern Physics A*, 33(24):1850143, aug 2018.

- [106] W C Chen, T R Gentile, R Erwin, S Watson, Q Ye, K L Krycka, and B B Maranville. ^3He spin filter based polarized neutron capability at the NIST center for neutron research. *Journal of Physics: Conference Series*, 528:012014, jul 2014.
- [107] P. Geltenbort, L. Göttl, R. Henneck, K. Kirch, A. Knecht, M. Kuźniak, B. Lauss, T. Lefort, A. Mtchedlishvili, M. Meier, M. Negrazus, G. Petzoldt, P. Ruettimann, V. Vrankovic, and G. Zsigmond. A compact, large-diameter adiabatic spinflipper for ultracold neutrons. *Nuclear Instruments and Methods in Physics Research Section A: Accelerators, Spectrometers, Detectors and Associated Equipment*, 608(1):132–138, 2009.
- [108] V.I. Luschikov and Yu.V. Taran. On the calculation of the neutron adiabatic spinflipper. *Nuclear Instruments and Methods in Physics Research Section A: Accelerators, Spectrometers, Detectors and Associated Equipment*, 228(1):159–160, 1984.
- [109] S. Afach, G. Ban, G. Bison, K. Bodek, Z. Chowdhuri, M. Daum, M. Fertl, B. Franke, P. Geltenbort, Z. D. Grujić, L. Hayen, V. Hélaine, R. Henneck, M. Kasprzak, Y. Kermaidic, K. Kirch, S. Komposch, A. Kozela, J. Krempel, B. Lauss, T. Lefort, Y. Lemièrre, A. Mtchedlishvili, O. Naviliat-Cuncic, F. M. Piegsa, G. Pignol, P. N. Prashanth, G. Quémener, M. Rawlik, D. Ries, D. Rebreyend, S. Roccia, D. Rozpedzik, P. Schmidt-Wellenburg, N. Severijns, A. Weis, E. Wursten, G. Wyszynski, J. Zejma, and G. Zsigmond. A device for simultaneous spin analysis of ultracold neutrons, 2015.
- [110] A. Abragam. *The Principles of Nuclear Magnetism*. International series of monographs on physics. Clarendon Press, 1961.

Acknowledgements

Many people participated directly and indirectly in the realization of this work. I would like to thank first my PhD director Gilles Ban and supervisor Thomas Lefort. I really appreciate all their professional advises given during the last three years. They showed me how to do research while enjoying an agreeable atmosphere. Their remarks were always constructive and well received.

I had the pleasure to work with two collaborations. First with the n2EDM people, with whom we discussed multiple times about the characterization of the GADGET detector; thank you for all your comments. Then, with the $n - n'$ collaboration, who made possible the experimental construction and analysis presented in this thesis. I would like to thank Stephanie, Mathieu, Guillaume, Benoit, Philipp, Tobias, Jianqi, Thomas (Brenner), Oscar and Pin-Jung. All the short and long meetings with them taught me more than any course at the university.

The technical and administrative support from LPC staff was also crucial for reaching the objectives of this work. In particular, I would like to thank Damien and David for their very efficient and friendly participation in the experiments, and to Aurélie and Veronique for their great assistance in the bureaucratic labor.

The LPC is well known because of its cheerful environment. After four years of being next to people there, I could not agree more with this perception. I am thankful to all LPC members, in particular to my PhD comrades for sharing so many moments at the front garden, *la salle “secrète”* and even at Caen’s outskirts for the BBQs and molkky. I could not include all the names, but thanks Savitri (for the parmigianas), Alexandre (for the emacs tips), Chloé (for your kindness), Chiru (for the bike-rides), Cyril, Jöel, Belen, Pierrick, Leo, Alex, Hoa, Taras, Aurelien, Nathan, Raissa, Anthony and Louis.

Certainly, work at home was inevitable during the pandemic. Roommates, who became colleagues, friends and family, were of special support for the accomplishment of this work. I would like to thank La mona (por la música), Bastien (for *les frites*), Salo (for the discussions), Lucie (for the laughs), BenAnouk, Amalia, Helo, Lea, Chloé (Dieras) and Anto for making *La coloc* a cozy place.

In addition, thanks to all the friends who sent their encouragement even from the distance (Juli, Felix, Ana, Flo, Édou, Kena, Lena, Laura, Mirti, Miri and Ari) and to my family for giving me all the confidence. Thanks, ma, pa and mano. Special thanks to Dani, Alison, Omi, Caro and Juanpa for cross-checking this manuscript.

I could difficultly find a person who motivated me more than Sol. I owe you all the good feelings that I can see through your eyes. Thank you for coming from the hidden world.